Analysis of Microlensing Events with Latest Generation Telescopes

Sarang Shah

A thesis submitted in partial fulfilment

of the requirement for the degree of

Doctor of Philosophy in Physics at the

University of Canterbury

University of Canterbury

2019

Disclaimer

The research described in this thesis was carried out in the Department of Physics and Astronomy at the University of Canterbury under the supervision of Assoc. Prof. Michael D. Albrow of the University of Canterbury. While most of the work contained in the thesis is my own, and is original, in writing this thesis I have felt free to incorporate the insights provided to me by other people.

Chapter 1 is a review on basics of gravitational microlensing, photometry and data analysis of the microlensing events. It also discusses the effects involved in modelling of gravitational microlensing events and the use of microlensing to detect extra-solar planets. Chapter 2 is based on the bayesian analysis of the galactic model if all of the necessary microlensing quantities to estimate lens mass and distance are not known. Chapter 3 and Chapter 4 deals with the application of this galactic model to the single lens single source events $OGLE-2017-BLG-0192$ and $OGLE-2017-BLG-0103$ where orbital parallax is used to constrain the mass and distance of the lens. Chapter 5 is based on the concept of measuring parallax from space and in the later part of the chapter, the analysis of the microlensing event $OGLE-2017-BLG-1170$ is presented. Chapter 6 and Chapter 7 deal with the analysis of the planetary events $OGLE-2017-BLG-1647$ and $OGLE-2017-BLG-0380$ respectively. The results of all the chapters are yet to be published in research journals.

Be bee like busy.

Abstract

Gravitational microlensing is an astronomical phenomenon where the gravity of a foreground massive object bends the rays of light of a background source into images. Effectively, the background source appears to be magnified with respect to time. Since this does not require detection of light from the lens, gravitational microlensing can be used to study different populations of objects in the galaxy, even the extra-solar planets. This phenomenon was practically formulated and investigated since the last decade of 20^{th} century by a few observing groups. Today gravitational microlensing is observed and monitored by fourth generation telescopes towards high density stellar fields like the Galactic Bulge, Large and Small Magellanic clouds. With the increased capabilities there are numerous microlensing events that are detected but not yet analysed. Analysing these events, especially formed by a binary lens is not only challenging but tedious task. However with a suitable model that explains the light curve, we can estimate the mass and distance to the objects that are unlikely to be detected by other methods like direct imaging, transit and radial velocity.

In this thesis, I have shown how the microlensing data analysis can be done which not only includes filtering of the photometric data but also fitting of the appropriate microlensing model to the data. I also show how the prior knowledge about the nature of galaxy towards galactic bulge, the galactic model and higher order effects in microlensing can be used to constrain the lens mass and distance. I have analysed five microlensing events in this thesis. OGLE-2017-BLG-0192 and OGLE-2017-BLG-0103 are single lens single source events. The light curve of these events are explained by the orbital parallax effect. This galactic model analysis for these events gives the lens as a low mass star in the galactic disc. OGLE-2017-BLG-1170 is a microlensing event where the asymmetry in the peak of the light curve is caused by a secondary companion to the lens. This event was also observed due to Spitzer telescope which enabled us to measure the space parallax for this event. This galactic model analysis gives a pair of super-Jupiters located in the galactic bulge. OGLE-2018-BLG-1647 is a cusp approach microlensing event with a spike in the light curve close to the peak. The galactic model analysis of this event shows that the lens is a system of a high mass brown dwarf host and a Jupiter mass companion. The light curve of OGLE-2017-BLG-0380 needs a heuristic analysis and the small bump on the decreasing side can be explained by binary lens orbital motion of two masses in the galactic bulge where the primary is a dwarf star and the secondary companion is a brown dwarf.

The analysis of these binary lens events show that there are pair of low mass objects in the galaxy which can be detected by only by gravitational microlensing. Unfortunately these events cannot be studied further by other methods because of the faintness and large

distance to the lens. Nevertheless, growing samples of such low mass binaries suggest that there is a big population of such objects or even isolated low mass objects present in the galaxy. Overall, in this thesis, I show how helpful the latest generation microlensing survey telescopes are proving to characterise the gravitational micro-lenses.

Acknowledgements

I would like express my gratitude to my supervisor Assoc. Prof. Michael D. Albrow for his supervision. His guidance has helped me to realise the research potential of this field. I am grateful for the freedom and encouragement he has given me to pursue my own research and at times making sure I stayed on the right path. I am also grateful to Assoc. Prof. David Wiltshire for agreeing to be my co-supervisor.

This work was funded by the Marsden Fund Scholarship and also the departmental scholarship provided by the Department of Physics and Astronomy (2016) of the University of Canterbury.

In our research group, I would like to thank Dr. Antonio Herrera Martin for his friendship and constructive discussions. I would also like to Dr. Cheng-Yeng Lee and Dr. Mark Aartsen for the same. In the university, the friendship and companionship of Asta Heinesen, Aamirezza Rassi, Dr. Yongzuang Li, Usman Shahid, Srinidhi Bhessette, Pratik Solanki, Mukesh Devari is very much appreciated.

Outside physics, I am grateful to the operation friendship group organised by Russell James and others. I appreciate the love and care given by Russell, Helen, Margaret, Toby and others. I am also grateful to my school teachers, undergrad professors and post-grad professors in India who were very inspiring and motivating. I acknowledge the guidance of Mr. Rupesh Nerkar as well as Ms. Apurva Jakhadi who have motivated me for the right path since childhood. I also appreciate the role of his organisation for promoting science - "Vidnyan Prabodhini" to give me exposure in the field of experimental science in India. I am also grateful to other organisations like "Vidnyan Vedh" and "Aaryabhatta Academy" who have not only taught me the art of solving difficult problems in life, but have also helped me to develop a scientific approach towards life since childhood.

Lastly but not least, I would like to thank my mother, my wife and friends in India for their endless love and support during my thesis. They provided me with much needed care and understanding during my crucial times thus enabling me to focus on my research.

Dedicated to my mother.

Contents

Chapter 1

Introduction

1.1 Gravitational Lensing

Gravitational lensing is an astronomical phenomenon where the gravity of a foreground massive object bends the rays of light of a background source into images. This phenomenon was originally proposed by Henry Cavendish which was not published (Will, 1988). Johann Georg von Soldner later calculated and published the amount of bending of light based on Newton's corpuscular theory of light using a different approach than Henry Cavensish's (Jaki, 1978). Considering gravity as the geometric property of space-time, Einstein (1936) proposed more accurate theory of deflection of light due to gravity. He worked on the idea of bending of light rays due to gravity in the year 1912 even before proposing the general theory of relativity though he had doubted its possible observation Renn et al. (1997). However, the idea of bending of light due to gravity was first tested by Dyson et al. (1923) on 29^{th} May 1919, where the Sun's gravity bent the light from the stars in the Taurus constellation. This was observed during a solar eclipse observed from Principe island. Following this observation, it was shown later by Chwolson (1924) that if the lens is perfectly aligned with the source, the images will form a ring-like shape centred on the lens originally called "Chwolson Ring" but later termed as "Einstein Ring". The radius of this ring as projected on the lens plane is

$$r_E = \sqrt{\frac{4GM}{c^2}\frac{D_L(D_s - D_L)}{D_s}} \tag{1.1}$$

where,

1. G = Gravitational Constant

2. M = Mass of the lens
3. c = speed of light
4. D_L = distance to the lens
5. D_s = distance to the source

When a source passes across the Einstein radius of a point mass lens, it forms two images. One of these images is inside while the other is outside the Einstein ring (Figure 1.1). Due to the conservation of surface brightness, the effective brightness of the source increases momentarily i.e. it is magnified. This phenomenon is very rare and occurs only when the lens passes very close to the line of sight towards the source. For a point mass lens,

$$\beta = \theta - \alpha_d \tag{1.2}$$

where,

1. β = angular separation between the lens and the source.
2. θ = angular separation between the image and the lens.
3. α_d = angular separation between the image and the source.

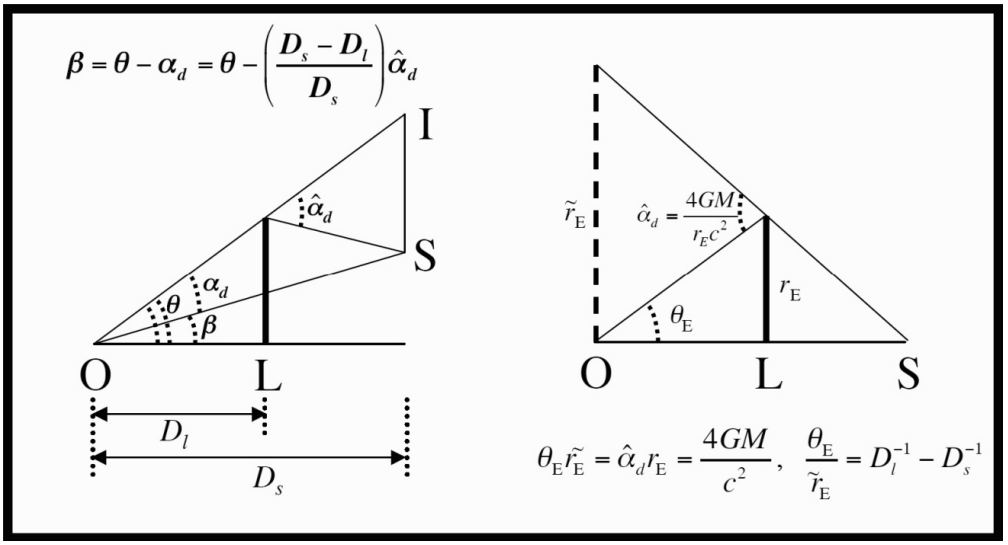

Figure 1.1: The basic geometry in microlensing. **O** is the observer, 'L' is the lens, 'I' is the image formed and 'S' is the source. Figure adapted from Gaudi (2010).

When the lens is a stellar mass, gravitational lensing is called *Gravitational Microlensing* (Paczynski, 1986). For the sources and lenses in the galaxy, the typical value of α_d is the order of milli-arcseconds so the individual images cannot be resolved. Also, α_d is

proportional to the mass of the lens (Eq. 1.3). So, for more massive lenses the angular separation between the images and the source is large. In this thesis, we follow the formalism of Gould (2000), where all the microlensing variables are evaluated in the observer plane. Referring to the basic geometry in (Figure 1.1), α_d in terms of an angle called as *angle of deflection*, $\hat{\alpha}_d$ which is the angle between the source and image on the lens plane

$$\alpha_d D_s = \hat{\alpha}_d (D_s - D_l); \quad \alpha_d = \hat{\alpha}_d \frac{(D_s - D_l)}{D_s} = \frac{4GM}{c^2 D_l \theta} \frac{(D_s - D_l)}{D_s} \tag{1.3}$$

where $\hat{\alpha}_d = \frac{4GM}{c^2 D_l \theta}$. Thus, we can re-write the lensing equation (1.2) as

$$\beta = \theta - \frac{4GM}{c^2 \theta} \frac{D_s - D_l}{D_s D_l} \tag{1.4}$$

When the angular separation between the lens and the source is zero, i.e. $\beta = 0$, $\theta = \hat{\alpha}_d$ i.e. the images are formed into Einstein ring having angular size θ_E $\left(\text{where } \theta_E = \sqrt{\frac{4GM}{c^2}\left(\frac{1}{D_l} - \frac{1}{D_s}\right)}\right)$.

1.1.1 Single Lenses in Microlensing

Gravitational Microlensing due to single lenses i.e. point mass lens is the simplest form of gravitational microlensing usually observed towards galactic bulge, large and small Magellanic Clouds due to higher rate. The average mass of these lenses is $0.6 M_\odot$ (Suzuki et al., 2018). However, the mass spectrum ranges from isolated planetary masses (Gould et al., 2009, Mróz et al., 2017, Poindexter et al., 2005) to black holes (Agol et al., 2002, Bennett et al., 2002a,b, Mao et al., 2002). The formalism for gravitational microlensing was initially proposed to explore the heavier MACHO's/dark matter in the galaxy (Kiraga & Paczynski, 1994, Paczynski, 1986). However, as the observation techniques improved, it is possible to study lens masses down to the mass of brown dwarfs (Gould et al., 2009). Microlensing even has capability to detect freely floating planets or planets in very wide separation around the host star up to the mass of Mars (Han, 2003, Mróz et al., 2019, Mróz et al., 2017, Penny et al., 2019). Rewriting the lens equation (1.4) in units of angular Einstein radius

$$\frac{\beta}{\theta_E} = \frac{\theta}{\theta_E} - \frac{\theta_E}{\theta} \quad \rightarrow \quad u = y - y^{-1} \tag{1.5}$$

where u = $\frac{\beta}{\theta_E}$ is the angular source position and y = $\frac{\theta}{\theta_E}$ is the angular image position, both normalised to angular Einstein radius. As mentioned above, when a source crosses the Einstein ring of the lens, it forms two images on its opposite sides (±) of the lens. In the case of a relative lens-source rectilinear motion (Figure 1.2), the trajectory of the source on the lens plane at time t is

$$u = \sqrt{{u_0}^2 + \left(\frac{t - t_0}{t_E}\right)^2} \tag{1.6}$$

where,

1. u_0 = closest angular approach between lens and source
2. t_0 = time of the closest angular approach between lens and source.
3. t_E = the time required by the source to cross the Einstein radius of the lens.

The position of these images can be obtained by rearranging and solving equation (1.5)

$$y^2 - y - uy = 0 \rightarrow y_{\pm} = \frac{1}{2}\Big(u \pm (u^2 + 4)\Big)^{\frac{1}{2}} \tag{1.7}$$

The magnification, which is the ratio of the area of the images to the area of the source is visible as the relative increase in brightness of the source (Figure 1.3) which is a function of time when the source is moving relative to the lens.

$$A = \frac{Area_{Image}}{Area_{source}} = \frac{u^2 + 2}{u\sqrt{u^2 + 4}} \tag{1.8}$$

Using equation (1.7) and equation (1.8), we can plot magnification as a function of time for different values of u_0 (Figure 1.3). The resultant curve is called Paczyński Curve, and the characteristic microlensing parameters are (u_0, t_0, t_E). We see from Figure (1.3), that as the value of u_0 is reduced, we get higher magnification (Paczynski, 1986). Towards the galactic bulge, a range of parameters (u_0, t_0, t_E) produce observable microlensing events. However to practically identify a microlensing event, an approximate requirement is that the peak magnification must be greater than 1.34 which corresponds to the u_0 from 0 to 1.

1.1.2 Binary Lenses

Although the majority of the detected microlensing events are produced by single lens, some fraction of them are due to binary lenses. It was proposed by Griest (1991) and

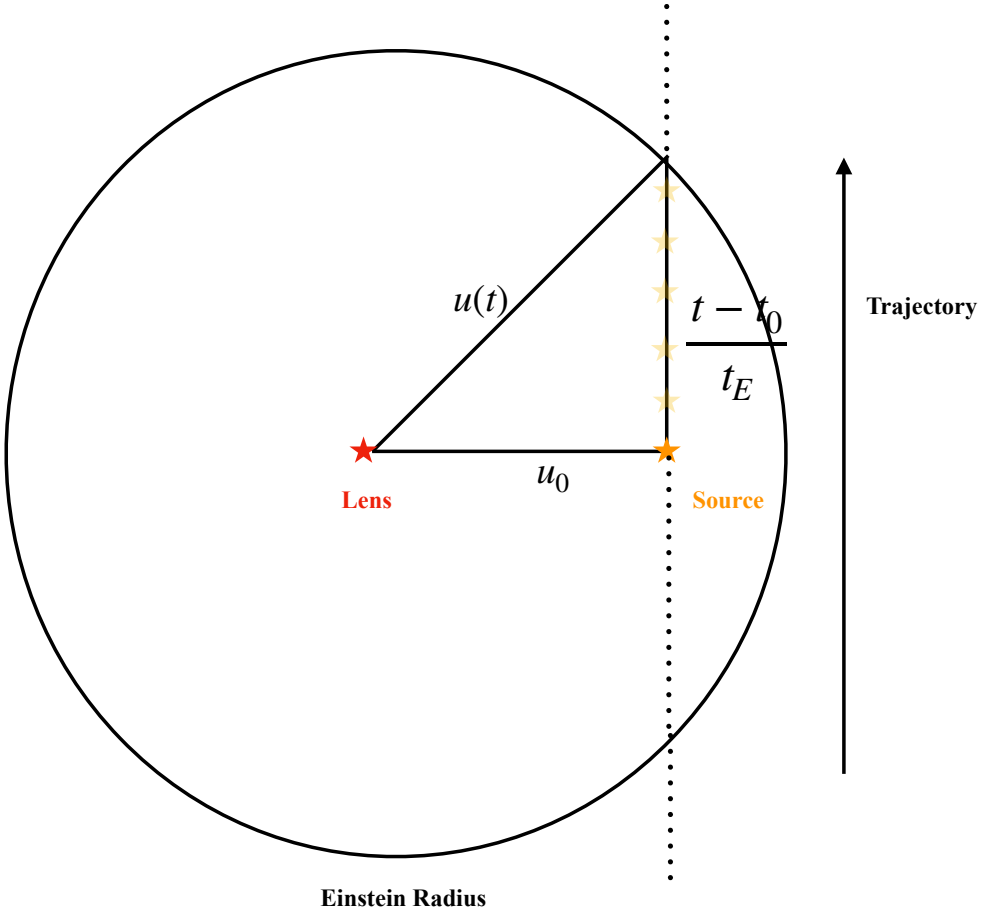

Figure 1.2: The figure showing the source trajectory on the lens plane giving rise to single lens microlensing event.

Paczynski (1991) that objects like brown dwarf in binary lens could be detected if a bulge star undergoes microlensing due to a disk star. Mao & Paczynski (1991) proposed that using the formalism of (Schneider & Weiss, 1986) and (Witt, 1990), binary lens microlensing events towards the galactic bulge could also lead to detection of exoplanets. Gould & Loeb (1992) showed that with the necessary practical setup and adequate observations, binary lenses with exoplanets could be detected. This method relied on survey and follow up strategies where interesting events could be observed with high cadence. Though the method led to the detection of several binary lenses by the end of twentieth century (Albrow et al., 1998, Alcock et al., 2001, Dominik & Hirshfeld, 1996, EROS Collaboration et al., 1998, Rhie & Bennett, 1996), it was in early 21^{st} century that the first exoplanet was detected by this method (Bond et al., 2004). After the initial detection of binary lens microlensing events, theoretical research began studying the parameter space of binary lenses and the information that could be extracted by modelling them (Albrow et al., 1998, 1999, Bozza, 2000, Dominik, 1998, Griest & Safizadeh, 1998).

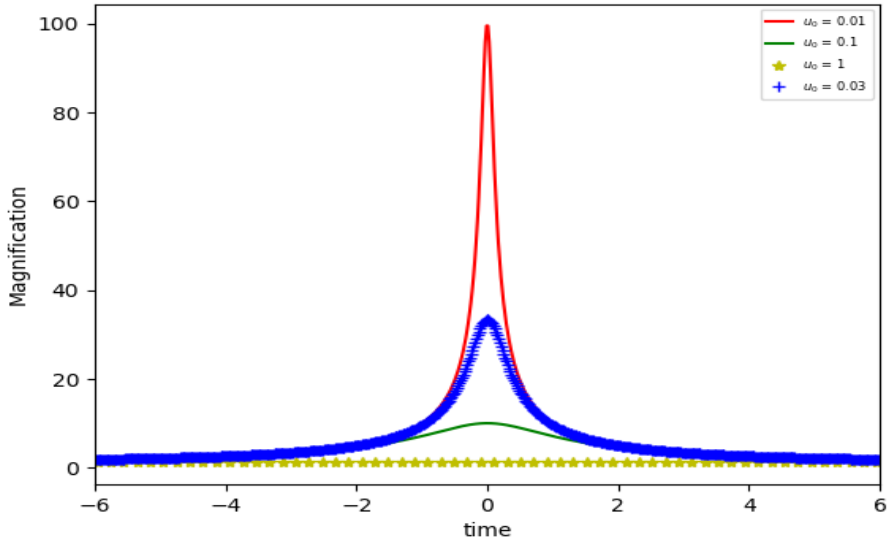

Figure 1.3: The magnification curve for a single lens event with respect to time. The angular lens source separation normalised to angular Einstein radius $(u_0) = 0.1$ and it takes 22 days for the source to cross the Einstein radius of the lens.

For example (Griest & Safizadeh, 1998) proposed that high magnification events could show planetary signatures at the peak due to perturbation of the central caustic[1] because of source trajectory being close to or passing through the central caustic[2], Dominik (1998) and Bozza (2000) studied the nature of extreme binaries and the caustics produced by them, Albrow et al. (1998) determined that the the photometry of the binary lens $MACHO - 97 - BLG - 41$ could be best explained when the lens was allowed to rotate around the companion, Gaudi (1998) found that binary source microlensing events having high flux ratio can mimic planetary signals and Albrow et al. (1999) determined the amount of relative lens source proper motion by analysing a caustic crossing event - $MACHO - 98 - SMC - 1$. Unlike single lenses, binary lenses are computationally expensive to analyse and require significant parts of the light curve to be densely monitored by observations to avoid parameter degeneracies (Bachelet et al., 2018, Choi et al., 2012, Dominik, 2009, Han, 2009, Han et al., 2018, Hwang et al., 2013, 2018, Park et al., 2014, Skowron et al., 2018). Nevertheless, numerous binary lens microlensing events with verifiable lens mass and distance have been analysed due to advancements in computational capabilities.

For binary lenses we can express image and source positions on the complex plane of the source,

[1] Caustics in case of binary lens are the line structure that represent infinite magnification. They are defined later in the chapter.

[2] This is caused by planets orbiting extremely close or far from the host star. This is known as $s \rightarrow s^{-1}$ degeneracy and is discussed in Chapter 5 and Chapter 6

$$\zeta = u_1 + iu_2; \quad z = y_1 + iy_2 \tag{1.9}$$

Thus, for two lenses, the lensing equation (1.3) can be re-written as

$$\zeta = z - \frac{\epsilon_1}{\overline{z} - \overline{z}_{m_1}} - \frac{\epsilon_2}{\overline{z} - \overline{z}_{m_2}} \tag{1.10}$$

where, $\epsilon_{1,2} = \frac{m_{1,2}}{M_{total}}$ are the weighted masses of each component, $z_{m,1,2}$ are the positions of the masses 1 and 2 and $\overline{z}_{m,1,2}$ are their complex conjugates respectively (Witt, 1990). This equation leads to a 5^{th} order complex polynomial (Witt & Mao, 1995) of z which requires numerical methods like *Contour Integration* Bozza (2010), Dominik (2007), Schramm & Kayser (1987), *Image Centred Inverse Ray Shooting* (Bennett, 2010, Rhie & Bennett, 1996) and hexadecapole (Gould, 2008, Pejcha & Heyrovský, 2009) to find the roots which are the images.

Each binary lens forms a set of closed curves on the source plane where the magnification becomes infinite; these curves are called *caustics* (Figure 1.4). There are three or five real image positions depending upon whether the source trajectory crosses the caustic. The magnification of the source due to binary lens is given by equation (1.11) which is the inverse of the determinant of the Jacobian evaluated at the position of the source [3],

$$A = \frac{1}{detJ}, \quad detJ = 1 - \left| \sum_{n=1}^{2} (\frac{\epsilon_n}{\overline{z} - \overline{z}_{m,n}})^2 \right| \tag{1.11}$$

Unlike a single lens magnification, calculating binary lens magnification requires 7 parameters: the Paczyński parameters u_0, t_0 and t_E, the mass ratio q, the separation normalised to angular Einstein radius, s, angular source size normalised to angular Einstein radius, ρ and the angle of the source trajectory on the lens plane ϕ. As an example of a caustic, we show a magnification map in Figure (1.4). Each pixel of a magnification map represents the value of magnification that the source experiences on each point in the complex source plane. At certain regions around the lenses where the magnification becomes infinite it can be seen as caustics.

If the source is assumed as point, the magnification becomes infinite when it straddles the caustic. However, in reality the source has a finite size which smoothens the peak of magnification. The part of the source which crosses the caustic first experiences a

[3] Appendix E: McDougall A, 2014, Gravitational microlensing: An automated high-performance modelling system, http://hdl.handle.net/10092/9973

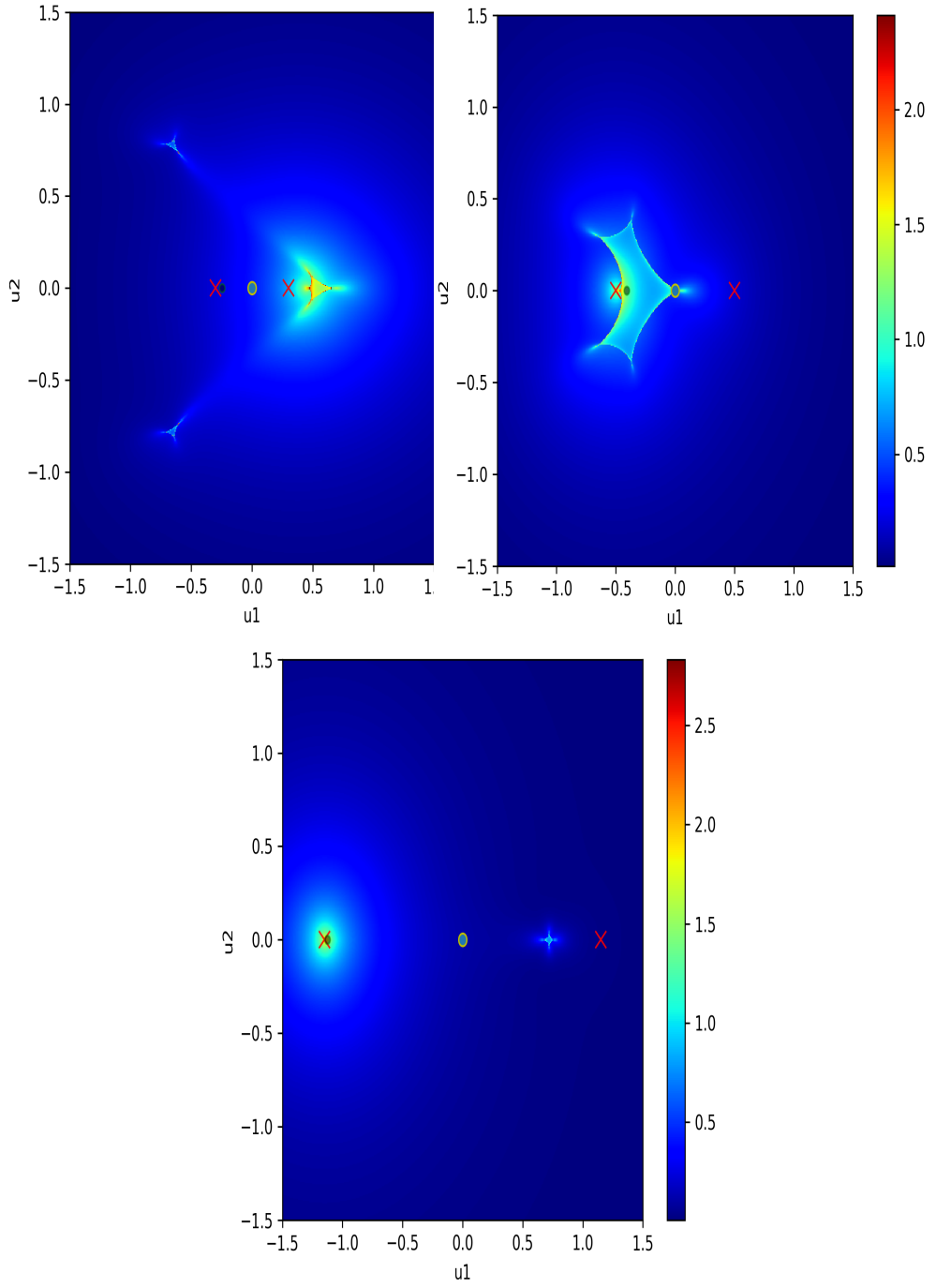

Figure 1.4: The figures show the magnification maps for various mass and separation ratios. (a) shows the caustic formed when the companion lies inside the Einstein radius of the primary. This is called close binary where the caustic structure shown is formed due to $[(s, q) = (0.6, 0.1)]$. (b) shows the case when the companion lies close to the Einstein radius of the primary. In this case the caustic structure formed is called as Resonant caustic. The resonant caustic shown is formed using $[(s, q) = (1.0, 0.1)]$. (c) shows the case when the separation between the companions is very larger than the Einstein radius of the primary. In this case a central caustic and a planetary caustics are formed. The caustic structure shown is formed using $[(s, q) = (2.3, 0.1)]$.

higher magnification than the succeeding part. When the source leaves the caustic, the part which leaves first decreases in magnification followed by the succeeding part. The magnification that the source experiences inside the caustics is lower than on the caustics which reflects a decrease in magnification. Also it is incorrect to assume uniform brightness of the source as the source is brightest at the centre and decreases in brightness radially outwards. This effect is called *Limb Darkening* (Bennett, 2010),

$$I_{L.D.} = 1 - \Gamma\left(1 - \sqrt{1 - (\frac{r}{\rho})^2}\right) \tag{1.12}$$

where $I_{L.D.}$ is the normalised brightness at a distance r from the centre of the source star having radius ρ and Γ is the limb-darkening coefficient. In this thesis, binary lens light curves are analysed adopting a fixed value for the limb darkening co-efficient (Γ) = 0.53 which is typical value of red giant source stars towards the bulge with temperature around 5500K (Claret, 2000). The case of single lens is simpler as it has only one point caustic which is centred on the lens itself while a binary lens has multiple line caustics either connected or disjoint. Depending on the q and s, the caustics can be divided into three categories: close (s<<1), resonant (s $\sim$ 1) and wide (s>>1).

1.2 Data collecting sites

After realising the significance of the microlensing method not only in detecting MACHOs but also exoplanets (Mao & Paczynski, 1991), Gould & Loeb (1992) laid down the practical requirements of detecting exoplanets. It was proposed that the microlensing events observed by survey telescopes and events can yield a planetary perturbation, especially high magnification events (Griest & Safizadeh, 1998). These events could be observed densely by follow-up telescope networks spread across the globe. Initially, groups like OGLE (Udalski et al., 1994), MACHO (Bennett et al., 1993), EROS (Aubourg et al., 1994) started searching for microlensing events with the aim of finding planets and they were supplemented by targeted follow-up by the PLANET and μ-FUN networks. Currently, with modern generation CCD wide field cameras, 3 major groups observe and detect microlensing events in a wide area of the sky towards the galactic bulge and Magellanic Clouds - OGLE, KMTNet and MOA.

1.2.1 Optical Gravitational Lensing Experiment (OGLE)

Optical Gravitational Lensing Experiment (OGLE) was started in 1992 with 1.0m Swope telescope at Las Campanas Observatory, Chile. This led to the first detection of a

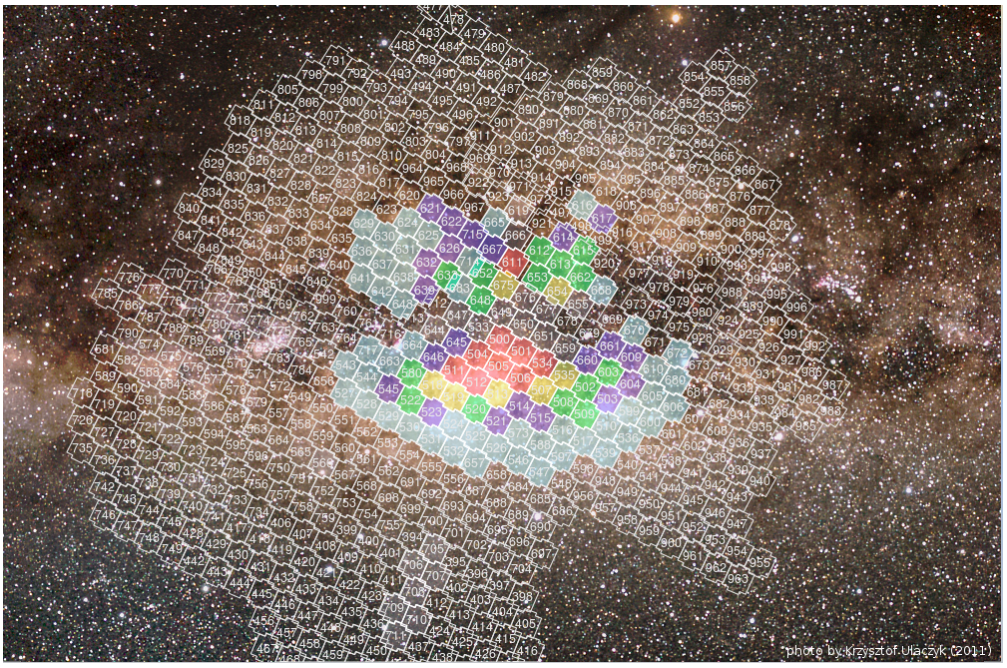

Figure 1.5: The sky map showing OGLE fields. Figure adopted from Udalski et al. (2015a).

microlensing event towards galactic centre (Alcock et al., 1997a, Aubourg et al., 1993, Udalski & Szymanski, 1995). OGLE implemented an *Early Warning System* [4] software to identify and alert ongoing microlensing events (Udalski et al., 1994). This system has proved beneficial as it always alerts the microlensing community to select events for follow-up observations. To date, OGLE has undergone several upgrades in equipment and data management as it is the oldest survey telescope. Currently, OGLE is in its fourth phase and not only monitors the galactic bulge, but also the LMC and SMC Udalski et al. (2015a). OGLE-IV has a 1.3m Ritchey-Cretien optical telescope with a field of view of $1.5 deg^2$. This field of view is covered by 32 mosaic CCD detectors with a resolution of 2048 x 4102 pixels. OGLE-IV thereby covers $3000 deg^2$ area of the sky regularly. Its main observations are done in I-band and the photometry ranges from 12<I<21 mag for the galactic bulge. Figure 1.5 shows the OGLE sky map which is monitored for galactic bulge microlensing events. Central bulge fields are densely monitored with cadence rates of red → 10-30 per night, yellow → 3-10 per night, green → 1-3 per night, blue → 0.5-1 per night, cyan → less than 0.5 per night and transparent fields are observed occasionally. In the year 2018, EWS detected 1803 microlensing events.

[4] ogle.astrouw.edu.pl/ogle4/ews

1.2.2 Korea Microlensing Telescope Network (KMTNet)

Korea Microlensing Telescope Network (KMTNet) is a project started by Korea Astronomy Science Institute (KASI) (Kim et al., 2016). It is an array of three 1.6m wide telescopes in Siding Spring Observatory (SSO; KMT-A) in Australia, South African Astronomical Observatory (SAAO; KMT-S) in South Africa and Cerro-Tololo Inter-American Observatory (CTIO; KMT-C) in Chile. These telescopes are wide field survey telescopes having mosaic CCD cameras producing a 2x2 deg^2 field of view (Figure 1.6). Since KMTNet telescopes are at similar latitudes but in different continents in the Southern Hemisphere, it can monitor the galactic bulge 24-hours per day (weather permitting). The KMTNet detectors are a mosaic of four 8k x 8k CCDs. In March of 2019, KMTNet has also started its alert system which alerts microlensing events discovered by KMTNet only. [5]

1.2.3 Microlensing Observations in Astrophysics (MOA)

Microlensing Observations in Astrophysics is a joint project started in 1995 by Nagoya University, Japan, the New Zealand universities of Auckland, Canterbury, Massey and Victoria as well Carter Observatory also at New Zealand. Initially MOA made observations not only to detect and characterise microlensing events but also to measure optical depth towards the galactic bulge using its 0.6m Boller and Chivens 61-cm f/6.25 Cassegrain telescope at Mt. John University Observatory of the University of Canterbury (Sumi et al., 2003). MOA collaboration detected the first confirmed microlensing planet along with OGLE collaboration in early 21^{st} century using this telescope (Bond et al., 2004).

MOA has later upgraded twice and currently it is operating with a wide field mosaic CCD camera mounted at the prime focus of the 1.8m MOA telescope. The camera has ten chips with 2k x 4k pixels that covers 2.2 deg^2 field of view (Sako et al., 2008). Using this technology and a fascinating location at Lake Tekapo, New Zealand, MOA group at Mt. John's regularly monitors dense stellar fields in the galactic bulge, LMC and SMC not only to detect and characterise planetary microlensing events but also to analyse finite source microlensing events, detect planets by transit method, search variable stars, detect optical afterglows from gamma ray bursts and searches dark matter (Hearnshaw et al., 2005). MOA observation fields towards the galactic bulge are shown in Figure (1.7).

[5] http://kmtnet.kasi.re.kr/ulens/event/2019/

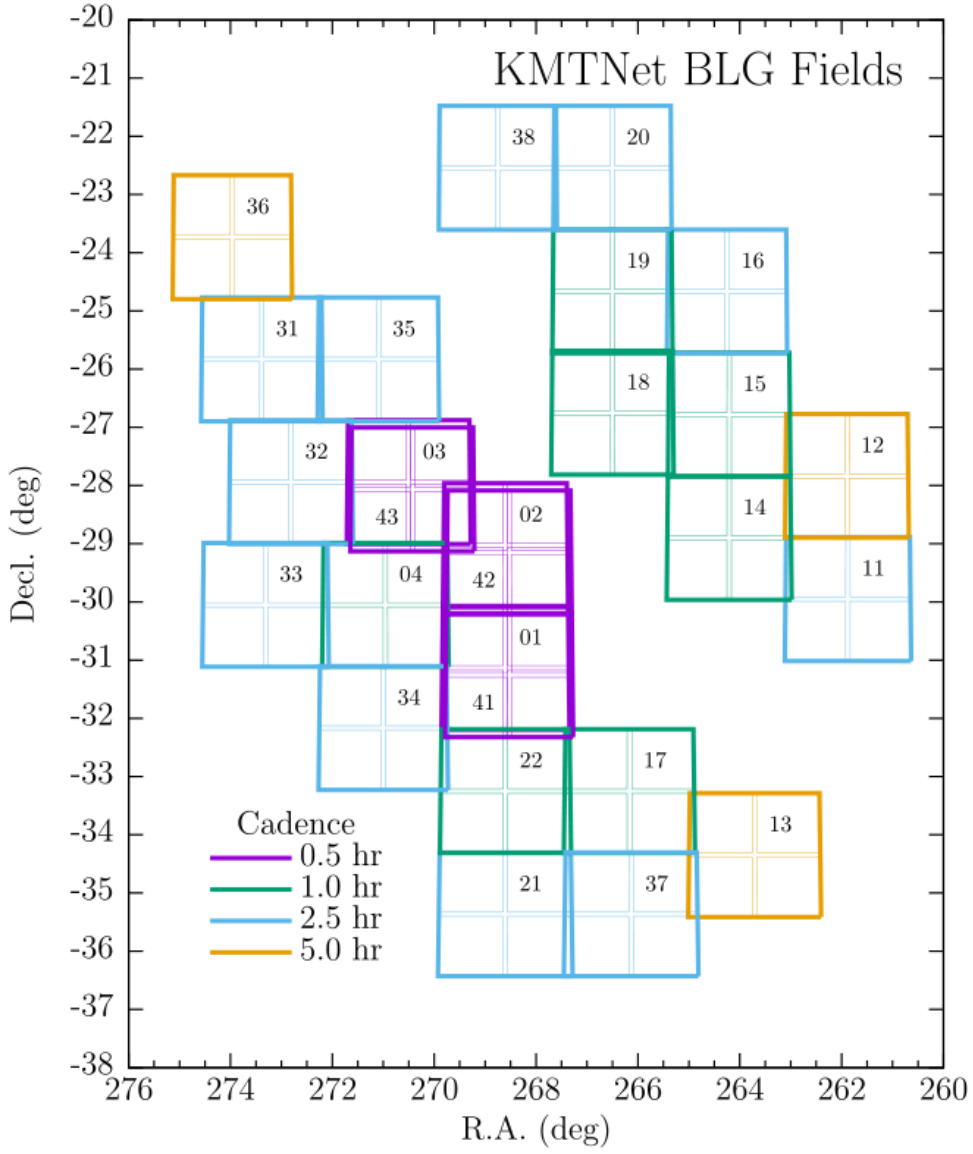

Figure 1.6: The sky map showing KMTNet fields. Plot taken from Kim et al. (2018).

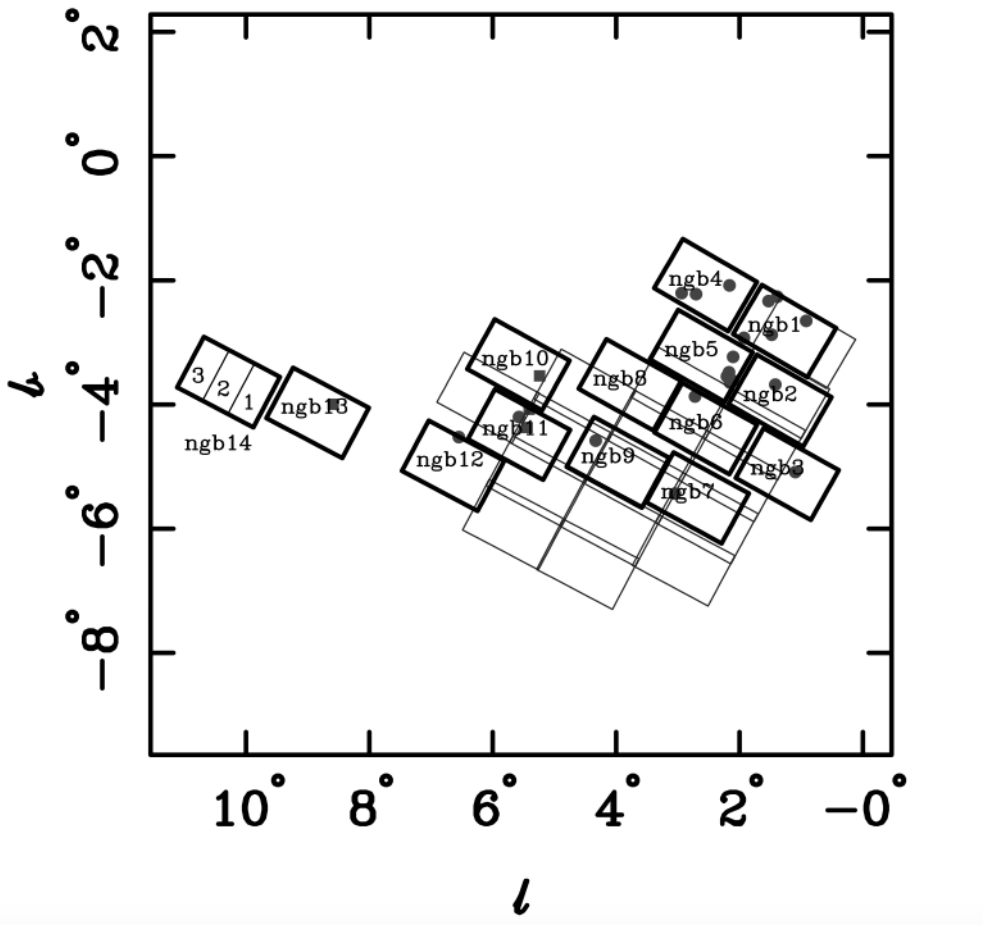

Figure 1.7: The sky map showing MOA fields. Plot taken from Bond et al. (2001).

1.3 Microlensing Modelling

1.3.1 Data reduction

The images from the observation sites (KMTNet only) are reduced to obtain time series photometry of the event. OGLE collaboration usually do not provide the images and hence we could not process OGLE images for the events discussed in this thesis with pyDIA and had to rely on their preliminary photometry on OGLE-EWS. At later stage when the results are confirmed, the OGLE collaboration could be requested.The image reduction software used in this thesis is pyDIA (Albrow, 2017), which is based on the difference imaging algorithm of Alard & Lupton (1998). The basic idea of this analysis is to select the best images from a set of given images and then subtract all other images from it. All the constant brightness stars are expected to cancel out from this difference while only variable brightness stars remain. Since the micro-lensed source star is a variable brightness star, we can extract a time series photometry of the source star. This algorithm has undergone modifications by Bramich et al. (2013) where gaussian polynomial kernels are replaced by delta-basis kernels for better photometry of the source star which lies in crowded fields towards bulge. pyDIA requires the pixel location of the source star and the area around the source star where the source star is to be searched for. It selects the images with smallest full-width at half-maximum (FWHM) of the source star and lowest background noise level out of the loaded images which are considered as reference images. The photometry of this reference image yields the reference flux, and equation (1.13) is used to obtain the difference image.

$$d_f(t)^n = T(t)^n - r_f \otimes K^n, \tag{1.13}$$

where $T(t)$ is the target image as a function of time, r_f is the reference image, and K is the convolution kernel. In Figure (1.8), an example of a reference image, target image and the difference image is shown. The source star is at peak magnification and is highlighted by the green circle in the difference image. It is expected to have a good photometry of the source star as telescope noise can interfere with the signal of the source star which may lead to false interpretation of the parameters (Bachelet et al., 2012, Woźniak & Paczyński, 1997).

1.3.2 Data filtering

Reduction of the images with pyDIA gives us a considerable information about the photometry of the event. The features obtained from the photometry are the time of the

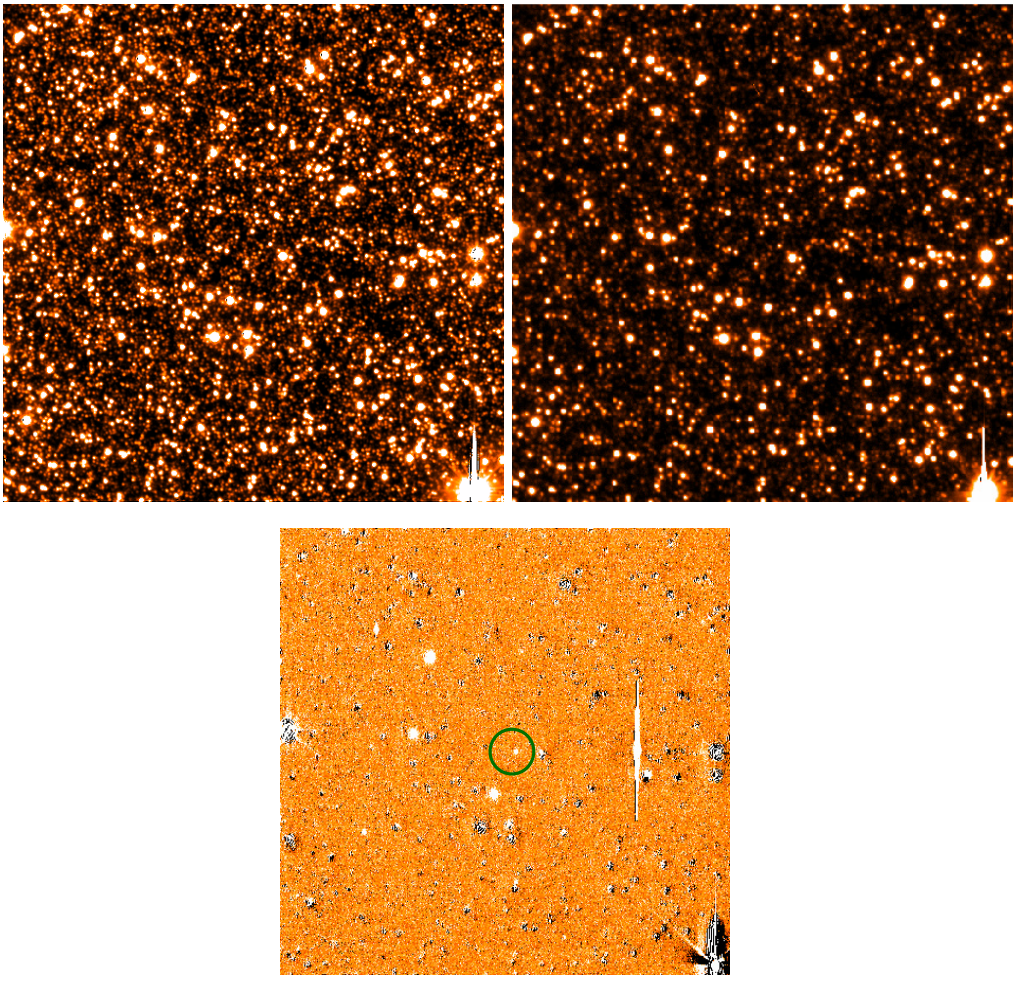

Figure 1.8: The figure starting from top left show the reference image, target image and difference image selected by pyDIA. The difference image analysis is performed for all the other images having this image as reference. The source star in this difference image is at peak magnification highlighted by green circle.

observation, difference flux (δf), uncertainties in the difference flux ($\sigma\delta f$), the apparent magnitude (mag.), uncertainties in apparent magnitude ($\sigma mag.$), quality factor denoting quality of the observation (Q), full width at half maximum of the PSF on the image (FWHM), roundness of the PSF on the image (Roundness), the sky level in the image and the signal to noise ratio in the image. These additional fields help us to identify and remove poor photometric measurements. In Appendix (B), we have shown the criteria which we have used to filter each data set for the events discussed in this thesis. For the photometry in I-band, pyDIA assumes a zero point (z.p.) of 28 with respect to which the difference magnitudes and the uncertainties in difference magnitudes are calculated whereas for the photometry in V-band, it assumes a zero point of 28.65.

Often the full moon affects the photometry by increasing the background sky level. The images during this period maybe affected due to this if the moon is close to the bulge

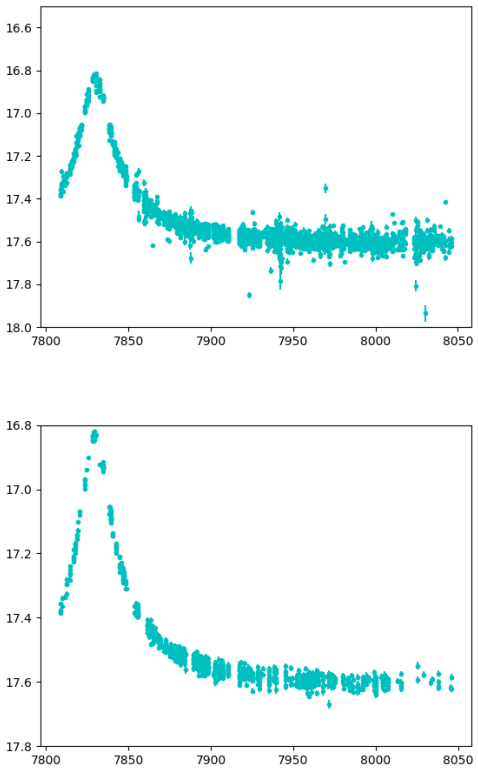

Figure 1.9: The time series photometry of the event $OGLE-2017-BLG-0103$ where the raw and filtered light curves are plotted.

eg. in case of the event *OGLE-2018-BLG-1647* discussed in Chapter 5. If the source star happens to be faint or close to bright stars, signal to noise ratio may be affected e.g. in case of *OGLE-2017-BLG-0103* and *OGLE-2017-BLG-0192* discussed in Chapter 3 and Chapter 4. The other features are affected if the source star happens to lie close to the edge of the image. This is when vignetting and aberration effects of the telescope optics affect the quality of the image at the edges. See the example in case of the event *OGLE-2018-BLG-0380* (Chapter 7) where the KMTNet field BLG42 is affected by this effect. Figure (1.9) shows the light curve of the microlensing event *OGLE-2017-BLG-0103* after plotting the time series photometry of the KMT-S dataset for the BLG02 field both filtered and unfiltered. The KMT-Net data was reduced with of pyDIA and filtered on the basis of background sky level, signal level, Q factor of the image and FWHM value of the source star on the image.

After obtaining good quality data, a light curve model is found by exploring the parameters space which best fits to the data. For any n^{th} image, the total flux of the source star (f) is a function of time which can be modelled as

$$M_n(t) = A(t)f_s + f_b \tag{1.14}$$

where $A(t)$ is the magnification of the source star, f_s is the source flux and f_b is the blend flux. The blending or blend flux is due to contamination of the light in the photometry of the source star due to neighbouring stars, or the lens itself (Bachelet et al., 2018, 2012, Beaulieu et al., 2016, Yee, 2015). Usually, positive values of blend flux are expected for a physical solution but in some cases negative value of blending up to a certain extent is permitted if the source lies in the mottled background stars of the crowded fields in the bulge (Albrow et al., 2018, Jiang et al., 2004, Park et al., 2004). This purely depends on the accuracy of the photometry packages doing the data reduction. Since we do not have direct information about the source and blended flux, we fit a model (M_n(t) = $A(t)f_s$ + f_b) to the observed light curve which gives f_s and f_b.

1.4 Exploring parameters space

1.4.1 Point source point lens (PSPL) parameters search

The process to model the observed light curve begins with a $PSPL$ model, which is characterised by the Paczyński parameters - (u_0, t_0 and t_E). To determine how well these parameters define the observed light curve, a statistical test is required. We use the χ^2 statistical test to determine the goodness of the fit,

$$\chi^2 = \sum_{n=1}^{n=N} \Big[\frac{(f_n(t) - M_n(t))^2}{2y_{err,n}^2} \Big] \tag{1.15}$$

where f_n(t) is the observed data point, $M_n(t)$ is the model through the data point and y_{err} is the uncertainty in it. The method used in the modelling is the *Bayesian Inference*,

$$P(parameter|data) \propto P(data|paramter) \times P(parameter) \tag{1.16}$$

where P(parameters|data) is the posterior probability of the parameter given the prior probability P(parameter) and the likelihood: P(data|parameter). The posterior probability is related to the likelihood function

$$L \propto e^{-\frac{\chi^2}{2}}, \tag{1.17}$$

To find the model, a process is needed to explore the parameter space. Parameters u_0, t_0 and t_E can be guessed from the light curve where $u_0 \sim 1/A_{max}$, t_0 is the time of the peak magnification and $t_E \sim$ FWHM of the light curve. In order to minimise the χ^2 these guesses are seeded to *emcee*, a python module (Foreman-Mackey et al., 2013) that

samples from the probability distribution. emcee is based on the Metropolis-Hasting algorithm of Markov Chain Monte Carlo (MCMC) technique. This technique is based on Markov chains and Monte Carlo integration which uses *Bayes' theorem* (Eq. 1.16) that finds the posterior distribution of the parameters by exploring the parameter space and maximising the likelihood function (Eq. 1.17) (Goodman & Weare, 2010, Metropolis et al., 1953). emcee utilises ensemble samplers which has numerous "walkers" that move through the parameter space one at a time that is based on partial resampling (Liu, 2008) and the rules of Metropolis-Hastings technique.

The prior probability function in equation (1.16) are uniform priors for the parameters described by,

$$\begin{aligned} P(u_0) &= 1 \rightarrow (0 < u_0 < 1); \\ P(t_0) &= 1 \rightarrow (7000 < t_0 < 9000); \\ P(t_E) &= 1 \rightarrow (0.1 < t_E < 600) \end{aligned} \tag{1.18}$$

where the prior in t_0 is in HJD-2450000 days.

1.4.2 Binary lens parameter search

We use the *MORSE* code developed by McDougall & Albrow (2016). For modelling of a light curve involving binary lens. The number of parameters increase as the lens is a system of two masses. As mentioned section (1.1.2), the static binary model is dependant on 7 parameters: u_0, t_0, t_E, ρ, α, s and q. The starting guess of the parameters for emcee can be either found by the heuristic analysis of the light curve (Chapter 7) or by performing a grid search, performed over a logarithmic scale of (s,q) with the grid having dimensions (-0.7,0.7,-4.0,0.0). These dimensions of the (s,q) grid represent the ability of microlensing to detect the binary lenses in this range of parameter space. In this search method, for each element of the grid a magnification map is made (Figure 1.4). For any trajectory of the source on the magnification map, u_0 and α determine the shape of the light curve. Thus for each element of (s,q), u_0 and ϕ are searched from the range (0,1) and (0,2π) so that the shape of the model matches the actual light curve. For the fixed value of these parameters the other parameters t_E, t_0 and ρ are found using simplex downhill approach for minimising χ^2. The finite source parameter ρ is searched over the values in the logarithmic range (-3.0,0.0) so that peak of the model smoothens out to match the shape of the observed light curve. This range over which

ρ is searched is the typical value of the that we detect towards bulge. This method can be used to produce a $\Delta\chi^2$ [6] map over (log$s$, log$q$) to locate the possible solution regions. The element corresponding to the minimum $\Delta\chi^2$ on this map is further minimised using the *emcee* algorithm.

1.5 Presence of higher order effects in the event

Apart from the standard parameters required to model the microlensing light curve, several higher order effects are required to constrain the nature of the lens. Sometimes these effects can also explain the poor fit of the basic model [7] to the light curve. The higher order effects and their properties are described in this section.

1.5.1 Orbital Parallax

Microlensing parallax is an effect due to change in position of the observer while observing an microlensing event which manifests as an apparent non-rectilinear source trajectory. In case of orbital parallax, the acceleration of the Earth around the Sun makes the trajectory to be non-linear. Orbital Parallax is often most relevant when the time-scale of the event is long (∼60 days) (Gould et al. (1994), Alcock et al. (1995), Mao et al. (2002), Soszyński et al. (2001), Bond et al. (2002), Bennett et al. (2002b), Bennett et al. (2002a), Smith (2003)). The resultant light curve is asymmetric about base, or asymmetric about top in case of single lens events depending on the direction of relative lens-source motion. To the extent the motion is parallel to the acceleration of the Earth, the light curve is asymmetric about base and the perpendicular extent produces an asymmetric top (Bennett et al., 2002a, Smith et al., 2005). Microlensing parallax is a vector quantity which has direction parallel to lens-source relative proper motion and magnitude of inverse of the projected Einstein radius ($\tilde{r}_E$) (Figure 1.10, Eq. 1.19),

$$\pi_{\mathbf{E}} = \frac{\tilde{\mathbf{v}}_{\mathbf{rel}}}{\tilde{v}_{rel}^2 t_E} \quad = \frac{1}{\tilde{r}_E} A.U. \tag{1.19}$$

The size of the projected Einstein radius of the lens to the Earth's orbit is also relevant for the detectability of orbital parallax. The size of the projected Einstein radius for a typical lens towards galactic bulge is ∼ 1-2 A.U. Thus, the displacement of the earth in 60 days forms a standard ruler to measure the parallax (Figure 1.10). The importance of microlensing parallax is because it is useful to calculate the mass of the lens,

[6] $\Delta\chi^2 = \chi^2_{dq_{element}}$ - χ^2_{best}
[7] or static binary lens model in case of binary lens

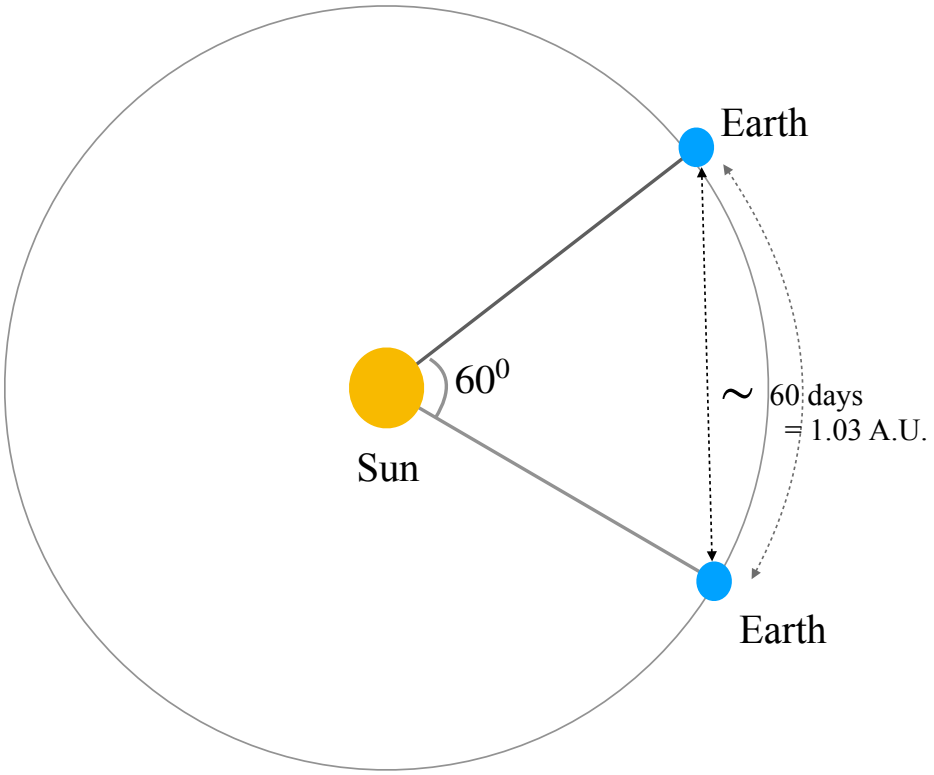

Figure 1.10: The projected r_E for the lenses towards bulge on the ecliptic plane $\sim$ 1.03 A.U. Earth displaces by this amount in 60 days. The displacement equal to the projected Einstein radius of the lens helps in measuring the orbital parallax.

$$M = \frac{\pi_{rel}}{\kappa \pi_E^2} \quad = \frac{\theta_E}{\kappa \pi_E}; \quad \pi_{rel} = A.U.\left(\frac{1}{D_L} - \frac{1}{D_s}\right) \tag{1.20}$$

where $\kappa = 8.1$ mas $M_\odot^{-1}$, μ_{rel} is the relative lens-source proper motion and π_{rel} is the relative lens-source parallax [8]. The first microlensing event with an orbital parallax was discovered towards the bulge by Alcock et al. (1995). This has been followed by several other detections, some of which may be due to black hole lenses (Agol et al., 2002, Bennett et al., 2002a,b, Poindexter et al., 2005). Statistically, a higher value of t_E is produced by a higher mass of the lens (Dominik, 2006). Measuring π_E thus helps in constraining the mass of the lens. However, slow moving lenses can also produce a high t_E.

Although detecting a parallax signal can help in constraining the location and mass of the lens, orbital parallax is subjected to a four fold degeneracy. In Figure (1.11), the diagram showing the components of the parallel and perpendicular parallax vectors to

[8] mas = milli-arcseconds

the acceleration of the Sun in the sky is shown. For events where parallax is weakly detected, degeneracy is likely to be present.[9] Smith et al. (2003) proposed that there exists a degeneracy in events with weak parallax which is called *Constant acceleration degeneracy*. This degeneracy implies that if the observer-lens-source are assumed in a constant accelerated motion, the magnitude of the physical acceleration will be the same but the projected acceleration will be different in the degenerate solutions. Therefore solutions related by this degeneracy will give different values of t_E. Gould (2004) extended this work to events having orbital parallax and discovered the *Jerk-Parallax* ($\boldsymbol{\pi_j}$) degeneracy by analysing the event MACHO-LMC-5 in the geocentric frame [10]. In geocentric frame orbital parallax is modelled by two parameters: π_{EE} and π_{EN} which are the components of the parallax in the North and East direction of the sky plane. Jerk parallax degeneracy is important as the two different pairs of the solutions give different mass and distance to the lens. For events that lie close to the ecliptic, Jiang et al. (2004) and Poindexter et al. (2005) showed that there exists an *ecliptic degeneracy* which is characterised by $(u_0, \pi_{E,\perp}) \rightarrow -(u_0, \pi_{E,\perp})$. Though the continuous degeneracies highlighted by Smith et al. (2003) and Gould (2004) are usually broken in events with $t_E \geq 58$ days, Poindexter et al. (2005) showed that degeneracies may also be present for longer timescale events lying close to ecliptic, due to existence of the ecliptic degeneracy.

The jerk of the Sun comes into picture through the higher order terms in the Taylor expansion equation describing lens source trajectory as described by equation (1.6) which can also be expressed as,

$$u(t) = \sqrt{\tau^2(t) + \beta^2(t)} \tag{1.21}$$

where,

$$\tau(t) = \frac{t - t_0}{t_E} + \delta\tau(t); \quad \beta(t) = u_0 + \delta\beta(t) \tag{1.22}$$

where u_0 is the minimum lens-source separation normalised to θ_E, t_0 is the time of this minimum separation, t_E is the timescale of the event. ($\delta\tau$, $\delta\beta$) are the parameters describing deviation in time and deviation in minimum lens-source angular separation respectively. These parameters describe the deviation in the apparent trajectory affected by the parallax.

[9] Computationally, weak parallax events are those that do not give significant reduction in χ^2 as compared to a PSPL fit and have relatively constant acceleration.

[10] Geocentric frame is defined by equation (5) of Gould (2004)

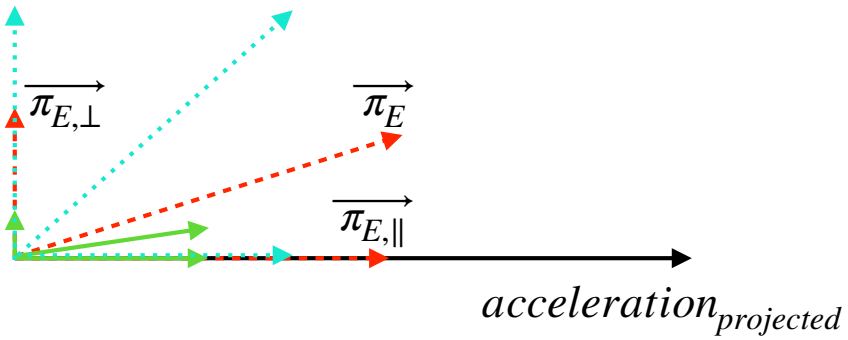

Figure 1.11: The different magnitudes of π_E and their components parallel and perpendicular to the acceleration of the Sun in the sky. $\pi_{E,\parallel}$ is better constrained in a light curve and is responsible for the asymmetry at the base of the light curve while $\pi_{E,\perp}$ is responsible for asymmetry at the peak of the light curve. *cyan* colour denotes strong parallax signal in the light curve which has no degenerate solution, *red* colour denotes moderate parallax vector which may have degenerate solutions and *green* colour denotes weak parallax vector which will suffer from *Jerk Parallax* degenerate solutions. The degeneracy depends on the scale of $\pi_{E,\perp}$.

When the acceleration of the earth is considered, the Sun has a positional offset $\Delta(s)$ (Figure 1.12). $(\delta\tau,\, \delta\beta)$ are related to positional offset by

$$(\delta\tau, \delta\beta) = \pi_E \mathbf{\Delta s} = (\pi_\mathbf{E}.\mathbf{\Delta s}, \pi_\mathbf{E} \times \mathbf{\Delta s}) \tag{1.23}$$

following the formalism given by Gould (2004). Equation (1.23) can be expanded as

$$(\delta\tau, \delta\beta) = [\Delta s_n(t)\pi_{E,N} + \Delta s_e(t)\pi_{E,E}, -\Delta s_n(t)\pi_{E,E} + \Delta s_e(t)\pi_{E,N}] \tag{1.24}$$

In its general form equation (1.6) can be Taylor expanded to,

$$\mathbf{u}(t-t_0) = \mathbf{u_0} + \frac{t-t_0}{\mathbf{t_E}} + \pi_E\Big(\frac{1}{2}\alpha(t-t_0)^2 + \frac{1}{6}\mathbf{j}(t-t_0)^3\Big) \tag{1.25}$$

where, α is the apparent acceleration of the Sun projected on the plane of the sky and $j = \frac{d\alpha}{dt}$ is the apparent jerk of the Sun. $\boldsymbol{u}_0$ and $\boldsymbol{t}_E$ are assumed orthogonal to each other. Squaring Eq. (1.25) yields

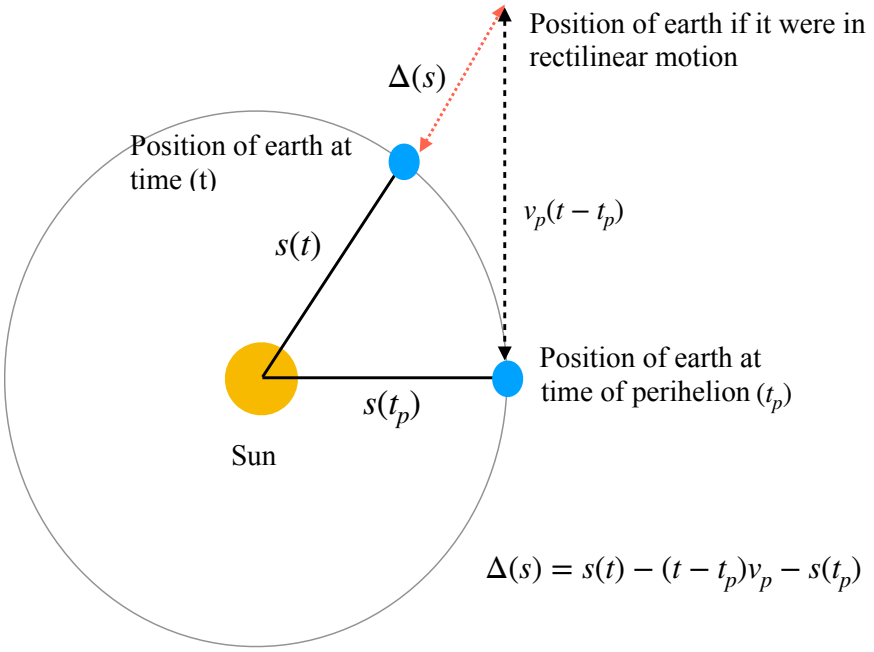

Figure 1.12: The position of the earth around the Sun. t_p is the time of perihelion and $s(t_p)$ is the position at perihelion which is used as a reference position. If earth were in rectilinear motion, it would continue to travel in a straight line. However since it is in constant acceleration around the Sun, the Sun has an offset in position ($\Delta(s)$).

$$u(t)^2 = \left\{ \mathbf{u_0} + \frac{t-t_0}{\mathbf{t_E}} + \pi_E \left(\frac{1}{2}\alpha(t-t_0)^2 + \frac{1}{6}\mathbf{j}(t-t_0)^3 \right) \right\}^2 = \sum_{i=0}^{\infty} C_i t^i \tag{1.26}$$

The coefficients of this equation come out to be,

$$\begin{aligned} C_0 &= u_0^2; \\ C_1 &= 0; \\ C_2 &= -\alpha u_0 \pi_{E,\perp} + t_E^{-2}; \\ C_3 &= \alpha \frac{\pi_{E,\parallel}}{t_E} + \frac{1}{4}\alpha^2 t_E u_0 (\pi_E \times \pi_j); \\ C_4 &= \frac{\alpha^2}{4}(\pi_E^2 + \frac{4}{3}\frac{\mathbf{j}}{\alpha^2 t_E} \cdot \pi_E) + \frac{1}{12}\frac{\Omega_\oplus^2}{\alpha} u_0 \pi_{E,\perp} \end{aligned} \tag{1.27}$$

Here $\Omega_\oplus = 2\pi yr^{-1}$ is the angular distance covered by earth around Sun in one year. The Jerk-parallax is given by,

$$\pi_j \equiv \frac{4}{3}\frac{j}{\alpha^2} t_E, \tag{1.28}$$

$\pi_{E,\parallel}$ and $\pi_{E,\perp}$ are the components of parallax parallel and perpendicular to the apparent acceleration/path of the Sun in the plane of the sky. As shown in Figure 1.13, $\pi_{E,\parallel}$ is usually better constrained than ($\pi_{E,\perp}$) (Gould et al., 1994) and therefore it is the perpendicular component that is responsible for the degenerate solutions. Jerk Parallax degeneracy tells us that there are two sets of parallax solutions which yield the same values of the above coefficients $(C_0, C_1, C_2, C_3, C_4)$ but with different t_E and π_E related by

$$\Delta t_E \simeq -\frac{\alpha t_E^2}{2}(\pi_{E,\perp}\Delta u_0 + u_0 \Delta\pi_{E,\perp})t_E \tag{1.29}$$

$$\pi'_{E,\perp} = -(\pi_{E,\perp} + \pi_{j,\perp}) \tag{1.30}$$

$$\pi_{j,\perp} = -\frac{4}{3}\frac{year}{2\pi t_E}\frac{sin\beta_{ecl}}{(cos^2\psi sin^2\beta_{ecl} + sin^2\psi)^{3/2}} \tag{1.31}$$

$$\pi'_{E,\parallel} = \pi_{E,\parallel} \tag{1.32}$$

Usually, the degenerate components of the parallax are found analytically i.e. by finding the projected acceleration and the components of π_E parallel and perpendicular to this acceleration to evaluate the new solution. However, since the Galactic bulge lies close to ecliptic, the north component of parallax is similar to perpendicular component of parallax. Therefore Jerk-parallax degenerate solution can be found by flipping the sign of π_{EN}. It is also found using emcee that the presence of Jerk-Parallax degeneracy can be seen in the bimodal distribution of t_0, t_E and π_{EN} (Chapter 4).

Another aspect of the existence of this degeneracy is the jerk velocity which varies through the year and is maximum on equinoxes towards galactic bulge.

$$\tilde{v}_j = \frac{-3}{4}\quad\frac{(cos^2\psi sin^2\beta_{ecl} + sin^2\psi)^{3/2}}{sin\beta_{ecl}} v_\oplus \tag{1.33}$$

Here, β_{ecl} is the ecliptic latitude of the event, $\psi = \frac{2\pi(t_0 - t_p)}{365.25}$ is the phase of the earth's orbit at t_0, t_p is the time of perihelion and $v_\oplus$ is the mean velocity of the earth ~ 30km/s. Towards the galactic bulge, v_j depends on the time of the year and is maximum during equinoxes.

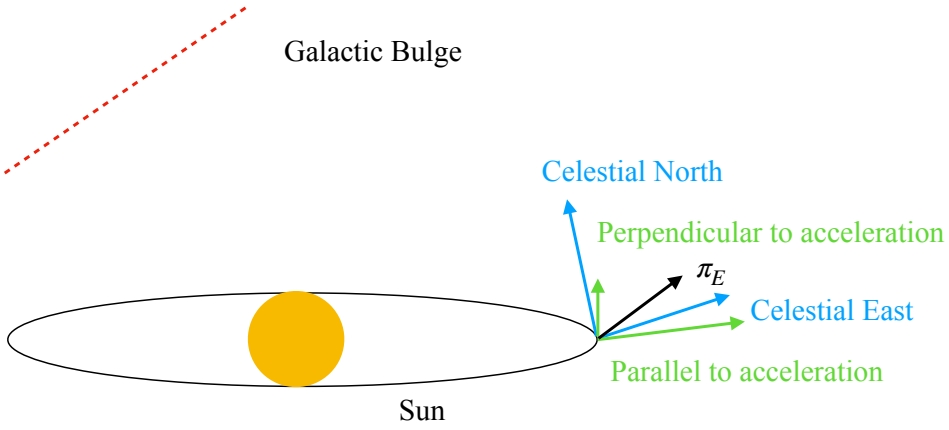

Figure 1.13: The celestial axes and the $(\parallel, \perp)$ axes. The galactic bulge is shown as an orange dotted line inclined to the ecliptic plane at an angle of 60^0. $\boldsymbol{\pi}_E$ vector is shown which is projected in celestial frame. $\pi_{E,N} \sim \pi_\perp$ can be visualised from the figure. The celestial east direction coincides with the $\parallel$ direction during equinoxes. Thus close to this period, asymmetry is expected at the base of microlensing events having orbital parallax signal.

In cases where the light curve does not yield a measurement of parallax, other methods like *Bayesian Analysis* of the galactic model priors, *Adaptive Optics Imaging*, resolution of lens and source after few years using HST, astrometric microlensing and spectroscopic followup observations have been used to estimate the lens mass and distance (Alcock et al., 1995, Bachelet et al., 2018, Barry et al., 2016, Batista et al., 2011, 2014, Beaulieu et al., 2016, Bennett et al., 2008, Bhattacharya et al., 2017, Dominik, 1998, Dominik & Sahu, 2000, Fukui et al., 2015, Jung et al., 2018a, Kains et al., 2017, Koshimoto et al., 2017, Santerne et al., 2016).

1.5.2 Binary lens orbital motion

When two masses form a bound binary system, they orbit around each other. In reality the lens motion is in three dimensions (Dominik, 1998), but the dimension parallel to the line of sight can be neglected for typical timescale of the microlensing events as it does not have any effect prominent on the light curve. Thus effective motion is in two dimensions, which affects the binary lens separation ratio and the angle between the trajectory and the binary axis (Albrow et al., 1998, Dong et al., 2009, Hwang et al., 2011, Ryu et al., 2010, Shin et al., 2012, Skowron et al., 2011)(Figure 1.14). Since caustic structures in binary lens system depend on the separation normalised to angular Einstein radius (s), lens orbital motion causes change in the caustic structures (Skowron et al., 2011). In fact this phenomenon has helped in explaining the light curve of the event

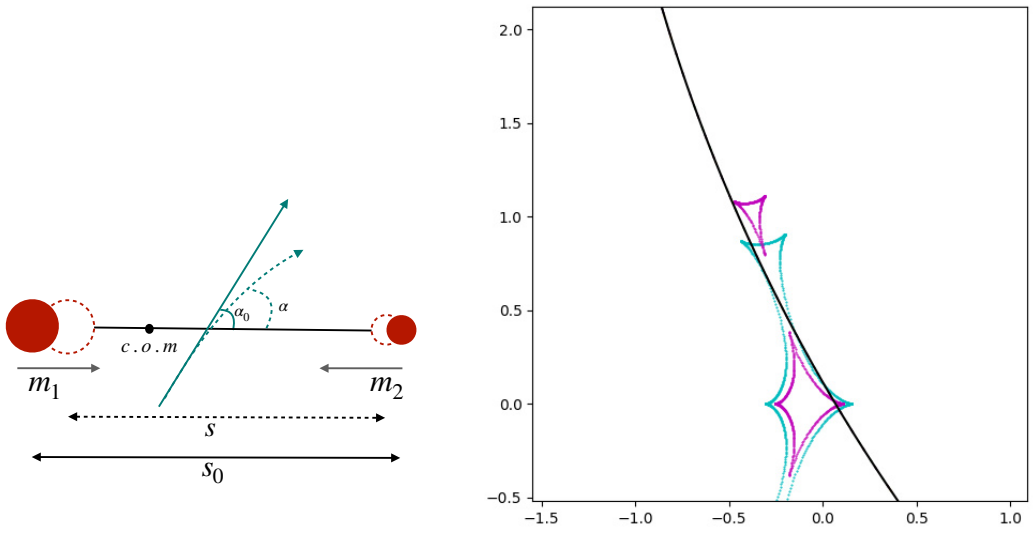

Figure 1.14: (a) shows the two effective dimensional motion of the binary lens system. In the figure, the two masses m_1 and m_2 are moving towards their centre of mass ($c.o.m$) shown by grey arrows. The original separation is s_0 and the new position after time t is s. The new position of masses are represented by red coloured dotted circles. Similarly, the rectilinear source trajectory is shown by ***cyan*** line. Due to the change in angle between the lenses, the effective trajectory is curved as shown by *cyan* dotted line. Equation (1.34) describes this motion. (b) shows the variation in the caustic structure due to the orbital motion of the lens. *magenta* is the caustic structure when the separation ratio is s_0 and *cyan* is the caustic structure when the separation ratio changes to s. Similarly the effective curved trajectory is also shown by a black line.

$OGLE-2013-BLG-0723$ which was originally analysed by Udalski et al. (2015b) as a three body system comprising a Venus mass planet orbiting a a brown dwarf which also orbits a stellar mass. Han et al. (2016) later explained this light curve with two lenses in close separation and having orbital motion. Following Albrow et al. (2000),

$$s = s_0 + \frac{ds}{dt}; \quad \alpha = \alpha_0 + \frac{d\alpha}{dt} \tag{1.34}$$

where ds/dt and dα/dt are the rate of change of the separation ratio s_0 and trajectory angle α_0 respectively. The sign of d?/dt determines whether the source turns right or left with respect to its original trajectory.

1.5.3 Binary source

Like the lens, a source can also be a binary. If the lens passes close to both the sources, a binary source anomaly is produced Griest & Hu (1992). More than 15% of the sources towards the bulge are expected to be binary stars. A binary source anomaly can mimic a planetary perturbation on the light curve if one of the source which is much brighter than the companion passes close to the Einstein ring of the lens Gaudi (1998), Jung et al.

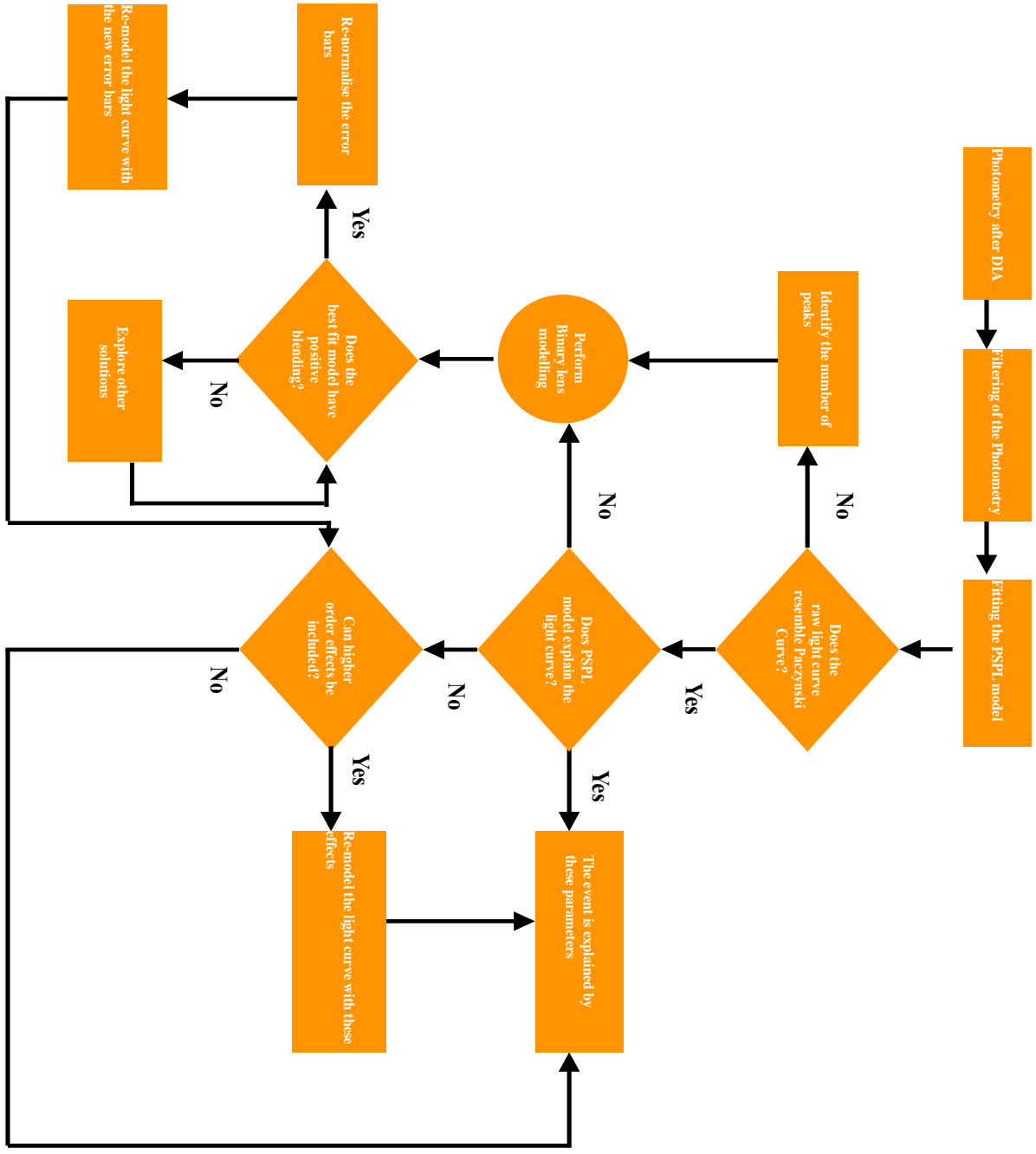

Figure 1.15: A flow chart of the procedure to model Microlensing events.

(2017).

The higher order effects described above must be investigated one after the other and then altogether to get the global solution. However, the light curve not always has the information about these effects. Figure (1.15) shows a tree diagram for the procedure to be adopted while modelling a microlensing event.

1.6 Renormalisation of uncertainties in magnitudes

As done by Bachelet et al. (2012), Miyake et al. (2012), it is good to adjust the uncertainties in magnitudes estimated by the photometry-packages because they can be underestimated when the event is bright. Renormalising of uncertainties gives equal weightage to different datasets used in the modelling, thereby helping to estimate the appropriate distribution of parameters. In this thesis, we use the method prescribed by Yee et al. (2012) to renormalise the uncertainties in the magnitudes,

$$\sigma_{new} = \kappa\sqrt{\sigma^2 + e^2_{min}} \tag{1.35}$$

where σ_{new} is the renormalised uncertainty in magnitude, σ is the original uncertainty in magnitude estimated by pyDIA, κ is the scale factor and e is a term added to σ such that $\chi^2/dof = 1$. e_{min} is the term that is required for high magnification data points. So, in order to renormalise the uncertainties, we sort the points according to magnification. We select high magnification points according to the criteria such that the number of high magnification points is greater than the number of parameters for the model. We then solve two simultaneous equations to get the values of e and κ,

$$\chi^2_{new,h}/N_h - 1 = 0; \quad \chi^2_{new,l}/N_l - 1 = 0 \tag{1.36}$$

where $\chi^2_{new} = \frac{(data-model)^2}{\sigma^2_{new}}$, N are the number of points and h and l are the suffixes for high magnification points and low magnification points respectively. The process of renormalisation of uncertainties usually involves finding the best fitting model first and then finding the values of e and κ.

1.7 Planet formation theories

The formation of planets is thought to happen during the birth of a new star. A protostar forms due to the gravitational collapse of a large molecular cloud. Due to angular momentum, this large cloud collapses onto a disk in a plane that is orthogonal to the cloud's total angular momentum. Followed by this, the new star accretes the majority of the cloud. It is believed that from the remaining cloud which is mainly dust, planetesimals. Rocky bodies are then formed due to gravitationally accreting the surrounding planetismals. Larger bodies thus formed collide and stick to each other which leads to protoplanets. Though the formation of terrestrial planets via this method is acceptable,

it fails to explain the existence of the giant planets. Till today, planet formation is explained by two main theories: core accretion and gravitational instability.

1.7.1 Core accretion theory

Core accretion is a widely accepted theory that is able to explain the existence of a large sample of planets at various separations and masses (Mizuno, 1980, Mizuno et al., 1978), and the ice and gas giant planet formation (Perryman, 2011). The theory explains that by the same process which is discussed above, large cores (5-20$M_{\oplus}$) of the proto-planetary disks are formed specifically beyond the snow line. The large distance from the host star reduces the gravitational influence and temperature resulting in the condensation of water and other compounds and increase the amount of matter that can be accreted. After reaching the critical mass (Bodenheimer & Pollack, 1986, Pollack et al., 1996), the rate of gas accretion exceeds the rate of planetismal accretion. This gas accretion rate grows exponentially due to which further accreted planetismals are supposedly broken from the gas drag and pressure. This contributes to the presence of heavy elements in the gas giants atmospheres.
The giant planet formation is very sensitive to the initial conditions of the cloud surrounding the star. Smaller cores of proto-planets take large period to form, which can result in the proto-planetary gas being dispersed before they are able to complete their gas accretion. If this happens then it forms an ice giant type of planet. All the planets, later, are believed to move away from their original orbits either by migration towards the inner region of the planetary system (Ida, 2019) or by gravitational scattering (Cloutier & Lin, 2013).

1.7.2 Gravitational disk instability theory

Gravitational disk instability theory is another mechanism that explains the formation of some giants (Boss, 1997, Durisen et al., 2007, Kuiper, 1951). The advantages of this theory is that it does not rely on any solid body accretion, and therefore planets forms in short time scales. It is based on the agreed fact that at some point in time, the proto-planetary disk will be gravitationally unstable. These instabilities lead to spiral arms in the disk that result in forming self-gravitating regions that lead to giant planets.

With two very different theories, a lot of research has focused on determining which is more likely to be true. There has been evidence that supports both the core accretion

(Mordasini et al., 2008), and gravitational instability (Boss, 2001) theories as individual and also as a mixture (Matsuo et al., 2007). Still we require a larger sample of planets to probe deeply into formation of bound planets and un-bound planets. Kepler mission has shown that hot planets are more common upto a radius of about 2.6-3.0 $R_{\oplus}$ (e.g., Fressin et al. (2013), Howard et al. (2010)). At distances larger than 10 AU, direct imaging method has found the presence young, massive planets, perhaps that did not undergo migration (e.g., Nielsen & Close (2010), Chauvin et al. (2015), Bowler et al. (2014)). However, there remains a large area of the exoplanet parameter space orbits beyond ∼1 AU and masses less than that of Jupiter that remains relatively unexplored by transit, radial velocity, and direct imaging techniques and to which gravitational microlensing is sensitive to. In Chapter (5), we show that the lens in case of the microlensing event OGLE-2017-BLG-1170 is a pair of super-Jupiters in the galactic bulge. This lens cannot be categorised as a freely floating planet or as distant planet from the host star nor a conventional planetary system. Investigation are much needed into formation of such systems and more samples need to be detected to create a mass function for such systems.

1.8 Microlensing planet discoveries

The understanding of our solar system is aided by the continuously increasing number of detection of planets [11]. Planet formation theories explain the formation of planets of various masses around different stars and planet detection techniques support or challenge them (Suzuki et al., 2018). Planetary signals in gravitational microlensing events are studied with the latest generation of telescopes which provide adequate coverage of the events (Yee et al., 2012). Tuomi et al. (2014) has found using the latest generation telescopes employing radial velocity method for local M-dwarfs, that every M-dwarf star has at least one low mass planet orbiting around it. Since gravitational microlensing method for planet detection is efficient for large distance towards bulge which other systems are not sensitive to, distant planetary systems (in bulge) are also being detected (Zhu et al., 2017). With this benefit, a statistical study of the planet location, frequency and type can be done (Poleski et al., 2018, Shvartzvald et al., 2016a, Suzuki et al., 2016, 2018). Based on various mass ratios and separation ratio, a variety of planets orbiting a variety of hosts can be detected by this method (Figure 1.16a,b). The advantage of microlensing is its sensitivity to a variety of companion masses at a distance much far from the host star where other methods are inefficient. At the time of writing this thesis, 90 exo-planetary systems have been detected (Figure 1.16 c) by gravitational microlensing. With the launch of $WFIRST$ mission, not only is this number is expected to rise

[11] http://exoplanet.eu

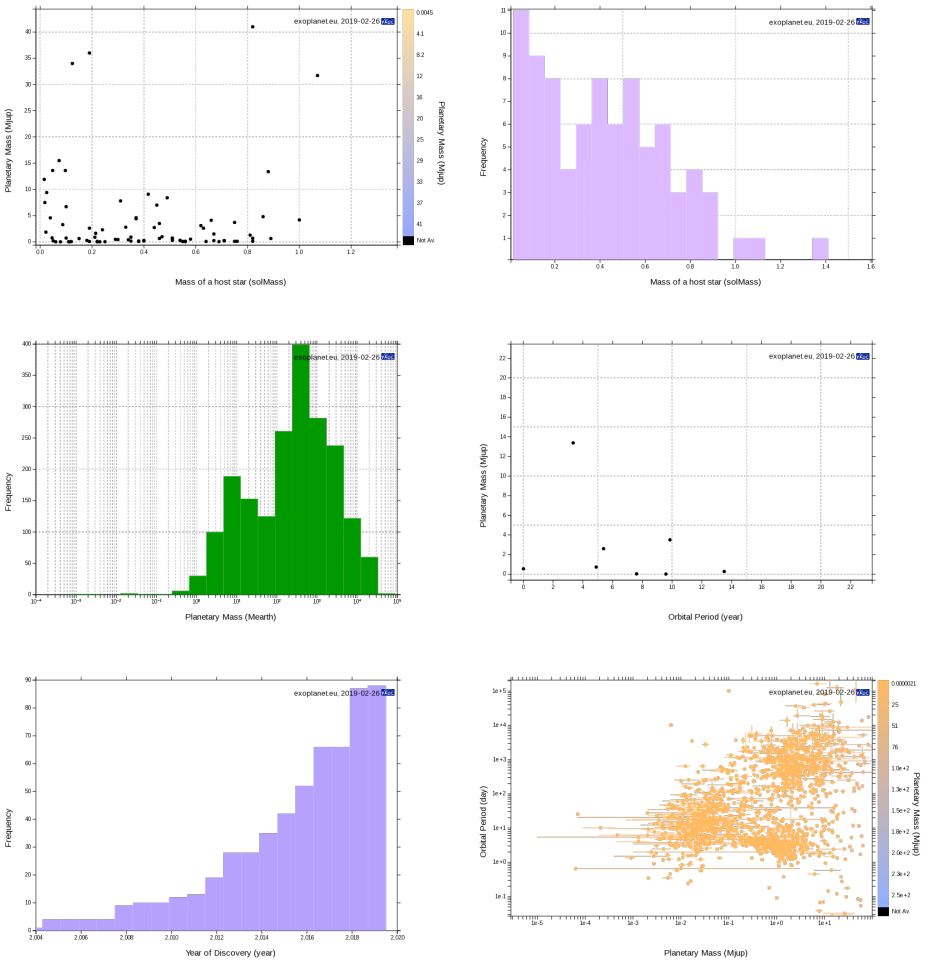

Figure 1.16: a)The mass ratio of the microlensing planets detected untill today, (b) the histogram plot for the host mass of the microlensing planetary detections untill date, (c) the histogram for the mass of the planet detected untill date, (d) planetary mass vs orbital period plot for the microlensing planet detections, (e) cumulative distribution for the number of planet detections since the beginning of 20^{th} century, (f) orbital period vs planetary mass plot for all the exoplanets detected by various other methods.

dramatically, but also the study of individual exoplanets is going to be possible (Bennett et al., 2018, Penny et al., 2019).

1.9 Wide Field Infrared Space Telescope (WFIRST) Mission

Due to a large number of exoplanets covering various parameter space are being detected by various detection methods, we are learning to understand the demographics of the planetary systems. This is also helping us to form statistical inference about the planetary formation process (Poleski et al., 2018, Suzuki et al., 2016, 2018) and the occurrence

rate of bound planets (Cassan et al., 2012). To explore the planetary science more, there is a need for more advanced high resolution space based survey which can probe the inner bulge which ground based surveys cannot.

WFIRST was considered by the 2010 decadal survey panel of NASA as its top priority large astrophysics mission, now estimated to be launched in the year 2025. It is an integration of several missions which will study dark energy with weak gravitational lensing, baryon acoustic oscillations, supernovae, gravitational microlensing survey and near infrared sky survey (Spergel et al., 2015). The primary purpose of the WFIRST microlensing survey would be to measure the microlensing event rate as a function of Galactic coordinates. It could achieve this because it is going to conduct its observations from space (L2 point around Sun) (Bennett et al., 2018) and will carry out observations in the near-IR bands transparent to the dust towards the galactic bulge in low galactic latitudes (Yee et al., 2014). Another purpose will be to compare the microlensing event rate from the ground based optical surveys in regions of overlap and quantify the relationship between near-IR and optical wavelengths. By measuring the near-IR source flux of the microlensing source stars WFIRST survey can also be used to characterise the source population towards the bulge and probe the uncertainties in the galactic models (which is one of the methods to infer lens mass and properties). WFIRST will also help in detecting planetary population in the innermost regions of the galactic bulge which will enable us to measure the relative frequency of the planets in the bulge and the disc without even inferring the lens mass. Nevertheless, this space based survey will also measure planet masses by methods like measuring the light from the lens with high resolution images and better photometry, astrometric microlensing and microlensing parallax thereby giving enough samples to understand the planetary mass distribution in the galaxy (Penny et al., 2019).

Since WFIRST is going to be launched as a multi-disciplinary space survey, it is a flagship mission of NASA. Therefore, parting from the conventional approaches of the space missions, WFIRST Microlensing Science Investigation Team (MicroSIT) has planned an effort to provide the WFIRST science easily accessible to entire astronomical community by providing WFIRST data, real-time analysis models, posterior distributions of the model parameters and by creating WFIRST Exoplanet Microlensing Community Science Team (CST) (Bennett et al., 2019).

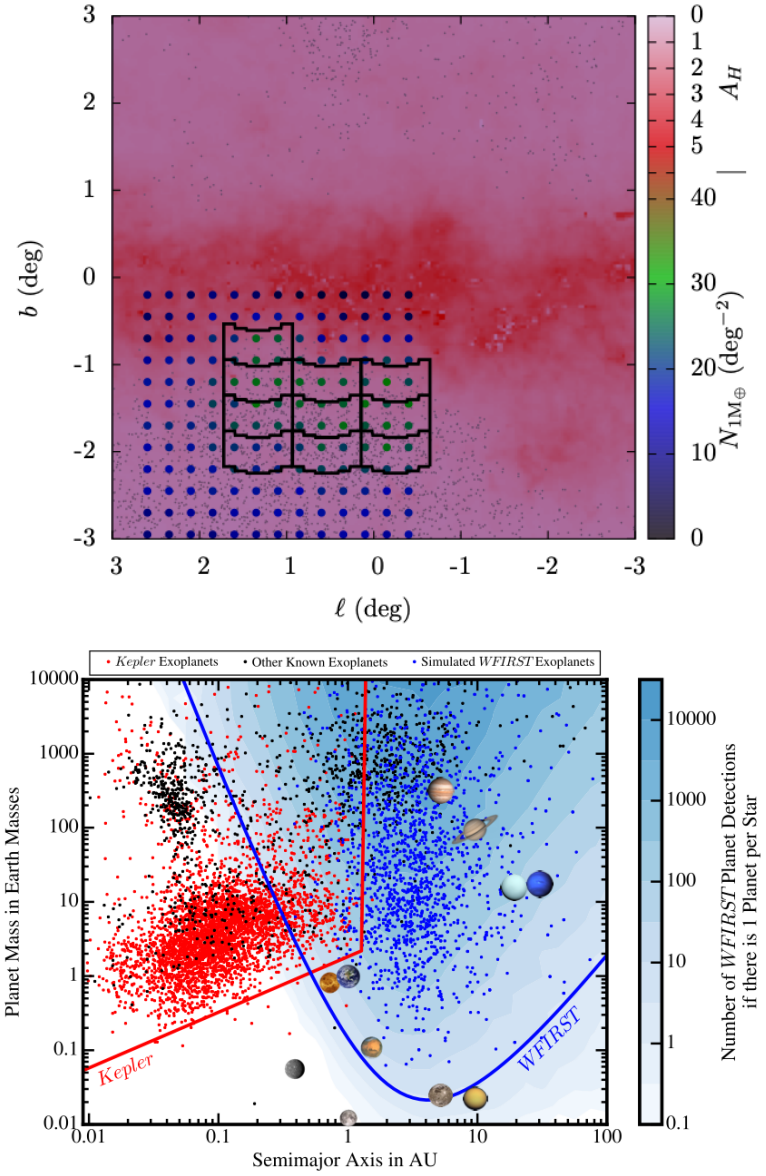

Figure 1.17: *(top)* WFIRST fields towards the extinction map of the galactic centre. Figure adopted from (Yee et al., 2014). *(bottom)* The planetary parameter space that WFIRST is sensitive and Kepler was sensitive to. Figure adopted from (Bennett et al., 2018)

1.10 Summary

This chapter presents the overview on Gravitational Microlensing and the applications of it. Microlensing is a powerful technique to determine the nature of the lens without detecting light from it. With the theoretical work of Gould & Loeb (1992), Mao & Paczynski (1991), Paczynski (1986) to detect dark lenses and exo-planetary systems, the growth of observing strategies and survey telescopes is introduced. Reducing the KMT-Net images with pyDIA software helps in removing bad photometric measurements. With an adequate time series photometry, the modelling of single lens and binary lens light curves is presented in brief. Microlensing models often require higher order effects like parallax, binary lens orbital motion and binary source to explain the light curve in a better way. These effects are presented in detail with necessary support of figures. Finally the statistics of the exo-planets detected with the help of microlensing is presented in the end. The modelling methods described here are used to model the microlensing events in following chapters.

Chapter (2) describes the galactic model in detail and how it is used throughout the thesis. Chapter (3) the light curve of $OGLE-2017-BLG-0192$ which is best explained by orbital parallax. We do not find any degeneracy in it. The galactic model gives the lens mass $0.61^{+0.51}_{-0.27}\ M_{\odot}$ at a distance of $1.7^{+0.7}_{-0.6}$ kpc. While fitting the orbital parallax model to the light curve of $OGLE-2017-BLG-01013$, we detect Jerk-parallax degeneracy. Chapter (4) explains the procedure to find the degenerate solutions. The best fitting solution to the light curve give the lens mass $0.18^{+0.15}_{-0.08}\ M_{\odot}$ at a distance of $2.1^{+0.8}_{-0.6}$ kpc. The location of the blend indicated that the blend is blue and faint object. If the lens was a major contributor to the blend light, it could possibly be a white dwarf. We therefore simulate isochrones for a sun like star at a distance of $2.1^{+0.8}_{-0.6}$ kpc using MIST package of Modules for Experiments in Stellar Astrophysics (MESA). We explore the possibility that the lens does not suffer any extinction or it suffers the same extinction as the red clump stars in the bulge. We however find that the lens could be a main sequence dwarf star and not a white dwarf. Chapter (5) describes the concept of space parallax and the use of Spitzer space telescope in measuring space parallax. We measure the space parallax for $OGLE-2017-BLG-1170$ and find that the lens is a pair of super-Jupiters located in the galactic bulge. Chapter (6) describes the model of the cusp approach event $OGLE-2018-BLG-1647$. It is found that the lens is a sub-Jupiter orbiting a stellar dwarf or a high mass brown dwarf primary located in the disc. Finally Chapter (7) deals with the heuristic analysis of the light curve of $OGLE-2018-BLG-0380$. Since we detect finite source effects in the analysis of this event and the position of the source on the CMD implies that it is a red giant star, we

use the Limb Darkening Coefficient (Γ) = 0.53. The Bayesian analysis suggests that the lens is a binary system of brown dwarf orbiting a low mass star or another heavy brown dwarf in the galactic bulge.

Chapter 2

Galactic Model

In this chapter I present the galactic model which can be used to produce a joint probability distribution of the lens and source properties. Various galactic models have been used by different authors based on the events rate equation (Alcock et al., 1995, 1997b, Batista et al., 2011, Bennett et al., 2002a,b, 2008, 2014, Clanton & Gaudi, 2014, Dominik, 2006, Han et al., 2017a,a, 2018, Miyake et al., 2012, Shan et al., 2019, Yee et al., 2012, Yoo et al., 2004), etc. The galactic model incorporates the probability that the source micro-lensed by a lens of mass M_L and at a distance D_L will produce a microlensing event of observed t_E from modelling. A Bayesian analysis based on a galactic model gives the posterior probability distributions for M_L and D_L. In this thesis, I perform a Bayesian analysis using the likelihood function given by Alcock et al. (1995).

2.0.1 Galactic Model Prior

When the microlensing model fitted to the light curve does not yield any information that can estimate the mass of the lens and the distance to the lens, it is difficult to understand the nature of the lens. Since the lens can be located in either disc or bulge ahead of the source, to deduce its mass and distance both π_E and θ_E must be known. The relative lens-source velocity (μ_{rel} or $\tilde{v}_{rel}$) is another tool to discriminate disc or bulge lens location of the lens,

$$\mu_{rel} = \frac{\theta_E}{t_E} = \frac{\tilde{v}_T}{D_L} \tag{2.1}$$

However, since the finite source effects (ρ) which gives θ_E is not measured from all the models fitted to the light curves, it again becomes a challenge to assume the location of the lens. t_E is hence degenerate in μ_{rel} and θ_E (Eq. 2.1). A slower moving low mass lens and a fast moving high mass lens can yield similar t_E's.

The event rate for microlensing, $\Gamma = n\sigma v_T$. $n \rightarrow \rho(x)$, represents the volume density that is dependant on distance to the lens [1], the lensing cross-section:$\sigma \propto R_E \propto \sqrt{x(1-x)}$ corresponds the Einstein ring of the lens and $v_T \equiv$ (1-x)$\tilde{v}_{rel}$ is the transverse velocity of the lens. Thus the differential rate of Γ is the probability of the location of the lens with a distance ratio x and velocity v_L described as

$$P(D_L, D_s, v_s) \propto \quad \frac{d\Gamma^3}{dx dv_s dv_L} \propto \sqrt{x(1-x)}\rho_L(x)\tilde{v}_{rel}(1-x)f_s(\mathbf{v}_s)f_L(\mathbf{v}_L), \tag{2.2}$$

where $v_s \equiv |\mathbf{v}_s|$ is the source velocity in the galactic reference frame, $\mathbf{v_L} = (1-x)(\mathbf{v}_\odot + \tilde{v}_{rel}) + x\mathbf{v}_s$ is the velocity of the lens in the galactic reference frame, $v_\odot$ is the velocity of the Sun in the galactic reference plane. To get a better constraint on the mass of the lens, we can consider the mass function of the lens in equation (2.2) by multiplying it by a factor of $\propto M^{1.5}\phi(M)$ (Bennett et al., 2002b). With this our galactic priors are,

$$P(D_L, D_s, v_s) \propto \sqrt{x(1-x)}\rho_L(x)\tilde{v}_{rel}(1-x)f_s(v_s)f_L(v_L)M^{3/2}\phi(M) \tag{2.3}$$

Thus, from the event rate equation, we get a joint probability distribution for the random variables representing lens and source location which is the product of the distribution for the density, velocity and mass of the lens. To evaluate equation (2.3), each of the distributions must be known as they form the prior probability of the lens mass and distance. Shan et al. (2019) have shown how the assumption of priors affects the Bayesian analysis results.

2.0.2 Prior distributions

To form the priors for velocity and density distributions, a co-ordinate system centred at the galactic centre where the x-axis corresponds to the line connecting Sun and galactic centre, y-axis is pointed along the galactic disc rotation and z-axis is pointed towards north galactic pole. Thus any position in the galaxy can be represented by three co-ordinates (x, y, z),

$$\begin{aligned} x &= R_0 - D_L cos(l)cos(b); \\ y &= D_L sin(l)cos(b) \\ z &= D_L sin(b) \end{aligned} \tag{2.4}$$

[1] x = ratio of the distance to the lens over the distance to the source = $\frac{D_L}{D_s}$

The model for disc density distribution of stars can be constructed following Bahcall (1999). In the galactic model used in this thesis, two components of the disc are used - thick and thin Jung et al. (2018b),

$$\rho_{r,z} = \rho_0 exp^{\frac{R_\odot}{h_R}} exp\Big[- \Big(\frac{r}{h_r} + \frac{z + z_\odot}{h_z} \Big) \Big] \tag{2.5}$$

Here, r = $\sqrt{x^2 + y^2}$, $z_\odot$ is the distance of the Sun above the galactic plane, h_r is the radial scale length and h_z is the vertical scale length. For the thick disc, (h_r, h_z)=(3600,900) pc and for the thin disc (h_r, h_z)=(2600,300) pc. A factor of 0.12 is used as the ratio of normalising densities for thick and thin disc (Jurić et al., 2008). The normalising factor of $\rho_0 = 0.14$ stars per pc^{-3} is used for the disc density distribution (Zhu et al., 2017).

The model used for the bulge density distribution of stars is the G2 model of Dwek et al. (1995). This model is a gaussian distribution centred at zero which requires a different coordinate system (x', y', z'). Here, the centre of the co-ordinate system is the galactic centre, but the longest axis is the x axis rotated by 20^o towards the positive galactic latitude (Clanton & Gaudi, 2014). The coordinates in this system is related to the coordinates in the previous coordinate system by the equations,

$$\begin{aligned} x' &= x\cos(20^0) + y\sin(20^0); \\ y' &= -x\sin(20^0) + y\cos(20^0); \\ z' &= z \end{aligned} \tag{2.6}$$

The density of the stars in the bulge is then,

$$\rho_{bulge} = \rho_0 \Big(e^{-\frac{r_s^2}{2}} \Big) \tag{2.7}$$

where $\rho_0 = 13.7$ stars per pc^{-3}, is the normalisation factor(Robin et al., 2003) and r_s is radial coordinate defined from in the above defined coordinate system,

$$r_s^2 = \Big\{ \Big[(\frac{x'^2}{x_0}) + (\frac{y'^2}{y_0}) + (\frac{z'^2}{z_0}) \Big] \Big\}, \tag{2.8}$$

where (x_0, y_0, z_0) = (1580,620,430) pc. The density profile for the disc and bulge towards the Baade's Window are shown in Figure (2.1). In the galactic model, a density distribution is applied for the source as well as the lens stars and source distance is not assumed to be fixed.

For the velocity distribution, the Han & Gould (1995) velocity model is considered. In this model, it is assumed that the stars in the disc and bulge have gaussian velocity distributions. For the disc, the distribution of the velocity along the y-direction is centred on 220km/s whereas for the z-direction and the bulge it is centred on zero km/s. In fact, although the bulge has some rotational velocity Bensby et al. (2017), it is much smaller than the dispersion of its stars. The dispersion of the stars in the disk is assumed to be 30km/s along y-direction and 20km/s along z-direction. Similarly, the dispersion of stellar velocities in the bulge is assumed to be 110km/s in each direction. Since the line of sight i.e. x velocities do not affect the microlensing event, the velocities and dispersions along this direction are not considered. Thus the velocity models for the disk and the bulge are,

$$\begin{aligned}
f_L(v_{L,y,disc}) &= \frac{1}{\sqrt{2\pi\sigma_{y,disc}}} e^{-\left(\frac{(v_{L,y}-220)^2}{2\sigma^2_{y,disc}}\right)}; \\
f_L(v_{L,z,disc}) &= \frac{1}{\sqrt{2\pi\sigma_{z,disc}}} e^{-\left(\frac{v^2_{L,z}}{2\sigma^2_{z,disc}}\right)}; \\
f_L(v_{L,y,bulge}) &= \frac{1}{\sqrt{2\pi\sigma_{y,bulge}}} e^{-\left(\frac{v^2_{L,y}}{2\sigma^2_{y,bulge}}\right)}; \\
f_L(v_{L,z,bulge}) &= \frac{1}{\sqrt{2\pi\sigma_{z,bulge}}} e^{-\left(\frac{v^2_{L,z}}{2\sigma^2_{z,bulge}}\right)};
\end{aligned} \tag{2.9}$$

where $v_{L,y} = (1-x)(v_{\odot,y} + v_{\tilde{helio}}) + xv_{s,y}$ and $v_{L,z} = (1-x)(v_{\odot,z} + v_{\tilde{helio}}) + xv_{s,z}$ are the velocities of the lens in y and z directions. The galactic disk moves with 220km/s towards positive y direction and the Sun has a peculiar velocity of (16,7)km/s in y and z directions respectively. Therefore, the velocity of the Sun along y and z is 236km/s and 7km/s respectively. The final velocity distribution for the disk and the bulge is $f_L(v_{L,disc}) = f_L(v_{L,y})f_L(v_L, z)$ and $f_L(v_{L,bulge}) = f_L(v_{L,y})f_L(v_L, z)$ respectively. v_{helio} is found by adding the instantaneous velocity of the earth at the peak of the event to the geocentric projected relative lens source projected velocity. This procedure is described in Appendix (A).

For the mass function prior, the galactic model is tried with the mass functions of Chabrier (2003). It is however seen that t_E strongly constrains the mass of the lens therefore the choice of mass functions does not have a strong impact on the posterior distribution. In equation (2.3), the mass is written as a function of (D_L, D_s, π_E) through equation (1.19).

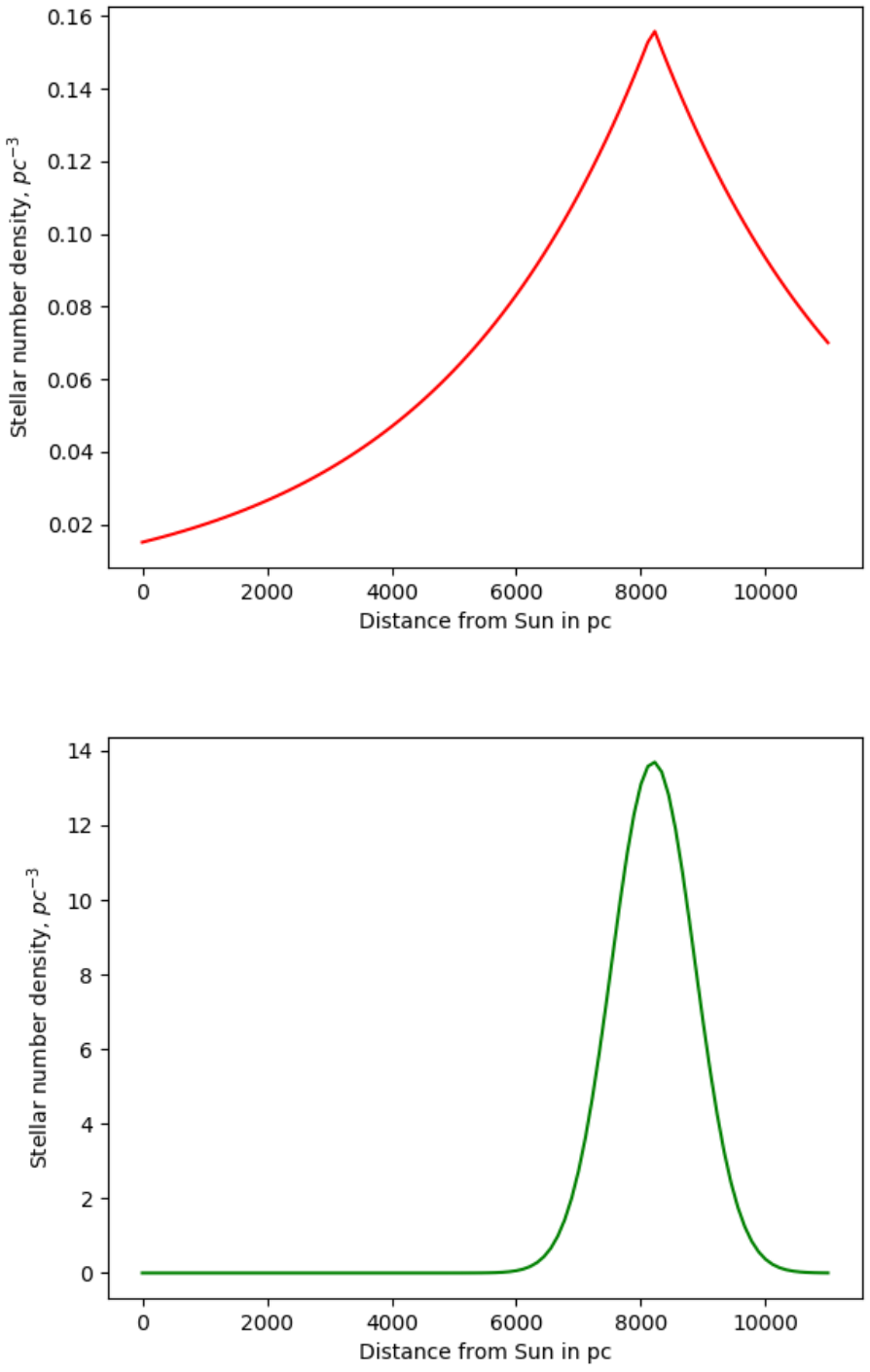

Figure 2.1: The density profiles for disk (red) and bulge (green) towards Baade's Window.

2.0.3 Posterior Probability distribution

In the chapters discussed in this thesis, finite source size ρ is not measured from the light curve model except for Chapter (7). Therefore, the samples of t_E and π_E are used to obtain the posterior probability distributions for the lens parameters given the galactic model. To apply *Bayes'* theorem and obtain the posterior probabilities of the galactic model variables, the samples of π_E and t_E serve as the likelihood probability and the equation (2.3) is used as prior probability. The posterior probability then can be written as

$$P(D_L, D_s, v_s) = \sqrt{\frac{D_L}{D_s}(1 - \frac{D_L}{D_s})}\rho_L(x)\frac{1}{\pi_E t_E} f_s(v_s) f_L(v_L)\Big(\frac{\pi_{rel}}{\kappa\pi_E^2}\Big)^{3/2}\phi(M) \tag{2.10}$$

The posterior probability is evaluated using emcee (Foreman-Mackey et al., 2013). The parameters of the walkers in emcee are distance to the lens (D_L), distance to the source (D_s) and the velocity of the source (v_s). To obtain the probability, we evaluate the posterior probability of each sample of t_E, π_E or ρ [2] at each step of emcee and then sum them. emcee is run until the chains converge to get the posterior probability of the distance to the lens, distance to the source and velocity of the source. This probability is then used to find the distribution for the lens mass. For the microlensing events towards the galactic bulge, we usually assume that the source happens to reside in the bulge. Nevertheless, it is good to see the posterior probability for the location of the evaluated source as it depends on the values of t_E and π_E from microlensing model. In events where parallax is not detected, the galactic model loses the constraint due to parallax on the lens mass and distance.

2.1 Discussion

In this chapter I present a description of how I have found the lens distance and mass using the galactic model equation and microlensing model samples of t_E and π_E. The galactic model prior equation (2.3) is the joint probability distribution of the velocity distribution of the lens and source, the density distribution in the disc and bulge applied to lens and source and the mass function applied to the lens. Equation (2.10) is the probability that a source at a distance D_s is micro-lensed by a lens of a mass M_L and at a distance D_L. With the galactic priors and samples of t_E or π_E or both, the Bayesian analysis helps to find the lens properties where ρ or π_E or both are not measured from

[2] Analysis of the galactic model when the samples of ρ are used is shown in Chapter (7)

fitting a microlensing model to the light curve. The evaluation of the galactic model is specific to the choice of the prior distributions and can be confirmed with follow-up observations. I use equation (2.10) to find the properties of the lens in this thesis.

Chapter 3

Analysis of the event OGLE-2017-BLG-0192

In this chapter, I present the analysis for the event $OGLE-2017-BLG-0192$ which has parallax signatures in it. As described in section (1.5.1), the continuous degeneracies highlighted by Smith et al. (2003) and Gould (2004) are usually broken in events having $t_E \geq 60$ days. However, as shown by Poindexter et al. (2005), degeneracies may also be present for longer timescale events lying close to ecliptic, due to existence of ecliptic degeneracy.

3.1 Observations and Data reductions

3.1.1 OGLE

$OGLE-2017-BLG-0192$ was the 192^{2nd} event detected by the Early Warning System (EWS) of Optical Gravitational Lensing Experiment (OGLE) in the year 2017. It was observed towards $(R.A., Dec) = (18:10:34.45, -26:50:25.9)$ in galactic bulge by the 1.3m Warsaw Telescope by the Las Campanas Observatory in Chile (Udalski et al. (2015a)) in the field 518.09 of OGLE. Galactic co-ordinates for this event are $(l, b) = (4.57154^o, -3.7277^o)$ [1].

[1] https://ned.ipac.caltech.edu for the conversion to galactic co-ordinates

3.1.2 KMTNet

This event was separately observed by the Korean Microlensing Telescope Network (KMTNet) through its three 1.8m telescopes in Chile, South Africa and Australia. KMTNet telescopes are equipped with 4 deg^2 wide field cameras to monitor the Galactic Bulge Kim et al. (2016). OGLE-2017-BLG-0192 was observed in the BLG31 field by KMTNet.

3.2 Data Reductions

The KMTNet images in I and V band for the field BLG02 were reduced using the pyDIA software Albrow et al. (2018) which is based on the delta-basis-function approach of Bramich et al. (2013). After reducing the KMTNet images, pyDIA provides the photometry of the micro-lensed star in 10 columns viz. time in JD, difference flux, uncertainties corresponding to difference flux, apparent magnitude, uncertainty in apparent magnitude, quality factor of data, full width at half maximum (FWHM) of the star, PSF of the star, roundness of the star on the image, sky quality during observation and the signal strength of the source star. The data was filtered based on these columns for each dataset. For the SSO and CTIO (I-band) data set, no data point was allowed to have uncertainty in the magnitude greater than 0.1 of the magnitude, Q $\geq$ 2, FWHM $\geq$ 10 and roundness $\geq$ 1.15. The same criteria for filtering the data based on Q, FWHM and roundness was applied to the other observatory data sets of KMTNet. Since the time stamp for these images was in 2450000 - Julian Days (JD), we convert it to 2450000 - Heliocentric Julian Days (HJD).

$OGLE-2017-BLG-0192$ was observed towards the beginning of the bulge observing season of 2017. Therefore data is missing on the early rising part of the light curve. However, we do get a long baseline with some outliers on the decreasing side of the event. The OGLE data was downloaded from the EWS page for Microlensing[2].

3.3 Analysis

A single lens fit to the light curve was made using the system developed by McDougall & Albrow (2016) (*Gravitational Microlensing - An Automated High Performance Modelling system*)[3]. This model gives us $u_0 = 0.134 \pm 0.005$, $t_0 = 7853.78 \pm 0.06$ (HJD-2450000 DAYS) and $t_E = 122.701 \pm 0.066$ days (Figure (3.1)).

[2]http://ogle.astrouw.edu.pl/ogle4/ews/
[3]http://www2.phys.canterbury.ac.nz/ u-lenser

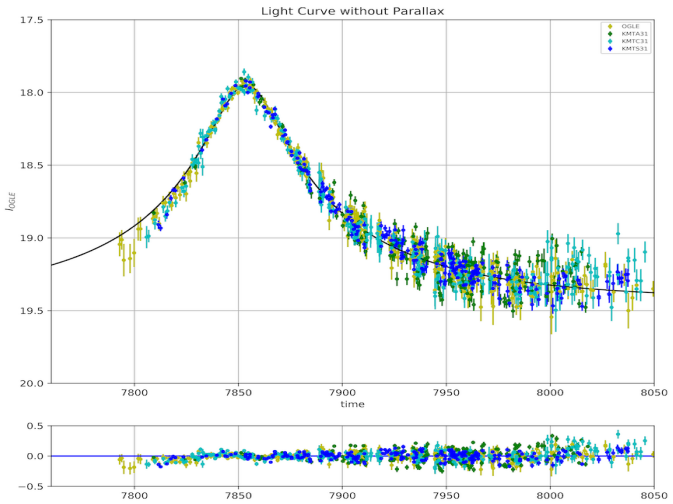

Figure 3.1: The standard Paczyński light curve for the event

Keeping these parameters fixed, we then add orbital parallax and perform a coarse grid search minimising χ^2 over the parallax ($\pi_{E,E}$, $\pi_{E,N}$) plane. The dimensions of the grid are (-8,8,-8,8). This yields $(\pi_{E,E}, \pi_{E,N})$ = (0.12012, -0.392392) (Figure (3.2)).

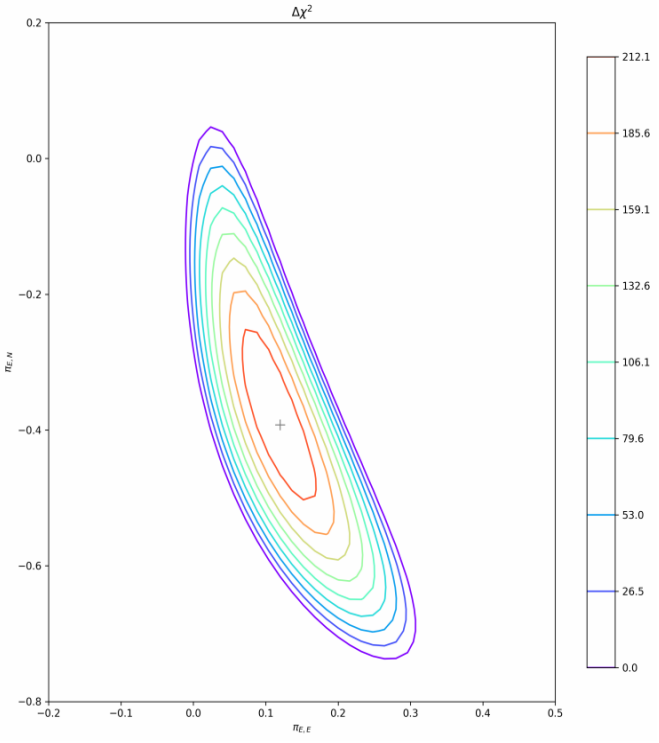

Figure 3.2: The $\Delta\chi^2$ contours obtained after performing a coarse grid search over π_E plane where $\Delta\chi^2 = \chi^2_{PSPL}$ - $\chi^2_{parallax}$. The minima is at the blue cross in the innermost level.

After seeding these parameters to emcee (Foreman-Mackey et al., 2013), the walkers move to a stationary distribution i.e. converge the chains to a solution (Figure (3.3)). We renormalise the uncertainties in the magnitudes (section (1.6)) using this model. The values of κ and e_{min} for each dataset are given in Table (3.1). We run this model again using the renormalised uncertainties and the walkers reach a distribution shown in Figure (3.4). We call this model P1.

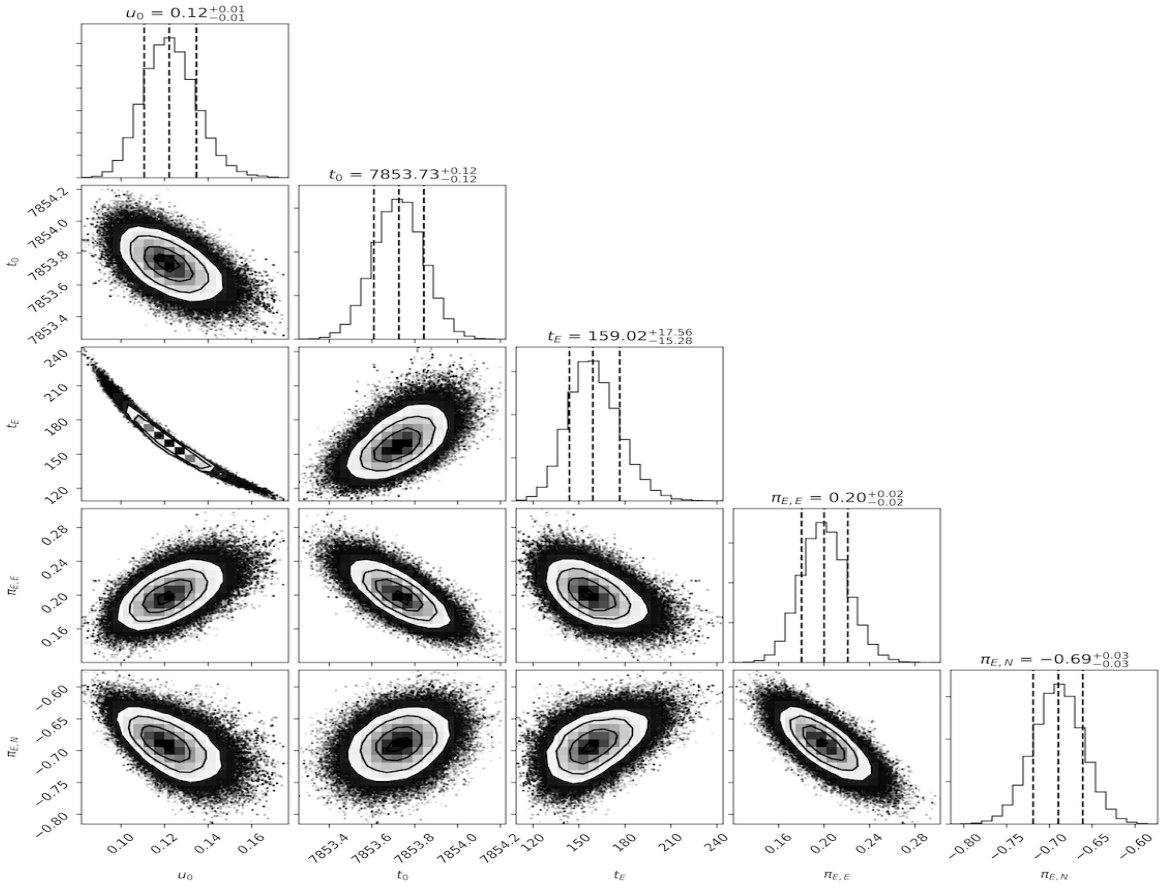

Figure 3.3: The covariance plot of the P1 model before renormalisation of the uncertainties.

Parameters to renormalise uncertainties		
Dataset	κ	e_{min}
OGLE	1.235	0.0
KMT-A01	2.895	0.0
KMT-C02	1.253	0.021
KMT-S02	1.898	0.010

Table 3.1: The scale factor κ and extra term e_{min} added to each dataset after renormalisation of uncertainty in magnitude in order to make $\chi^2/dof \sim 1$. This process gives equal weight to each dataset during modelling.

Constant-acceleration degeneracy (Smith et al., 2003) is realised by seeding MCMC with the sign of u_0 flipped and other parameters of the first parallax solution the same. This yields a different set of parameters corresponding to a different minimum. We label this solution as P2 which is shown in Figure (3.5). As pointed out of Poindexter et al. (2005), Skowron et al. (2011), the other two solutions can be explored by flipping the sign of $\pi_{E,N}$. Thus we seed emcee with the parameters of P1 and P2 solutions but reversing the sign of π_{EN}. The walkers reach new solutions P3 and P4 respectively which are slightly worse in χ^2 (Figures (3.6) and (3.7)). In Figure (3.8), we show the cumulative distribution of $\Delta\chi^2$ vs t_0 where $\Delta\chi^2 = \chi^2_{single}$ - $\chi^2_{parallax}$ for each data set that was used.

For OGL-2017-BLG-0192, we find that the orbital parallax solutions are with $\Delta\chi^2 \sim 8$, 28 and 41 where $\Delta\chi^2 = \chi^2_{best}$ - $\chi^2_{parallax}$. Considering the $\Delta\chi^2$, it can be said that the degeneracy is broken, but there are four solutions for the event because:

1. The ecliptic co-ordinates of the event are $(\lambda,\beta) = (272.6083^o, -3.422916^o)$, the event is close to ecliptic. Events lying close to ecliptic plane are affected by ecliptic degeneracy $(u_0,\pi_{E,N}) \rightarrow -(u_0,\pi_{E,N})$. If an event suffers from ecliptic degeneracy, there may exist a constant-acceleration degeneracy solution. These two degeneracies are responsible for the four observed discrete solutions.

2. Though t_E for the event is relatively high, there is a significant asymmetry in the light curve around the base and also around the top which indicates that both the component of parallax which is parallel ($\pi_{E,\parallel}$) as well as perpendicular ($\pi_{E,\perp}$) to the apparent acceleration of the Sun in the plane of the sky are large.

3. The event occurs close to the vernal equinox of 2017. In this period, Sun is travelling away from Galactic Bulge which indicates the jerk velocity is high, $v_j = 374$km/s (equation (1.33)).

4. The perpendicular component of Jerk, $\pi_{j,\perp} = 0.007$ (equation (1.31)). The degenerate $\pi'_{E,\perp}$ = -$(\pi_{E,\perp} + \pi_{j,\perp}) \sim \pi'_{E,N}$ will be large. Thus the continuous degeneracy breaks into discrete degeneracy for this event.

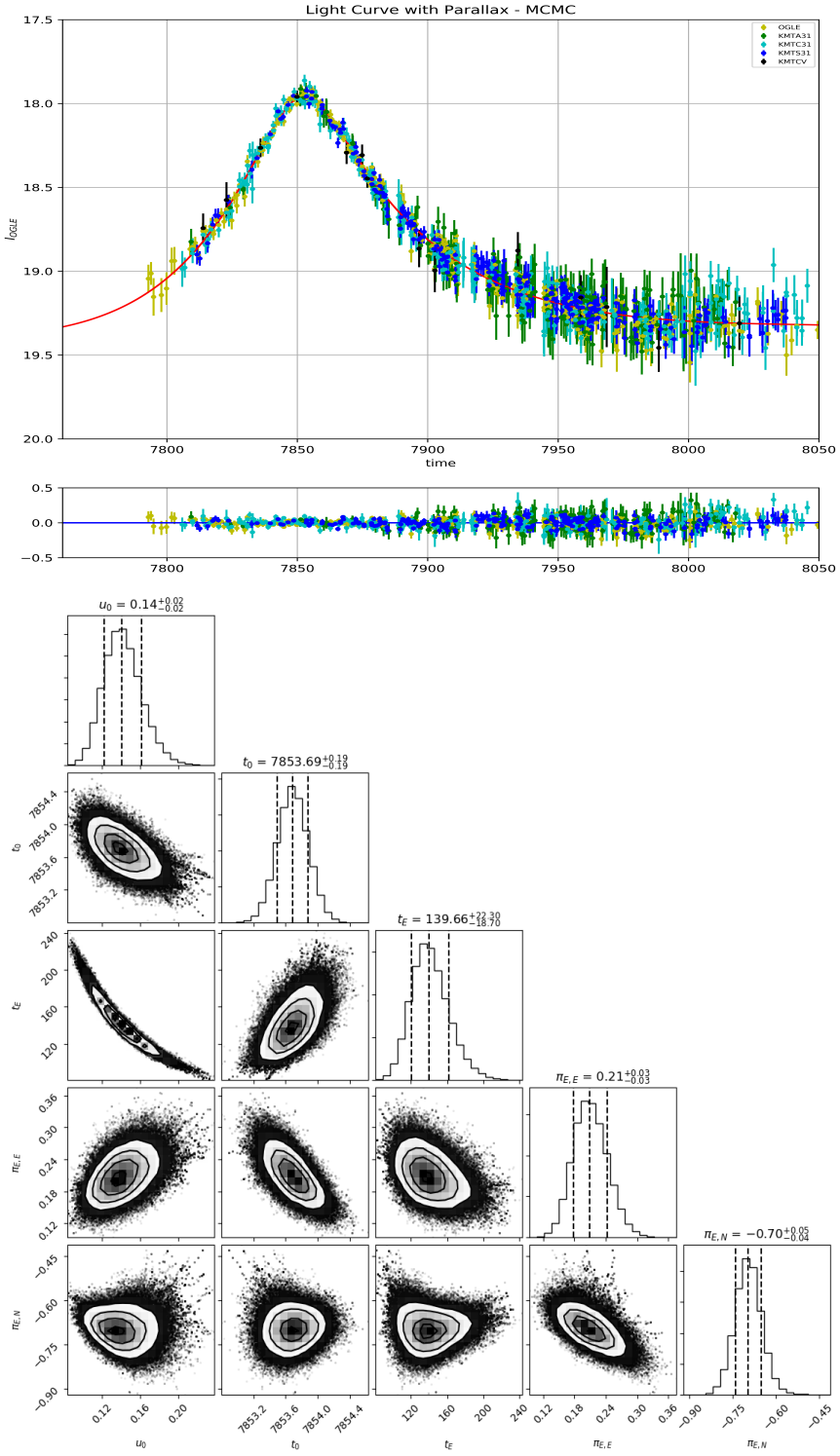

Figure 3.4: The fit to the light curve with the orbital parallax and the covariance plot after renormalising the uncertainties.

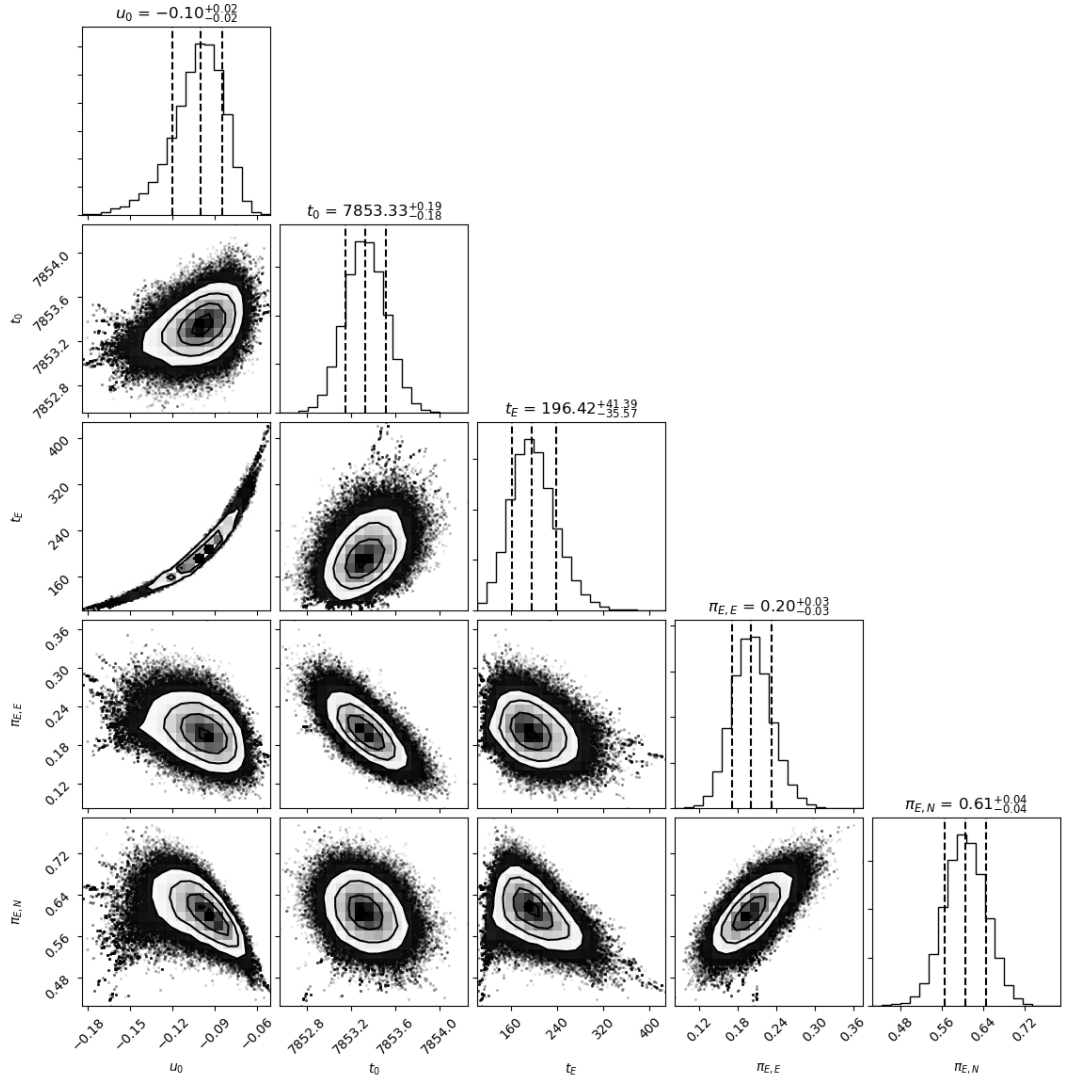

Figure 3.5: The covariance plots obtained after fitting P2 model to the light curve.

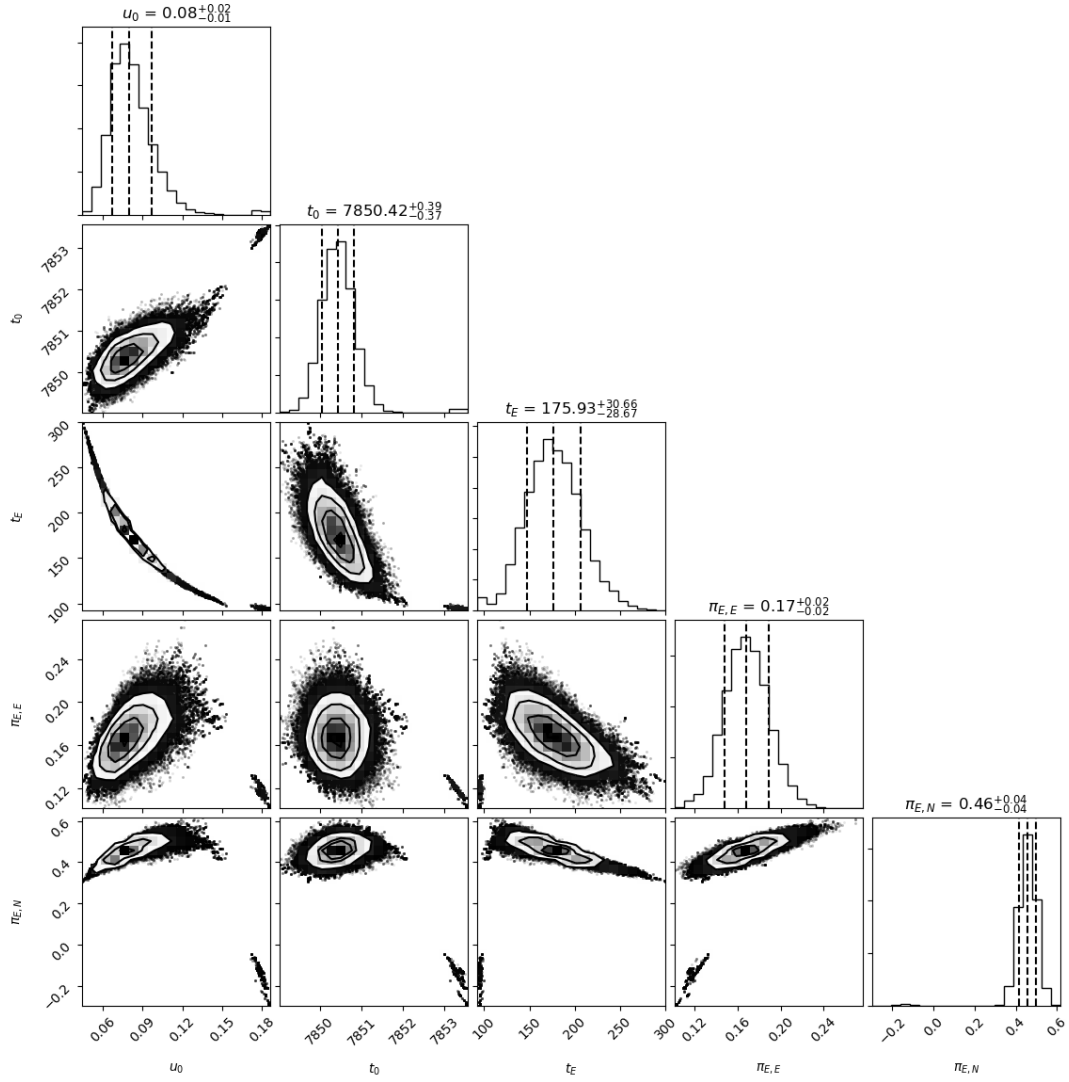

Figure 3.6: The covariance plots obtained after fitting P3 model to the light curve. The isolated points correspond to the distribution of the parameters of P1 model.

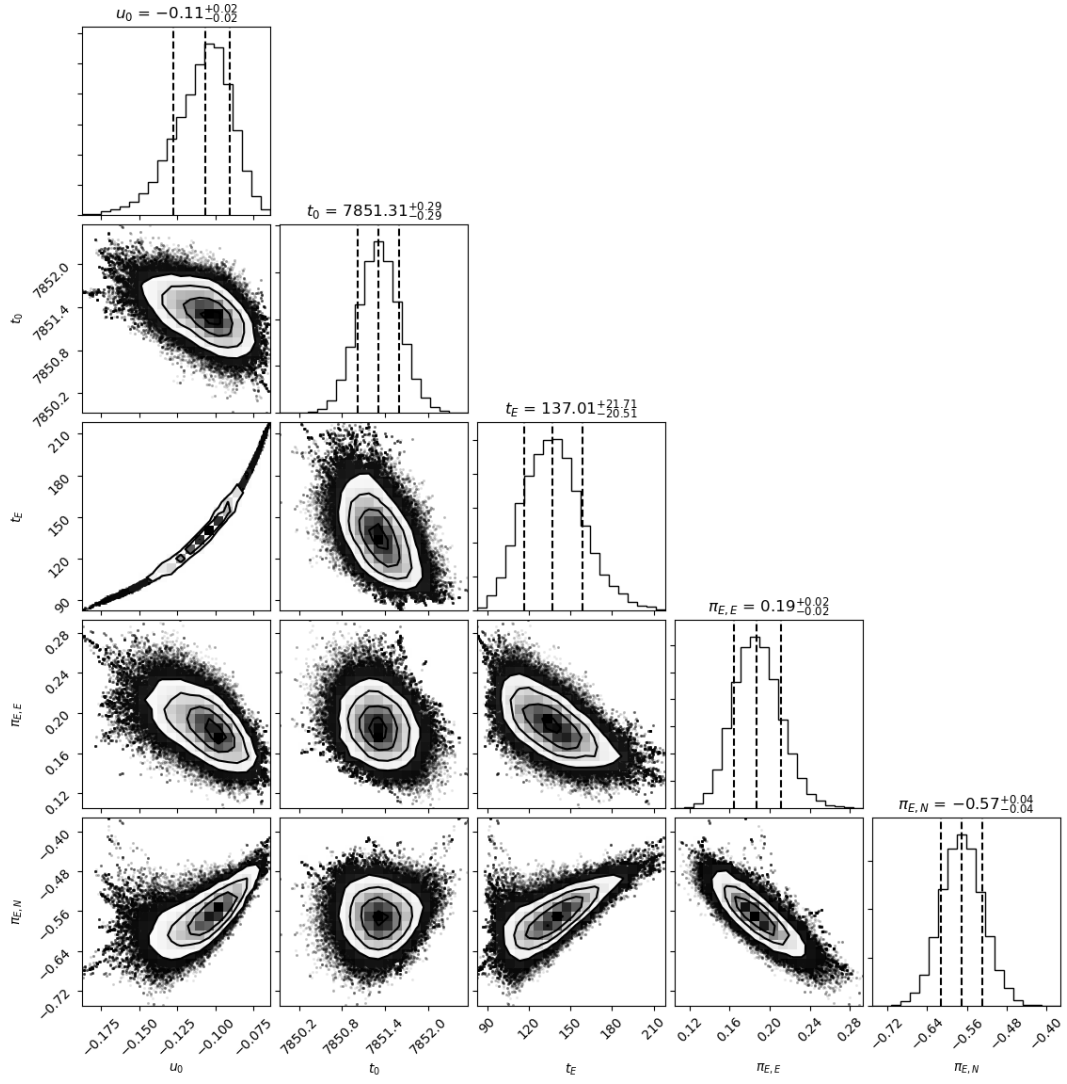

Figure 3.7: The covariance plots obtained after fitting P4 model to the light curve.

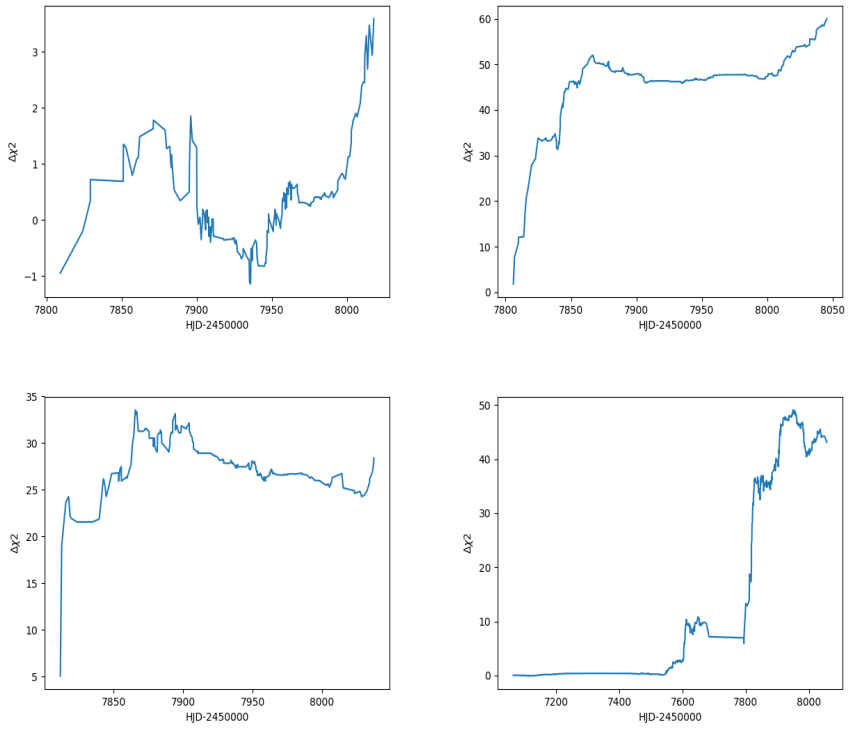

Figure 3.8: The figures show the plot for cumulative $\Delta\chi^2$ vs t_0 for KMT-A, KMT-C, KMT-S and OGLE from left top. $\Delta\chi^2 = \chi^2_{single}$ - $\chi^2_{parallax}$. We see a trivial decrease in the $\Delta\chi^2$ in the period between (HJD-2450000) 7900 and 7950 when the event reaches the baseline. This is most likely due to contamination of the sky by the Moon which shines close to the galactic bulge during this period.

3.4 Source Properties

We fit the P1 model with the V-band data of KMT-C02 field to obtain the source and the blend flux in the V-band. Since pyDIA also gives the location of the centroid of the Red Clump on the CMD we can estimate the position of the source and blend on the CMD. Table (3.3) shows the blend and source flux for the KMT-C31 data set. Using these fluxes, we find the location of the source and blend on the CMD (Figure (3.9)).

3.5 Galactic Model

In the case of OGL-2017-BLG-0192, there are no finite source effects detected. But we can estimate the lens mass and position from the bayesian analysis of the galactic model constrained by π_E and t_E (Chapter (2)). When the source and the lens distances are allowed to be free parameters in the galactic model, we find that we get a bi-modal distribution for the lens distance distribution with the source being in the bulge. We

Parameters of different fits					
Parameter	PSPL	P1	P2	P3	P4
χ^2	4810.660	1539.73	1548.62	1581.93	1568.16
u_0	0.134 ± 0.005	0.14 ± 0.02	-0.10 ± 0.02	$0.08^{+0.02}_{-0.01}$	-0.11 ± 0.02
t_0 (days)	7853.78 ± 0.06	7853.69 ± 0.19	$7853.33^{+0.19}_{-0.18}$	$7850.42^{+0.39}_{-0.37}$	7851.31 ± 0.29
t_E (days)	122.701 ± 0.066	$139.97^{+22.16}_{-19.37}$	$196.42^{+41.39}_{-35.57}$	$175.93^{+30.66}_{-28.87}$	$137.01^{+21.71}_{-20.51}$
$\pi_{E,E}$	-	0.21 ± 0.03	0.20 ± 0.03	0.17 ± 0.02	0.19 ± 0.02
$\pi_{E,N}$	-	$-0.70^{+0.05}_{-0.04}$	0.61 ± 0.04	0.46 ± 0.04	-0.57 ± 0.04

Table 3.2: The table showing the parameters with their 16^{th}, 50^{th} and 84^{th} percentiles for PSPL and degenerate orbital Parallax models. (a) P1 is the original solution obtained after minimising χ^2 using MCMC. (b) P2 is the solution seeded with sign of u_0 reversed from P1 (c) P3 is the jerk parallax degenerate solution corresponding to P1 (d) P4 is the jerk parallax degenerate solution corresponding to P2.

Blend and source flux		
Site	F_b	F_s
OGLE	1308.13 ± 12.37	1374.07 ± 6.00
KMT-A31	15648.11 ± 653.16	19737.93 ± 316.31
KMT-C31	13156.13 ± 293.72	11615.34 ± 102.09
KMT-S31	18077.67 ± 467.27	23099.35 ± 190.98
KMT-CV	3392.98 ± 1079.45	9362.67 ± 297.55

Table 3.3: Source and blend flux with their uncertainties for P1 model.

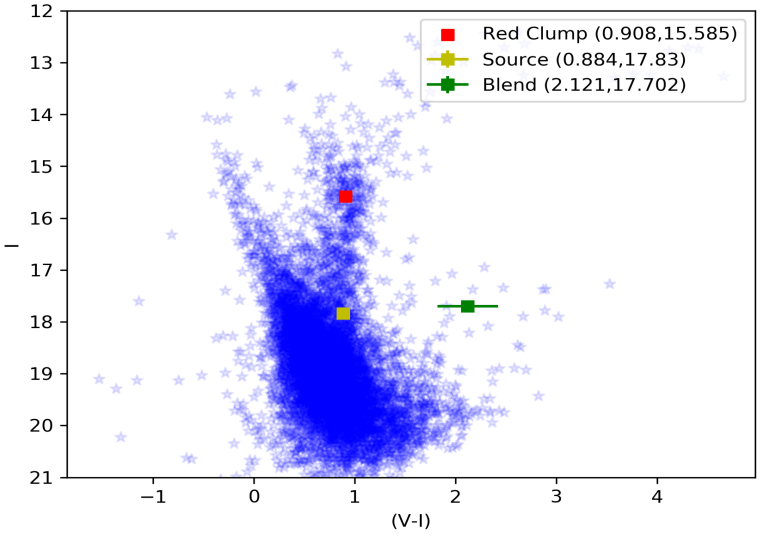

Figure 3.9: The CMD constructed using KMT-C images for I and V band. The locations of the source and blend are similar for all the solutions.

therefore perform the analysis separately for the disc and the bulge location of the lens while the source is assumed to lie in the bulge. The galactic model then favours the disc

location of the lens by 86%. The results for the lens mass and distance for the P1 model are presented in Figure (3.10).

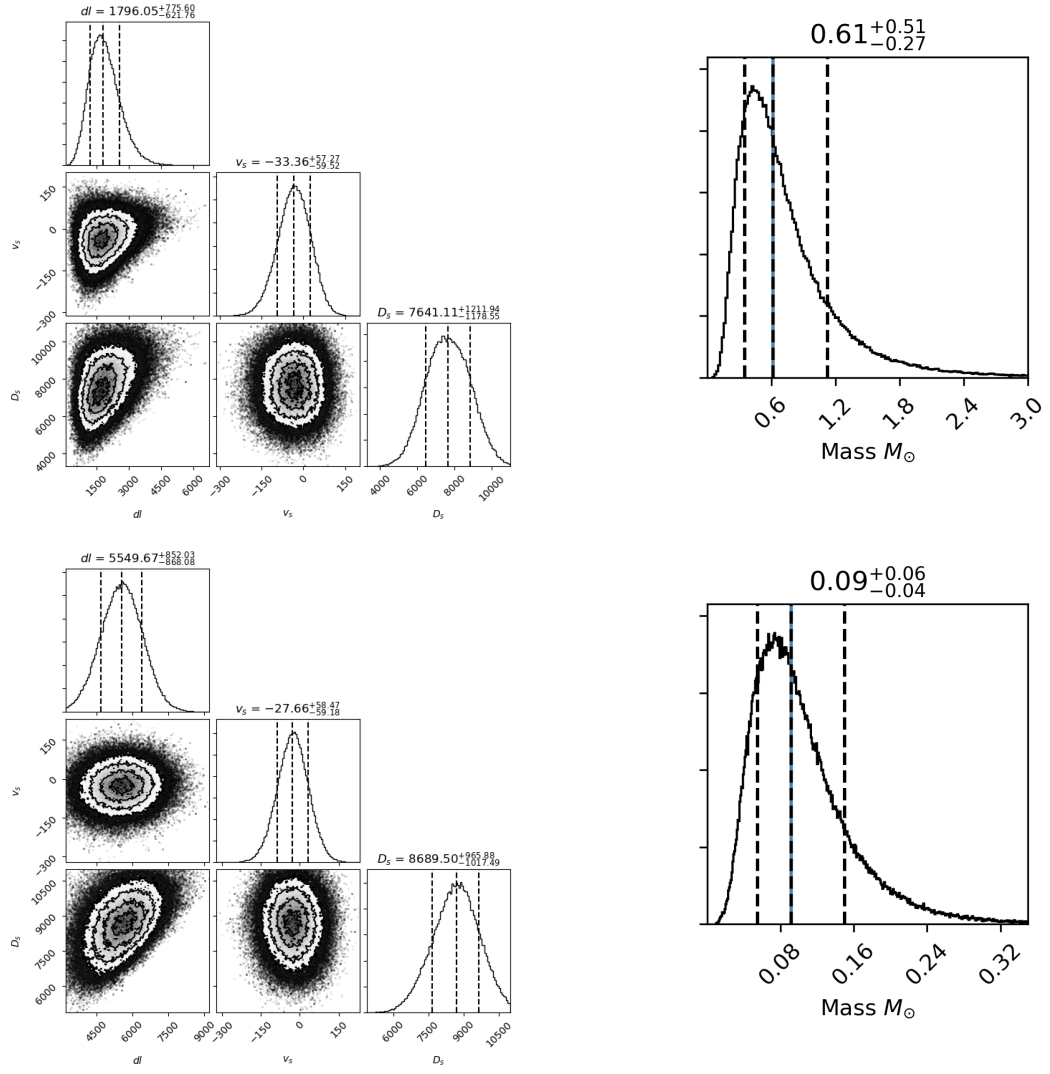

Figure 3.10: Galactic model results for P1 microlensing model. The blue line in the mass shows the shows the median of the distribution. The results are shown as 16^{th}, 50^{th} and 84^{th} quantile.

3.6 Discussion

I have analysed the event OGLE-2017-BLG-0192 and found that the asymmetry in the light curve can be explained due to orbital parallax effect. When the orbital motion of the Earth was included, it was found that the light curve suffers from discrete degeneracy where parallax contours are disjoint. The reason for this degeneracy is that t_E of this event is high enough to break the continuous degeneracy, but due to proximity of the event to the ecliptic might have led to distinct parallax solutions. Presence of orbital parallax is also evident from the asymmetry in the light curve both about the base and about the peak. Renormalisation of uncertainties differentiated the best solution (P1) from the other solutions (Table (3.2)). Using the CMD, it can be seen that the blend is significantly redder than the field stars and there is also a lot of uncertainty in its colour. So the lens is not the major contributor to the blended light. Since blend is the upper limit on the lens brightness, it can be concluded that both the lens can be a main-sequence star like the source star. Bayesian analysis of the galactic model by constraining it with π_E and t_E of the P1 model yields the mass of the lens as $0.6^{+0.51}_{-0.27} M_\odot$ located at $1.79^{+0.77}_{-0.62}$kpc or a $0.09^{+0.06}_{-0.04} M_\odot$ located at $5.54^{+0.85}_{-0.82}$kpc. Bayesian analysis prefers the disc location of lens by 86%.

Chapter 4

Analysis of the event OGLE-2017-BLG-0103

In this chapter, I present the analysis of the event $OGLE-2017-BLG-0103$ which suffers from *Jerk Parallax* degeneracy. The ecliptic coordinates for this event are (λ,β) = ($268.3696^0, -6.58350^0$). Also, the event peaks close to the vernal equinox of 2017 when the acceleration of the earth is nearly perpendicular to the galactic bulge. Using equation (1.33), we find $v_j \sim 165$km/s. In the case of OGL-2017-BLG-0103, it is found that the parallax signal is moderate. The source star for this event is relatively faint and hence the photometry might be contaminated due to neighbouring stars towards the line of sight.

4.1 Observations and Data Reductions

4.1.1 OGLE

OGLE-2017-BLG-0103 is the 103rd event detected by the Early Warning System (EWS) of the *Optical Gravitational Lensing Experiment* (OGLE). It was observed towards the galactic bulge through its 1.3m Warsaw Telescope at the Las Campanas Observatory in Chile Udalski et al. (2015a) in the field *BLG501.11*.The equatorial co-ordinates of this event as $\alpha = 17:52:31.49$, $\delta = -30:00:44.4$ which can be translated to galactic co-ordinates as $l = 359.85008^o$, $b = -1.84077^o$. I use *https://ned.ipac.caltech.edu* to convert the equatorial coordinates to galactic coordinates.

4.1.2 KMTNet

OGLE-2017-BLG-0103 was also observed separately by the *Korean Microlensing Telescope Network* (KMTNet) through its three 1.8m telescopes in Chile, South Africa and Australia. KMTNet telescopes are equipped with $4deg^2$ wide field cameras to monitor the galactic field Kim et al. (2016). OGLE-2017-BLG-0103 was observed in two fields - BLGA02 and BLGA42 by KMTNet.

4.1.3 Data Reduction

KMTNet images for the field BLG02 were reduced using the pyDIA software Albrow (2017) which is based on difference image analysis using the delta-basis-function approach of Bramich et al. (2013). The data was filtered based on different criteria for each data set. For the KMT-A and KMT-C (I-band) data set, no data point was allowed to have uncertainty in the magnitude greater than 0.1. Since both the data sets are clean, there was no more need for additional filtering. For the KMT-S (I-band) data, no data points were allowed having uncertainty in magnitude >0.1, Q>1.2, FWHM>2, Roundness>1.3. For the CTIO V-band data, we do not allow any points having uncertainty in magnitude ≥0.1, Q≥1.2, FWHM≥2 and Roundness≥1.3. We convert the time of these observations from JD to Heliocentric Julian Days (HJD).
Since this event was also observed towards the beginning of the bulge observing season of 2017, there were no data points on the baseline before the start of this event. However, there is a long baseline with some outliers on the decreasing side of the event. OGLE data was downloaded from the EWS page for Microlensing page[1] and the KMTNet data for the field BLG42 was downloaded from their internal webpage[2].

4.2 Analysis

The single lens fit to the light curve was done using the system developed by McDougall & Albrow (2016). This fit yields $u_0 = 0.099 \pm 0.001$, $t_0 = 7829.9 \pm 0.01$ in units of HJD-2450000 days and $t_E = 73.12 \pm 0.12$ days. The corresponding light curve is shown in Figure (4.1).

We then add orbital parallax through equation (1.24) and perform a coarse grid search minimising χ^2 over the ($\pi_{E,E}$, $\pi_{E,N}$) plane where the dimensions of the grid were (-8,8,-8,8). This search yielded minima at $(\pi_{E,E}, \pi_{E,N}) = (0.184, -0.168)$ (Figure (4.2)). These

[1] http://ogle.astrouw.edu.pl/ogle4/ews/
[2] http://kmtnet.kasi.re.kr/ulens

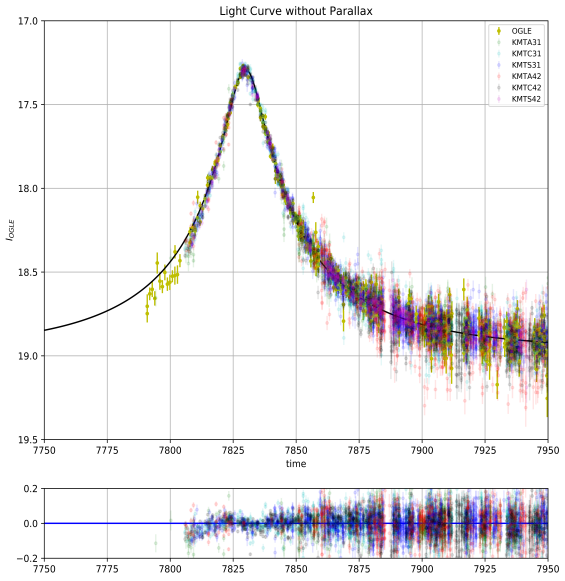

Figure 4.1: PSPL light curve which shows poor fit on the rising side of the light curve.

parameters were then seeded to emcee (Foreman-Mackey et al., 2013) which yielded the parameter distributions shown in Figure (4.4). We call this model as P1.

Uncertainties in magnitudes were re-normalised based on this solution (section (1.6)). The values of e_{min} and κ are shown in Table 4.1. The P1 model was re-run which converged to a solution shown in Figure (4.5), where we see the Jerk-Parallax degeneracy in the bimodal distribution of π_{EN}, t_E and t_0. We term solution corresponding to the left mode in the distribution of π_{EN} as P3. To explore the constant acceleration degeneracy, we seed MCMC with the parameters of model P1 but with the sign of u_0 reversed. The walkers converge to a new solution shown in Figure (4.6), which also has a bimodal distribution of π_{EN}, t_E and t_0 . We call the right side of the bimodal distribution of π_{EN} P2 and left side as P4. P3 and P4 are the Jerk-Parallax solutions corresponding to P1 and P2.

4.2.1 Alternative method to find jerk parallax solutions

We show an alternative method to find the Jerk-Parallax degenerate solutions that is proposed by Gould (2004) and used by Jiang et al. (2004) and Park et al. (2004). However, since the event lies close to ecliptic, degeneracy in $\pi_{E,\perp}$ is reflected as the degeneracy in π_{EN}. This is why we get bimodal distribution of π_{EN}. For this we find the celestial position of the Sun at the peak of the event by using the method given by Soszyński et al. (2001) (Appendix (A)). The first and second order derivatives with respect to time

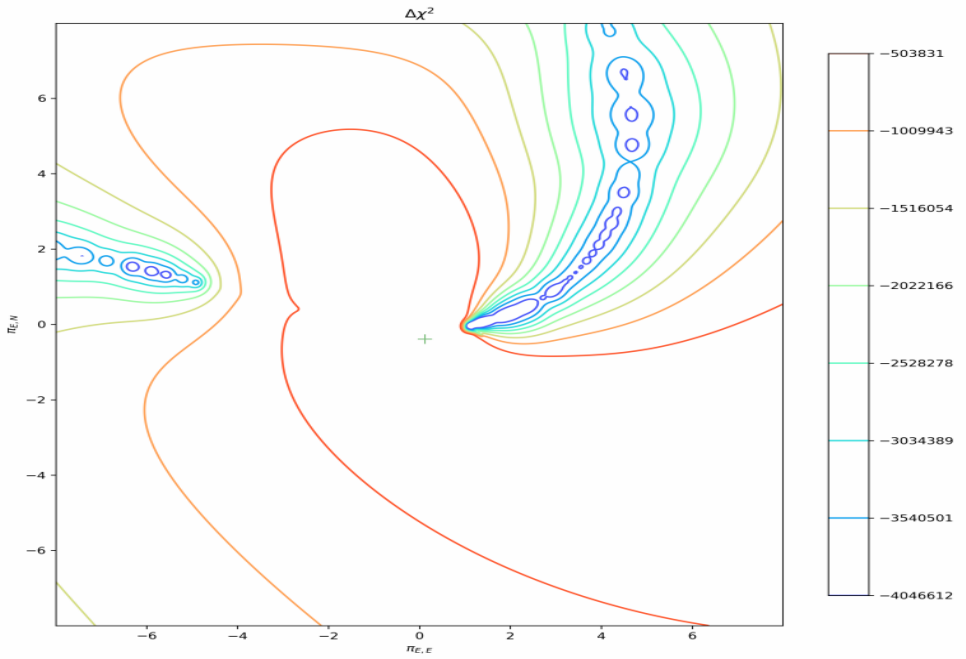

Figure 4.2: The $\Delta\chi^2$ contours obtained after performing a coarse grid search over π_E plane where $\Delta\chi^2 = \chi^2_{PSPL}$ - $\chi^2_{parallax}$. The minima is at the blue cross in the innermost level.

Parameters to renormalise uncertainties		
Dataset	κ	e_{min}
OGLE	1.407	0.0
KMT-A01	2.654	0.009
KMT-C02	2.785	0.007
KMT-S02	1.278	0.006
KMT-A42	2.914	0.009
KMT-C42	2.524	0.010
KMT-S42	1.313	0.006

Table 4.1: The scale factor κ and extra term e_{min} added to each dataset after renormalisation of uncertainty in magnitude in order to make $\chi^2/dof \sim 1$. This process gives equal weight to each dataset during modelling. Suffices 02 and 42 for the KMTNet datasets represent the fields BLG02 and BLG42 fields respectively.

give the velocity and acceleration in the celestial north and east directions respectively,

$$\alpha(N,E) = (1.21 \times 10^{-3}, 7.07 \times 10^{-5}) km/day^2; \quad v_{\oplus}(N,E) = (-1.27, 29.95) km/s \quad (4.1)$$

The acceleration was then projected on to the plane of the sky using the formulation of An et al. (2002),

$$\alpha_{w,projected} = \alpha sin(\lambda_{\odot} - \lambda_0); \quad \alpha_{n,projected} = \alpha cos(\lambda_{\odot} - \lambda_0) sin(\beta_0) \quad (4.2)$$

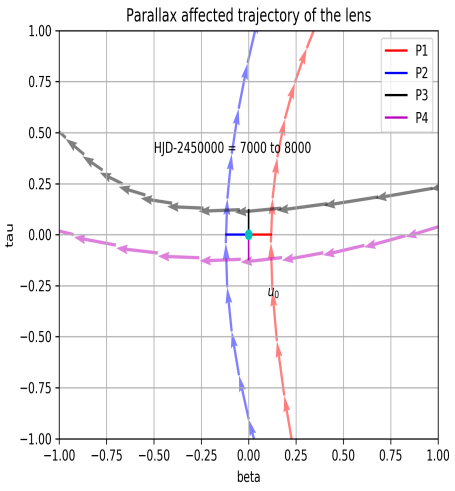

(a) The trajectories corresponding to different parallax solutions

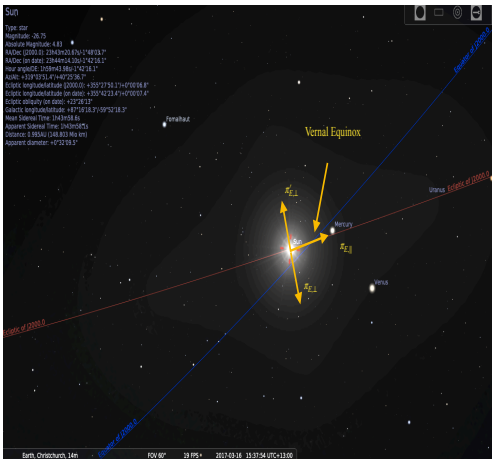

(b) The path of the sun in the plane of the sky

Figure 4.3: (a) shows different trajectories corresponding to the obtained jerk-parallax solutions. “red" trajectory corresponds to P1, “blue" corresponds to P2, “black" corresponds to P3 and ’magenta’ corresponds to P4. From Table (4.2), we can see that the values of $\Delta\tau$ and $\Delta\beta$ are not very different. This is the reason for similar deviation of the trajectories in different solutions. (b) shows the path of the sun projected in the plane of the sky during the peak of the event. Since the event occurred close to the vernal equinox the sun’s projected acceleration is along the ecliptic towards the intersection of both the planes. The jerk velocity at this time for this event is ∼165.62 km/s.

where λ_0, β_0 are the ecliptic co-ordinates of the event and $\lambda_\odot$ is the phase of the earth’s orbit. Thus,

$$\alpha(n, e) = (-2.44 \times 10^{-7}, 1.49 \times 10^{-4}) km/day^2 \tag{4.3}$$

The projected acceleration points 359.80^0 north through east in the ecliptic plane. The parallax contours are elongated in the direction perpendicular to this direction 269.9^0. From Figure (4.5), it is clearly evident that for the Jerk-Parallax solution (which we have labeled as P3 solution), $\pi_{E,N}$ lies between -0.3 and -0.6 and there is no change in $\pi_{E,E}$. To find the jerk-parallax solution P3, we find the parallel and perpendicular components of the parallax to the acceleration of the Sun,

$$\pi_{E,\parallel}, \pi_{E,\perp} = (0.43, 0.00) \tag{4.4}$$

Using equation (1.30), we get $\pi_{j,\perp} = 0.17$. Thus,

$$\pi^{'}_{E,\parallel}, \pi^{'}_{E,\perp} = (0.43, -0.17) \tag{4.5}$$

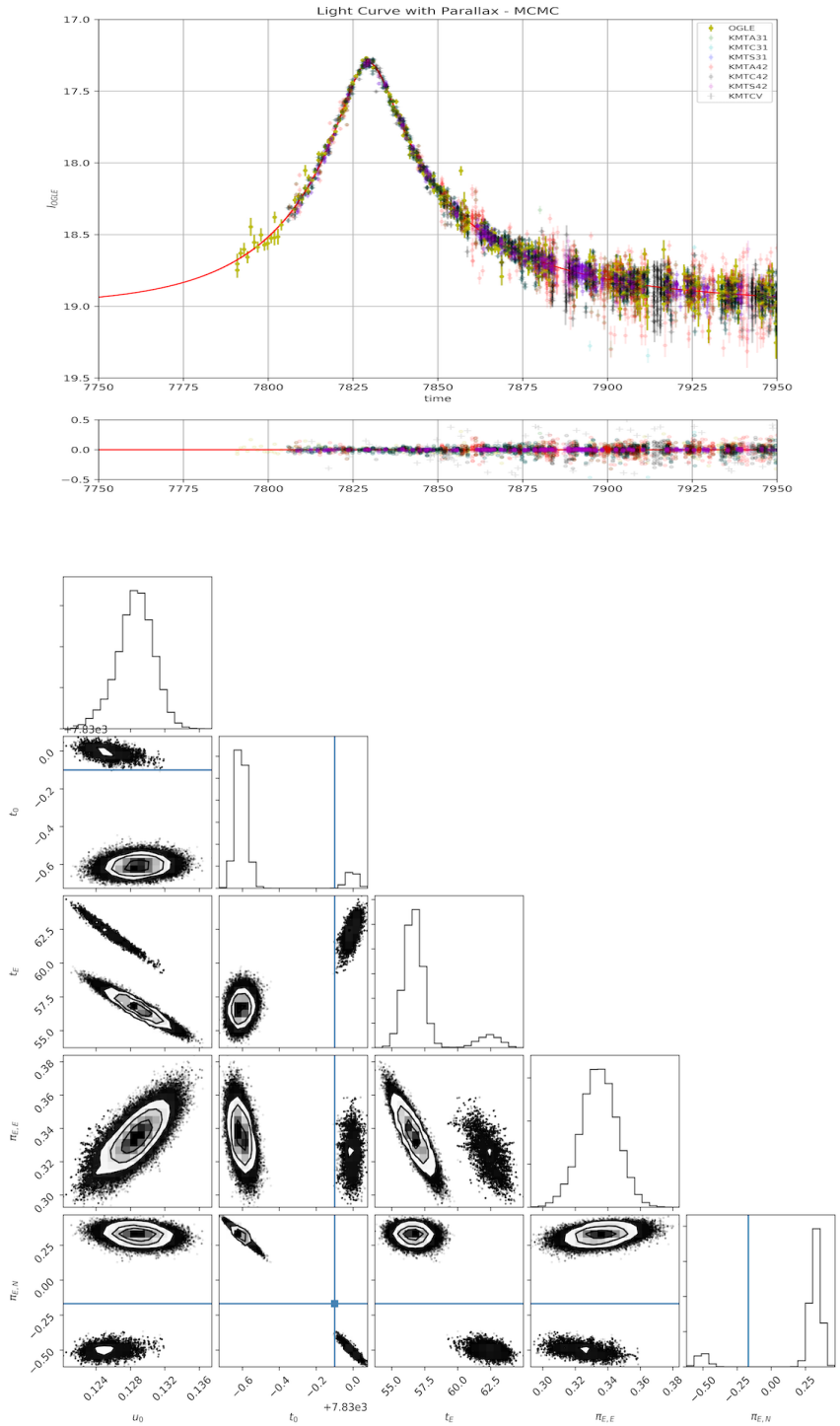

Figure 4.4: The fit to the light curve with the orbital parallax and the covariance plot before renormalising the uncertainties. The blue lines are the points where the emcee is started.

The path of the sun in the plane of the sky can be visualised using Figure (4.3) which shows the projected acceleration of the Sun close to vernal equinox and also the degeneracy in the event. The image is a screenshot of *Stellarium* v.0.15.1[3]. Since *OGLE* –

[3]www.stellarium.org

$2017-BLG-0103$ peaked close to the vernal equinox the sun's projected acceleration is along the ecliptic towards the intersection of both the planes. The jerk velocity at this time for this event obtained is ∼165.62 km/s (equation (1.33)).
From Figure (4.5), we see that the covariances between the degenerate π_E are perpendicular to each other. The direction of $\boldsymbol{\pi_E}$ is the direction of $\boldsymbol{\mu}_{rel}$ in the adopted frame of reference. Therefore, the direction of $\boldsymbol{\mu}_{rel}$ for P3 will be perpendicular to the direction of $\boldsymbol{\mu}_{rel}$ in P1 solution. Having the direction of $\boldsymbol{\mu}_{rel}$ for P1 solution as $\arctan(\pi_{EN}/\pi_{E,E})$ $= 47^0$ in the celestial frame, the direction of $\boldsymbol{\mu}_{rel}$ for P3 solution should be 137^0. Thus, we can convert $(\pi'_{E,\parallel}, \pi'_{E,\perp})$ to celestial frame,

$$\pi_{E,E}, \pi_{E,N} = (0.30, -0.34) \tag{4.6}$$

After seeding MCMC with the Paczyński parameters of the P1 solution and the parallax parameters in (4.6), it was found that the degenerate parallax parameters are $\pi_{E,E}, \pi_{E,N}$ = (0.30,-0.50). Furthermore, t_0 and t_E also converge to the other mode of the bimodal distribution of the samples. Similarly we find the other jerk parallax solution P4 which corresponds to P2 solution. The pair of P1 and P4 solutions as well as the pair of P2 and P3 solutions give a similar mass and distance to the lens (see section (4.3)).

This analysis shows that the Jerk-Parallax solution can be found directly from the triangle plots. In all the solutions it is observed that $\pi_{E,\parallel} > \pi_{E,\perp}$ which is seen in the light curve as well. The trajectories corresponding to these solutions are shown in Figure (4.3) and the samples of the parameters corresponding to each solution with their 16^{th}, 50^{th} and 84^{th} percentile values are shown in Table (4.2).

Parameters of different fits					
Parameter	PSPL	P1	P2	P3	P4
χ^2	49123.42	11298.62	11297.50	11296.86	11294.40
u_0	0.099 ± 0.001	0.123 ± 0.001	-0.122 ± 0.001	0.123 ± 0.001	-0.123 ± 0.001
t_0 (days)	7829.90 ± 0.01	$7829.44^{+0.09}_{-0.07}$	7829.67 ± 0.03	$7830.05^{+0.06}_{-0.08}$	7829.67 ± 0.03
t_E (days)	73.12 ± 0.01	$58.26^{+1.62}_{-1.55}$	60.42 ± 2.12	$63.91^{+2.22}_{-2.11}$	60.23 ± 2.06
$\pi_{E,E}$	-	$0.31^{+0.02}_{-0.02}$	0.30 ± 0.02	$0.30^{+0.02}_{-0.02}$	0.30 ± 0.02
$\pi_{E,N}$	-	$0.32^{+0.08}_{-0.10}$	-0.02 ± 0.41	$-0.50^{+0.11}_{-0.08}$	0.02 ± 0.40

Table 4.2: The table showing 16^{th}, 50^{th} and 84^{th} percentile values for the sample of parameters corresponding to each mode of the distribution of π_{EN}. P3 and P4 models are obtained by investigating the Jerk-Parallax degeneracy for P1 and P2 models.

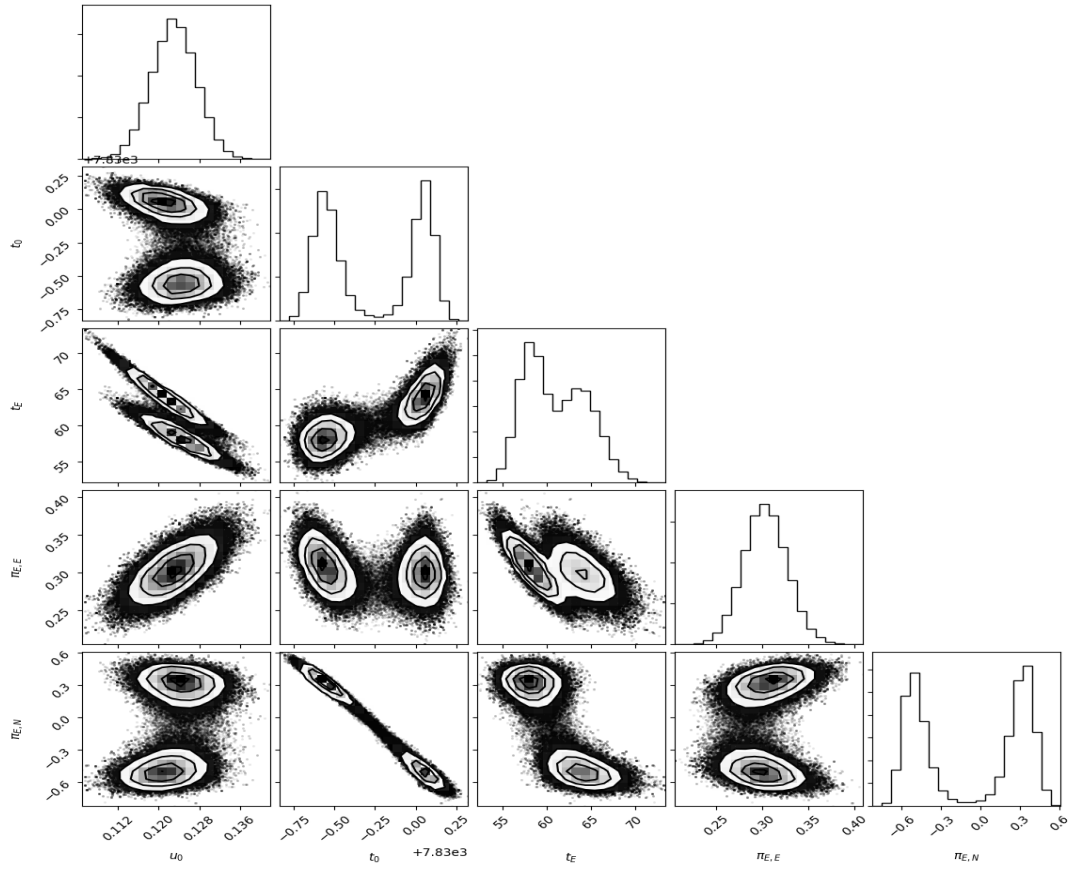

Figure 4.5: Triangle plot for P1 and P3 solution. The Jerk-Parallax solution P3 is the left mode of the bimodal distribution of π_{EN}, t_E and t_0.

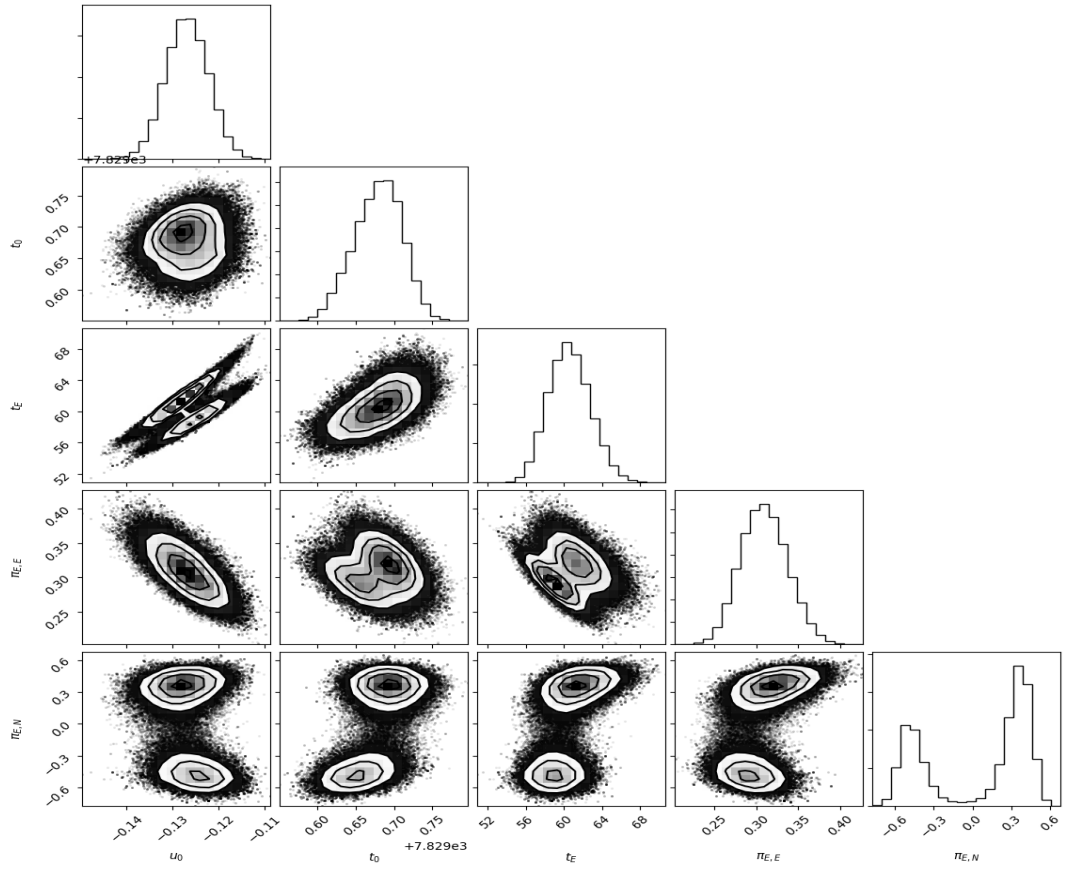

Figure 4.6: Triangle plot for P2 and P4 solution. The Jerk-Parallax solution P4 is the left mode of the bimodal distribution of π_{EN}, t_E and t_0.

4.3 Galactic Model

Since there is no detection of finite source effects in OGLE-2017-BLG-0103, we form a galactic model as described in Chapter 2 to estimate the lens mass and distance of the lens. When we constrain it using the samples of π_E and t_E of the each degenerate model, we find that the distribution of the distance to the lens (D_L) is bimodal. Therefore we explore the disc and bulge location of lens separately. The galactic model favours disc location of the lens by $\sim 90\%$ for each model. We show all the solutions in Figures (4.7 - 4.10) and display the lens mass and distance for each solution in Table (4.3).

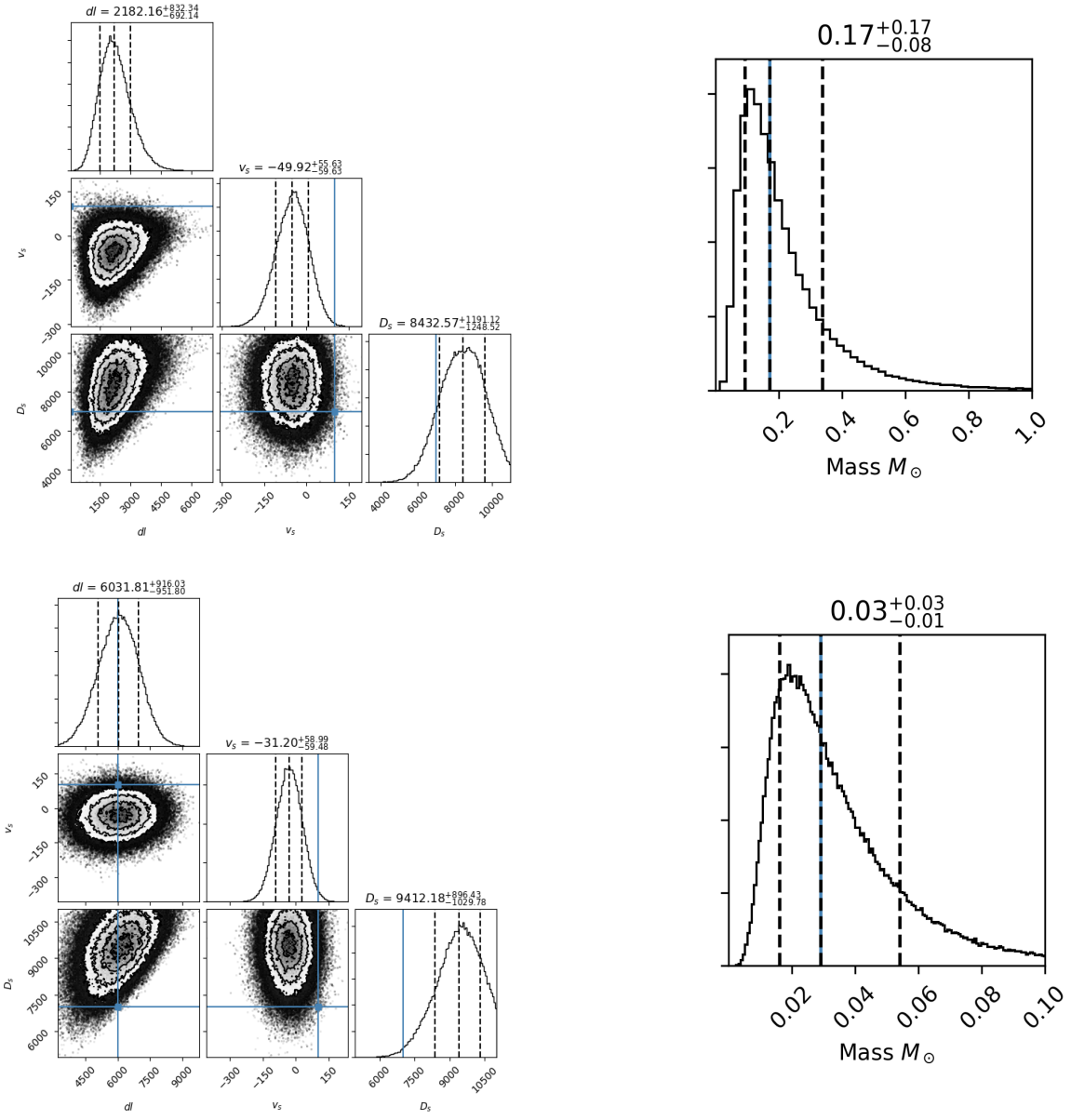

Figure 4.7: The galactic model results for P1 model showing the distribution of D_L, v_s, D_s and M_L. The top solution is for a disc location of the lens and the bottom solution is for the bulge location of the lens.

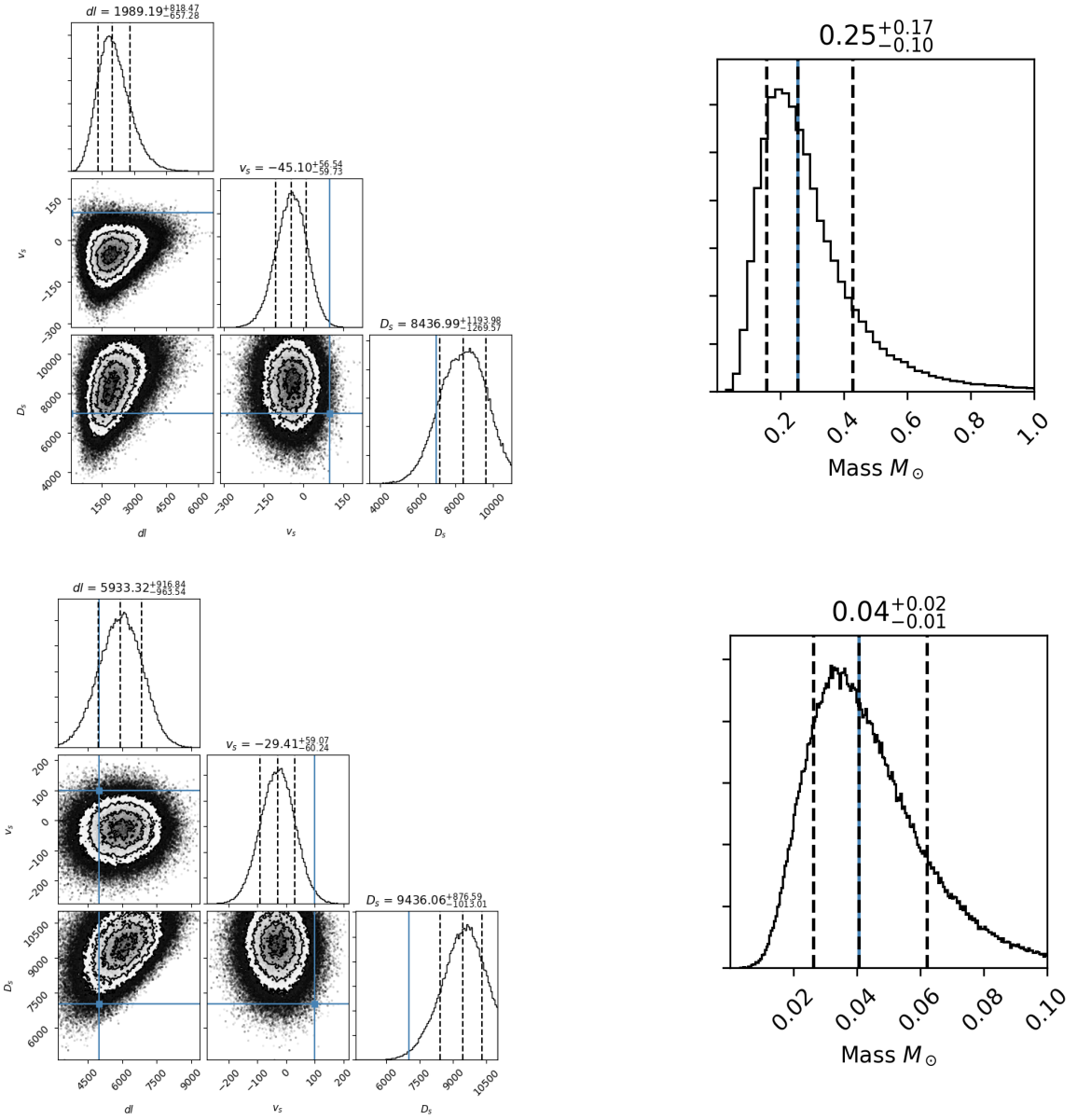

Figure 4.8: The galactic model results for P2 model showing the distribution of D_L, v_s, D_s and M_L. The top solution is for a disc location of the lens and the bottom solution is for the bulge location of the lens.

4.4 Source Properties

Due to adequate coverage of this event by different observatories, the source and blend flux for this event are fairly constrained. We fit the V-band data of the KMT-C BLG-02 field to the model which gives the source flux and the blend flux in the V-band. We use the I band source and blend fluxes of the KMT-C BLG02 field to locate the position of the source and the blend on the CMD formed by the stars in the BLG02 field of the KMT-C dataset (Figure (4.11)). The source and the blend flux for the KMT-C BLG02 dataset in I and V band are shown in Table (4.4)

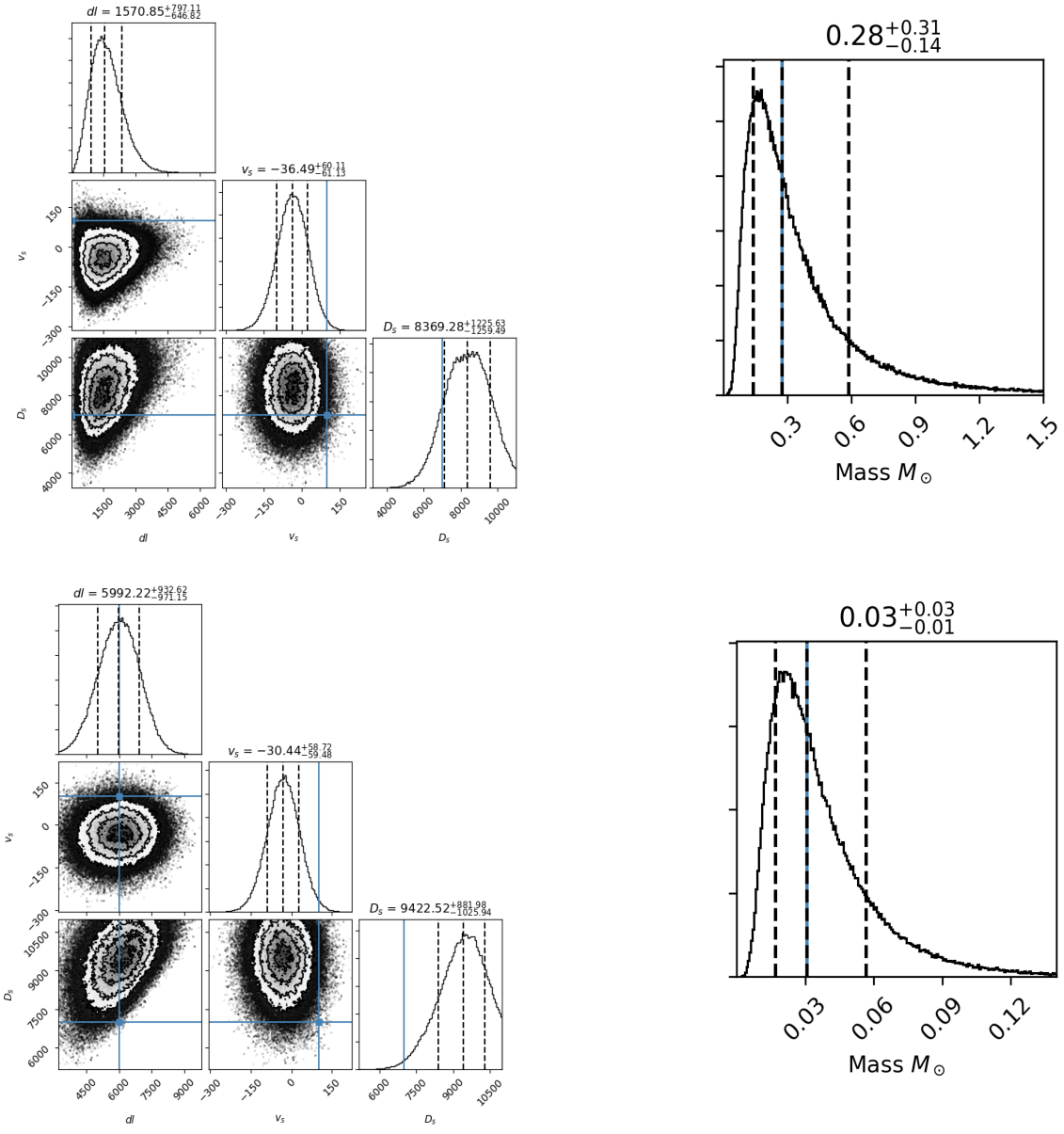

Figure 4.9: The galactic model results for P3 model showing the distribution of D_L, v_s, D_s and M_L. The top solution is for a disc location of the lens and the bottom solution is for the bulge location of the lens.

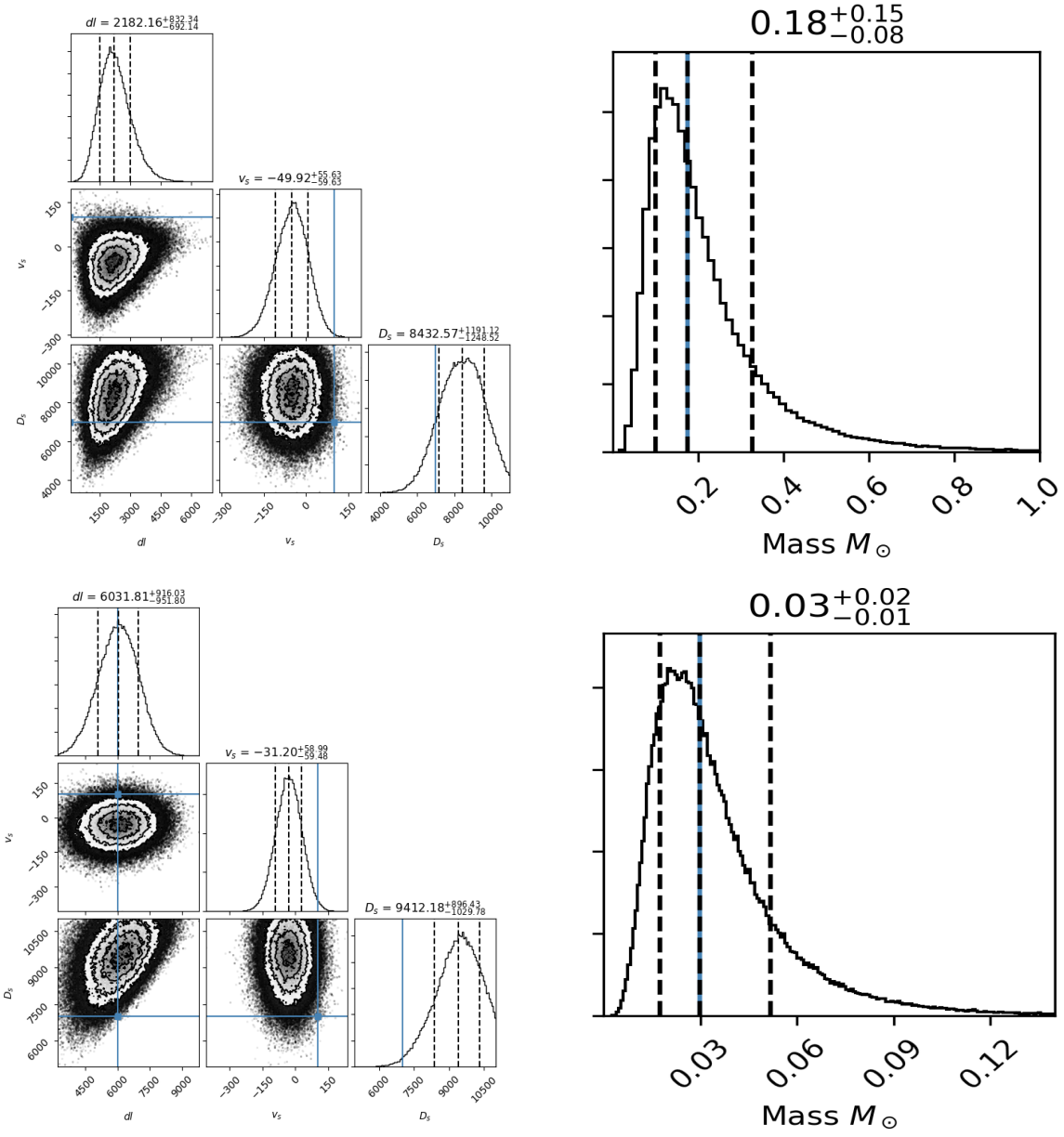

Figure 4.10: The galactic model results for P4 model showing the distribution of D_L, v_s, D_s and M_L. The top solution is for a disc location of the lens and the bottom solution is for the bulge location of the lens.

Lens Properties				
Parameter	P1	P2	P3	P4
$M_{L,disc}$ $(M_\odot)$	$0.17^{+0.17}_{-0.08}$	$0.25^{+0.17}_{-0.10}$	$0.28^{+0.31}_{-0.14}$	$0.18^{+0.15}_{-0.08}$
$M_{L,bulge}$ $(M_\odot)$	$0.03^{+0.03}_{-0.01}$	$0.04^{+0.02}_{-0.01}$	$0.03^{+0.03}_{-0.01}$	$0.03^{+0.02}_{-0.01}$
$D_{L,disc}$(kpc)	$2.18^{+0.83}_{-0.69}$	$1.98^{+0.81}_{-0.65}$	$1.57^{+0.79}_{-0.64}$	$2.18^{+0.83}_{-0.69}$
$D_{L,bulge}$(kpc)	$6.03^{+0.91}_{-0.95}$	$5.93^{+0.91}_{-0.96}$	$5.99^{+0.93}_{-0.97}$	$6.03^{+0.91}_{-0.95}$
$D_{s,disc}$(kpc)	$8.43^{+1.19}_{-1.12}$	$8.43^{+1.19}_{-1.26}$	$8.36^{+1.22}_{-1.25}$	$8.43^{+1.19}_{-1.24}$
$D_{s,bulge}$ (kpc)	$9.41^{+0.89}_{-1.02}$	$9.41^{+0.87}_{-1.01}$	$9.42^{+0.88}_{-1.02}$	$9.41^{+0.89}_{-1.02}$

Table 4.3: The galactic model results for each degenerate solution. The pair of P1 and P4 solutions as well as the pair of P2 and P3 solutions give a similar mass and distance to the lens.

Blend and source flux		
Site	F_b	F_s
KMT-C02	2225.23 ± 15.98	2327.07 ± 7.39
KMT-CV	441.42 ± 8.10	304.15 ± 3.21

Table 4.4: The source and the blend fluxes in I and V bands respectively for the KMT-C BLG02 dataset.

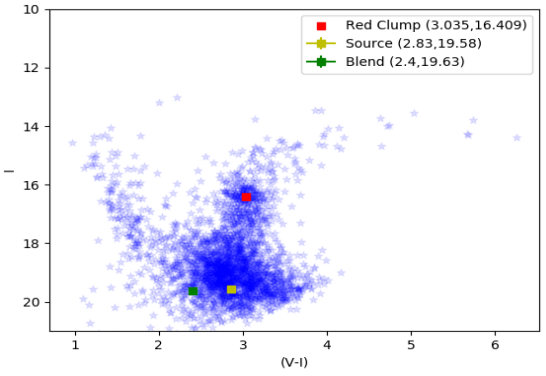

CMD showing RC centroid, source and blend position for P1 model

Figure 4.11: The CMD constructed using KMT-C images for I and V band. The locations of the source and blend are similar for all the solutions.

4.4.1 Investigating the nature of the blend

From Figure (4.11), we see that the the blend lies on faint blue side of the CMD. In order to verify the nature of the blend on this location and whether it is compatible with being the lens, we perform additional analysis using its colour. For this *Modules for Experiments in Stellar Astrophysics* (Paxton et al., 2011, 2013, 2015, 2018) (MESA)'s *MIST* package was used Choi et al. (2016), Dotter (2016). *MESA Isochrone and Stellar Tracks* is a package that simulates stellar evolutionary tracks, theoretical isochrones and synthetic photometry models [4]. Using MIST package, mass-luminosity relations were generated for a solar metallicity and solar age star. From this relations, the absolute brightness for the estimated mass of the lens was calculated (both with and without the total bulge extinction towards line of sight) at the distance derived from the galactic model in V and I bands respectively. The contours showing the position of the lens on the CMD if the lens suffers no extinction (left contour) and if it suffers the same amount of extinction as the red clump stars towards the line of sight (right contour) are displayed in Figure (4.12). In principle, the lens must lie between the two sets of contours on the CMD if it is a Sun type star and the blend position is compatible with it being a disk lens with little extinction.

[4]The package can be downloaded from: http://waps.cfa.harvard.edu/MIST

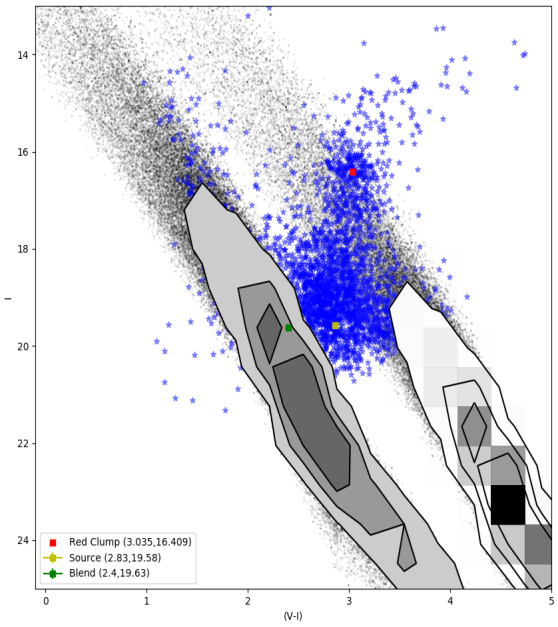

Figure 4.12: The contours of lens location on the CMD if the lens suffers no extinction (left contour) and if it suffers the same amount of extinction as the red clump stars towards the line of sight (right contour). The confidence levels are 1σ, 2σ and 3σ from darkest to lightest colour on both the contours.

4.5 Discussion

In this chapter, I have presented the analysis of the event OGLE-2017-BLG-0103 and found that the asymmetry in the light curve can be explained due to orbital parallax effects. After including the orbital motion of the earth, it was found out that the event suffers from Jerk-Parallax degeneracy. The reason for this degeneracy is that t_E of this event is close to 60 days and v_j is high enough to be close to the transverse velocity of the disc lenses. It was also found out that the parallel component of the $\boldsymbol{\pi}_E$ is significantly higher than the perpendicular component since the event peaked close to the vernal equinox of 2017. This effect is also evident from the asymmetry in the light curve. Jerk-Parallax solutions were found analytically, but it is also shown that these solutions can be obtained from the bimodal distribution of π_{EN}, t_E and t_0. Using galactic model it was found that the least χ^2 solution: P4, gives the lens mass of $0.18^{+0.15}_{-0.08}$ $M_\odot$ lying at a distance of $2.18^{+0.83}_{-0.69}$ kpc. Since the blend is significantly bluer than the field stars we use simulated MIST isochrones for Sun like star at the derived distribution of the lens mass and distance. These isochrones were used to find the absolute brightness of the lens in V and I bands respectively. Using this we find that the lens is unlikely a white-dwarf object and that it must be a low mass main-sequence star in the disk.

Chapter 5

Analysis of the event OGLE-2017-BLG-1170

5.1 Introduction

Space Microlensing parallax, though proposed by Refsdal (1966), is being utilised now in the microlensing field after the formulation of practical techniques by Gaudi & Gould (1997a), Gould (1995), etc. The concept of space parallax is to observe a microlensing event simultaneously from Earth and space. Since the microlensing event is observed from two different locations, the resultant light curves would be different, as the impact parameter u_0 and the time for minimum lens source separation t_0 would be different. The differences $\Delta\beta = u_{0,Earth} - u_{0,satellite}$ and $\Delta\tau = \frac{t_{0,Earth} - t_{0,satellite}}{t_E}$ is used to find the microlensing parallax,

$$\pi_E = \pm\frac{AU}{D_\perp}(\pm\Delta\beta, \Delta\tau) \quad = (\pi_{EE}, \pi_{E,N}) \tag{5.1}$$

where $D_\perp$ is the separation between the Earth and satellite in AU. Typically this separation between both must be around $\sim$ 1AU as majority of the microlensing events towards the bulge have a projected Einstein radius $\sim$ 1AU, which is comparable to Earth's orbit (Gaudi & Gould, 1997a, Smith et al., 2005).

The use of observations by an infrared satellite to measure microlensing parallaxes was proposed by Gould (1995). It was argued from the studies by Gaudi & Gould (1997a) that the measurement of the transverse velocity of the lenses projected on to ecliptic plane (v_{helio}) can be used to distinguish among the lensing populations in the disc, bulge and Magellanic Clouds. Based on the approach to monitor microlensing events of the

bulge and LMC by Gould & Loeb (1992) and Kiraga & Paczynski (1994), events detected by the microlensing observing groups (OGLE-I, MACHO, EROS) were/are monitored by follow-up telescope networks μFUN, PLANET, MINDSETp and ROBONET-II groups (Albrow et al., 1998, Tsapras et al., 2009) etc. and found that the optical depth towards the Galactic Bulge was more than expected (Mróz et al., 2019, Udalski et al., 1994).
In its early stage, microlensing observations were carried out at a low cadence rate not suitable for detecting planets. The number of space telescopes started increasing at the end of 20^{th} century and this was supported by the fact that ground based observations of microlensing observations towards the bulge had increased. Real-time data analysis with increased cadence rate and better photometry was started by OGLE-III project with their telescope set up in Warsaw, Chile (Udalski, 2003). This was followed by the MOA-I telescope at Mt. John Observatory, New Zealand (Bond et al., 2001). With this the number of microlensing events detections started to increase to ~ 2000/year and the first microlensing planet was detected and confirmed by Bond et al. (2004).

Although a variety of microlensing events are detected towards the Galactic Bulge, they themselves do not reveal the nature of the lens as their light-curves are degenerate the mass of the lens and distance to the lens Dominik (1998), meaning that a lower-mass lens closer to Earth and a higher-mass lens closer to the source can give the same Einstein radius crossing time. While fitting a microlensing light curve yields t_E, it does not give the mass and distance to the lens unless π_E and θ_E are also measured. Although π_E can be measured for objects that are closer to Earth through orbital parallax effect, it is biased towards slow moving or heavier lenses. Measuring significant orbital parallax also requires that $t_E \geq 58 days$, (Gould, 2004).

Another method to measure π_E is through terrestrial parallax which is possible when extreme magnification events are observed from two or more different locations on Earth (An et al., 2002, Gould et al., 2009, Yee et al., 2009). However both of these methods are biased towards particular type of events mentioned above. To break this bias, it is necessary to measure π_E via space parallax which can be used for low magnification/relatively short t_E events.

Dong et al. (2007) used Spitzer for the first time to measure a space based parallax for the event (*OGLE-2005-SMC-001*) towards the Small Magellanic Clouds. After successfully measuring the satellite parallax and hence the lens mass and distance, he showed that Spitzer can be used for constraining lens properties such as mass and distance.

Following the start of a new generation of observation and event detection telescopes *OGLE-IV, MOA-III* and later *KMTNet*, Yee et al. (2012), detected the first microlensing

planet which was fairly below the threshold of detection but showed the fact that these telescopes had better sensitivity to planets in high magnification events [1]. Using this analysis, it was argued that if the ground observations had been complemented by space observations, the degeneracy in mass and Einstein timescale could have been broken.

Because of its characteristics, Gould (2007) developed a technique for using Warm Spitzer mission for measuring space parallaxes not only to measure the mass function, particularly in the brown dwarf mass range, towards the bulge but also the distances to the lenses. Followed by this, Yee et al. (2015a) measured the properties of an isolated star (*OGLE-2014-BLG-0939*) by measuring parallax with the help of Spitzer when the Spitzer microlensing team was granted 100 hours of *Director's Discretionary time* (Calchi Novati et al., 2015a, Yee et al., 2015b, Zhu et al., 2017). This was the time when the feasibility of Spitzer was tested in measuring space parallax towards bulge. Using the pilot program, Calchi Novati et al. (2015a) measured the parallaxes of 21 events and defined a cumulative distribution of the distances of those lenses based on their kinematics. Out of the 170 microlensing sample events observed by Spitzer in 2015, Zhu et al. (2017) analysed the 50 that were observed with high cadence by Spitzer to measure sensitivity towards detecting planets and also developed a methodology to study the galactic distribution of planets. It was predicted that $1/3^{rd}$ of the planetary detections with Spitzer must be in bulge. This challenged the finding of Penny et al. (2016) using ground based observations only who argued that Galactic Bulge might be devoid of planets due to extreme radiation environment in the bulge.

Zhu et al. (2015) showed that Spitzer observations of low to moderate ground based magnification events have significant probability to detect planets. Ideally these events would be a perfectly unbiased sample to measure parallax and sensitivity to planets. Yee et al. (2015b) made protocols to select events for Spitzer observations which aim at maximum planet sensitivity and create a distribution of planet distance and mass detected towards bulge to understand the *Galactic Distribution of Planets*. The primary objective of the ongoing Spitzer mission towards the bulge is to find the relative population of the planets in the disk and the bulge from a statistical analysis. According to the criteria of Yee et al. (2015b), an event is selected for objective observations if it is expected to yield a measurable parallax, and an event is selected for subjective observations if it is selected for some specific reasons by the Spitzer Microlensing team. All the Spitzer observations after the pilot program are made with this criteria.

[1] Gould et al. (2010) estimates that $\Delta\chi^2$ = 350-700 is appropriate to claim a detection of a planet

The Spitzer microlensing campaign (before and after implementing the Yee et al. (2015b) criteria) has helped in constraining the mass, distance and transverse velocity of a variety of lenses towards bulge. It has helped in discovering a stellar remanent in a largely separated binary system (Shvartzvald et al., 2015), brown dwarf objects (Shvartzvald et al., 2016b), a counter-rotating brown dwarf (Shvartzvald et al., 2018), a pair of brown dwarfs (Albrow et al., 2018), isolated brown dwarf (Zhu et al., 2016), planetary companions in disc (Poleski et al., 2016, Shvartzvald et al., 2017, Street et al., 2016), and bulge (Ryu et al., 2018), binary stellar system (Han et al., 2016). In addition, Spitzer has also helped to break several observational degeneracies which otherwise could be difficult from the ground-only based observations (Bozza et al., 2016, Calchi Novati et al., 2018, Wang et al., 2018).

Following the idea of cheap, space-based parallaxes by Gould & Yee (2012), Shin et al. (2018) practically tested this by measuring the space parallax of the event $OGLE-2016-BLG-1054$ and showed that only three Spitzer data points (one at the base and one on either side of the peak) are required to constrain the parallax for high-magnification events. This has increased the scope of Spitzer to observe ground-based high magnification single-lens events in addition to the on going mission.

Other space observatories such as K2 (Gould & Horne, 2013, Zhu et al., 2017), SWIFT (Shvartzvald et al., 2017) can also be used for measuring space parallaxes. Muraki et al. (2011) analysed an event $MOA-2009-BLG-266Lb$ from space using the EPOXI spacecraft located at 0.1 AU However, the preference of Spitzer over other space telescopes for space parallax measurements is because:

1. It is in Earth trailing orbit with the rate of 0.1AU/year (Figure 1 of Gould (2007)) and has sufficient separation from Earth to measure parallax towards Galactic Bulge.

2. It works in L-band and has a spatial resolution comparable to ground based surveys.

3. It has a good response time which can be used to point it towards targets at short notice.

However, it has a major disadvantage that it can observe targets towards the Bulge for only two 38-day intervals per year due to its orbit and only one of the two intervals can be used to simultaneously observe the microlensing events towards the bulge. This restricts Spitzer observations to shorter timescale events possibly due to freely floating planets. These challenges are proposed to be overcome by the WFIRST mission to be launched in 2025 (Penny et al., 2019, Street et al., 2018).

5.1.1 Degeneracies

Following equation (5.1), space-based parallax measurements have four-fold degeneracies in π_E generically. Mathematically, the difference in the light curves seen from Earth and Spitzer can be represented by two parameters viz. $\Delta\tau$ and $\Delta\beta$ which are difference in the time of the peaks and difference in the impact parameters respectively. A two-fold degeneracy arises because of the $\pm$ sign in $\Delta\beta$, which means that the trajectory passes on the opposite side of the lens. The other two fold degeneracy arises because of the $\pm$ sign at the front of the equation which means the reversal in the parity of the entire equation with the lens reversing the side it passes the source.

Single lens events are prone to this four-fold degeneracy because the point lens caustic is rotationally invariant. However, the two-fold degeneracy is usually broken in case of binary lens events because of difference in geometry of magnification pattern. Also, if the event is observed from one more satellite apart from Spitzer, the four-fold degeneracy would be broken (Gould et al. (1994)). To test this idea, SWIFT and Kepler have been used to break the four fold degeneracies in events OGLE-2015-BLG-1319 and MOA-2016-BLG-290 (Shvartzvald et al., 2016b, Zhu et al., 2017) respectively.

5.1.2 Nature of lightcurve of the event: OGLE-2017-BLG-1170

OGLE-2017-BLG-1170 is a moderately magnified ($A{\sim}10$) event of the *Chang-Refsdal* (here after CR) type. The light-curve of the event is very similar to a Paczyński Curve except for the asymmetry at the peak (inset of Figure 5.2). This suggests the event is not a PSPL event. When the secondary mass, is outside the Einstein ring of the primary mass we term it as a wide binary, while if it lies inside the Einstein ring, it is called a close binary (Dominik, 1999). A wide binary system has two independent caustics - one central caustic (Chung et al., 2005) and one planetary caustic (Han, 2006), while the close binary has three caustics - one central caustic and two planetary caustics. At the intermediate separation, the caustics join and form a resonant structure. The shape and size of the caustics depends on their mass ratio and separation. Asymmetry of a Paczyński-like lightcurve can be produced by a central caustic perturbation. This produces a similar lightcurve shape for wide and close binaries Albrow et al. (2002), Batista et al. (2014), Bozza (2000), Bozza et al. (2016), Choi et al. (2012), Dominik (1999), Gaudi & Gould (1997b), Griest & Safizadeh (1998), Kains et al. (2013), Miyazaki et al. (2018), Park et al. (2014), Shvartzvald et al. (2017). This is also popularly known as the $s \rightarrow s^{-1}$ or $close - wide$ degeneracy.

In the case of OGLE-2017-BLG-1170, we find that Spitzer data helps in breaking the close and wide degeneracy. The best solution is due to a close-binary system with mass

ratio q = 1.65±0.0 and separation of 0.42±0.01. We construct a galactic model towards the line of site of this event. The bayesian analysis of this galactic model yields a pair of super-Jupiters located in the galactic bulge.

5.2 Observations

5.2.1 OGLE

The event was detected by the Early Warning System of the Optical Gravitational Lensing Experiment (OGLE) with the observations conducted using the 1.3m Warsaw Telescope at the Las Campanas Observatory in Chile (Udalski et al., 2015a). This event was detected towards the Galactic Bulge in their field $BLG613.12$. The equatorial coordinates are $(\alpha, \delta)_{J2000}$ = (17:30:18:90, -29:20:34.5) (hh:mm:ss and ^{o},$'$, "). This corresponds to (l, b) = (357.86991858^o, 2.60721152^o), in the galactic co-ordinate system. We use (https://ned.ipac.caltech.edu) to convert from equatorial to galactic coordinates.

5.2.2 KMTNet

The event was also observed separately by KMTNet in their field "BLG11" (Kim et al., 2016). The KMTNet observations were carried out using their three 1.6m telescopes located at *Cerro Torolo Inter-American Observatory, Chile (KMT-C)*, *South African Astronomical Observatory in South Africa (KMT-S)* and the *Sliding Spring Observatory, Australia (KMT-A)*. This field has high cadence rate of 4 per hour with the main observations in the I-band and supporting observations in the V-band.

5.2.3 Spitzer Observations

OGLE-2017-BLG-1170 was also observed by the Spitzer Space Telescope in the infrared region of the spectrum at a wavelength of 3.6μm using the IRAC instrument (Fazio et al., 2004, Gould, 2007).This event was selected objectively on the basis of the protocols given by Yee et al. (2015b) as a part of multi-year project to measure the Galactic distribution of planets. There are 26 Spitzer observations contributing to the Spitzer light curve from HJD-2450000 7935.24 to 7962.62. Spitzer observed this event with relatively high cadence and the observations cover both the wing and the peak of the light curve, which enables us to constrain Spitzer source flux. The photometry of Spitzer observations was extracted by the special algorithm developed by Calchi Novati et al. (2015b). We get the position of the Spitzer relative to Earth during these observations from the Horizons Ephemeris System (http://ssd.jpl.nasa.gov/horizons).

5.2.4 Data Reductions

Data was reduced for the KMTNet observations using the pyDIA software Albrow et al. (2018). This software is based on the difference imaging algorithm of Bramich et al. (2013). The data for all the KMTNet telescopes was filtered using the condition that the Q ≤ 2 and roundness ≤ 2. The final raw light curves of the KMTNet data which are used for modelling are shown in Figure (5.1) and number of data points corresponding to each observatory in Table (5.1). The data points are selected from HJD-2450000 = 7850 to 8030 days.

Number of data points per observatory and corresponding band of observations		
Observatory	Number of Data points	Band
OGLE	106	I
KMT-A	267	I
KMT-C	104	I
KMT-S	105	I
KMT-CV	24	V
Spitzer	26	L

Table 5.1: The table showing number of data points of the light curve used for modelling corresponding to each observatory.

5.3 Light curve Analysis

5.3.1 Single Lens model

Initially, the PSPL model was fitted to the light curve. This fit was done by the system developed by McDougall & Albrow (2016), and the fit gave the standard Paczyński parameters shown in Table (5.2).

Parameters and uncertainties of the PSPL fit	
Parameter	Value
χ^2	1021.961
u_0	0.270 $\pm$ 0.005
t_0	7947.29 $\pm$ 0.0143
t_E	20.33 $\pm$ 0.006

Table 5.2: The table showing PSPL fit parameters with their uncertainties to the light curve.

Figure (5.2) shows that the PSPL fit is reasonable as the base of the light curve matches the standard Paczyński Microlensing Curve. However, the peak is not fitted well by the model and residuals between (HJD - 2450000) 7925 and 7975 suggest the presence of a companion. This secondary component might be a companion to the lens or a companion to the source. It is also possible that the light curve is affected by the orbital motion of the Earth where the projected velocity of the lens is nearly perpendicular to the orbital

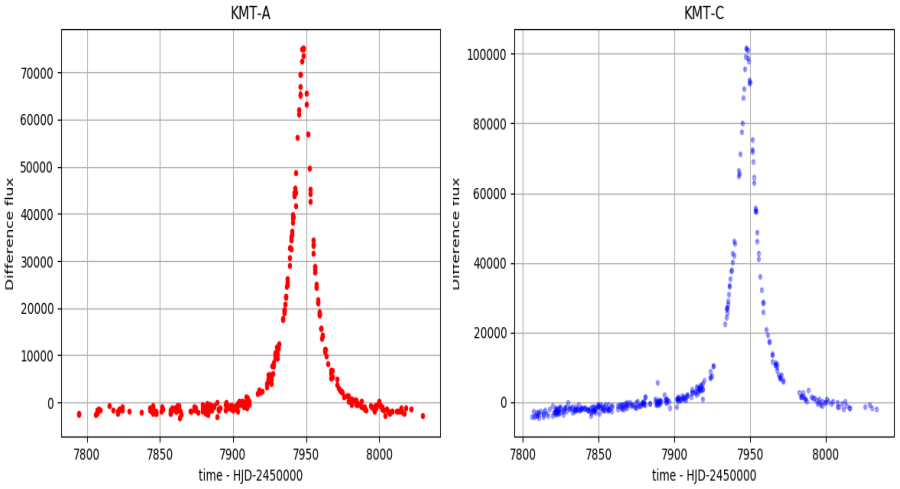

(a)Final raw light curve for KMT-A. (b)Final raw light curve for KMT-C.

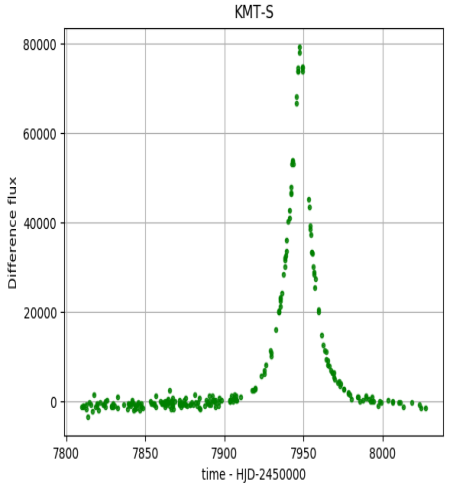

(c)Final raw light curve for KMT-S.

Figure 5.1: The plots show the final filtered light curve which we use in modelling the ground based data

.

plane of the Earth. This results in a perpendicular component of the parallax vector larger than Bennett et al. (2002a,b), Gould (1992), Smith et al. (2005). Towards the Galactic Bulge this can manifest as $\pi_{E,N} >> \pi_{E,E}$. Therefore the possibilities of either orbital parallax or a companion to either lens or source is explored.

5.3.2 Orbital Parallax Model

To model the light curve with orbital parallax, the geocentric formalism of Gould (2004) was used [2]. Initially a coarse grid search was performed over the π_E plane to find parallax

[2]In the orbital parallax and binary source models, we have used the renormalised uncertainties described later in section (5.3.5)

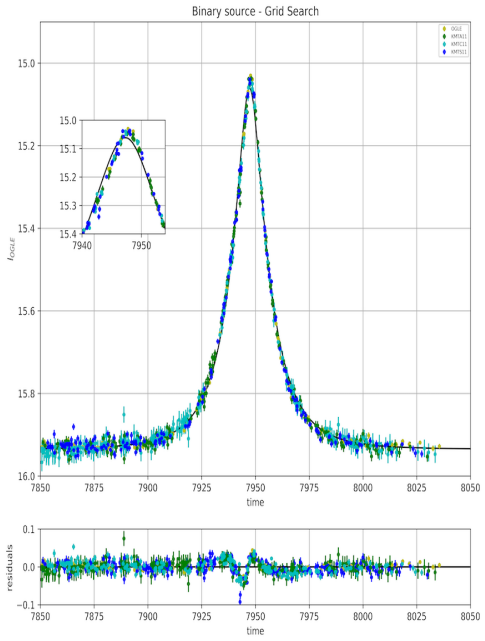

Standard PSPL fit to the light curve.

Figure 5.2: The plots show the PSPL model fit to the light curve and the residuals show the perturbation at the peak due to a secondary object that is also seen in the inset figure.

components to reduce χ^2. The grid search yielded a χ^2 minimum at $(\pi_{EE}, \pi_{EN} = 0.95, 0.50)$. Using this as a starting guess for emcee Foreman-Mackey et al. (2013), the walkers converged to the parameters listed in Table (5.3) and shown in Figure (5.3). It can be concluded that the orbital parallax model does not fit the light curve adequately.

Parameters of Orbital Parallax fit	
Parameter	Value
χ^2	1014.405
u_0	0.231± 0.006
t_0 (days)	7948.238 ± 0.046
t_E (days)	22.195 ± 0.422
$\pi_{E,E}$	2.918 ± 0.075
$\pi_{E,N}$	2.364 ± 0.482
π_E	3.755 ± 0.866
$\frac{f_s}{f_b}_{OGLE}$	0.066
$\frac{f_s}{f_b}_{KMT-A11}$	0.728
$\frac{f_s}{f_b}_{KMT-C11}$	0.639
$\frac{f_s}{f_b}_{KMT-S11}$	0.722

Table 5.3: The table showing mean parameters and their uncertainties of fit for orbital Parallax model. We can see that the model converges to a very high parallax solution but $\pi_{E,N} \not> \pi_{E,E}$.

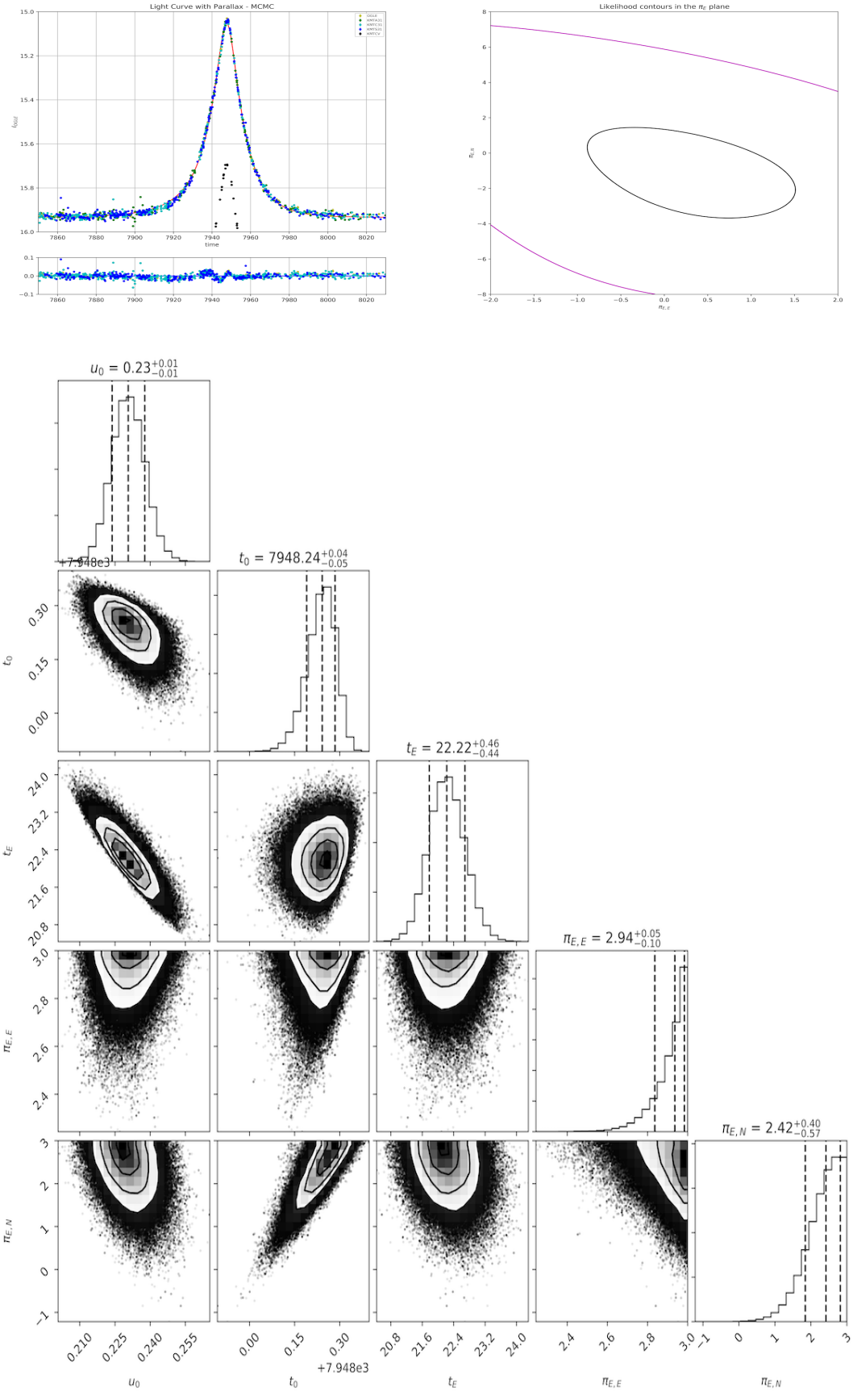

Figure 5.3: Plots show the model fitted to the light curve including the orbital parallax effect of the Earth, the χ^2 contour map when a grid search is performed over π_E plane and the covariance distribution between the parameters of the model. The value on the top of each histogram are the median and 1σ level of the distribution.

5.3.3 Binary Source

Another reason for an asymmetric peak can be that an event comprises of a single lens and binary source (Dominik, 1998, Griest & Hu, 1992). An asymmetric peak event may occur if one of the source stars pass through the lensing zone (a region around the lens on the source plane which can cause detectable magnification) while other source star is close to it. Gaudi (1998) pointed out that a binary source with a large flux ratio between its components can mimic a small perturbation on the light curve which can be mistaken as a planetary perturbation. Hwang et al. (2013), Jung et al. (2017) practically showed that the degeneracy between binary source perturbations and binary lens perturbations can be severe in interpreting the signal by analysing the event.

5.3.3.1 Binary Source Modelling Approach

To include binary source in the model, a formalism given by Jung et al. (2017) was used. It was assumed that the binary source star system is moving at the constant transverse velocity through the projected Einstein radius on the source plane. The PSPL magnification due to each star A_1 and A_2 was calculated and the net magnification defined as,

$$A_{net} = \frac{A_1 + q_{BS} A_2}{1 + q_{BS}} \tag{5.2}$$

where q_{BS} is the flux ratio between the two stars $\left(q_{BS} = F_2/F_1\right)$. The magnification of the two stars can calculated individually as a function of their respective impact parameters and times of minimum approach; $A_i(u_{0,i}, t_{0,i})$ (i=1,2).

$$A_i = \frac{u_i^2 + 2}{u_i \sqrt{u_i^2 + 4}} \tag{5.3}$$

A coarse grid search in $(u_{01}, t_{01}, u_{02}, t_{02}, t_E, q_{BS})$ to minimise the χ^2 yielded 4 distinct minima where t_0, t_E, q_{BS} are constant but signs $u_{0,i}$ are opposite. χ^2 was minimised further by using emcee and eventually all the 4 distinct solutions converge to one minimum (Figure (5.4)). The parameters of the fit are listed in Table (5.4). However, we found out that though the model gave a reasonably good fit, the fit yielded a significant negative values for the blend flux for all the data sets. So this model was also discarded.

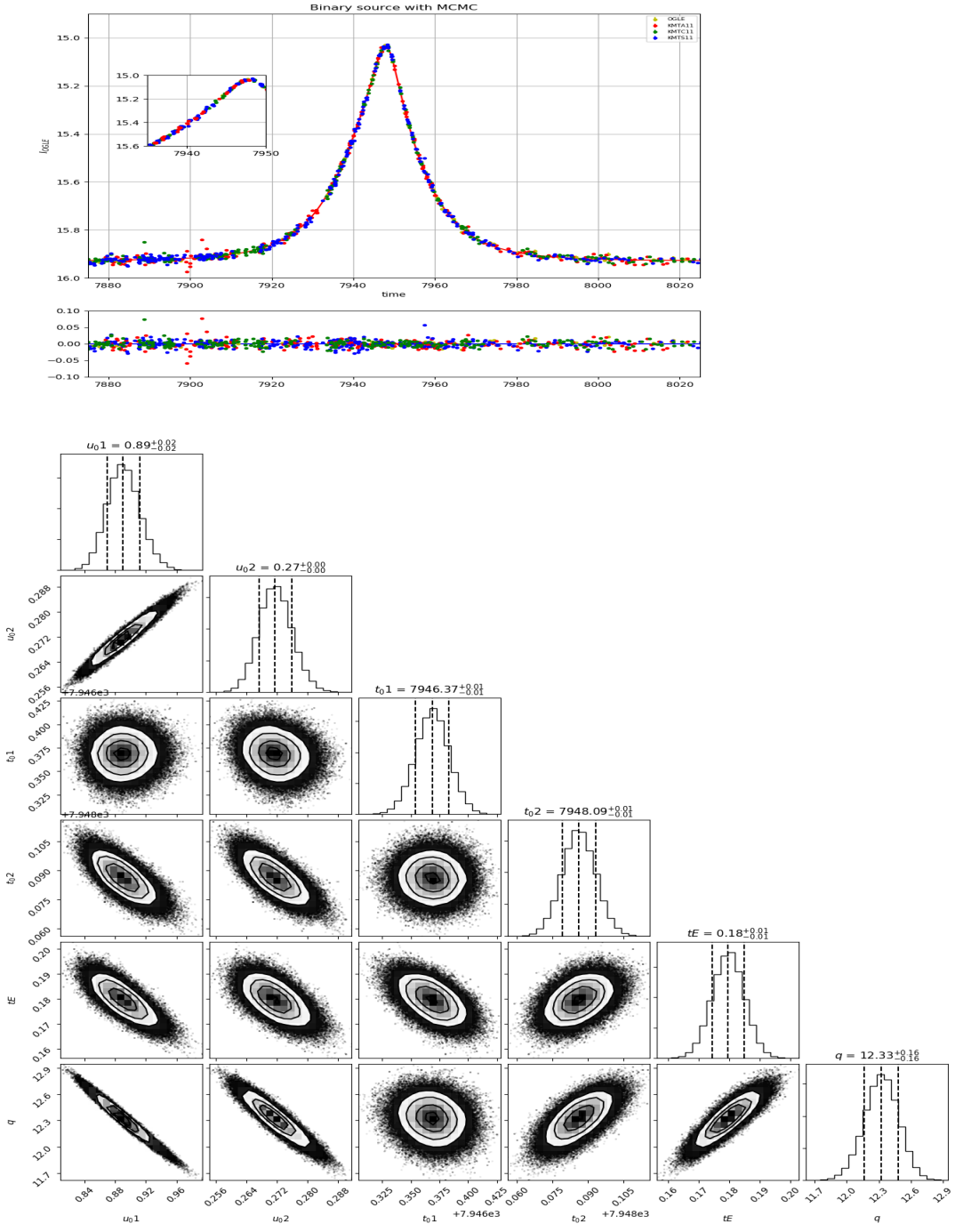

Figure 5.4: The plots show the single lens and binary source model fit to the light curve and the corresponding covariance distribution between the parameters of the model.

Parameters of Single Lens Binary Source fit				
Parameter	-/-	+/+	+/-	−/+
χ^2	1010.320	1010.405	1010.351	1010.339
$u_{0,1}$	-0.891 ± 0.02	0.891 ± 0.02	0.891 ± 0.02	-0.891 ± 0.02
$u_{0,2}$	-0.271 ± 0.005	0.271 ± 0.005	-0.271 ± 0.005	0.271 ± 0.005
$t_{0,1}$ (days)	7946.368 ± 0.016	7946.369 ± 0.016	7946.368 ± 0.016	7946.367 ± 0.016
$t_{0,2}$ (days)	7948.085 ± 0.007	7948.085 ± 0.007	7948.085 ± 0.007	7946.086 ± 0.007
t_E (days)	0.179 ± 0.005	0.179 ± 0.005	0.179 ± 0.005	0.179 ± 0.005
q_{BS}	12.318 ± 0.187	12.32 ± 0.150	12.318 ± 0.160	12.313 ± 0.165
$\frac{f_s}{f_b}_{OGLE}$	-2.56	-2.56	-2.55	-2.56
$\frac{f_s}{f_b}_{KMT-A11}$	-2.39	-2.38	-2.39	2.39
$\frac{f_s}{f_b}_{KMT-C11}$	-2.49	-2.49	-2.49	-2.48
$\frac{f_s}{f_b}_{KMT-S11}$	-2.40	-2.39	-2.40	-2.40

Table 5.4: The table showing mean parameters and their uncertainties of fit for single lens and binary source model. We get two solutions with different signs of u_{01} and u_{02} which are very identical.

5.3.4 Binary lens model

On closer inspection of the peak of the PSPL light curve (Figure (5.2)), it can be seen that the peak is sheared towards the right as the source passes close to the magnification region around the central caustic of the binary system. Central caustic perturbations show a feature on the peak indicating the presence of a planetary or binar-star companion (Bozza et al., 2012, Choi et al., 2012, Chung et al., 2005, Han, 2009, Han et al., 2016, Shin et al., 2012, Yee et al., 2012) . Chung et al. (2014) mentions that planets may induce a fractional deviation $\leq 2\%$ of the peak magnification which can be detected for moderate or low magnification events with current generation telescopes eg. MOA-2010-BLG-311 Yee et al. (2012). However in case of $OGLE-2017-BLG-1170$, there is no planetary perturbation near the peak of the magnification, but in fact the whole peak is sheared towards right. This suggests that the source is passing close to the central caustic but the companion is a heavier body than planet that is lying close to the Einstein ring of the primary and the source passes close to primary which gives rise to a light curve similar to Paczyński curve. At the closest approach, it experiences a deviation due to the secondary body. However, unlike central caustic perturbation events (which are high magnification events), OGLE-2017-BLG-1170 is a moderate magnification event ($A \sim 4.3$). Han (2009) analysed moderate magnification events due to central caustic perturbations and showed this type of moderately magnified events can distinguish themselves from planetary events by the nature of the perturbation. An important requirement for analysing central caustic perturbation events is that they must be observed with high cadence especially around the peak to avoid observational degeneracies. For example, Park et al. (2014) analysed the event {OGLE-2012-BLG-0455/MOA-2012-BLG-206} due to central caustic perturbations but found four degenerate solutions due

to inadequate coverage of the peak. Since there is sufficient coverage of the peak and throughout the event for {OGLE-2017-BLG-1170}, we do not expect data degeneracy in this case. However, since it is a moderately magnified non-caustic crossing event, finding a convincing solution is a challenge since multiple caustic geometries can give rise to such a light curve.

5.3.4.1 Binary lens Modelling Approach

For a binary lens, calculating the binary lens magnification requires solving the complex equation for image positions. The procedure described briefly in section (1.4.2) is followed. After doing the initial grid search over (d,q), we plot a map of $\Delta\chi^2$ over (log(d),log(q)) where $\Delta\chi^2 = \chi^2_{element_{d,q}} - \chi^2_{best}$ shown in Figure (5.5). To speed up the calculations, the magnification is computed in different ways,

1. If the source star is located more than 30 source radius away from the caustic, the magnification is calculated as the point source magnification.

2. If the source star is located between 3 and 30 source radii away from a caustic, the hexadecapole approximation is used to calculate the finite source magnification (Gould, 2008, Pejcha & Heyrovský, 2009).

3. Since the hexadecapole approximation fails for distances less than 3 source radii from caustics, the Image Centred Inverse Ray Shooting method Bennett (2010), Rhie & Bennett (1996) is used to calculate finite source magnification in this region. Though this method is computationally extensive, it is a very accurate way to calculate magnification when the source is close-to or straddling a caustic. Bennett (2010) shows that this method can also be used for triple lens modelling where the self-intersecting caustics give rise to complex magnification patterns.

5.3.4.2 Selecting the best solution

After further minimising the χ^2 of these solutions with emcee until the chains converged (equations (5.4 - 5.6)), it was found that the solutions fall into four categories: (d,q) of 3 solutions converge to (1.45,0.67), 4 solutions converge to (1.55,0.09), 2 solutions converge to (0.53,0.37) and 1 solution converges to (1.13,0.21). After checking the χ^2 and blending of these solutions it was found that the three solutions which correspond to similar χ^2 out of the 10 solutions, have significant negative blending. Though blending to some extent can be permitted, for these solutions, blending is severely negative and therefore we discard them as being unphysical. The solution corresponding to (s,q) = (1.13,0.21)

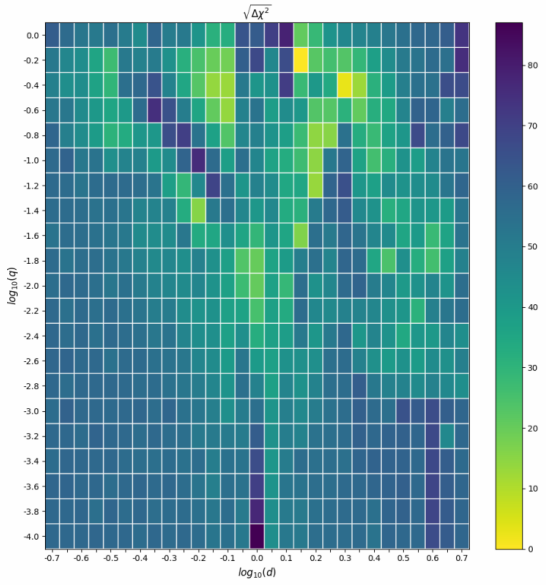

Figure 5.5: The plot shows the grid search over each value of d and q. For each element of the grid, (u_0, ϕ) are searched by grid search methods and (t_0, t_E, ρ) are minimised by Nelder-Meade method. The grid colours are $\Delta\chi^2 = \chi^2_{element_{(d,q)}} - \chi^2_{best}$.

also gives severe negative blending. The remaining two solutions have a positive value of blending and also have comparable χ^2. The χ^2 difference between the two solutions is only 20. To test whether these are degenerate solutions, they are further explored using emcee chains in steps of 200 until they converge according to the criteria,

$$\Delta lnp = lnp_{samples_0} - lnp_{samples_1} \leq \quad 0.2 \tag{5.4}$$

$$\Delta parameter = \left| \frac{mean_1 - mean_2}{std_1} \right| \leq \quad 0.05 \tag{5.5}$$

$$\sigma parameter = \left| \frac{std_1 - std_2}{std_1} \right| \leq \quad 0.05 \tag{5.6}$$

where $lnp_{samples_0} = \ln(\frac{\chi^2}{2})$ of the present set of samples, $lnp_{samples_1}$ = log of probability of the previous set of samples, $mean_1$ and $mean_2$ are the mean of the first half and the last half samples and std_1 is the standard deviation of the first half samples. The chains run until these conditions are met.

It was found that the close solution corresponding to (s,q) = (0.53,0.37) converge to χ^2 lower than the wide solution corresponding to (s,q) = (1.55,0.09). These solutions are labelled as P1 and P2 respectively and are shown in Figure (5.6) and Figure (5.7).

However, P1 model is discarded because it has severe negative blending. We note that these solutions are not related by the $s \rightarrow s^{-1}$ degeneracy.

The ground based model (P2) and the corresponding covariance between the parameters is shown in Figure (5.7). From Figure (5.7d), it can be seen that the source is passing through the extended magnification region around the cusps of the central caustic. In principle, though several trajectories with asymmetric peak may be possible for this kind of magnification pattern, keeping these solutions can be filtered out based on the value of blending.

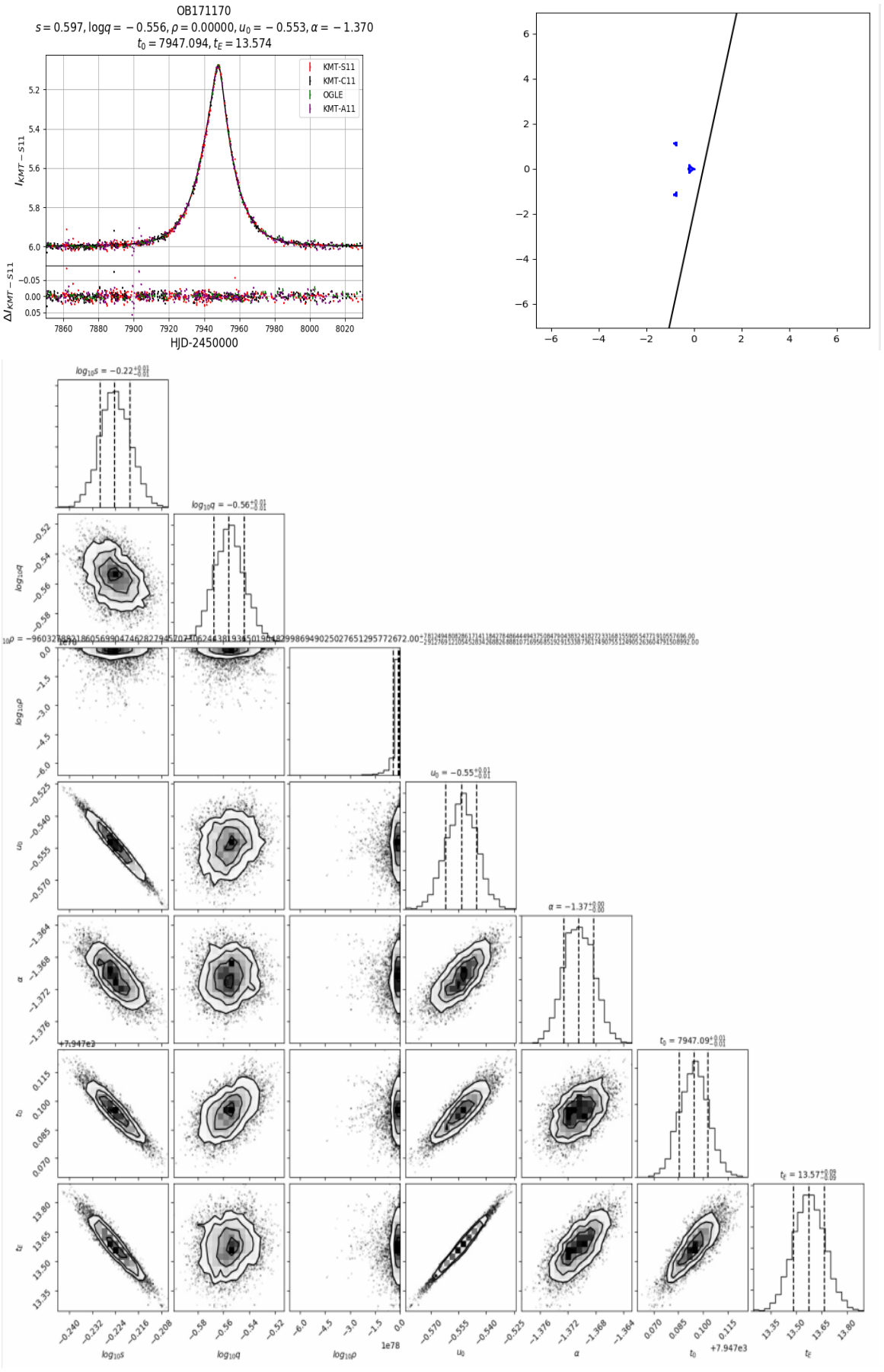

Figure 5.6: The plots show the light curve, the trajectory and the caustic giving rise to the observed magnification pattern for P1 model as well as the covariance between the parameters of the model. It can be seen that the trajectory is passing through the extended magnification region around the cusps of central caustic giving rise to the observed magnification pattern.

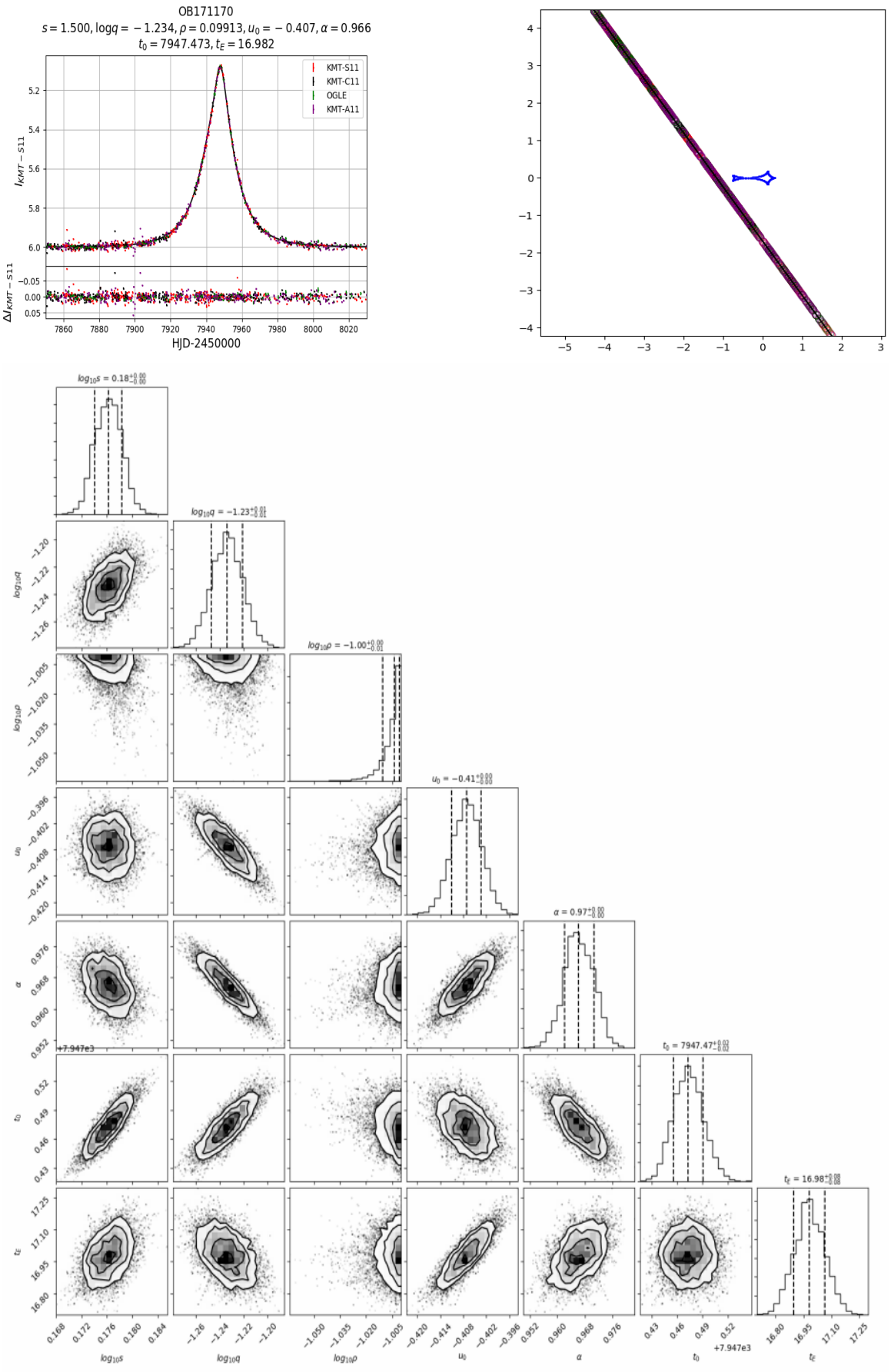

Figure 5.7: The plots show the light curve, the trajectory and the caustic giving rise to the observed magnification pattern for P2 model as well as the covariance between the parameters of the model. It can be seen that the trajectory is passing through the extended magnification region around the cusps of central caustic giving rise to the observed magnification pattern.

5.3.5 Renormalisation of uncertainties in magnitudes

The model (P2) was used to renormalise the error bars in the data points so that $\chi^2/dof \sim 1$ for each dataset (1.6). In order to renormalise the uncertainties, the procedure of Yee et al. (2012) was followed. The values of κ and e for the different datasets are given in Table (5.6). We re-run the P2 model based on the renormalised uncertainties in magnitudes. The solution does not change very much except that the value of ρ becomes 0 (Figure (5.8)). All other models are fitted with this adjusted error bars.

Parameters for renormalising uncertainties in magnitude		
Site	κ	σ_{min}
KMT-A11	4.5027	0.0
KMT-C11	2.8598	0.0
KMT-S11	0.0140	0.8196
OGLE	0.7862	0.0072

Table 5.5: The parameters for the renormalisation of the error bars in the data points so that $\chi^2/dof \sim 1$.

5.3.5.1 Model corresponding to the trajectory reflected by lens axis

From the geometry of the caustic and the trajectory of the source, it can be said that if the trajectory passes through the extended magnification region of one cusp of central caustic, there can be a solution with a trajectory that is a reflected by the lens axis i.e. it passes through the extended magnification region of the other cusp of the central caustic. When emcee was seeded with $\phi^{'} = \phi + \frac{\pi}{2}$ (ϕ = trajectory angle of the P2 solution) without altering the other parameters, the emcee converged to a new solution with a negative blending and χ^2 less by 66. This solution is labelled as P3 which is shown in Figure (5.9).

5.3.5.2 Close-wide degenerate solution

The microlensing events due to central caustic perturbations are well known to suffer from *close−wide* degeneracy Albrow et al. (2002), Bozza (2000), Chung et al. (2005), Dominik (1999). The reason for this degeneracy is the similar magnification pattern around the central caustics of the close and wide binary. Though Chang-Refsdal approximation can be applied in case of wide binary and close binary Dominik (1999), this approximation starts to fail as the caustic becomes resonant. A wide binary and a close binary lens are characterised by their shear γ and Quadrupole Q respectively which describe the external perturbation due to the secondary component. γ and Q are given by

$$\gamma = \frac{q_w}{d_w^2(1+q_w)}; \quad Q = \frac{d_c^2 q_c}{(1+q_c)^2} \tag{5.7}$$

where the subscript c and w are for close and wide case respectively. If the magnitude of γ and Q are equal and are less than 1, we can say that the $s \rightarrow s^{-1}$ degeneracy exists. Albrow et al. (2002) determines a correspondence between the two classes of binary lens.

$$d_c^2 d_w^2 (1+q_w) = \frac{q_w}{q_c}(1+q_c)^2 \tag{5.8}$$

$$d_c d_w (1+q_w)^{\frac{1}{2}} = \frac{1+q_c}{1-q_c} \tag{5.9}$$

For the best ground based solution i.e. P2, the value of $\gamma = 0.029$ (equation (5.7)). Equation (5.8) and Equation (5.9) give the value of $(d_c, q_c) = (0.65, 0.07)$ which gives the value of Q = 0.025 $\neq \gamma$. When the emcee is seeded with the above caustic parameters, our solution converges to $(d_c, q_c) = (0.496, 0.175)$. This solution has lower χ^2 by 48 and is labelled as P4 in Table (5.6) and shown in Figure (5.9). Though P4 solution has lower χ^2, it also has significant negative blending. This χ^2 is less than that of single lens and binary source which also has negative value of blending.

Parameters after renormalisation of uncertainties			
Parameter	P2	P3	P4
χ^2	956.65	889.46	908.17
u_0	$-0.45^{+0.02}_{-0.03}$	$-0.75^{+0.02}_{-0.01}$	$-0.62^{+0.03}_{-0.03}$
t_0 (days)	$7947.62^{+0.15}_{-0.11}$	$7945.74^{+0.06}_{-0.05}$	7945.96 ± 0.05
t_E (days)	$16.43^{+0.38}_{-0.46}$	$12.25^{+0.19}_{-0.17}$	$13.55^{+0.43}_{-0.42}$
d	1.51 ± +0.01	1.28 ± 0.0	0.50 ±+0.02
q	$0.07^{+0.08}_{-0.07}$	0.28 ± 0.02	0.17 ± 0.02
ϕ	$0.93^{+0.03}_{-0.03}$	2.79 ± 0.01	0.85 ± 0.02
ρ	0.0	0.0	0.0
$\frac{f_s}{f_b}_{OGLE}$	2.83 ± 0.90	-2.26 ± 0.93	-4.20 ± 0.91
$\frac{f_s}{f_b}_{KMT-A11}$	3.44 ± 0.90	-2.13 ± 0.90	-3.65 ± 0.90
$\frac{f_s}{f_b}_{KMT-C11}$	3.04 ± 0.92	-2.21 ± 0.93	-3.97± 0.93
$\frac{f_s}{f_b}_{KMT-S11}$	3.32 ± 0.93	-2.15 ± 0.94	-3.78 ± 0.93

Table 5.6: The table showing mean parameters for the fits corresponding to P2, P3 and P4 models. Though P3 solution has least χ^2, it also has significant negative blending.

5.3.6 Including Spitzer light curve in the binary lens analysis

Having appropriate ground based solutions, the Spitzer light curve can be included in the analysis for measuring space parallax. Due to offset in its location relative to Earth,

a different light curve from Spitzer spacecraft is expected because Spitzer sees the trajectory different to Earth which yields different value for (u_0, t_0). This difference gives the microlensing parallax (Equation (5.1)). However, as mentioned before, the space parallax also comes with a four-fold degeneracy that needs to be analysed. Analogous to orbital parallax, ($\Delta\beta$,$\Delta\tau$) are defined so that they yield the difference in the impact parameters and corresponding times as seen by Earth and Spitzer

5.3.6.1 Modelling Approach with Spitzer Data

Since the trajectory of Spitzer is offset in time and space, initially a grid search minimising the χ^2 with ground and Spitzer data combined is performed in the ($\Delta\tau$ and $\Delta\beta$) plane. The search is performed over where the parameters of P2 model are held constant. This gives us approximate values of $u_{0,spitzer}, t_{0,spitzer}$. In case of $OGLE-2017-BLG-1170$, the χ^2 minimum for this grid search was obtained at ($\Delta\tau$, $\Delta\beta$)= (0.08,-0.02). We show the χ^2 contour plot in Figure (5.11). The low values of $\Delta\tau$ and $\Delta\beta$ for which χ^2 is minimum indicates that Spitzer light-curve might have similar shape compared to the ground based light curve.

Converting these values of $(\Delta\tau, \Delta\beta)$ to (π_{EE}, π_{EN}) (equation (5.1)) and P2 ground based solution when seeded to emcee, the walkers converge to a solution shown in Figure (5.12). For the models (P2 and P3), the parallax degeneracy breaks down to two fold i.e. pp ($+u_{0,earth}$ and $+u_{0,spitzer}$) and mm (-$u_{0,earth}$ and -$u_{0,spitzer}$) as the trajectories pm and mp give different light curves and a significantly worse χ^2.The symmetry breaks down because of the asymmetric nature of the magnification pattern around the caustics. However for P4 solution (least χ^2 solution), instead of pp and mm, the solutions converge to pp and mp. A possible reason for this could be the magnification pattern around the central caustic for the (s,q) values of P4 solution. In these plots, red is the trajectory seen by Spitzer and black is the trajectory seen from Earth. Due to the parallax, the effective trajectory is bent as seen by the observer. The plots also show the celestial north and east direction projected on to the plane of the sky at the peak of the event. Primary and secondary lenses are denoted by green and magenta circles respectively which form the corresponding caustic shapes. We also explore the ground based P3, and P4 solution with these values of $\Delta\tau$ and $\Delta\beta$ when seeded to emcee and the walkers converge to the solution shown in Figure (5.13 and 5.14) The covariance plots for all these solutions are shown in Figures (5.15 to 5.20).

Table (5.7) list the parameters of the fit and their uncertainties. The close-pp and close-mm solutions yield significantly low values of blending. The best solution is the close-pp

solution. The Spitzer observations are with high cadence which gives good constraint on the Spitzer source flux. Also, since the grid search in ($\Delta\beta$,$\Delta\tau$) yields a single minima, no colour-constraint is applied Calchi Novati et al. (2015a).

Parameters of fit						
Parameter	P2-mm	P2-pp	P4-mm	P4-pm	P3-mm	P3-pp
χ^2	1727.01	1725.88	1669.34	1627.47	1754.58	1700.31
s	$1.62^{+0.0}_{-0.0}$	$1.62^{+0.0}_{-0.0}$	$0.41^{+0.01}_{-0.0}$	$0.42^{+0.01}_{-0.01}$	1.20 ± 0.0	1.62 ± 0.0
q	$0.05^{+0.02}_{-0.02}$	$0.05^{+0.02}_{-0.02}$	$1.41^{+0.02}_{-0.03}$	$1.65^{+0.02}_{-0.02}$	0.29 ± 0.0	0.05 ± 0.01
ρ	$0.0^{+0.0}_{-0.0}$	$0.0^{+0.0}_{-0.0}$	$0.0^{+0.0}_{-0.0}$	$0.0^{+0.0}_{-0.0}$	$0.0^{+0.0}_{-0.0}$	$0.0^{+0.0}_{-0.0}$
u_0	$0.38^{+0.01}_{-0.01}$	$-0.37^{+0.01}_{-0.01}$	$0.45^{+0.02}_{-0.02}$	$-0.52^{+0.02}_{-0.03}$	0.81 ± 0.01	-0.38 ± 0.01
α	$5.25^{+0.01}_{-0.01}$	$1.03^{+0.01}_{-0.01}$	$6.14^{+0.01}_{-0.01}$	0.02 ± 0.0	3.52 ± 0.0	1.03±0.01
t_0	7947.52 ± 0.03	7947.213 ± 0.0	7946.87 ± 0.02	7946.97 ± 0.02	7946.17±0.03	7947.52±0.03
t_E (days)	$17.93^{+0.24}_{-0.25}$	$17.92^{+0.26}_{-0.23}$	$16.43^{+0.30}_{-0.35}$	$15.26^{+0.37}_{-0.42}$	$11.78^{+0.11}_{-0.12}$	$17.91^{+0.27}_{-0.27}$
$\pi_{E,E}$	-0.01 ± 0.0	-0.02 ± 0.0	-0.02 ± 0.0	-0.05 ± 0.03	-0.02±0.0	-0.02±0.0
$\pi_{E,N}$	-0.05 ± 0.0	0.05 ± 0.0	-0.06 ± 0.0	0.62 ± 0.03	-0.08 ± 0.0	0.05±0.0
$\frac{f_s}{f_b}_{OGLE}$	1.38 ± 0.89	1.34 ± 0.86	3.72 ± 0.85	18.09 ± 0.91	-1.95 ± 0.94	1.38 ± 0.93
$\frac{f_s}{f_b}_{KMT-A11}$	1.56 ± 89	1.51 ± 90	4.85 ± 90	286.01 ± 91	-1.87 ± 0.91	1.56 ± 91
$\frac{f_s}{f_b}_{KMT-C11}$	1.44 ± 0.84	1.40 ± 0.83	4.063 ± 0.84	28.31 ± 0.89	-1.92 ± 0.94	1.47 ± 0.93
$\frac{f_s}{f_b}_{KMT-S11}$	1.50 ± 0.89	1.46 ± 0.89	4.45 ± 0.86	63.91 ± 0.88	-1.89 ± 0.95	1.51± 0.90
$\frac{f_s}{f_b}_{Spitzer}$	0.92 ± 0.66	0.90 ± 0.68	2.28 ± 0.49	2.691 ± 0.53	-2.25 ± 0.71	0.92± 0.73

Table 5.7: The table showing mean parameters and their uncertainties of fit for P2, P3 and P4 ground based solutions with Spitzer data. mm indicates that both earth and Spitzer are seeing the trajectory on the negative side of the caustic, pp means that both earth and Spitzer are seeing the trajectory on the positive side of the caustic while mp means the trajectory seen by the Earth is on the negative side and the trajectory seen by Spitzer is on the positive side of the caustic.

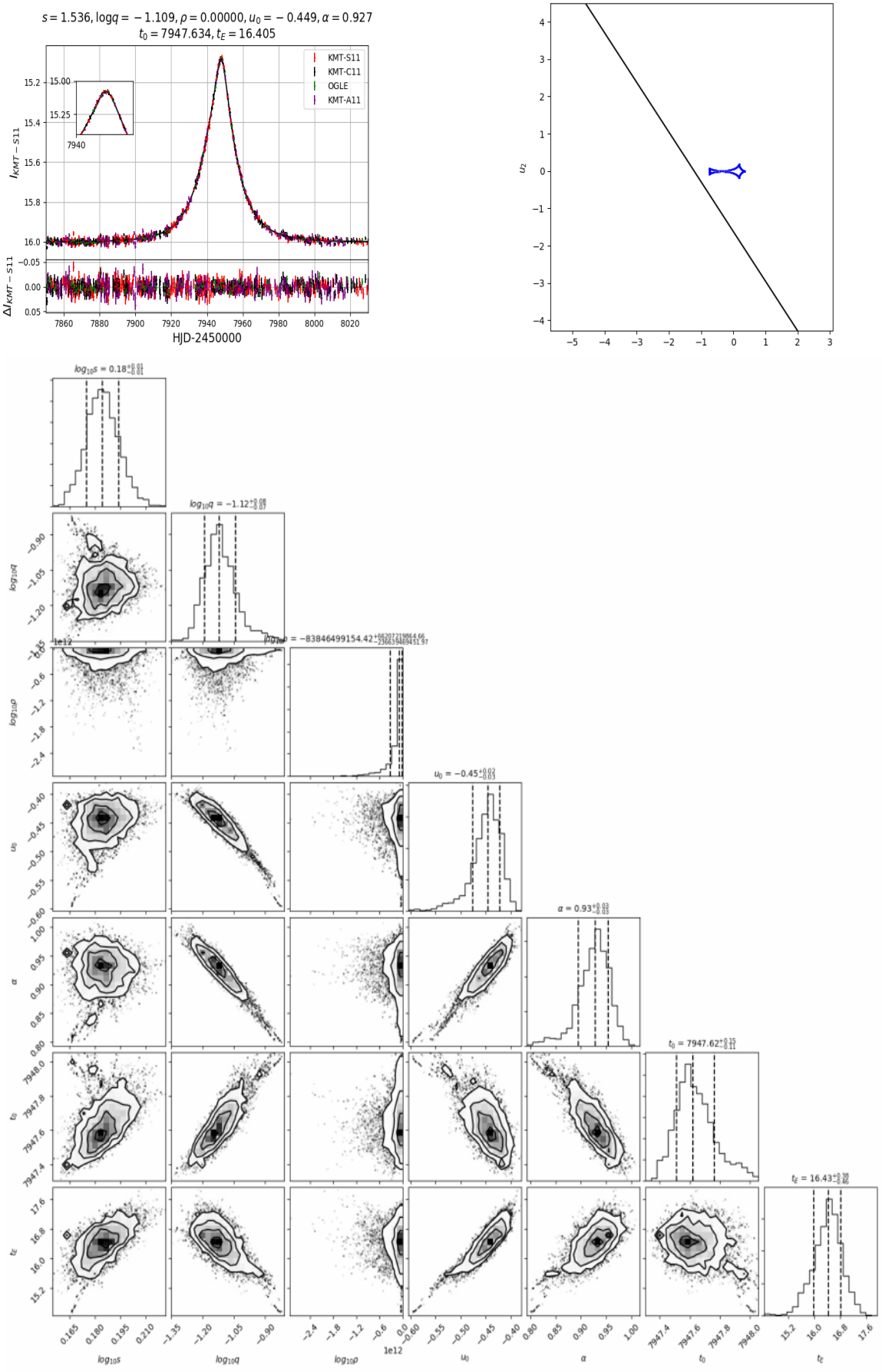

Figure 5.8: The figure shows the light curve, caustic and trajectory with renormalised uncertainties for the P2 solution. There is no significant change in the parameters of the solution except ρ.

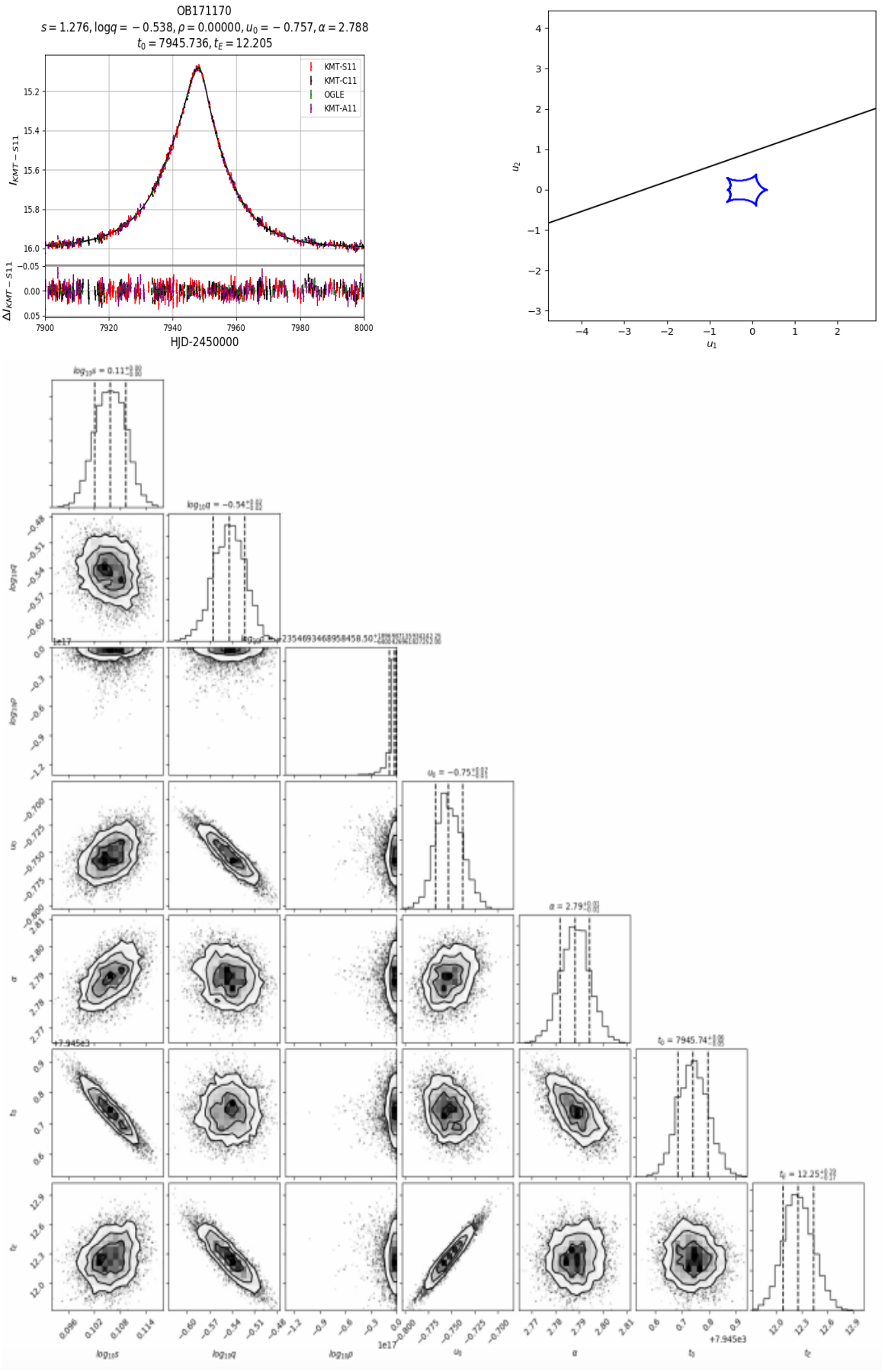

Figure 5.9: The plots show the fit of the P3 solution where the trajectory seeded to emcee is reflected by the lens axis from the trajectory of the P2 solution.

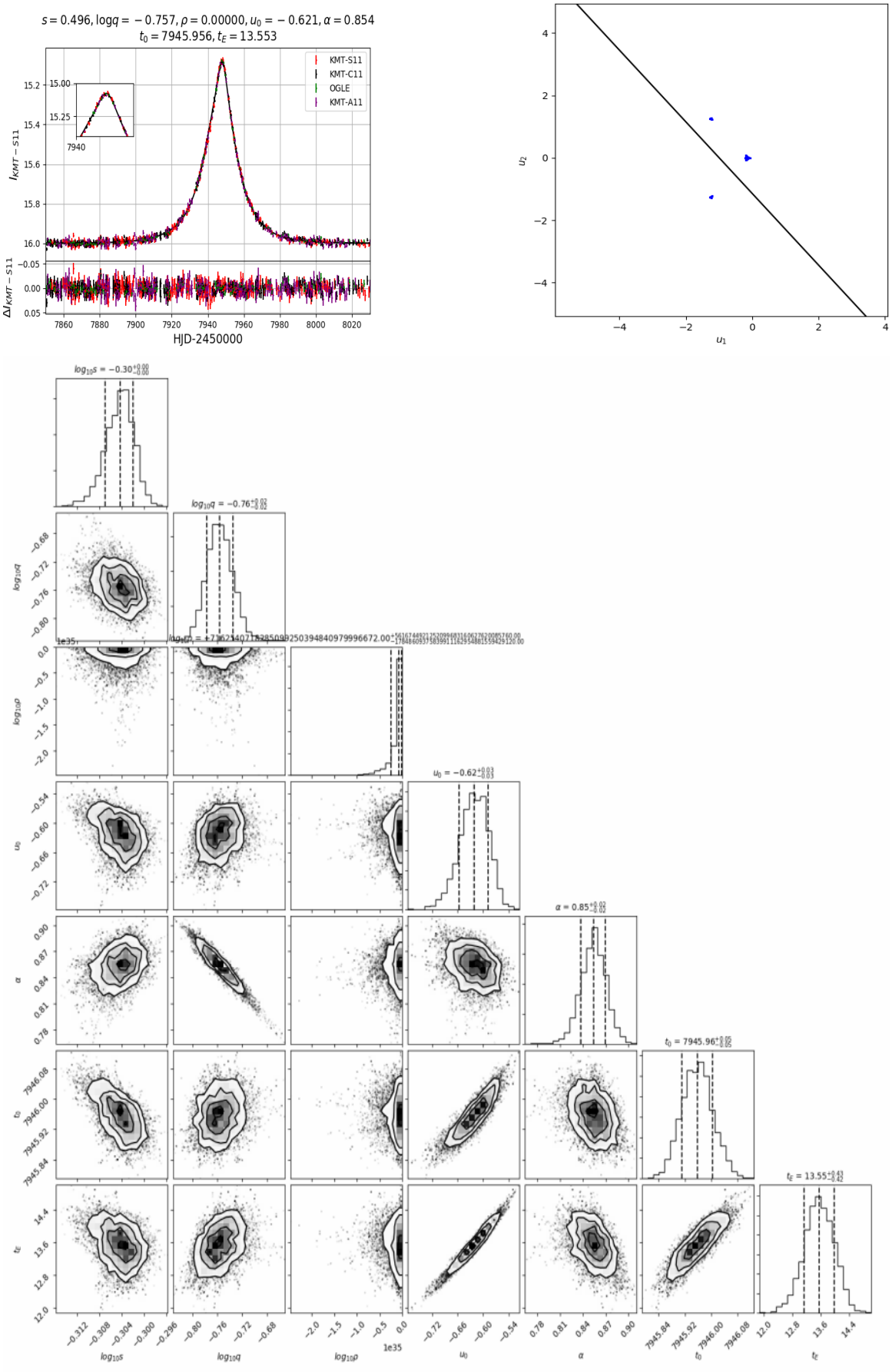

Figure 5.10: The plots show the light curve, the trajectory and the covariance plot corresponding to P4 model.

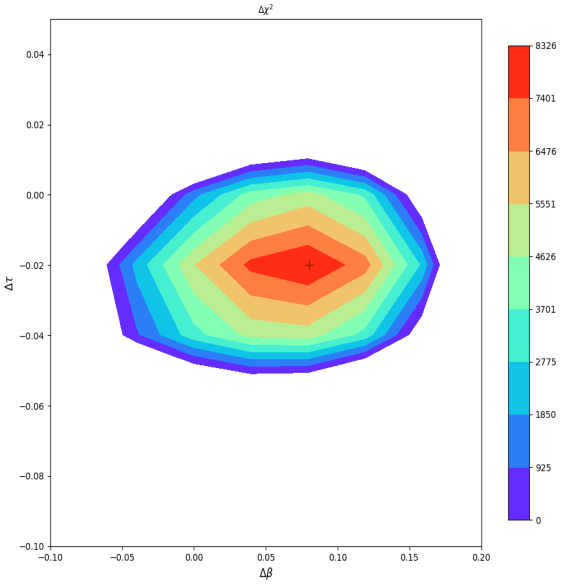

Figure 5.11: The map shows the different contour levels in the parallax plane with a grid search over $\Delta\tau$ and $\Delta\beta$ maximising the $\Delta\chi^2$ where $\Delta\chi^2 = \chi^2_{P2}$ - $\chi^2_{parallax}$. The ground based parameters are held constant during this grid search.

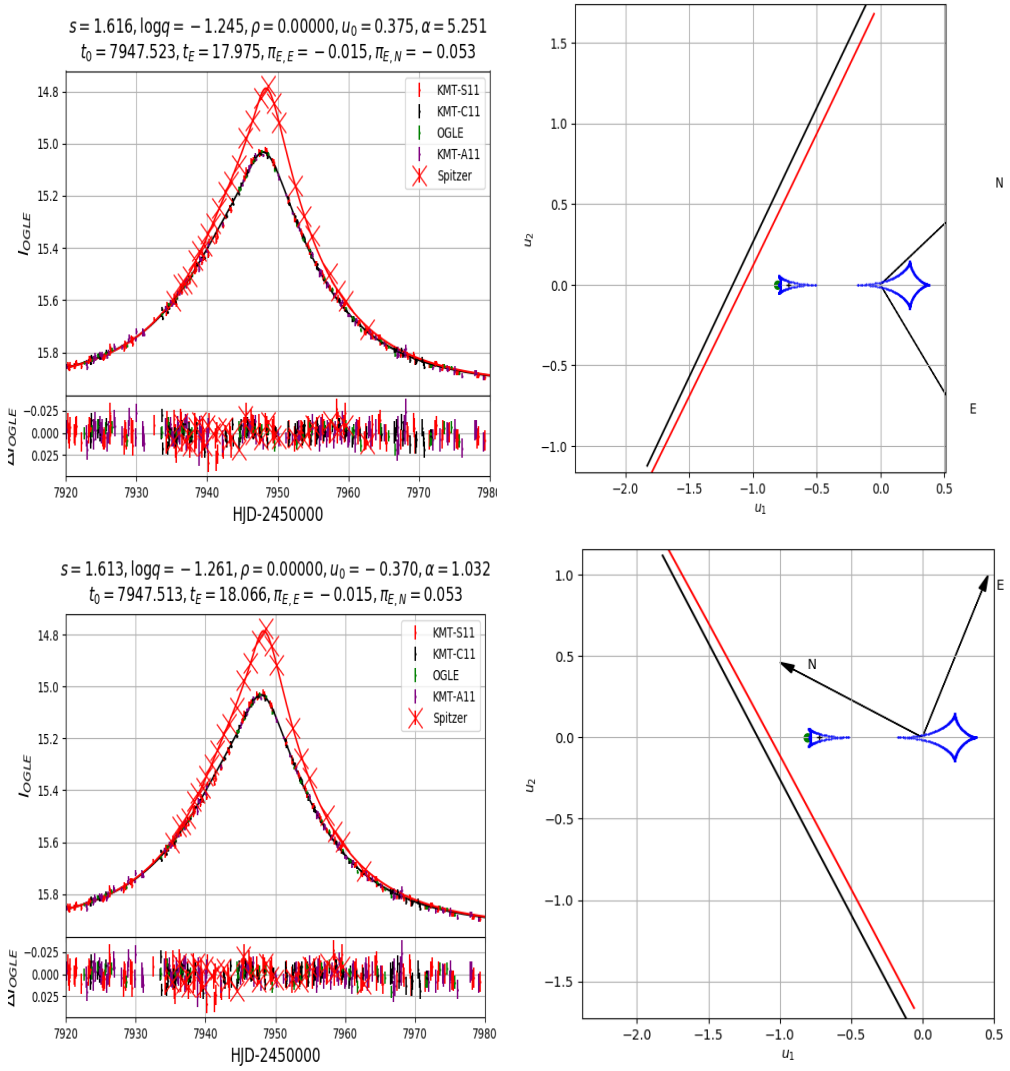

Figure 5.12: The plots show the different trajectories of the source as seen from Earth and Spitzer respectively when seeded with P2 ground based model. The upper solutions correspond to mm while the lower solutions correspond to pp degeneracy.

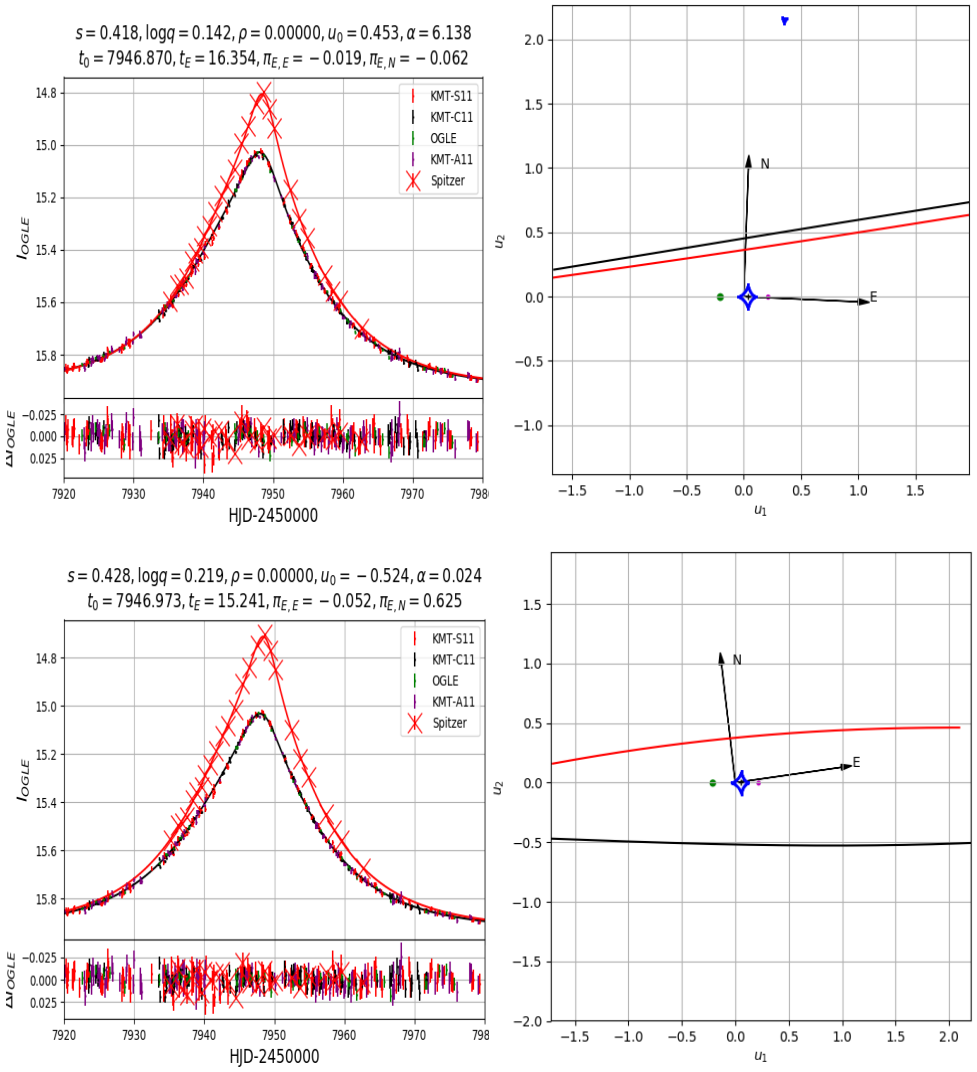

Figure 5.13: The plots show the different trajectories of the source as seen from Earth and Spitzer respectively when seeded with P4 ground based model. The upper solutions correspond to pp while the lower solutions correspond to mp degeneracy.

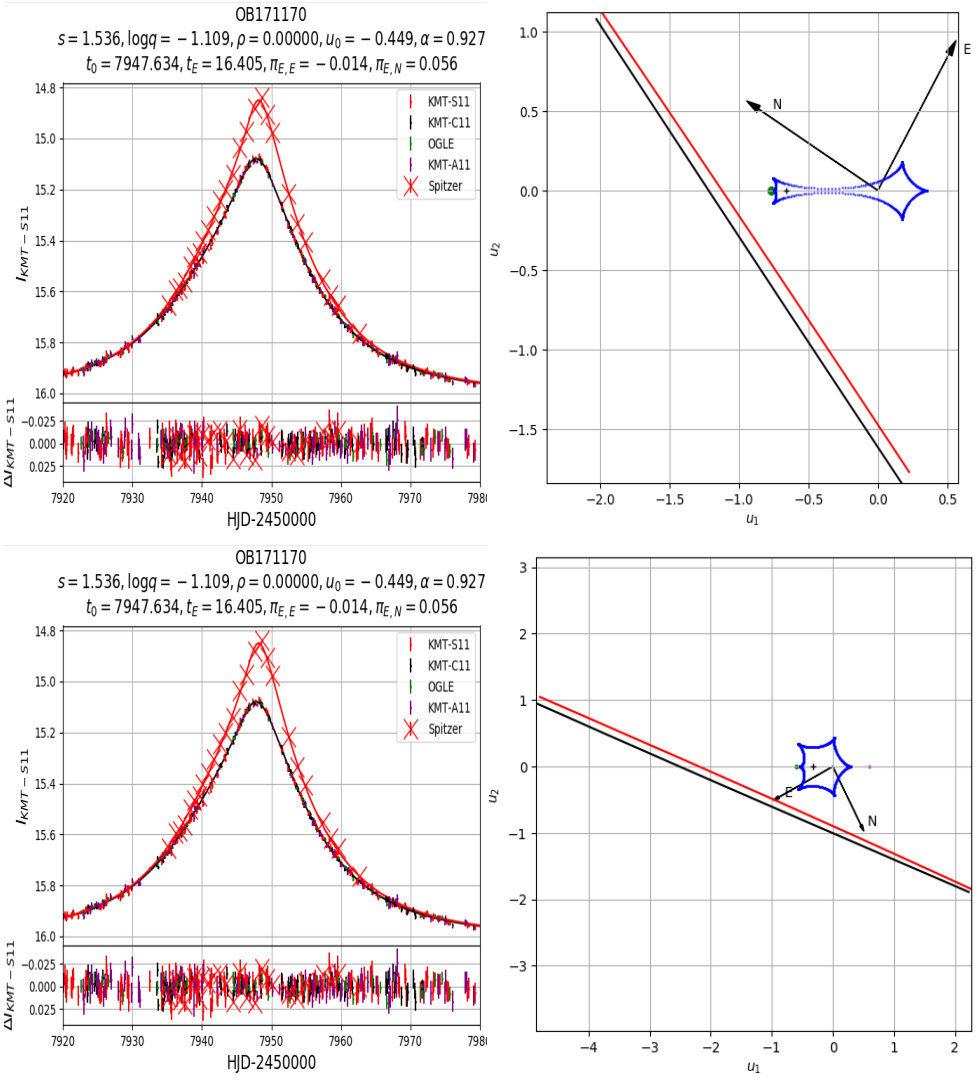

Figure 5.14: The plots show the different trajectories of the source as seen from Earth and Spitzer respectively when seeded with P3 ground based model. The upper solutions correspond to mm while the lower solutions correspond to pp degeneracy.

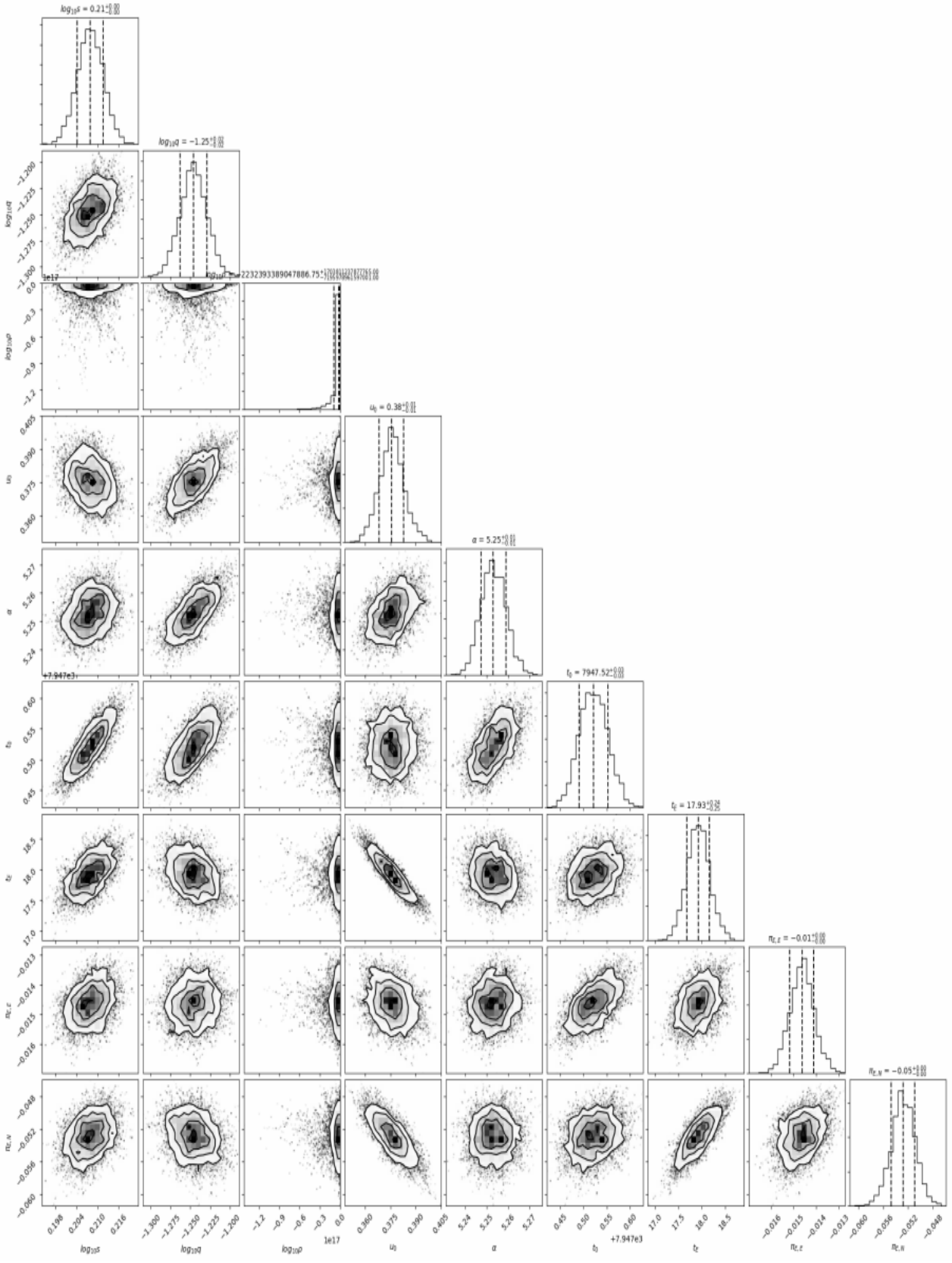

Figure 5.15: The plots show the 2 dimensional covariance for the emcee of wide-mm solution. Contours in these plots are the 0.5σ, 1σ, 1.5σ and 2σ levels of the parameters.

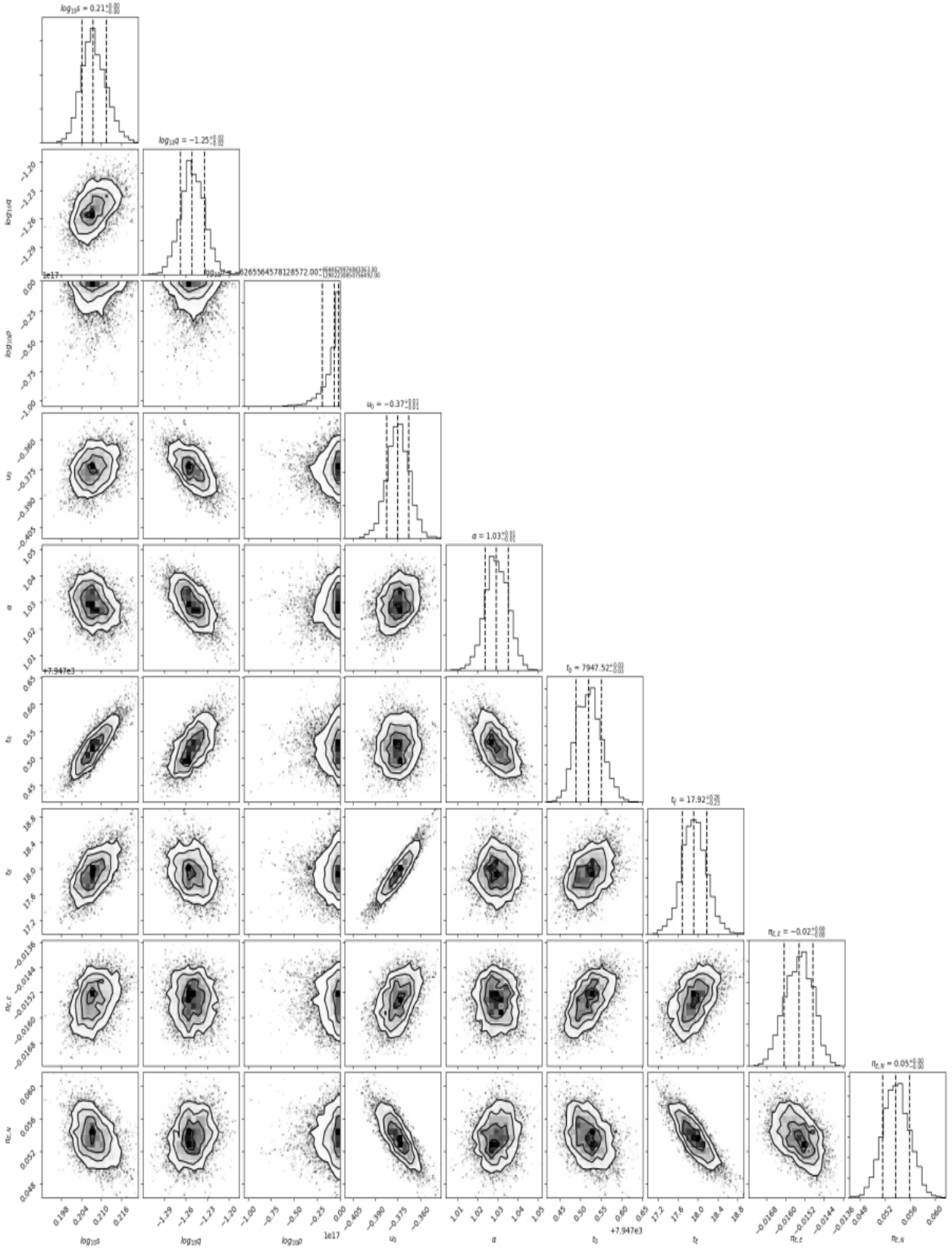

Figure 5.16: The plots show the 2 dimensional covariance for the emcee of the wide-pp solution. Contours in these plots are the 0.5σ, 1σ, 1.5σ and 2σ levels of the parameters.

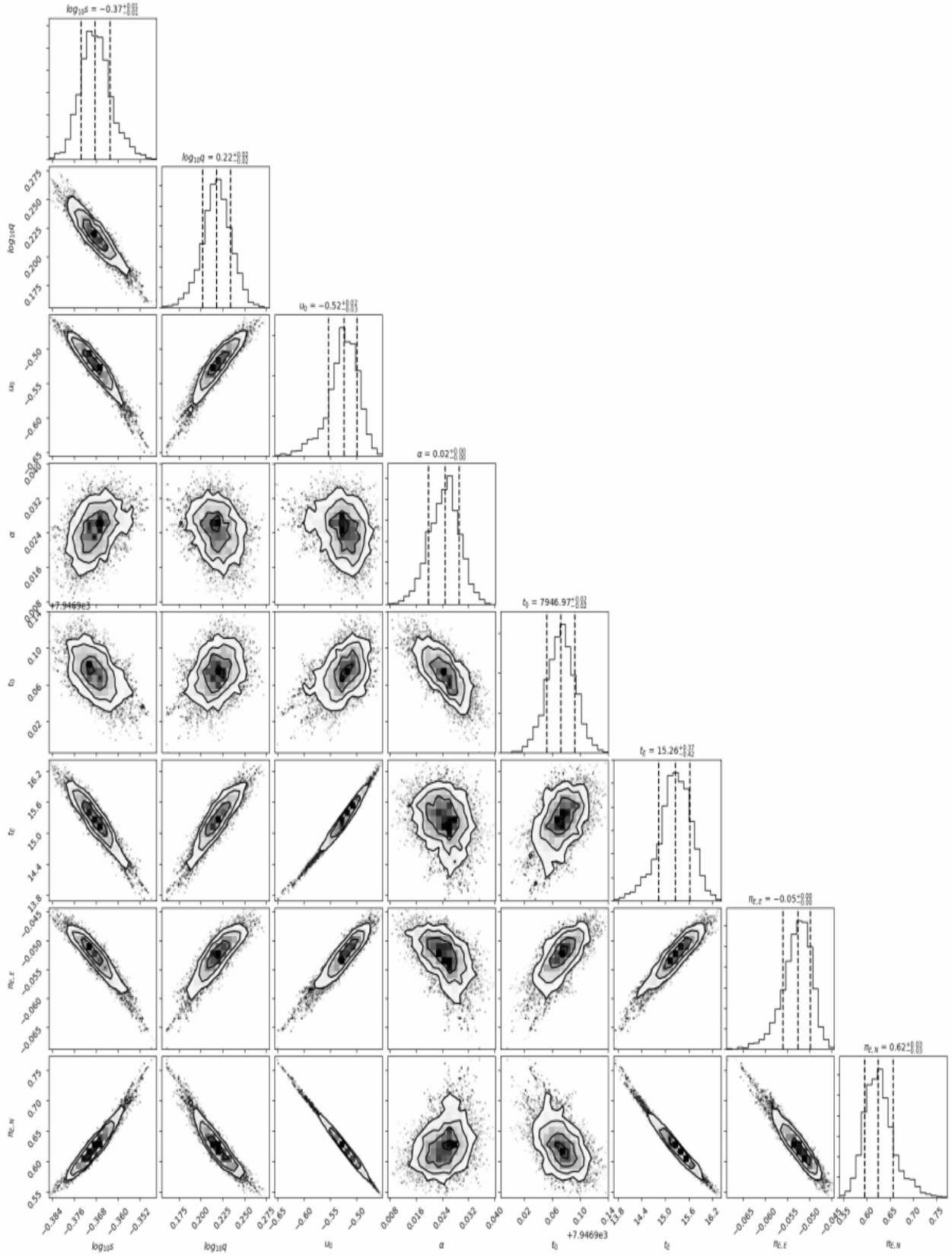

Figure 5.17: The plots show the 2 dimensional covariance for the emcee for close-mm solution. Contours in these plots are the 0.5σ, 1σ, 1.5σ and 2σ levels of the parameters.

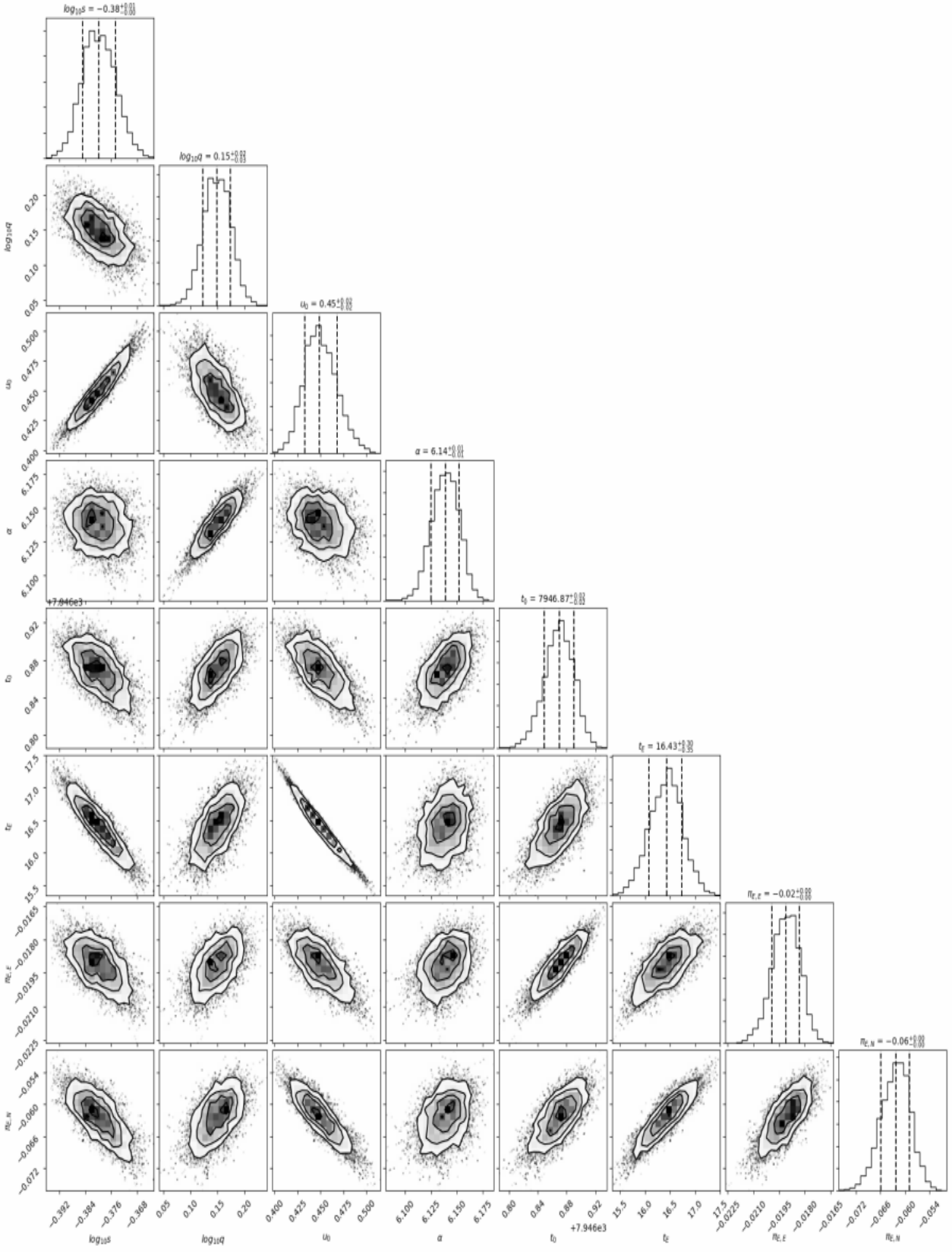

Figure 5.18: The plots show the 2 dimensional covariance for the emcee for close-mm solution. Contours in these plots are the 0.5σ, 1σ, 1.5σ and 2σ levels of the parameters.

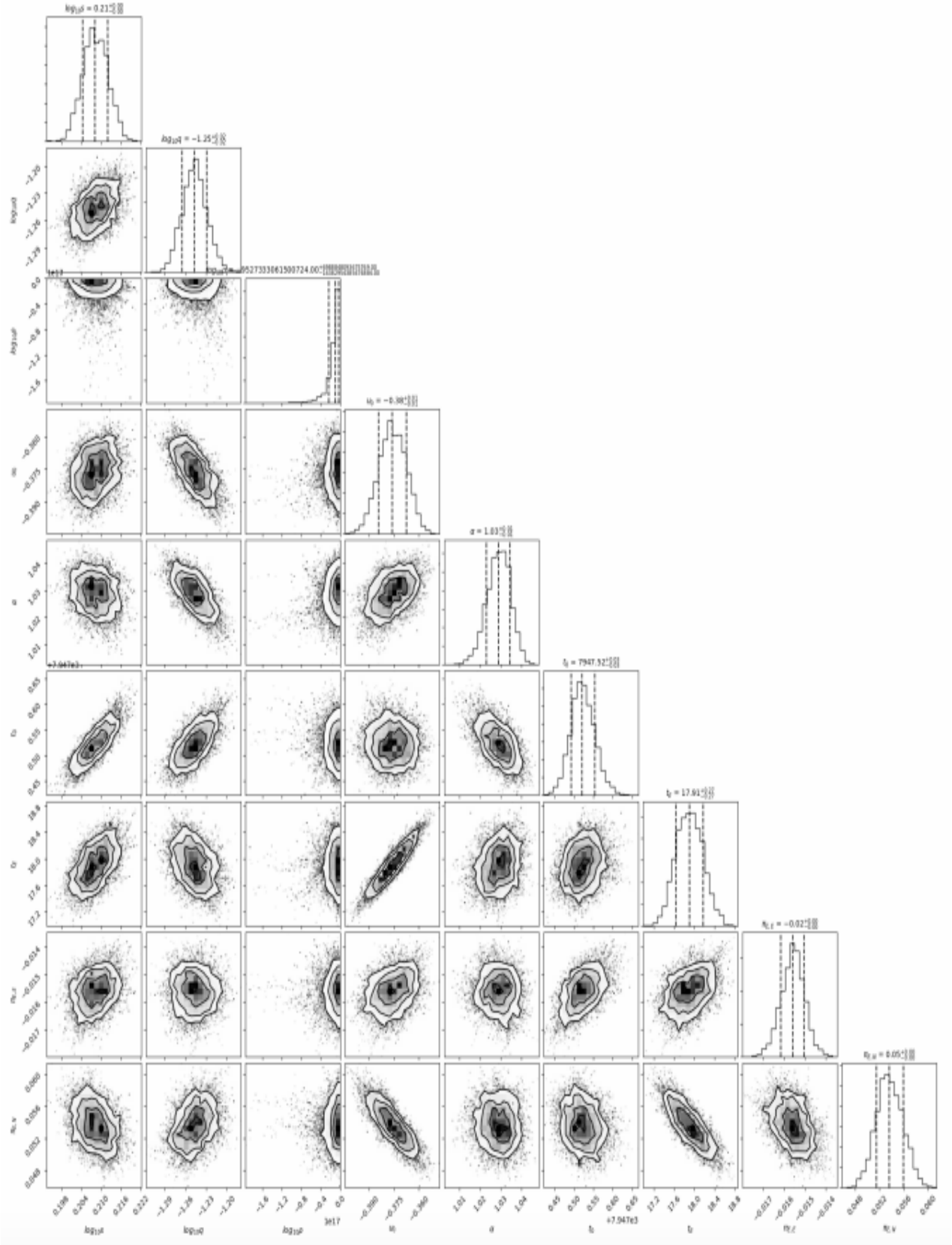

Figure 5.19: The plots show the 2 dimensional covariance for the emcee for P3-pp solution. Contours in these plots are the 0.5σ, 1σ, 1.5σ and 2σ levels of the parameters.

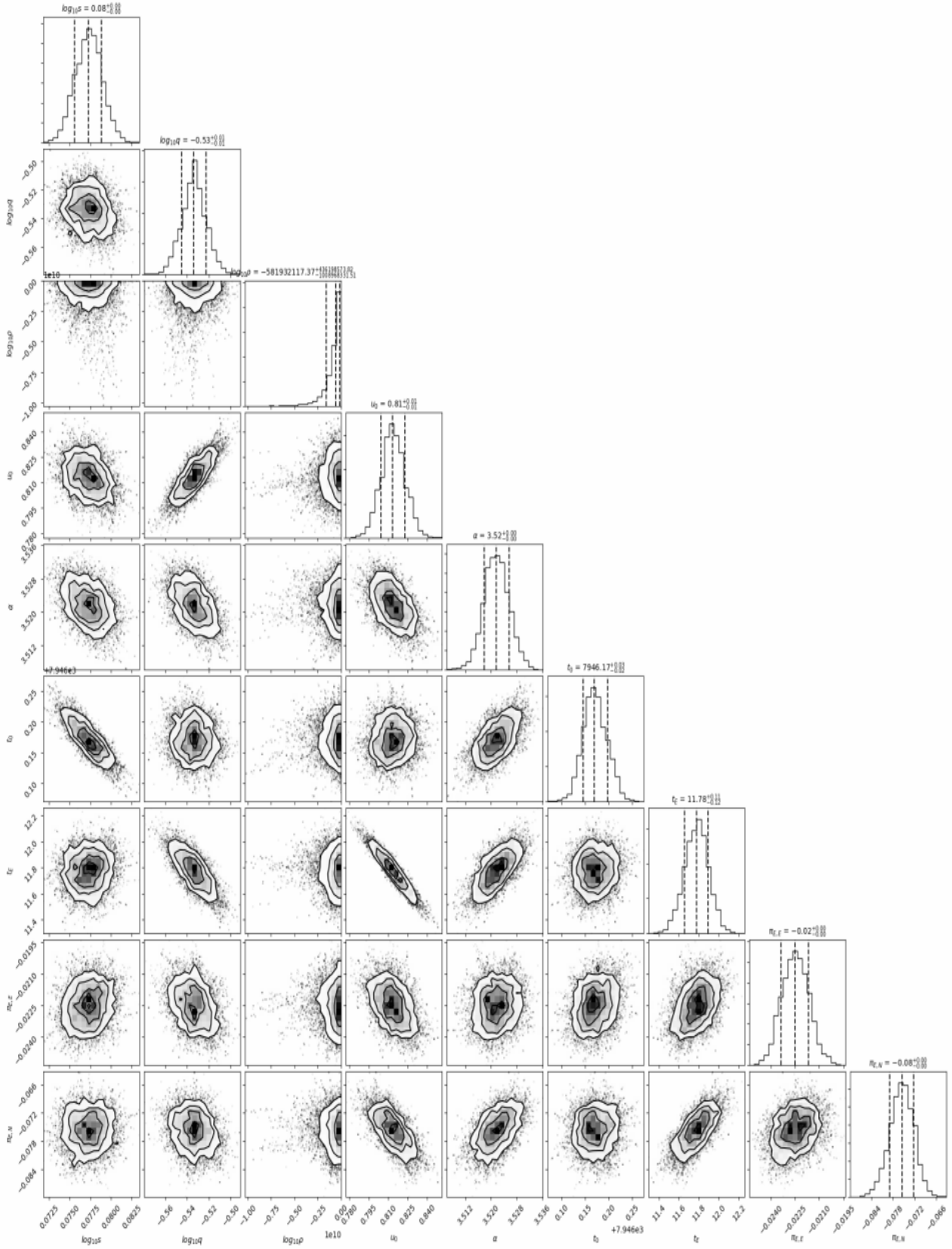

Figure 5.20: The plots show the 2 dimensional covariance for the emcee for perp-mm solution. Contours in these plots are the 0.5σ, 1σ, 1.5σ and 2σ levels of the parameters.

5.4 Galatic Model

Since ρ is not measured in our models for $OGLE-2017-BLG-1170$ the galactic model has to be relied upon to estimate properties of the lens (Chapter (2)). We compute the probability distributions for the lens mass and its distance for each model.

5.4.1 P4-pp solution

Since the P4-pp solution has the least χ^2, we perform the bayesian analysis of the Galactic model constrained by t_E and π_E of this solution. This yields the median value for the distance to the lens (D_L) $\sim$ 7.5kpc which *micro-lenses* the source at a median distance of 8.6kpc. Therefore, the mass of the lens is evaluated using equation (1.20). The mass of the lens is $4.91^{+2.13}_{-1.86} M_J$ which can be decomposed into individual masses,

$$M = M_1 + M_2; \quad q = \frac{M_2}{M_1} \tag{5.10}$$

where M is the mass of the system evaluated from the galactic model, M_1 is the mass of the primary lens component, M_2 is the mass of the secondary lens component and q is the mass ratio obtained from the fit to the light curve. For a median value of M = $4.91^{+2.13}_{-1.86} M_J$, $M_1 = 3.06^{+1.34}_{-1.16} M_J$ and $M_2 = 1.85^{+0.79}_{-0.70} M_J$ which indicates that this system is a pair of super-Jupiter masses in the galactic bulge. The projected physical separation between the lenses is

$$r_\perp = s D_l \theta_E \tag{5.11}$$

where D_l and θ_E are evaluated from the galactic model, s is the separation which is also a parameter of the fit to the light curve. For this solution, the median value for the projected physical separation between the two masses is $0.08^{+0.03}_{-0.03}$ AU. The distributions for these parameters are shown in Figure (5.21).

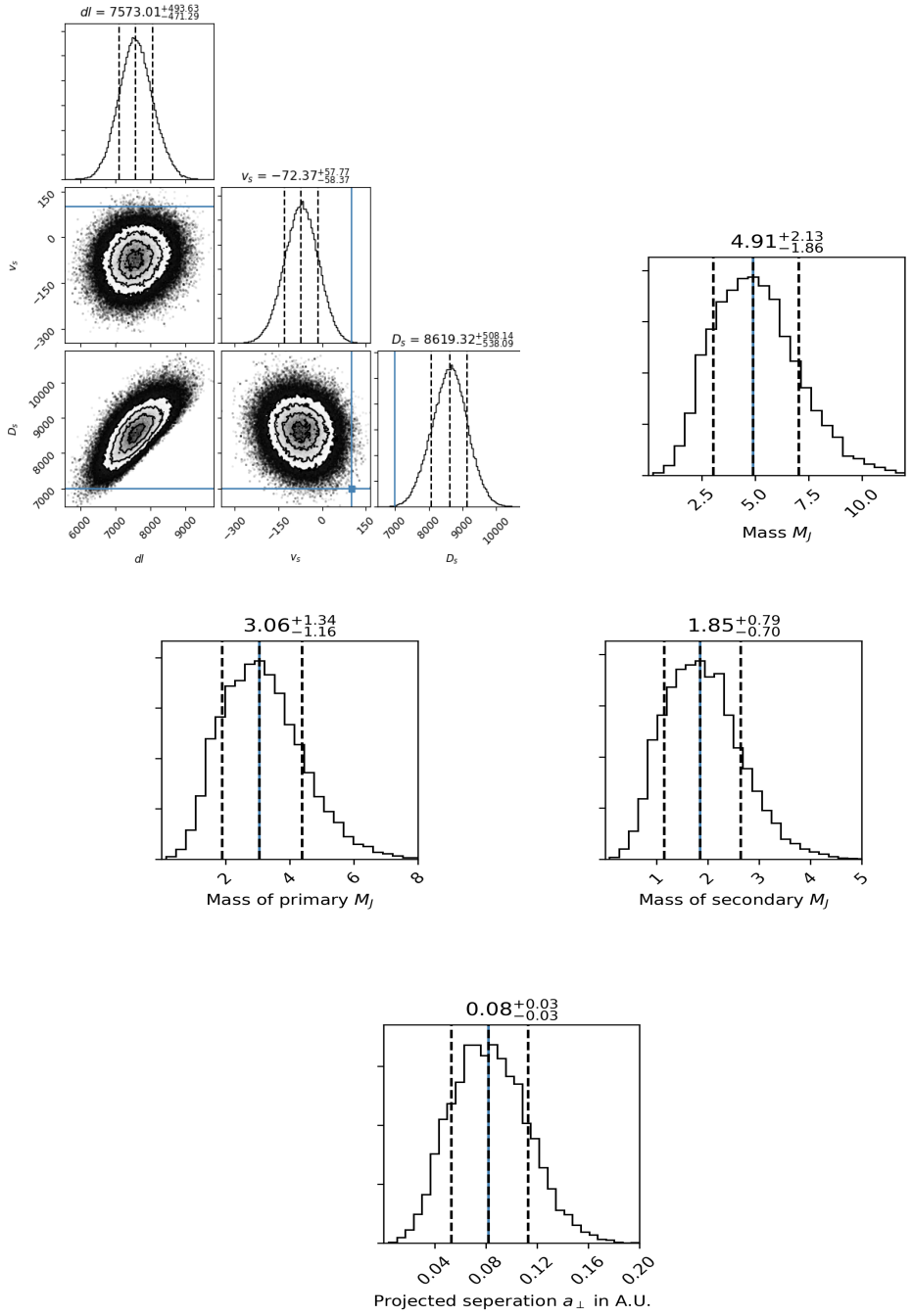

Figure 5.21: The plots of the galactic model results (close-pp solution) which show probability distribution for D_L, v_s, D_s and M, $M_{1,2}$ and $r_\perp$. The median distance to the lens is in bulge, implying that this is bulge-bulge microlensing event. The mass distribution indicates that this is a pair of super-Jupiters orbiting each other.

5.5 Source Properties

The best-fit model, close-pp, gives us the I-band source flux and blend flux and uncertainties in them. We fit the model with V-band data of KMT-C (CTIO) BLG-11 field and obtain the V-band source flux and blend flux. pyDIA gives us the brightness and colour of all the stars in this field and the centroid of the red-clump is found at ((V-I),I) = (3.256,16.919). We convert the fluxes to magnitudes for each band and find the brightness and colour of source and blend respectively. We plot the location of the source and blend on the CMD (Figure (5.22))

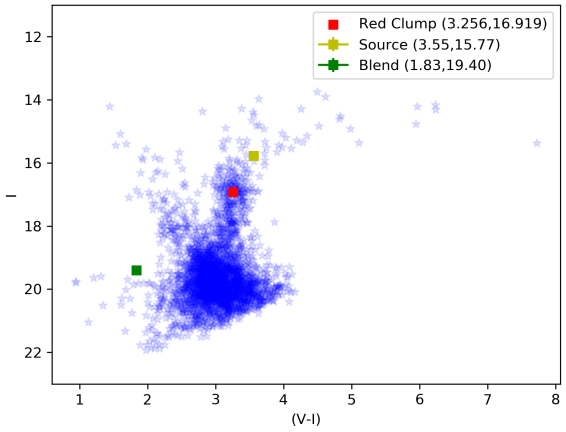

Figure 5.22: The CMD formed with the stars in the BLG-11 field of the KMT-C (CTIO) dataset. Source (yellow) is on the bulge turnoff region and the blend (green) is relatively bluer and fainter.

5.6 Discussion

In this chapter, I have presented the analysis of the non-caustic crossing event $OGLE-2017-BLG-1170$. Due to slight asymmetry at the peak, this event had multiple interpretations. It was found that the event can best explained by the static binary lens model. The analysis of the model (P3) was discarded because this model yielded negative value of blending flux. The renormalisation of uncertainties based on P2 model, gives equal weight to each dataset which made $\rho = 0$. Based on the new uncertainties, P2 model is analysed for an inherent close-wide ($s \rightarrow s^{-1}$) degeneracy which is related to caustic geometry. The resulting degenerate model (P4) is favoured by χ^2 but significant negative blending. Since the event was also observed with the Spitzer space telescope, this enabled measurement of the space parallax. The light curve was investigated for space parallax using the degenerate (P2 and P4) ground based solutions and it was seen that the light curve obtained from Spitzer was not very different from the ground based

light curve except that Spitzer saw a higher magnification in the event. This indicates a relatively small parallax and implies that the lens is a low mass binary or it is located close to the source (smaller π_{rel}). The least χ^2 solution was close-pp solution which gives the median value of $\pi_{rel} = 0.016$ mas, obtained from the galactic model distribution of distance to the lens and distance to the source. The close-pp solution implies that the lens is a pair of super-Jupiters with masses $3.06^{+1.34}_{-1.16}$ $M_{\odot}$ and $1.85^{+0.79}_{-0.70}$ $M_{Jupiter}$ located at a distance of $7.57^{+0.49}_{-0.47}$ kpc. Since we do not detect the signatures of orbital motion in this event, it is hard to say whether this system is bound or unbound.

Based on the simulations of Ma et al. (2016), the freely floating planet mass function peaks at Earth mass and Jupiter mass planets at 0.1 day and 1 day respectively. However, this is a unique system of a freely floating pair of planetary masses. Conventional theories of planet formation (Section (1.7)) tell that the planets grow from planetesimals before the gas runaway happens, but it does not say anything about the formation of freely floating binary planetary masses. Further investigations are required for the formation of such systems. Could this system be formed as binary planets from a gas cloud where stars are formed or they happened to come into gravitational influence of each other?

Location of this binary lens in the bulge explains why the t_E of this event is not very high. OGLE-2017-BLG-1170 is an event that would enter the galactic distribution sample of planets of Yee et al. (2012). This is another sample after Albrow et al. (2018) where a pair of super-Jupiters is found although the lens masses of Albrow et al. (2018) are higher than this sample. This will be useful in future analysis for the formation theories of isolated-planetary masses since gravitational microlensing is able to detect them.

Chapter 6

Analysis of the event OGLE-2018-BLG-1647

In this chapter I present the analysis of the event $OGLE-2017-BLG-1647$. This event has an anomaly of ~ 2 days which is a typical anomaly caused due to Jupiter mass planet (Dominik, 2006). I find that this event can be best explained with a close binary lens model and the source is a low mass dwarf star. I also investigate the presence of higher order effects like orbital parallax and lens orbital motion. Though the effect of orbital parallax is weakly present in the light curve, I find that there is no binary lens orbital motion effect present. Evaluating the galactic model based on the information of the event that we get from the model, it is found that lens is a pair of low mass sub-stellar primary and sub-Jupiter companion in the disc.

6.1 Data

6.1.1 Observations

$OGLE-2018-BLG-1647$ was detected towards galactic bulge by the *Early Warning System* of the $OGLE$ in their field $BLG507.14$ (Udalski et al., 2015a). The event peaked towards the end of the microlensing season of 2018 on 12^{th} September 2018. It was also observed by the three telescopes of KMTNet - (KMT-A), (KMT-S) and (KMT-C) in their fields $BLG01$ and $BLG41$ (Kim et al., 2016). The location of this event is (α, δ) = (17:55:50:98, -31:49:01.6) expressed in (hh:mm:ss and ^{o},$'$, "). This translates to the galactic coordinates (l, b) = (358.65140746^0, -3.36874720^0) [1].

[1] https://ned.ipac.caltech.edu/forms/calculator.html

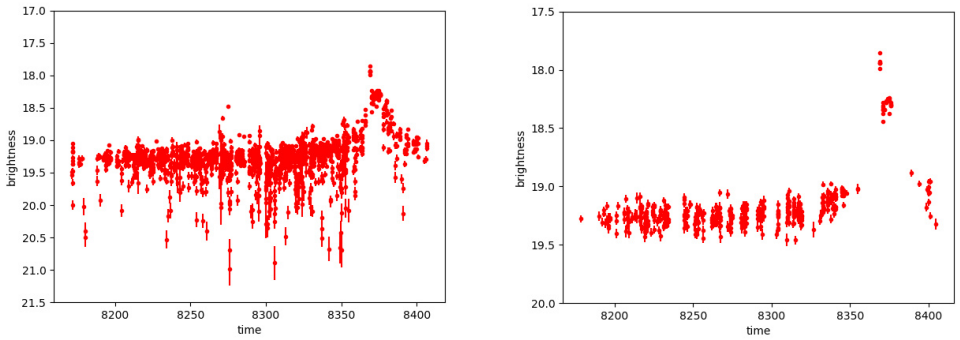

Figure 6.1: The plots show the raw photometry and filtered photometry for KMT-A BLG01 field dataset. The full moon interferes around HJD-245000 = 8345 and 8375.

6.1.2 Data reductions

OGLE photometry was taken from their webpage [2]. The KMTNet images were reduced with pyDIA software (Albrow, 2017). It was found that the photometry was poor around HJD-2450000 = 8345 and 8375. Using *Stellarium* software (version 0.15) which is an open source software package for simulating the sky for given time and location [3], it was understood that this is due to the presence of moon close to the galactic bulge at these times (Figure (6.2)). This reflects in the sky and signal column of the pyDIA output which shows abnormally high values. The KMTNet photometry was filtered based on several image quality criteria (Table (6.1) and Figure (6.1)).

Parameters of different fits							
Dataset	Magnitude	$\sigma_{magnitude}$	Q	FWHM	Roundness	Sky	Signal
KMT-A02	<19.7	<0.1	<1.2	< 2.5	-	< 2500	>400
KMT-A41	<19.7	<0.1	<1.1	< 2.3	1.3	< 2000	>400
KMT-C01	<19.45	<0.1	<1.5	< 2.2	-	< 1800	-
KMT-C41	<19.45	<0.1	<1.2	< 2.2	-	< 1800	-
KMT-S01	<19.5	<0.1	<1.5	< 2.3	-	< 2000	
KMT-S41	<19.5	<0.1	<1.5	< 2.3	-	< 2000	

Table 6.1: Criteria for filtering KMTNet data after the reduction of KMTNet images with pyDIA. Multiple conditions are set because the photometry of the event was affected due to the presence of moon close to the bulge. These conditions are set so that the outliers are removed but the event is preserved.

6.2 Light Curve Analysis

The event shows a clear anomaly close to the peak on the rising side of the light curve, which spans around 1.5 days. This suggests the presence of a lens companion, and a

[2] http://ogle.astrouw.edu.pl/ogle4/ews/2018/blg-1647.html
[3] https://stellarium.org

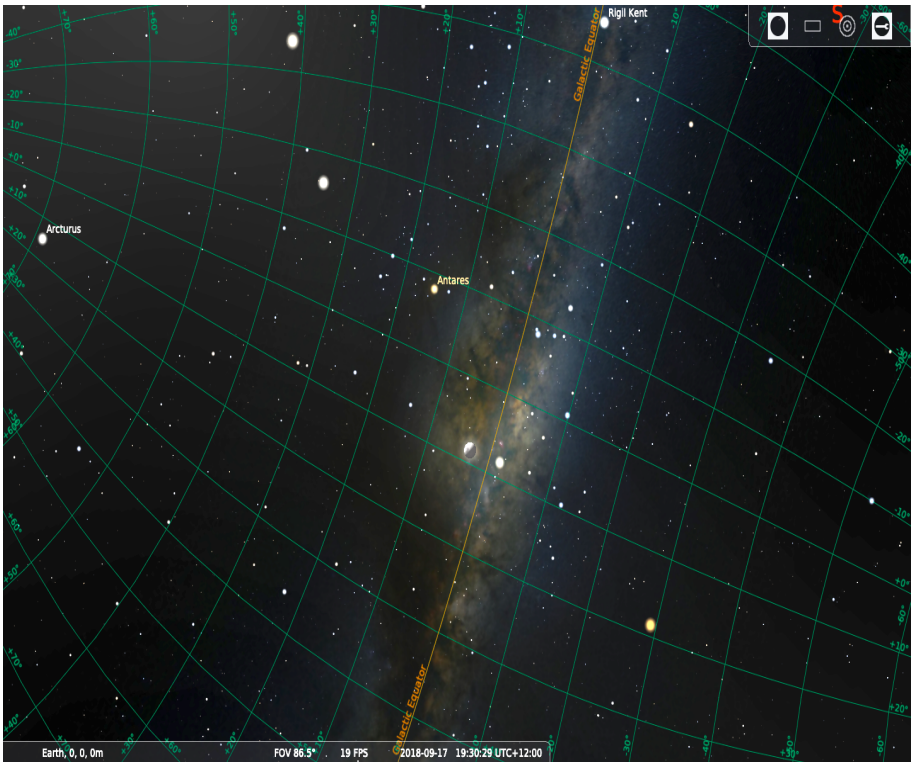

Figure 6.2: The screenshot of stellarium software at HJD-245000 = 8378 day. The moon is located in the bulge close to the galactic equator. The galactic grid is shown in green colour and the galactic equator is shown in orange colour. The full moon is more than 50% bright when it passes the galactic bulge. The location is set for SSO which has maximum interference due to moon.

trajectory that passes close to the induced caustic. The major image of the source passes through the Einstein ring of the secondary which gives rise to the spike on the rising side of the light curve. However, the location of this spike close to the peak of the light curve suggests that the source passes close to the central caustic. Since the Einstein radius is proportional to the square root of the mass of the lens, $\frac{t_{E,secondary}}{t_{E,primary}} = \sqrt{\frac{M_{secondary}}{M_{primary}}}$, yields the mass ratio of 0.001 as the deviation caused due secondary companion has time width $\sim$ 1.5 days, whereas the time width of the primary light curve is $\sim$ 55 days.

6.3 Static binary Lens model

The binary lens modelling of this light curve was performed following the procedure described in (section (1.4.2)). The grid search yields several solutions on the close binary and few on wide binary side (Figure (6.3)).

These solutions were sorted on the basis of χ^2 and first 10 minimum χ^2 solutions were seeded to emcee (Foreman-Mackey et al., 2013) to refine the solutions. The best solution is shown in Figure (6.4).

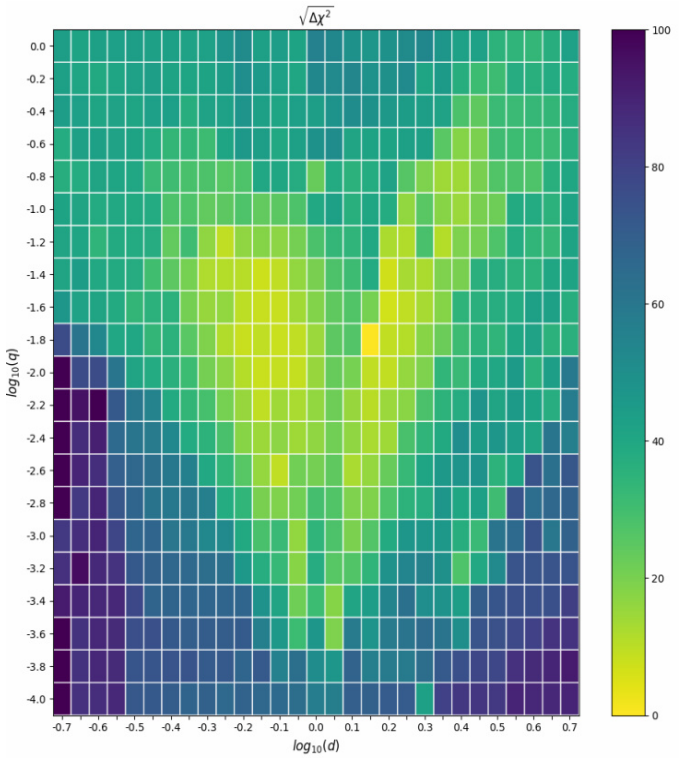

Figure 6.3: The plot shows the grid search over each value of d and q. For each element of the grid, (u_0, ϕ) are searched by grid search methods and (t_0, t_E, ρ) are minimised by simplex downhill methods. The grid colours are $\Delta\chi^2 = \chi^2_{element_{(d,q)}} - \chi^2_{best}$.

6.3.1 Renormalisation of error bars

The best fitting model described in the previous section was used to renormalise the error bars in the data points so that $\chi^2/dof \sim 1$ for each dataset (section (1.6)). In order to renormalise the uncertainties, the procedure of Yee et al. (2012) was followed. The values of κ and e for the different datasets are given in Table (6.2). The best fitting model changes dramatically after the renormalisation of the uncertainties since it gives equal weight to each dataset. This indicates that in the photometry packages may yield incorrect estimation of uncertainties in data. Smaller uncertainties, particularly around the peak may influence the value of ρ when the source does not cross caustic. Figure (6.5) shows the static binary lens model after renormalisation of uncertainties. In the new model, the high magnification bump gets constrained due to the data around HJD-2450000 = (8367 - 8372) but this model does not yield any finite source effects.

Parameters for renormalising uncertainties in magnitude		
Site	κ	σ_{min}
KMT-A01	1.286	0.0593
KMT-A41	2.218	0.0117
KMT-C01	2.734	0.0083
KMT-C41	2.007	0.0091
KMT-S01	2.196	0.0107
KMT-S41	2.975	0.0071
OGLE	1.103	0.0186

Table 6.2: The parameters for the renormalisation of the error bars in the data points so that $\chi^2/dof \sim 1$.

6.4 Modelling of higher order effects

6.4.1 Orbital Parallax

After renormalising the uncertainties, the presence of higher order effects in the light curve was investigated starting with the orbital parallax effect (section (1.5.1)). Parallax is often fitted to the light curve via - $(\pi_{E,N}, \pi_{E,E})$, which are the two components of parallax in the celestial frame of reference. It was found out that the inclusion of this effect in the light curve model lowers χ^2 only by 3.9 which leads to the conclusion that the orbital parallax effect is only marginally detected.

Although inclusion of orbital parallax did not lower the χ^2 by a significant amount, we detected the presence of jerk-parallax degeneracy in this light curve (section (1.5.1)). It is to be noted that since the single lens has a rotationally invariant point caustic, the four jerk-parallax solutions can be realised by substituting $(u_0 \rightarrow -u_0)$ and $(u_0, \pi_{E,N})$ $\rightarrow (-u_0, -\pi_{E,N})$. However, the line caustics for binary lenses instead have a reflection symmetry, which implies that the four jerk-parallax solutions can be found by substituting $(u_0, \alpha \rightarrow -u_0, -\alpha)$ and $(u_0, \alpha, \pi_{E,N}) \rightarrow (-u_0, -\alpha, -\pi_{E,N})$ (Poindexter et al., 2005, Skowron et al., 2011). Hereafter, (u_0, α, π_{EN}) is labelled as P1 solution, $(u_0, \alpha, -\pi_{EN})$ is labelled as P2 solution, $(-u_0, -\alpha, +\pi_{EN})$ is called as P3 solution and $(-u_0, -\alpha, -\pi_{E,N})$ is called as P4 solution. We investigate the jerk-parallax solutions by this substitution which are shown in Figure (6.6), (6.7), (6.8) and (6.9) and the parameter distribution is given in Table (6.3). We find that P1, P2 and P3 solutions are severely degenerate.

6.4.2 Binary lens Orbital Motion

Another higher order effect which can affect the light is orbital motion of the lens. Usually every binary lens will have some orbital motion around their centre of mass, however

detection of this effect depends on the proximity of the caustic to the source trajectory, the timescale of the event and the period of the binary lens orbit (1.5.2). It was found for this that there is no improvement in χ^2 with the inclusion of orbital motion.

In Table (6.3) we list the different parameters of the fit for the static binary model and the models that include parallax.

6.4.3 Check for close-wide degeneracy

Since almost every binary lens undergoing central caustic perturbation to the light curve suffers from *close* − *wide* degeneracy, the corresponding wide solution was searched for. For close caustic geometry $(d_c, q_c) = (0.79,\ 0.016)$, the corresponding wide caustic geometry $(d_w, q_w) = (1.27, 0.011)$ is obtained (equation (5.8) and equation (5.9)). Though $(d_c, q_c) \rightarrow (d_w, q_w)$, other parameters of the static binary lens model are expected to remain the same. However, when emcee is seeded with these values, we did not find any model that fits the light curve well (Figure (6.11)).

Parameters of the model					
Parameter	Static	P1	P2	P3	P4
χ^2	2186.07	2181.99	2182.00	2182.20	2184.48
u_0	$-0.09^{+0.01}_{-0.01}$	$-0.10^{+0.02}_{-0.01}$	$-0.12^{+0.02}_{-0.02}$	$0.10^{+0.01}_{-0.01}$	$0.10^{+0.01}_{-0.01}$
t_0	$8373.26^{+0.09}_{-0.09}$	$8373.29^{+0.44}_{-0.23}$	$8373.22^{+0.42}_{-0.19}$	$8374.48^{+0.44}_{-0.50}$	$8374.12^{+0.32}_{-0.36}$
t_E	$54.62^{+4.73}_{-4.79}$	$55.34^{+8.34}_{-5.22}$	$54.35^{+8.72}_{-4.80}$	$54.58^{+5.07}_{-4.34}$	$51.17^{+5.32}_{-3.99}$
α	$-2.26^{+0.01}_{-0.01}$	$-2.32^{+0.15}_{-0.07}$	$-2.35^{+0.14}_{-0.05}$	$2.40^{+0.06}_{-0.08}$	$2.38^{+0.04}_{-0.05}$
ρ	0.0	0.0	0.0	0.0	0.0
d	$0.74^{+0.03}_{-0.03}$	$0.77^{+0.03}_{-0.03}$	$0.75^{+0.02}_{-0.02}$	$0.74^{+0.01}_{-0.01}$	$0.70^{+0.02}_{-0.02}$
q	$0.02^{+0.00}_{-0.00}$	$0.01^{0.00}_{0.00}$	$0.01^{+0.00}_{-0.00}$	$0.01^{+0.03}_{-0.05}$	$0.02^{+0.09}_{-0.12}$
$\pi_{E,E}$	-	$0.05^{+0.12}_{-0.18}$	$0.08^{+0.14}_{-0.09}$	$0.24^{+0.21}_{-0.18}$	$0.34^{+0.19}_{-0.19}$
$\pi_{E,N}$	-	$0.97^{+0.89}_{-2.12}$	$1.45^{+0.53}_{-2.17}$	$-1.50^{+0.70}_{-0.44}$	$-1.50^{+0.51}_{-0.37}$
$\frac{f_s}{f_b}_{OGLE}$	0.22 ± 0.28	0.16 ± 0.18	0.248 ± 0.235	0.15 ± 0.18	0.18 ± 0.19
$\frac{f_s}{f_b}_{KMT-A01}$	0.21 ± 0.21	0.15 ± 0.17	0.236 ± 0.227	0.15 ± 0.16	0.17 ± 0.20
$\frac{f_s}{f_b}_{KMT-A41}$	0.23 ± 0.24	0.17 ± 0.19	0.26 ± 0.25	0.15 ± 0.17	0.19 ± 0.22
$\frac{f_s}{f_b}_{KMT-C01}$	0.23 ± 0.25	0.17 ± 0.01	0.26 ± 0.25	0.16 ± 0.16	0.19 ± 0.22
$\frac{f_s}{f_b}_{KMT-C41}$	0.24 ± 0.28	0.17 ± 0.19	0.271 ± 0.254	0.16 ± 0.14	0.21 ± 0.22
$\frac{f_s}{f_b}_{KMT-S01}$	0.25 ± 0.27	0.18 ± 0.21	0.291 ± 0.281	0.17 ± 0.15	0.21 ± 0.22
$\frac{f_s}{f_b}_{KMT-S41}$	1.01 ± 1.07	0.62 ± 0.74	1.229 ± 1.198	0.57 ± 0.48	0.74 ± 0.67

Table 6.3: The table showing parameters of fit and their uncertainties for static binary lens, binary lens with orbital parallax and binary lens orbital motion models. Models P1, P2 and P3 are severely degenerate.

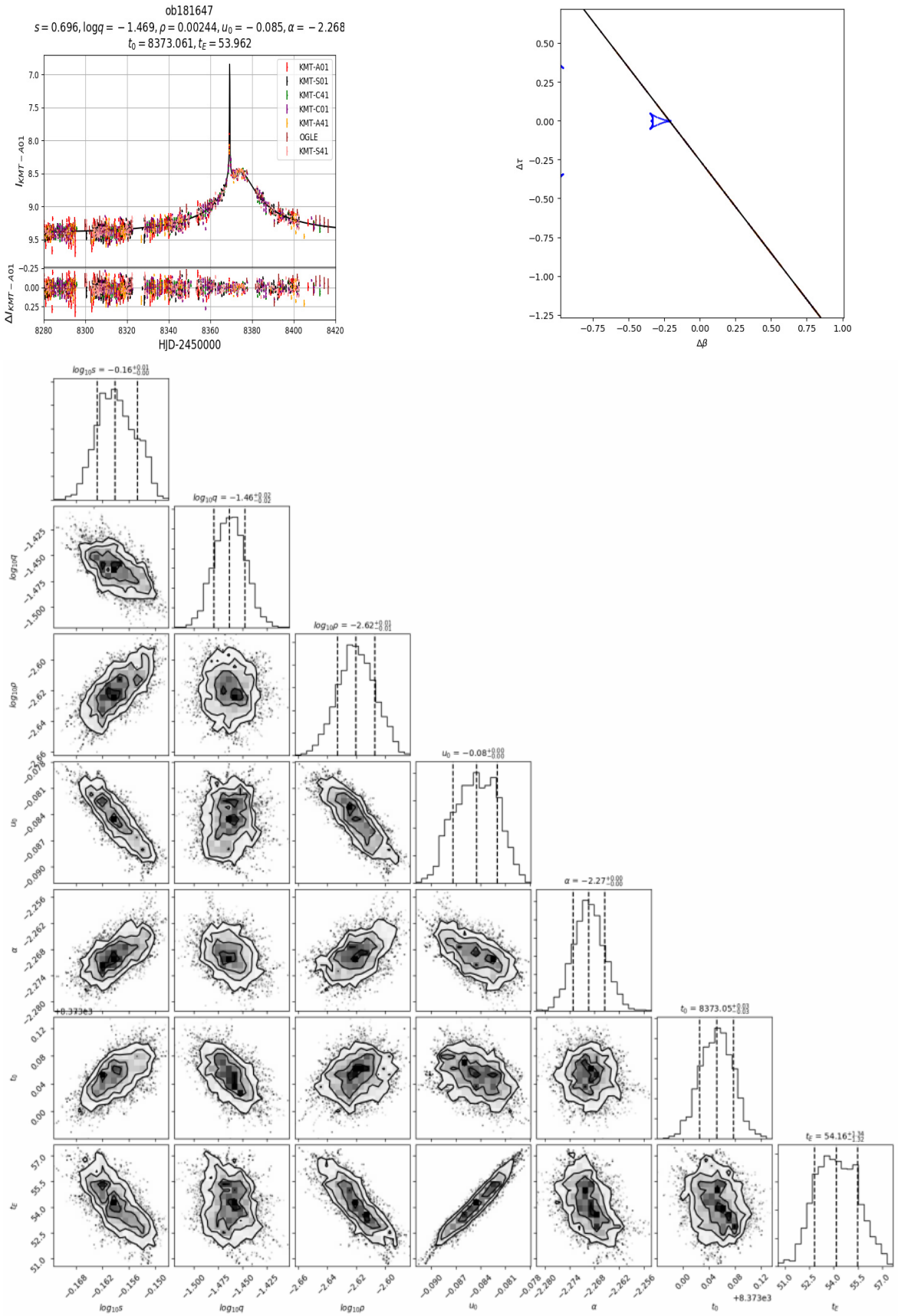

Figure 6.4: The plots show the best fitted model to the light curve, the corresponding caustic geometry and the covariance between the model parameters. The trajectory is rectilinear and is shown by black line passing at an angle $\alpha = -130^0$ from $-\Delta\beta$ direction. The trajectory touches the central cusp of the caustic which gives rise high magnification bump in the light curve.

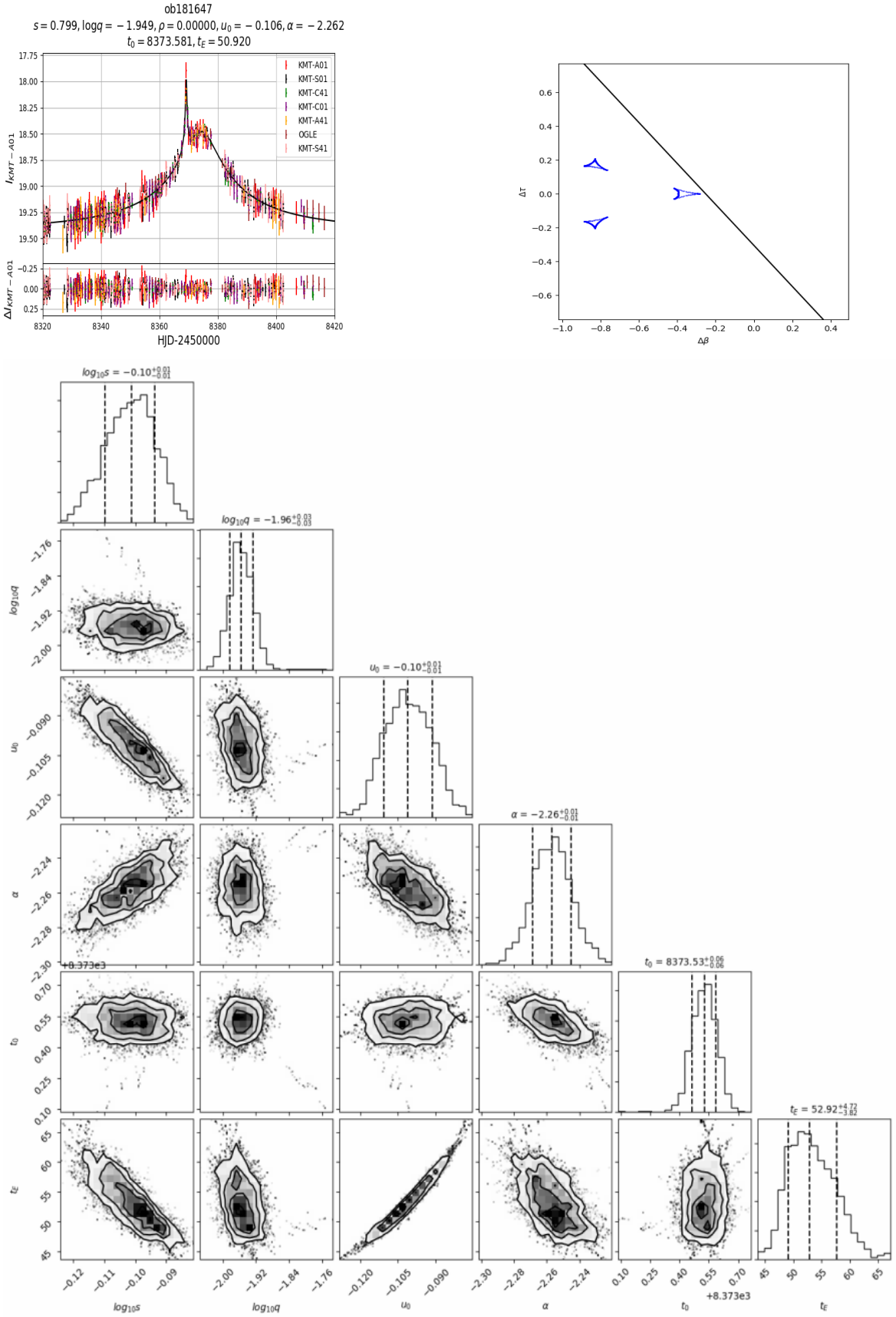

Figure 6.5: The plots show the fitted model to the light curve when error bars are renormalised, the caustic geometry and the covariance between the model parameters.

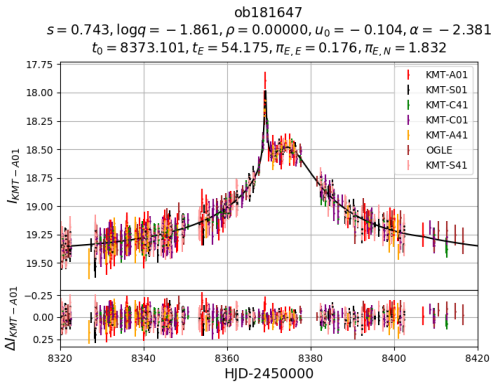

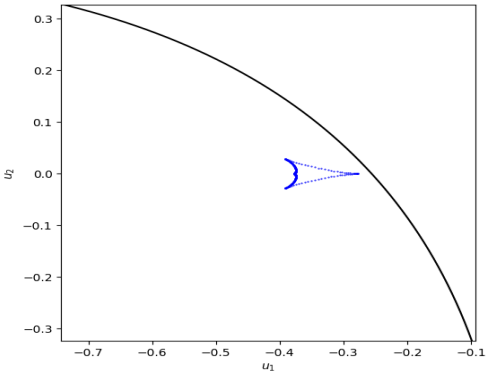

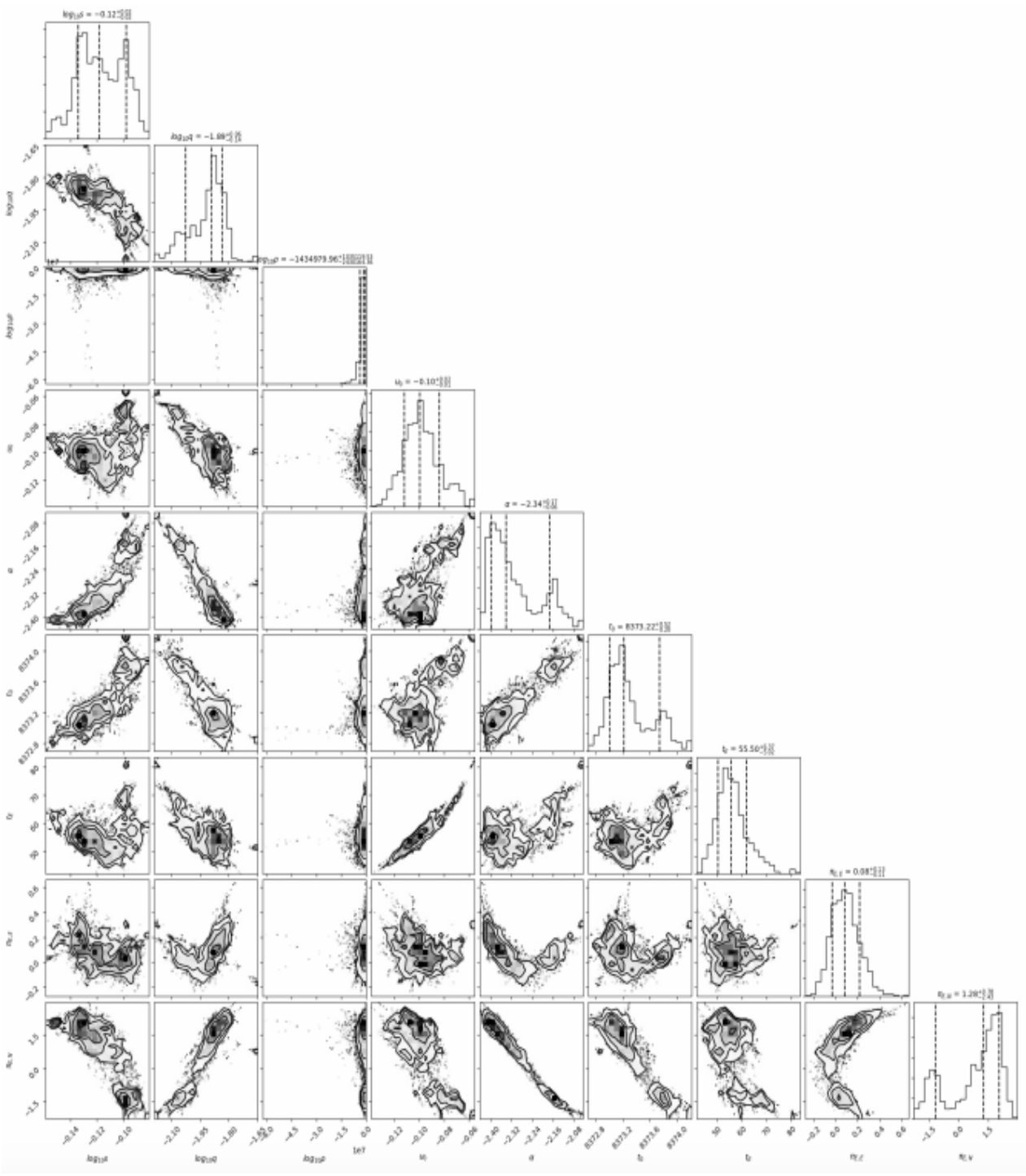

Figure 6.6: Figure showing light curve, caustic and the covariance between the model parameters for P1 model.

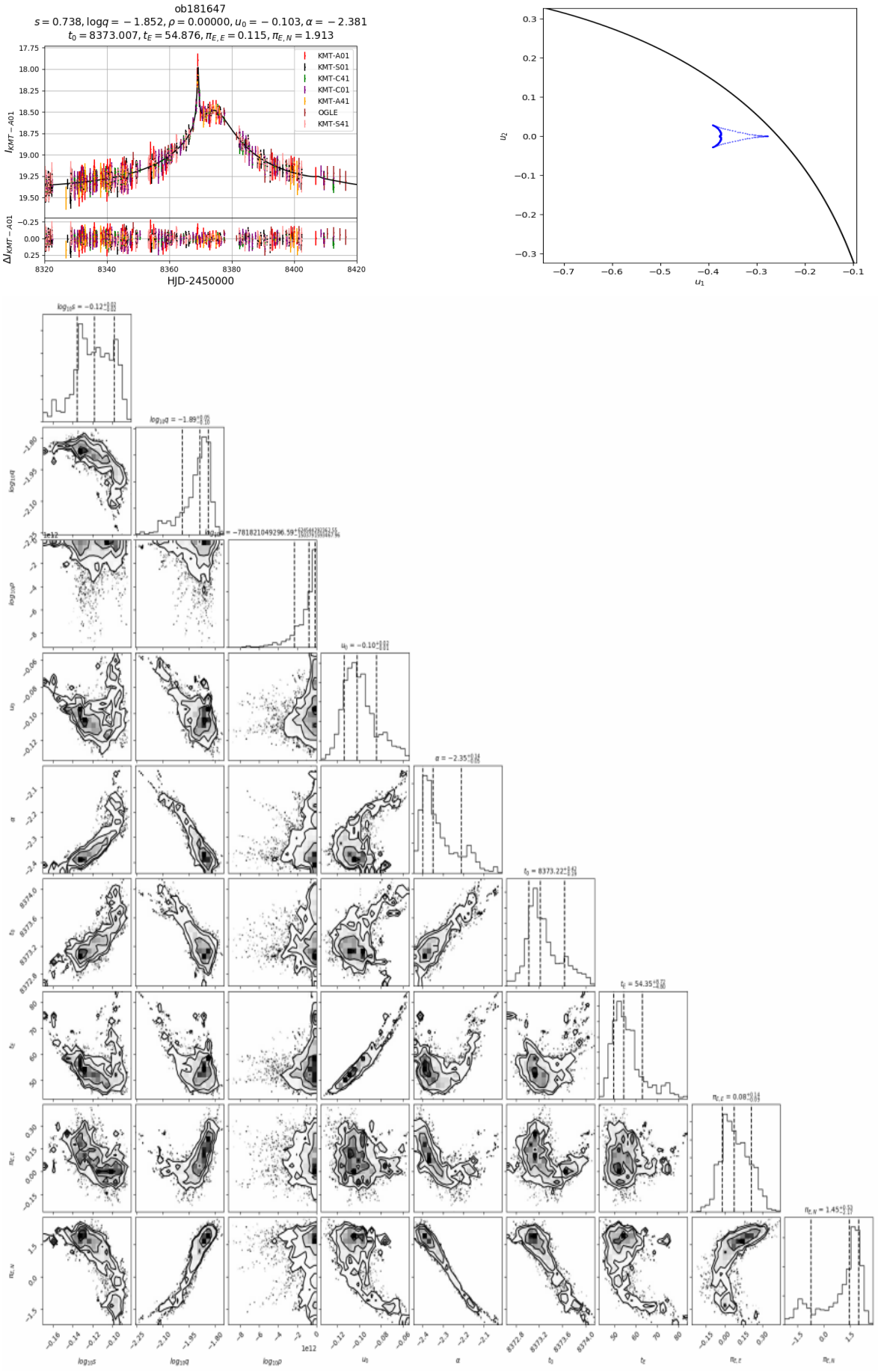

Figure 6.7: Figure showing light curve, caustic and the covariance between the model parameters for P2 model.

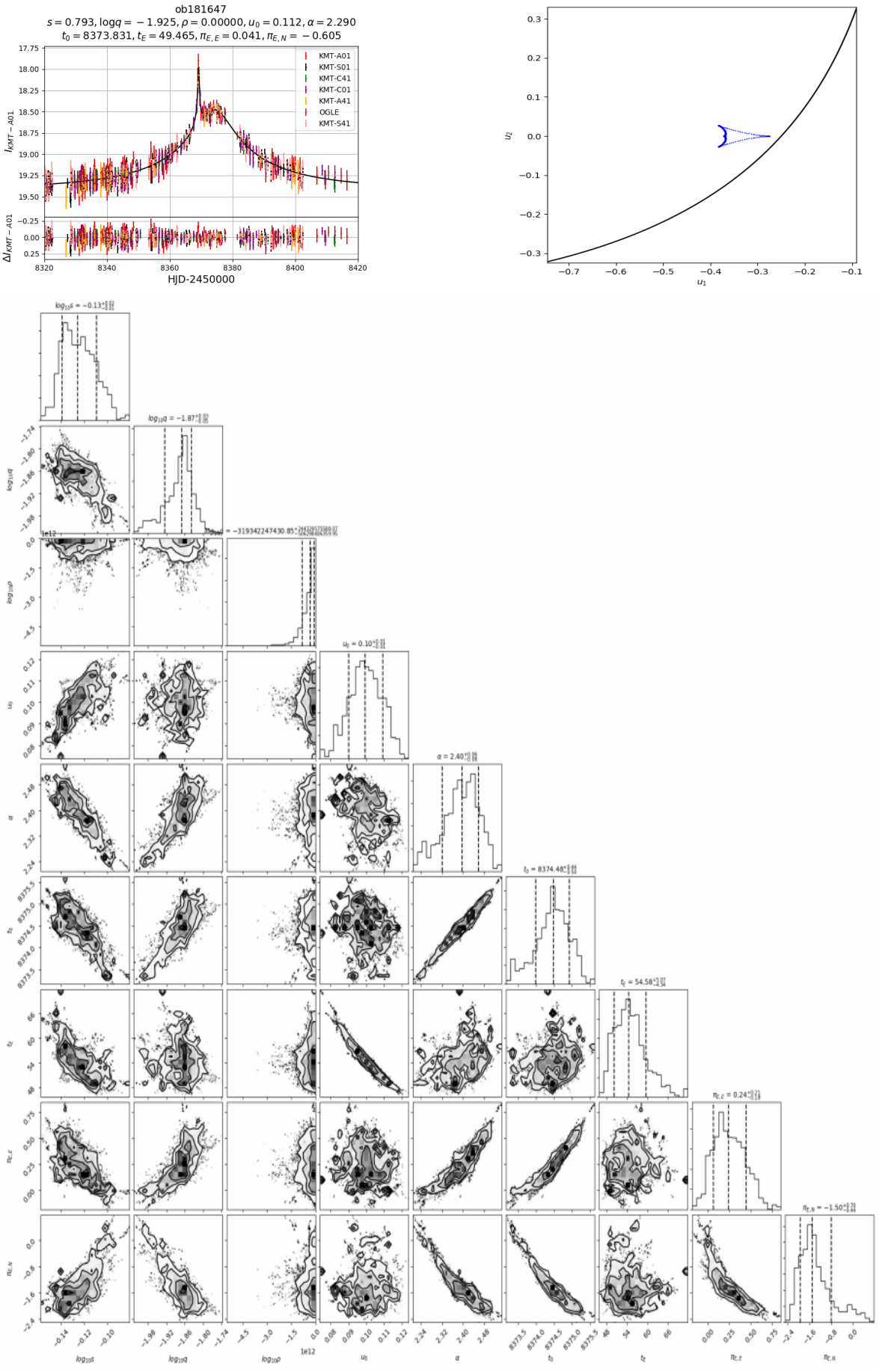

Figure 6.8: Figure showing light curve, caustic and the covariance between the model parameters for P3 model.

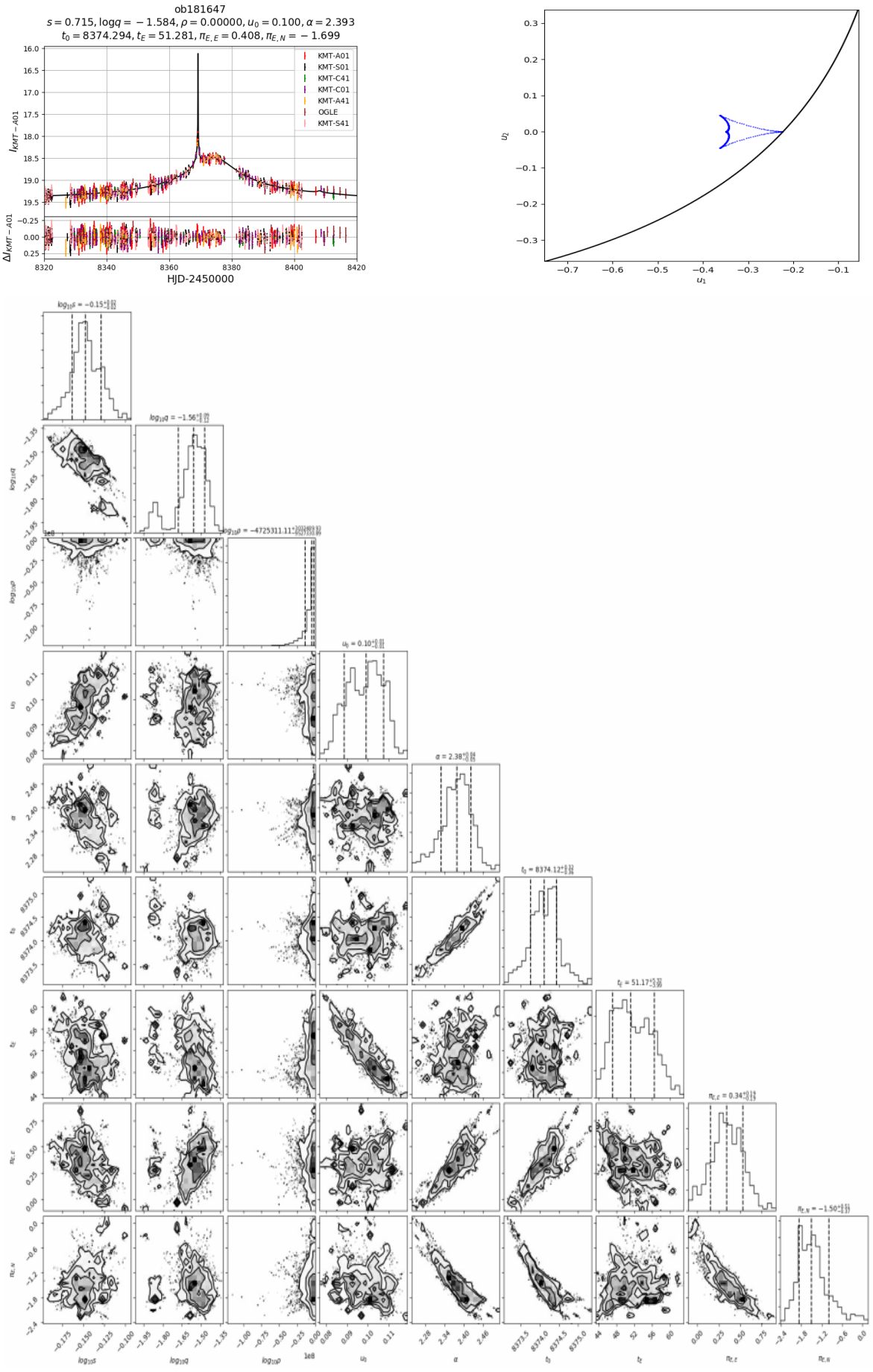

Figure 6.9: Figure showing light curve, caustic and the covariance between the model parameters for P4 model.

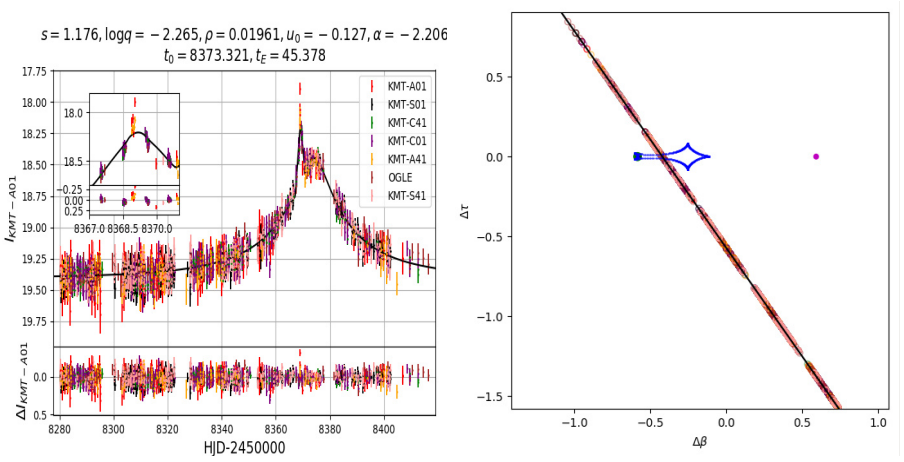

Figure 6.10: The plots show the fitted model to the light curve and the corresponding trajectory through the caustic when s>1. (b) shows the line caustics formed due to two lenses with mass ratio ~ 0.01 and separation ration s ~ 1.2 and the trajectory of the source passing at angle $\alpha = 50^0$ clockwise from $-\Delta\beta$ direction. The *green* dot is the primary lens and the *cyan* dot is the secondary lens. The caustic structure formed is resonant in nature where the planetary caustic is merged with central caustic. This is the reason why there is no close-wide degeneracy.

6.5 Source Properties

The source and blend positions on the CMD are found by their brightness and colour. We form the CMD for the stars in the KMT-C dataset of BLG01 field. The brightness of the source and blend for this dataset is obtained from the fluxes of P1 model (Table (6.3)). To obtain the source colour, we use the difference flux of this data set in I and V bands obtained from pyDIA. We divide the data into time bins of 0.025, 0.05,0.1,0.2 days. We plot the linear relation though I-band vs V-band difference flux in this bins and obtain the source colour (V-I) shown in Figure (6.11). We use the colour in plot 1: $(V - I) = (2.147 \pm 0.071)$ since the time difference between the data points when the event peaks is close to this bin width. pyDIA also gives the colour and brightness of red clump towards this field which enables us to plot the position of the source relative to the red-clump on the CMD. The location of the source on the CMD suggests that it is a low mass dwarf star. However, it is difficult to put a constraint on its location towards the bulge.

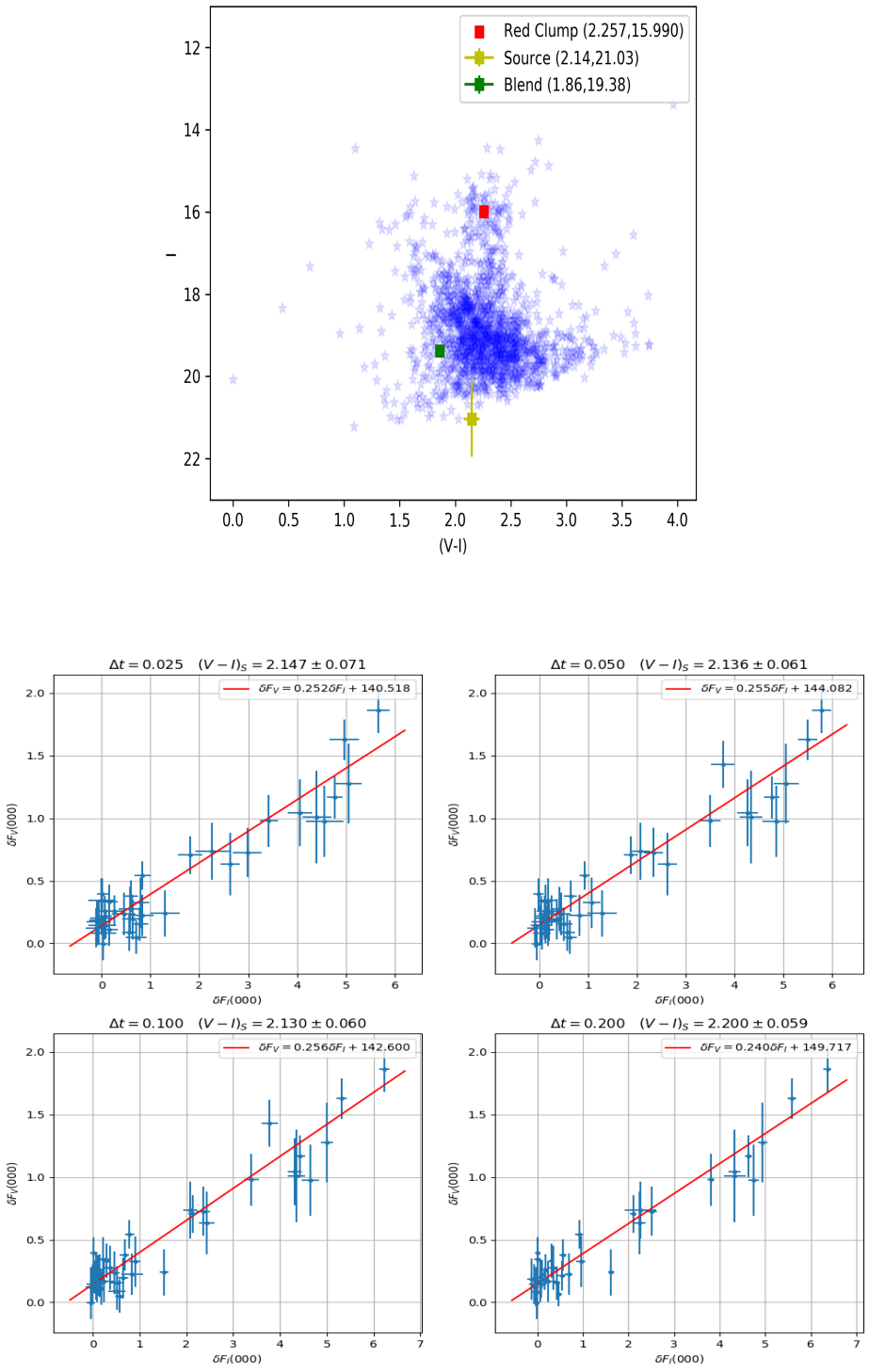

Figure 6.11: The CMD for KMT-C field BLG01 data set. The location of red clump on this CMD is shown in red colour, source in yellow colour and blend in blue colour.

6.6 Galactic Model

The mass and distance to the lens cannot be determined analytically because we do not measure ρ in any of the models. Parallax is only marginally detected and it provides very little constraint on the lens mass and distance via the galactic model. The only useful information we have about the event is t_E. We form the galactic model as described in Chapter (2) and investigate the lens properties of the P1 model first by keeping the source distance and the lens distance as a free parameter. We find that the galactic model gives the source to be located in the bulge and the lens to be located either in the disc or bulge. Therefore, assuming the source to be located in the bulge, we evaluate the galactic model separately for the disc and the bulge location of the lens. We find that there is 70% probability that the lens is located in the disc. Similarly we evaluate the galactic model for P2 and P3 models and we find that the lens is there is 90% and 88% chance that the lens lies in the disc. In Table (6.4), we show the 16^{th}, 50^{th} and 84^{th} percentile values of the lens mass, lens distance and source distance corresponding to each solution and displayed the galactic model results for each solution in Figure (6.12).

Lens Parameters for model P1		
Parameter	*DLBS*	*BLBS*
Mass of the system (M)	$0.08^{+0.16}_{-0.06} M_{\odot}$	$3.90^{+7.42}_{-2.97} M_J$
Mass of primary ($M_{primary}$)	$0.08^{+0.16}_{-0.06} M_{\odot}$	$3.85^{+7.32}_{-2.94} M_J$
Mass of secondary ($M_{secondary}$)	$1.72^{1.96}_{-0.73}$ M_J	$0.05^{0.09}_{-0.04}$ M_J
Distance to the Lens (D_L)	$1.73^{+0.97}_{-0.78}$ kpc	$7.29^{+0.52}_{-0.53}$ kpc
Lens Parameters for model P2		
Parameter	*DLBS*	*BLBS*
Mass of the system (M)	$0.03^{+0.14}_{-0.02} M_{\odot}$	$4.39^{+8.45}_{-3.29} M_J$
Mass of primary ($M_{primary}$)	$0.03^{+0.14}_{-0.02} M_{\odot}$	$4.33^{+8.34}_{-3.25} M_J$
Mass of secondary ($M_{secondary}$)	$0.40^{+1.60}_{-0.24}$ M_J	$0.05^{0.10}_{-0.04}$ M_J
Distance to the Lens (D_L)	$1.84^{+0.92}_{-0.79}$ kpc	$7.29^{+0.52}_{-0.53}$ kpc
Lens Parameters for model P3		
Parameter	*DLBS*	*BLBS*
Mass of the system (M)	$0.06^{+0.06}_{-0.03} M_{\odot}$	$3.49^{+3.19}_{-1.59} M_J$
Mass of primary ($M_{primary}$)	$0.06^{+0.06}_{-0.03} M_{\odot}$	$3.45^{+3.15}_{-1.57} M_J$
Mass of secondary ($M_{secondary}$)	$0.79^{+0.75}_{-0.41}$ M_J	$0.04^{+0.04}_{-0.02}$ M_J
Distance to the Lens (D_L)	$1.63^{+1.01}_{-0.78}$ kpc	$7.29^{+0.51}_{-0.52}$ kpc

Table 6.4: Lens mass and distance for the disc or bulge location of the lens for model P1, P2 and P3 from top. DLBS is disc lens and bulge source while BLBS is bulge lens and bulge source.

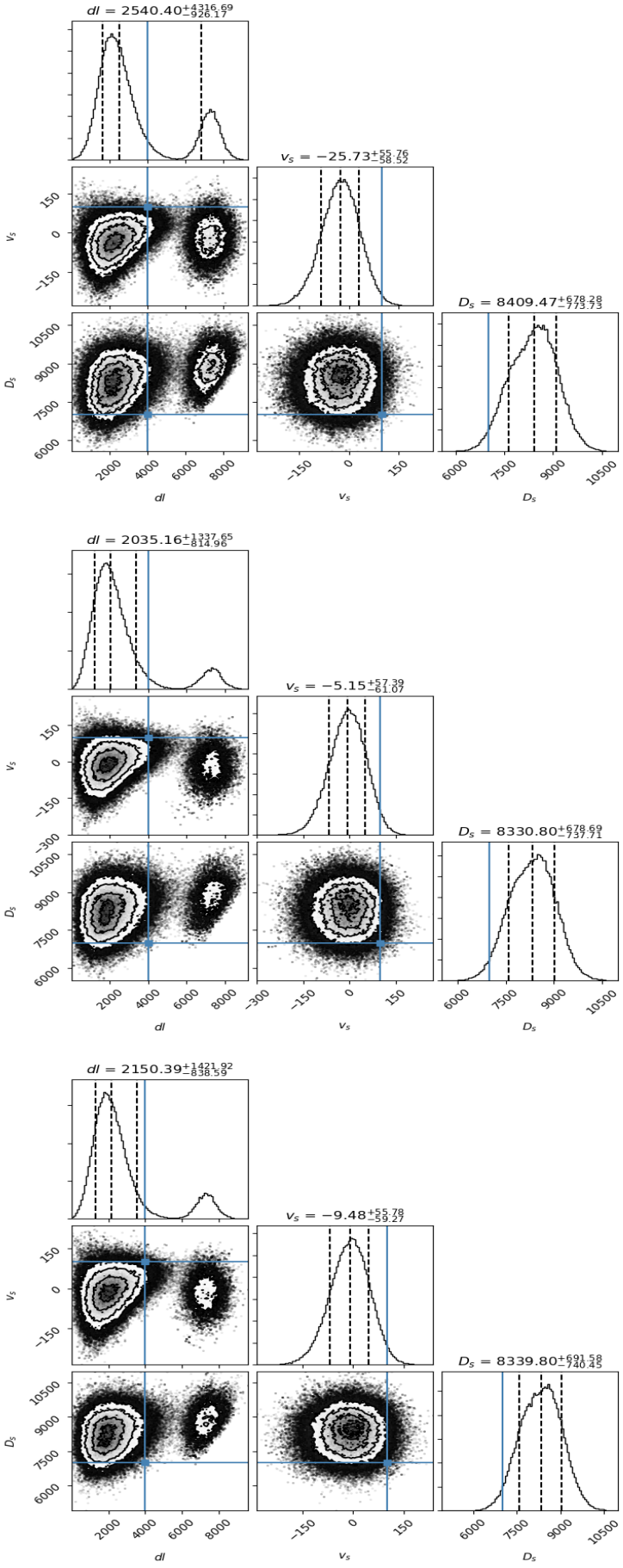

Figure 6.12: The bimodal lens distribution for P1, P2 and P3 models consecutively from top left.

6.7 Discussion

In this chapter I have analysed the non-caustic crossing binary lens event $OGLE-2018-BLG-1647$. The photometry of this event was affected due to the close proximity of the moon to the bulge during the event. However when these images were reduced with pyDIA software, the data points affected by moonlight were filtered out as described. The renormalisation of error bars changed the best fitted binary lens model since the error bars of data uncertainties gives equal weight to each data set by forcing $\chi^2/dof \sim 1$. Thus, this event shows the importance of renormalisation of uncertainties for binary lens events where the source crosses the caustic or passes close to it. This becomes further important when the photometry is affected by the non-systematics like moonlight. The t_E of this event is ~ 55 days, and orbital parallax effect with jerk-parallax degeneracy was detected. To explore the degenerate solutions of jerk-parallax degeneracy in binary lens microlensing events, asymmetry in the magnification pattern was taken into account and the four degenerate solutions were found by the substitution (u_0, α, π_{EN}) $\rightarrow (u_0, \alpha, -\pi_{EN})$, $(u_0, \alpha, \pi_{EN}) \rightarrow (-u_0, -\alpha, \pi_{EN})$ and $(u_0, \alpha, \pi_{EN}) \rightarrow (-u_0, -\alpha, -\pi_{EN})$. In the light curve, although the high magnification bump is due to source passing close to the central caustic of the close binary lens system, we find that there is no wide binary solution for this event. The reason is for events suffering close-wide degeneracy, other model parameters like u_0, t_0, t_E, ρ and α should remain the same. In this case the degeneracy is broken because the wide solution does not give a proper fit to the light curve. The evaluation of the galactic model based on the t_E and weakly detected π_E for the highly degenerate P1, P2 and P3 model yields a sub-Jupiter mass orbiting a sub-stellar mass host in the disc or a sub-Jupiter mass planet orbiting a super-Jupiter in the galactic bulge although the galactic model favours the disc location of the lens. Though it is difficult to constrain the mass of the lens and distance to the lens when parallax is weakly detected, this type of galactic model analysis yields an approximation for the lens mass and distance. Referring to the CMD formed by the stars in BLG01 field of KMT-C dataset, the position of the source and blend suggests that the event is heavily blended. It is very difficult to constrain the source distance using high resolution telescopes as it is very faint. Also the primary lens being a sub-stelllar object, it is unlikely to resolve the lens and the source in future. However, we are able to approximate the lens mass and distance assuming the source in the bulge.

Chapter 7

Analysis of the event OGLE-2018-BLG-0380

In this chapter, I present the analysis for the event $OGLE-2018-BLG-0380$. This event has two prominent peaks and a small perturbation ($\sim$ 2 days) towards the decreasing side of the light curve. Such a perturbation is typical of a typical Jupiter mass planet. However, there are some events where anomalous signatures can be explained by a close binary model (Albrow et al., 2002, Han et al., 2016, Udalski et al., 2015a). I show that for the event $OGLE-2018-BLG-0380$, a close binary model with the individual lenses in orbital motion is the only possible solution to explain the light curve.

7.1 Observations and Data reductions

7.1.1 OGLE

$OGLE-2018-BLG-0380$ was the 380^{th} event detected by the Early Warning System (EWS) of Optical Gravitational Lensing Experiment (OGLE) in the year 2018. It was observed towards $(R.A., Dec) = (17:53:26:55, -28:56:12.7)$ in galactic bulge by the 1.3m Warsaw Telescope by the Las Campanas Observatory in Chile (Udalski et al. (2015a)) in the field 500.02 of OGLE. Galactic co-ordinates for this event are $(l, b) = (0.87918910^o, -1.46833704^o)$. [1].

[1] https://ned.ipac.caltech.edu for the conversion to galactic co-ordinates

7.1.2 KMTNet

This event was separately observed by the Korean Microlensing Telescope Network (KMTNet) through its three 1.8m telescopes in Chile, South Africa and Australia (Kim et al., 2016). OGLE-2018-BLG-0380 was observed in their fields BLG02 and BLG42.

7.2 Data Reductions

The KMTNet images in I and V band for the field BLG02 and BLG42 were reduced using the pyDIA software Albrow (2017), which uses a difference image analysis based on the delta-basis-function approach of Bramich et al. (2013). After reducing the KMTNet images, it was found that the photometry of the BLG42 field was poor as the source star lies in the corner of most of the images except for CTIO. This was even the case with the pysis photometry available on KMTNet internal webpage [2]. Thus the photometry of the BLG02 field and the photometry of BLG42 field only with CTIO data was used in the modelling. pyDIA provides the photometry of the micro-lensed star in 10 columns viz. time in JD, difference flux, uncertainties corresponding to difference flux, apparent magnitude, uncertainty in apparent magnitude, quality factor of data, full width at half maximum (FWHM) of the star, PSF of the star, roundness of the star on the image, sky quality during observation and the signal strength of the source star. The reduced photometric data was filtered based on these columns for each dataset. For the SSO-A02 the data points having sky level less than 2800, signal greater than 400, FWHM less than 3.5 and quality factor larger than 1.25, were selected. For CTIO-BLG02, signal level greater than 380, FWHM less than 3.0 and quality factor less than 2.5 were selected. For CTIO-BLG42, FWHM less than 2.2 and an additional criteria with sky level less than 2500 was set for selection. For SAAO-BLG02, the data points having sky level less than 4500 and signal larger than 400 were selected. Similarly for V-band, the data points for CTIO-BLG02 and SAA0-BLG02, the data points having FWHM less than 2.8 and roundness number of the star less than 2 were selected. Since the time stamp for these images was in 2450000 - Julian Days (JD), the time of observation was converted to 2450000 - Heliocentric Julian Days (HJD).

The OGLE photometry was downloaded from the EWS page for Microlensing [3]. The event had good coverage from all the telescope sites. However, the third peak which is also the smallest peak, was covered only by KMTNet sites. KMTNet data therefore proved critical in this analysis to constrain the physical parameters of the lens.

[2] http://kmtnet.kasi.re.kr/ ulens/kyuha/internal/2018/view.php?event=OB180380
[3] http://ogle.astrouw.edu.pl/ogle4/ews/

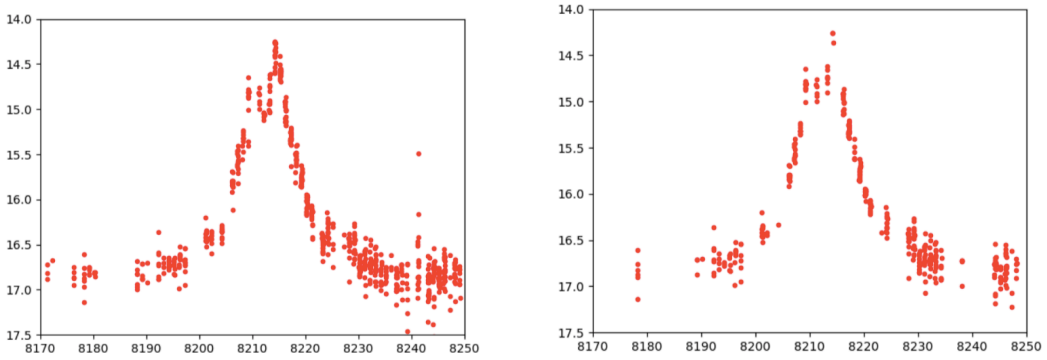

Figure 7.1: The raw and filtered photometry of KMT-SS0 BLG02 field. This photometry dataset is also discarded from the analysis of the event.

After plotting the light curve, a few outliers were discovered and removed manually from the datasets. The OGLE data points at HJD-245000 = 8202.74453, 8193.88795 and 8245.73694, KMT-SAAO data points at 8209.50097, KMT-CTIO BLG42 data points at 8203.88835, 8205.78133, 8208.80707, 8212.91786 and 8224.78738 were removed as outliers. It was noticed that in spite of thorough filtering, the KMT-SSO dataset for BLG02 field did not yield a good light curve - see Figure (7.1). So we decided to exclude it from the analysis. In the chapter, the names for KMT-CTIO BLG02 field is KMT-C02, KMT-CTIO BLG42 field is KMT-C42 and the name for KMT-SAAO BLG-02 is KMT-S02.

Number of data points per observatory and corresponding band of observations		
Observatory	Number of Data points	Band
OGLE	1378	I
KMT-C02	531	I
KMT-C42	464	I
KMT-S02	426	I
KMT-SV	36	V

Table 7.1: The table showing number of data points for each dataset used for modelling corresponding to each observatory.

7.3 Analysis

7.3.1 PSPL Model

The light curve clearly shows two distinct peaks with a third on the declining shoulder that is smaller in magnification. Clearly this could have been produced by a close binary system which has a central caustic and two planetary caustics (Han, 2006). The PSPL model fitted to this light curve (Figure (7.3)) yields the standard Paczyński parameters given in Table (7.2).

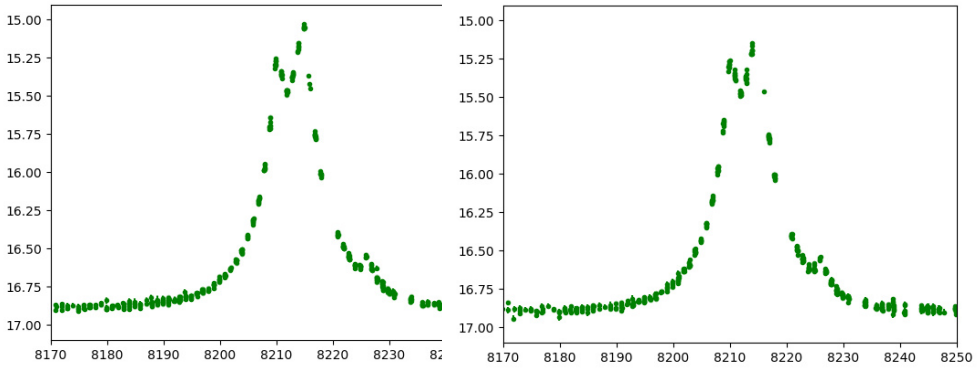

(a)Filtered light curve for KMT-C02. (b)Filtered light curve for KMT-C42.

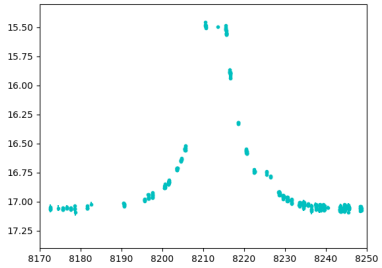

(c)Filtered light curve for KMT-S02.

Figure 7.2: The final filtered light curves used in the modelling.

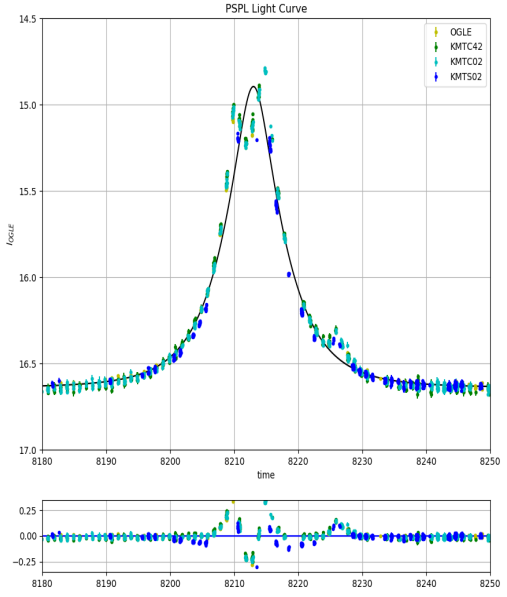

Figure 7.3: The plots show the PSPL model fit to the light curve and.

Parameters and uncertainties of the PSPL fit	
Parameter	Value
χ^2	6330.30
u_0	0.3245 ± 0.0036
t_0	8213.0 ± 0.0059
t_E	7.852 ± 0.0010

Table 7.2: The table showing PSPL fit parameters with their uncertainties to the light curve.

7.3.2 Binary lens Model

Since the PSPL model to the light curve did not yield a proper fit a binary lens model was explored. The HJD-2450000 times of the three peaks in the KMT-C02 dataset are: 8209.91370, 8214.77237 and 8225.83918. The grid search was performed first around top two peaks and then around second and the third peak. However, both the grid searches yield different solutions with majority of least χ^2 solutions on the wide separation side (Figure (7.4)). These grid search solutions with minimum χ^2 were seeded to MCMC to find the parameters a global χ^2 minimum. It was found that all the subsequent converged solutions produced models that passed through the top two peaks of the light-curve and failed to recognise the third short peak. Some of the solutions are shown in Figure (7.5).

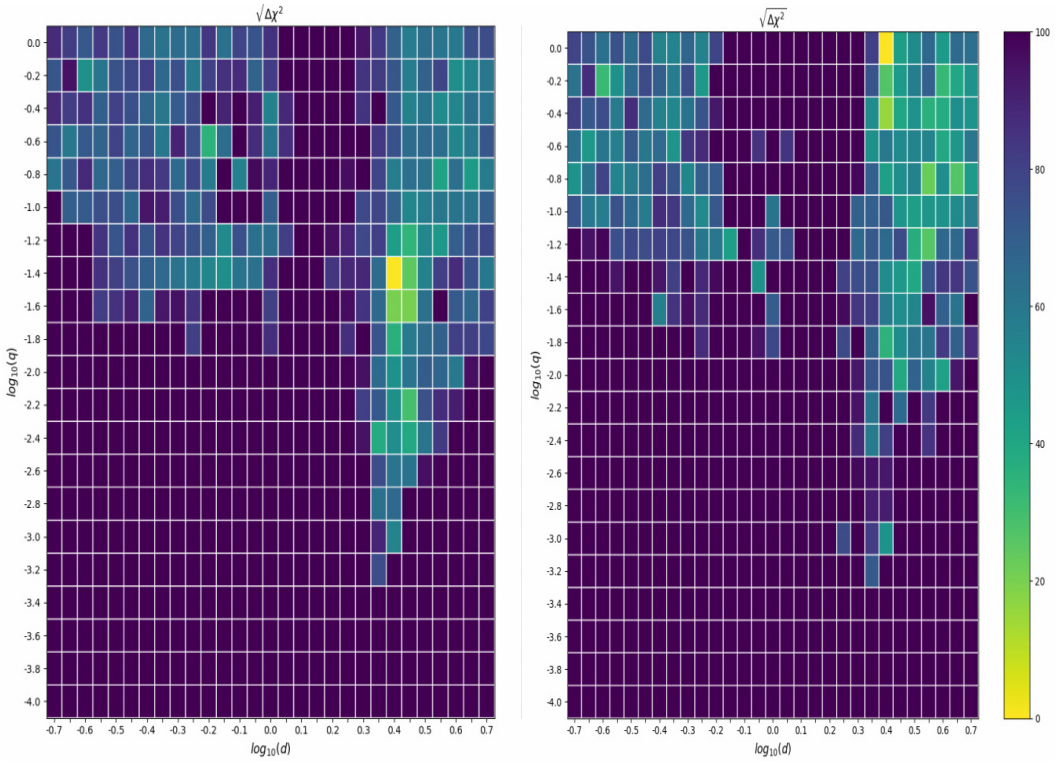

Figure 7.4: Plots showing grid search in dq plane. The left grid is when the top two peaks are considered while performing the grid search and the right grid is when the second and the third peaks are considered.

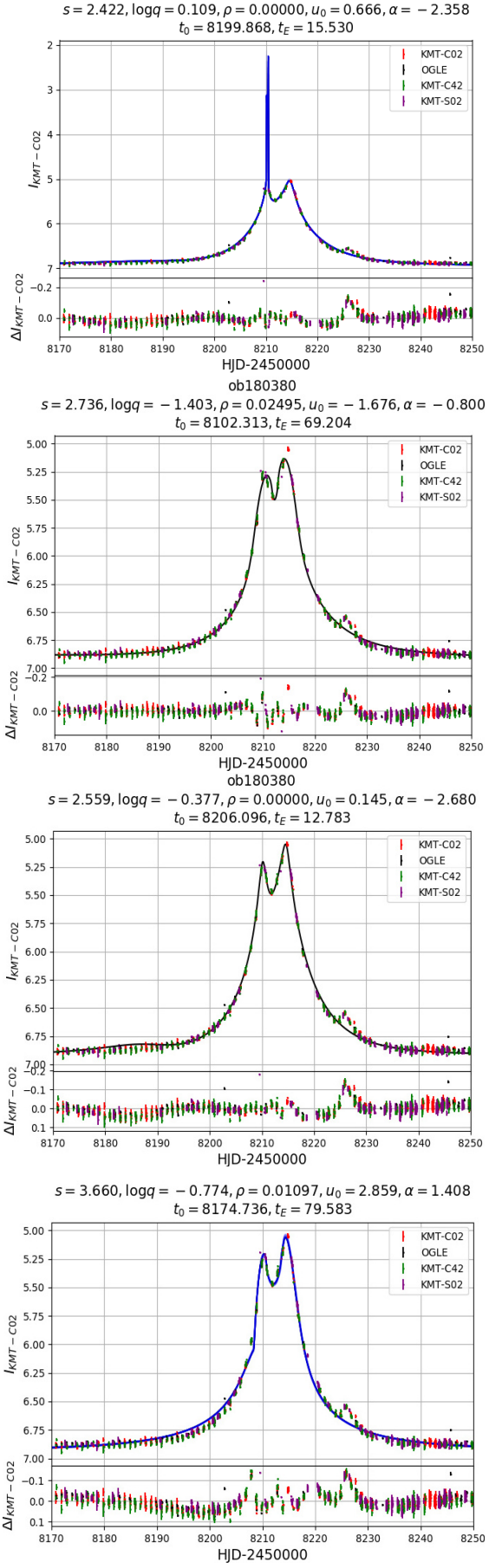

Figure 7.5: Plots showing the light curve when the minimum χ^2 points on the grids are further minimised by MCMC .

Clearly the grid search method failed to identify the model with three peaks. Therefore a heuristic analysis was done to find a suitable model.

7.3.3 Heuristic analysis

Heuristic analyses of the lightcurves has been performed previously by Hwang et al. (2018, 2019), Skowron et al. (2018) and others. A heuristic analysis of the light curve involves guessing the model parameters from the nature of the light curve. When seeded to MCMC, these parameters may yield a global minimum of χ^2 for the model fitted to the event. Determining the model parameters is direct from the light curve if the source crosses the caustic, but the microlensing event $OGLE-2018-BLG-0380$ seems feature cusp approach event rather than caustic crossings. Therefore the method for heuristic analysis does not work in the form used by the previous authors. From the nature of the light curve and separation between the two main peaks ($\sim$ 4.85 days), it can be seen that the source approaches a cusp of the caustic structure and it takes 4.85 days to traverse from one cusp to the other. Also, the second peak is higher than the first peak which indicates that the the source approach to second cusp is closer. The third perturbation is 12 days away from t_0 (from PSPL model) which indicates that the first two peaks may be due to the central caustic of a close binary lens and the third peak due to a planetary caustic. After a few trials, a close binary caustic with d=0.6 and q = 0.06 was found to match the first two peaks. These values were chosen after referring to Chung et al. (2005), Han (2006) and doing the trials in the changes in caustic structures according to d and q, especially the distance of the planetary caustic structures from binary axis. Having the Paczyński parameters from the PSPL fit, the value of ρ was chosen to be 0.003 (corresponding to a large source) as the peaks were smooth and the value of ϕ i.e. the angle at which the source trajectory cuts the binary axis was chosen by trials to get the third bump. The caustic and the model formed by these parameters before and after convergence with emcee is shown in Figure (7.6).

The heuristic model also misses the third peak after convergence. The solution to this problem was explored by employing binary lens orbital motion. Looking at the caustic with converged parameters, the third bump can be reinstated if the rectilinear trajectory bends to intersect the lower of the two planetary caustics. Since orbital motion of the binary lens manifests itself as change in the separation of the lens (which changes the caustic shape) and change in the effective trajectory looking at the caustic structure and the source trajectory (Figure (7.6)), the non-rectilinear trajectory that bends in such a way that it passes through the magnification region of the planetary caustic to produce

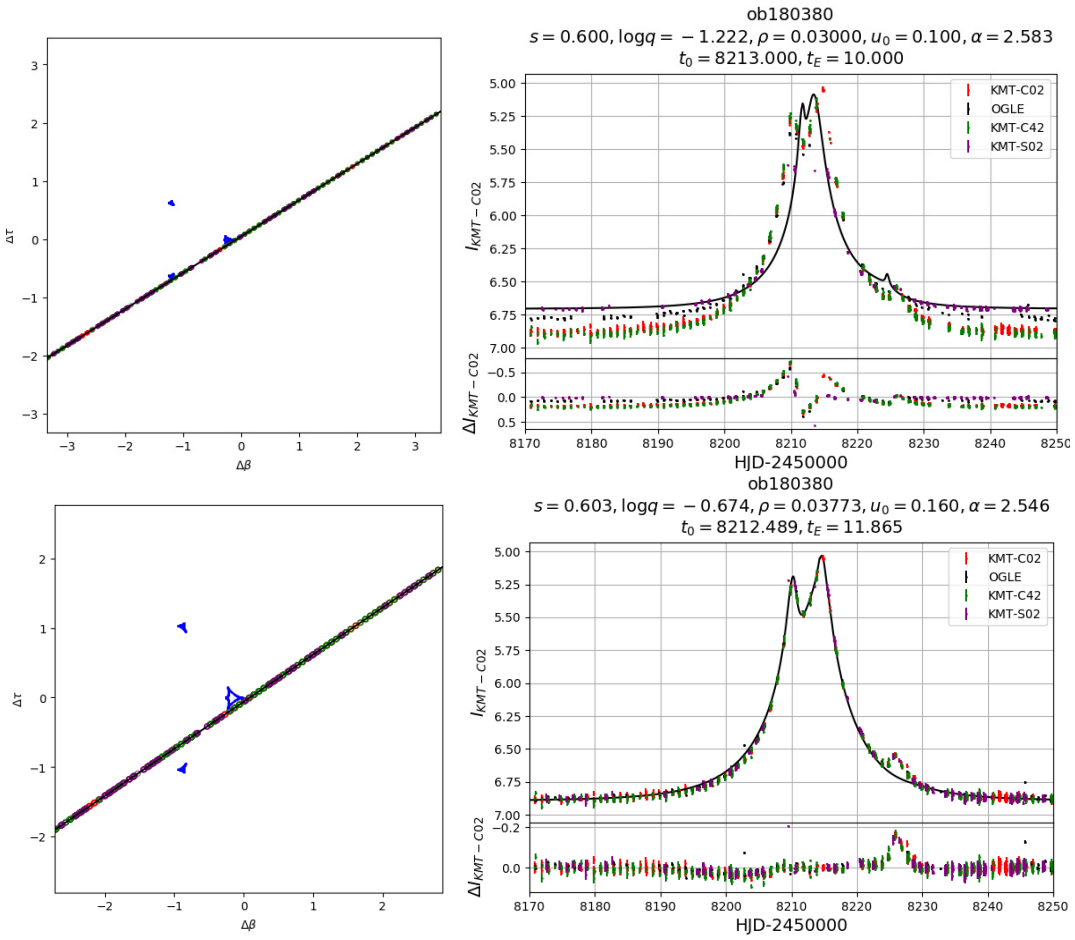

Figure 7.6: The top plots show the heuristically found parameters and the corresponding caustic and light curve. The bottom plots showing the caustic and light curve when the heuristic parameters are seeded and converged using MCMC.

a third deviation was found.

For this, a grid search was performed in the orbital motion ($\dot{\alpha}$) plane minimising the χ^2 while holding the static binary parameters constant. In the grid search, $\dot{s}$ was also kept constant at 0.0. In the grid search, the caustic structure yielded the value of $\dot{\alpha}$ = -0.5552764 radians per year. When the model was then converged using emcee, this value of $\dot{\alpha}$ did not yield a model with a third bump in the light-curve. A probable reason for this might be that the caustic structure also changes when the binary lens orbital motion is included. We therefore inspect the trajectory and manually find the value of $\dot{\alpha}$ heuristically. Seeing that a deviation $\sim 10^0$ required for the trajectory to cut the planetary caustic, from equation (1.34) we get (α - α_0) = $15 \times \frac{\pi}{180} = \dot{\alpha} \times t_E$. Converting the value of this $\dot{\alpha}$ to per year, we get $\dot{\alpha}$ = 6.37 per year. Seeding $(\dot{s}, \dot{\alpha})$ =(0.0, 6.37) to MCMC, the model which fits the observed light curve is obtained (Figure 7.8).

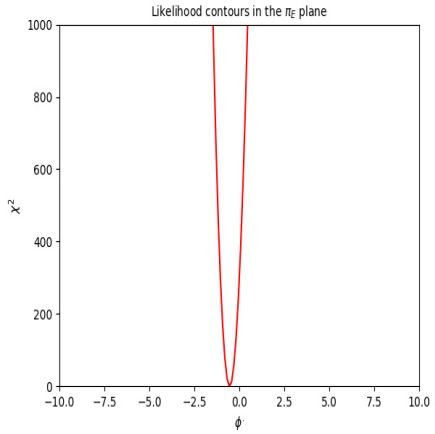

Figure 7.7: The grid search in lens orbital motion plane minimising chi^2. The value of $\dot{\alpha}$ for which the χ^2 is minimum is -0.5552764.

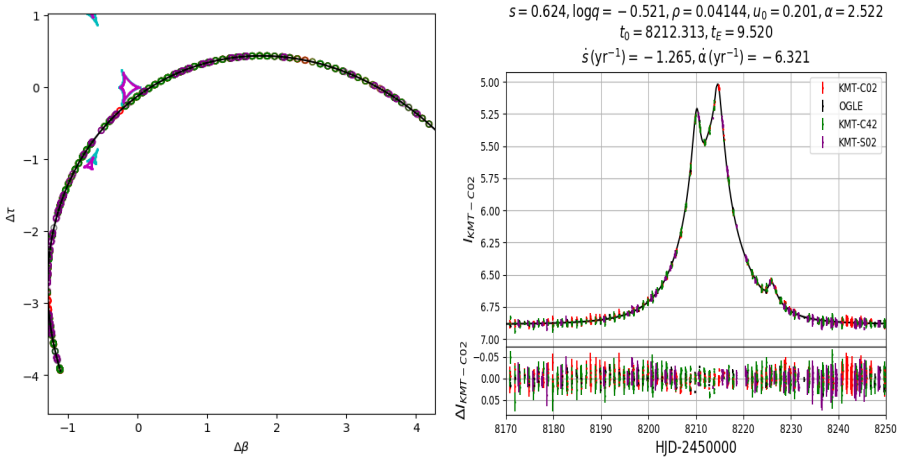

Figure 7.8: The plots show the caustic and fit to the light curve when the orbital motion parameters found by doing a grid search in the orbital motion plane are seeded and converged using MCMC.

7.3.4 Renormalisation of Uncertainties in magnitude

We renormalised the uncertainties based on the best fitted model described in the previous sub-section. We use procedure described in section (1.6) and equation (1.35) to renormalise the uncertainties in magnitudes for the different data sets used in the modelling. The values of κ and e are given in Table (7.3). Using these modified uncertainties, we re-run MCMC with the best solution. Figure (7.9) shows the best fit model to the light curve and Table (7.4) shows the best fit parameters with their uncertainties.

Parameters to renormalise the uncertainties		
Observatory	κ	e
$KMT-C02$	0.26695	0.04502
$KMT-C42$	0.32051	0.07174
$KMT-S02$	0.39219	0.03027
$OGLE$	0.00575	3.91259

Table 7.3: The table showing the parameters e and κ such that $\chi^2/dof\ sim\ 1$.

7.3.5 Including Orbital Parallax

After renormalising the uncertainties, the data sets give equal weightage to the model. We now investigate the effect of orbit of the earth present in the light curve. We add two extra parameters $(\pi_{EE}, \pi_{E,N}) = (0.0,0.0)$ to the model and explore the parameter space. It is however found out that χ^2 only improved by 0.14 which is not significant. The values of model parameters for the best fit model without renormalisation of uncertainties, best fit model with renormalisation of uncertainties and orbital parallax included in the best fit model are displayed in Table (7.4).

Parameters and uncertainties of fitted models			
Parameter	P1	P2	P3
χ^2	6185.54	1312.33	1312.19
u_0	$0.20^{+0.001}_{-0.001}$	$0.19^{+0.001}_{-0.002}$	$0.23^{+0.004}_{-0.005}$
t_0	$8212.31^{+0.10}_{-0.15}$	$8212.33^{+0.01}_{-0.01}$	$8212.56^{+0.25}_{-0.35}$
t_E	$9.52^{+0.03}_{-0.03}$	$9.76^{+0.06}_{-0.06}$	$9.74^{+0.07}_{-0.08}$
s	$0.63^{+0.01}_{-0.01}$	$0.610^{+0.01}_{-0.01}$	$0.61^{+0.01}_{-0.01}$
q	$0.30^{+0.01}_{-0.01}$	$0.29^{+0.01}_{-0.01}$	$0.28^{+0.01}_{-0.01}$
$log\rho$	$-1.38^{+0.01}_{-0.01}$	$-1.42^{+0.02}_{-0.02}$	$-1.43^{+0.02}_{-0.02}$
ϕ	$2.52^{+0.02}_{-0.02}$	$2.53^{+0.01}_{-0.02}$	$2.51^{+0.02}_{-0.01}$
$\dot{s}$	$-1.26^{+0.07}_{-0.06}$	$-0.82^{+0.10}_{-0.11}$	$-0.84^{+0.18}_{-0.20}$
$\dot{\alpha}$	$-6.32^{+0.04}_{-0.04}$	$-6.12^{+0.09}_{-0.09}$	$-6.87^{+1.05}_{-0.82}$
$\pi_{E,E}$	-	–	$0.47^{+0.43}_{-0.66}$
$\pi_{E,N}$	-	–	$-1.63^{-2.33}_{-1.96}$
$f_{s,OGLE}$	2208.43 ± 2.61	3.36 ± 0.02	3.37 ± 0.02
$f_{s,KMT-C02}$	29291.48 ± 15.31	2.793 ± 0.001	2.803 ± 0.002
$f_{s,KMT-C42}$	29251.37 ± 19.63	2.801 ± 0.001	2.811 ± 0.001
$f_{s,KMT-S02}$	23900.87 ± 20.26	2.271 ± 0.002	2.281 ± 0.002
$f_{b,OGLE}$	4.35 ± 3.67	3.67 ± 0.02	0.12 ± 0.02
$f_{b,KMT-C02}$	- 1407.11 ± 29.59	-0.006 ± 0.005	-0.023 ± 0.005
$f_{b,KMT-C42}$	-1513.49 ± 37.17	-0.03 ± 0.00	-0.042 ± 0.006
$f_{b,KMT-S02}$	-262.16 ± 28.58	0.078 ± 0.003	0.081± 0.005

Table 7.4: The table showing model and fit parameters with their uncertainties to the light curve of OGLE-2018-BLG-0380. P1 is the best solution, P2 is the best solution after renormalising uncertainties in magnitudes and P3 is the best model after including orbital parallax.

7.3.6 Source Star Properties

The values of the source flux and blended flux i.e. f_s and f_b are obtained after fitting the model to each observatory's data set. These values were used to locate the position of the

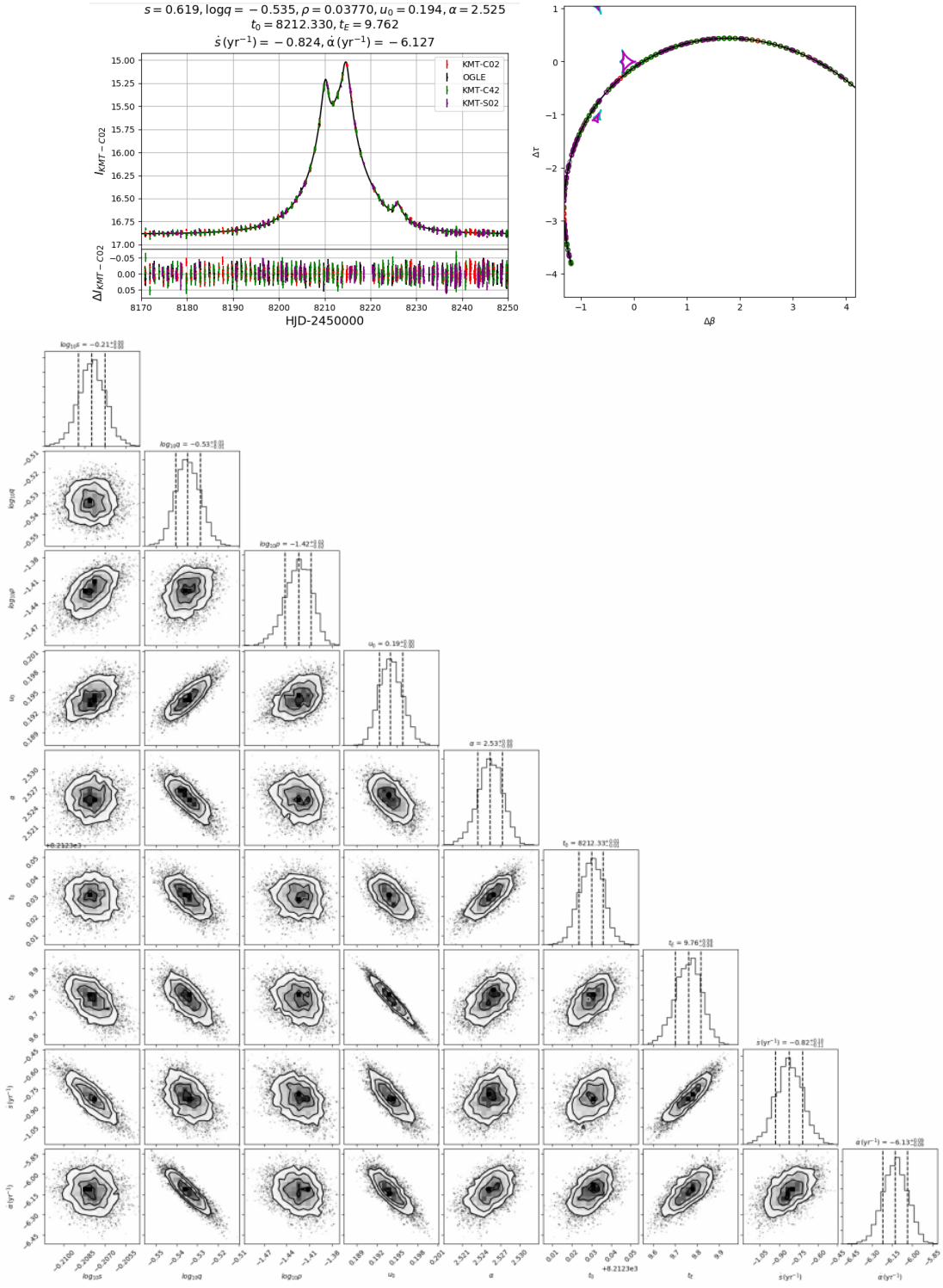

Figure 7.9: The plots show the light curve, trajectory and the marginalised distribution of parameters after renormalising the uncertainties.

source and blend on the Colour Magnitude Diagram (CMD). We consider P1 solution as the best solution and fit the V-band data for the KMT-S02 field to the light curve. The flux parameters obtained after fitting the model to KMT-S02 dataset are used to find the location of the source and blend on the CMD (Table (7.5)). The CMD is formed

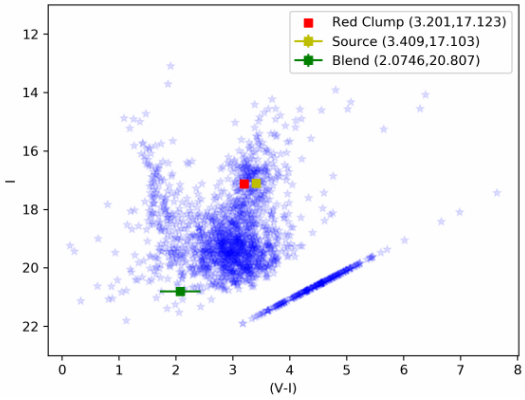

Figure 7.10: The CMD of the KMT-S02 field stars showing the red clump, source and the blend position.

with the stars in KMT-S02 field (Figure (7.10)).

Blend and source flux		
OM+Parallax	F_s	F_b
KMT-S02	2.284 ± 0.005	0.075 ± 0.005
KMT-SV	1813.11 ± 79.510	202.764 ± 100.621

Table 7.5: Source and blend flux with their uncertainties for KMT-S BLG02 field dataset. The diagonal points are the stars that are not resolved or are too faint for the photometry by py-DIA.

In the CMD (Figure (7.10)), it is seen that the blend is fainter and bluer than most of the stars in the BLG02 field of the KMT-S02 dataset. Also the t_E for the event is ~ 9 days which implies a low mass object (Dominik, 1998). The centroid of the red clump in the CMD, was found by pyDIA at $((V-I),I)_{RC,KMT-S02} = (3.201, 17.123)$ and the source was found at $((V-I),I)_{source} = (3.401 \pm 0.04, 17.103 \pm 0.001)$. Referring to the standard values for the red clump by Nataf et al. (2013), $((V-I),I)_{RC,0} = (1.06, 14.396)$, the reddening and extinction towards the direction of the event was calculated to be $(\Delta(V-I), \Delta I) = (2.141, 2.727)$. Thus the de-reddened colour and actual brightness of the source is found to be $((V-I),I)_{0,source} = (1.26 \pm 0.04, 14.376 \pm 0.001)$. In order to obtain the angular source size, the $(V-I)$ colour was converted to $(V-K)$ by using the colour-colour relations of Bessell & Brett (1988). The de-reddened $(V-K)$ colour of the source is found to be (2.8357 ± 0.0694). In order to obtain the angular source size, the $(V-I)$ colour was converted to $(V-K)$ by using the colour-colour relations of Bessell & Brett (1988). Since the position of source star on the CMD suggests it is red giant star, the conversion of $(V-I)$ to $(V-K)$ for giant stars is shown in Table (7.6).

On interpolating between de-reddened $(V-I)$ values for the source star colour, the de-reddened $(V-K)$ colour of the source is found to be (2.8357 ± 0.0694). The angular

Colour relations	
$(V-I)$	$(V-K)$
0.81	1.75
0.91	2.05
0.94	2.155
1.00	2.31
1.08	2.50
1.17	2.70
1.36	3.00
1.50	3.26
1.63	3.60
1.78	3.85
1.90	4.05
2.05	4.30
2.25	4.64
2.55	5.10
3.05	5.96

Table 7.6: Colour relations for conversion between $(V-I)$ to $(V-K)$ from Bessell & Brett (1988).

size of the source is then calculated by using the relation (7.1) given by (Kervella et al., 2004),

$$log2\theta_\star = 0.5410 + 0.2667(V-K)_0 - \frac{V_{source,0}}{5.0} \tag{7.1}$$

Thus, the angular radius of the source ($\theta_\star$) was found to be 7.410 ± 0.175 μas. Since ρ is the angular radius of the source normalised to angular Einstein radius i.e., $\rho = \frac{\theta_\star}{\theta_E}$, we find $\theta_E = 0.177 \pm 0.004$ mas.

7.3.7 Lens Properties

Since we do not detect significant parallax in the event $OGLE-2018-BLG-0380$, we try to infer lens properties from the Bayesian analysis of the galactic model which is constrained by the samples of t_E and θ_E. We form the galactic model priors based on the velocity distribution, density distribution and the Chabrier mass function (see Batista et al. (2011), Chabrier (2003), Jung et al. (2018a), Zhu et al. (2017) and others). In the galactic model, we kept the lens and source distances as well as source velocity to be free parameters. The Bayesian analysis of these priors constrained by the samples of t_E and θ_E gives a bi-modal distribution for the lens distance and it favours the bulge location by 64%. The posterior probability distributions for distance to the lens (D_L), distance to the source (D_s), velocity of the source (v_s) are shown in Figure (7.11). We find the posterior probability of the mass of the lens by using the equation (1.20).

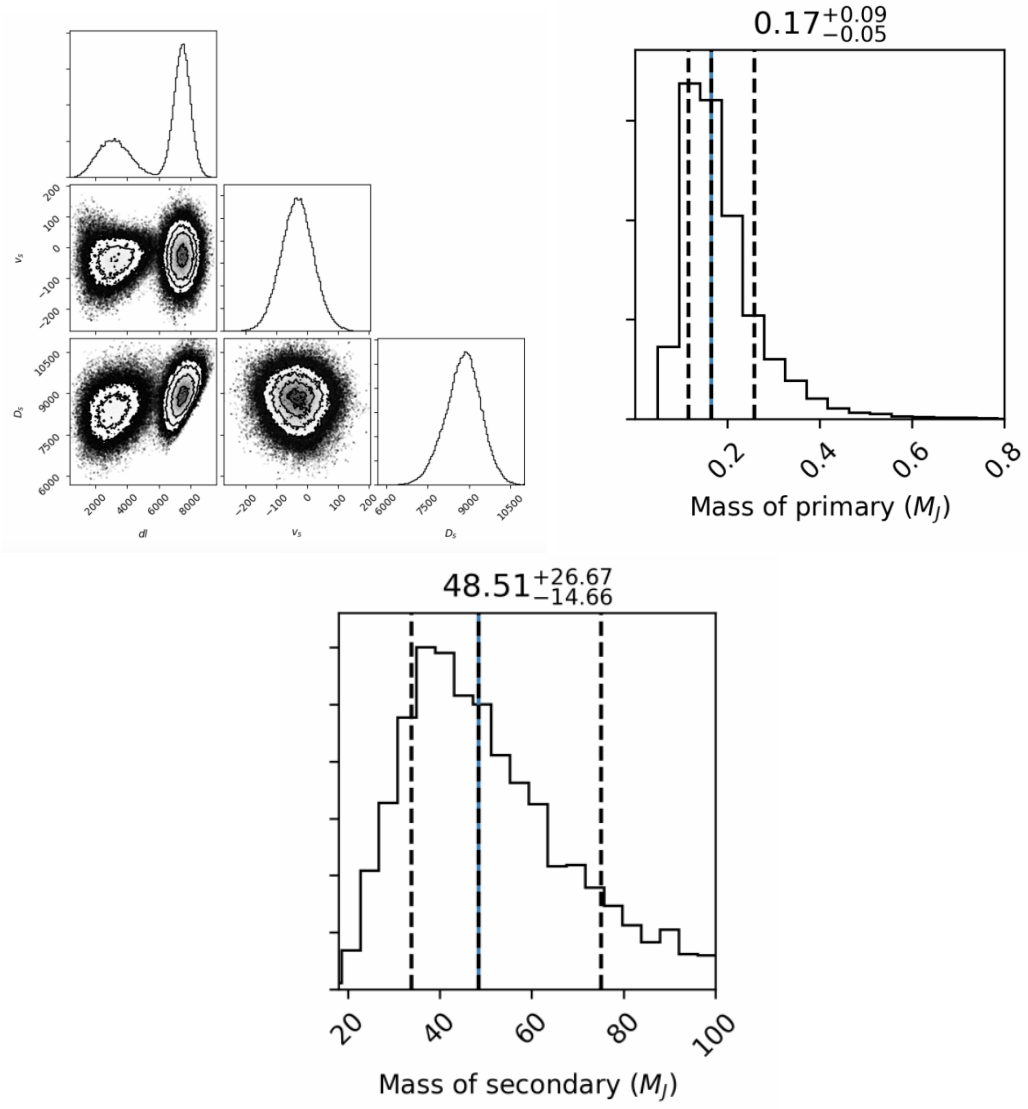

Figure 7.11: Posterior probability distributions obtained from Bayesian analysis of the galactic model show that primary mass is $\sim 18 M_J$ and secondary mass is $\sim 5 M_J$ and the system is located in the bulge. The blue line indicates the median of the distribution.

When the light curve is explained by orbital motion of the lens, the ratio of projected kinetic energy to potential energy ($K.E._{\perp}/P.E.$) is calculated to verify whether the system is bound. This ratio is defined by a parameter (β) (Batista et al., 2011, Dong et al., 2009, Han et al., 2016, 2017a,b, 2018, Shin et al., 2013),

$$\beta = \frac{(r_{\perp}/AU)^3}{8\pi^2(M/M_{\odot})}\left[\left(\frac{1}{s}\frac{ds}{dt}\right)^2 + \left(\frac{d\alpha}{dt}\right)^2\right] \tag{7.2}$$

For $OGLE-2018-BLG-0380$, we find $\beta = 2.096 \pm 0.16$ which fails to satisfy the above condition. Having $\beta \geq 1$ means that the system is not physically bound. In the galactic bulge, due to high density of stars, it is possible that two isolated objects happen to form

a binary system in the plane of the sky. The lens properties are summarised in Table 7.7.

Lens and Source properties	
Parameter	$Value$
θ_E (mas)	0.19946 ± 0.004
D_L(pc)	$7523.35^{+510.04}_{-515.91}$
D_s(pc)	$8215.19^{+551.29}_{-539.05}$
$M(M_\odot)$	$0.21^{+0.12}_{-0.06}$
$M_1(M_\odot)$	$0.17^{+0.09}_{-0.05}$
$M_2(M_J)$	$48.51^{+26.67}_{-14.66}$
$r_\perp$ (AU)	0.89 ± 0.08
β	2.096 ± 0.16

Table 7.7: Lens mass, lens and source distance and parameter β estimated from Bayesian analysis of galactic model .

7.4 Discussion

In this chapter, I have presented the analysis for the microlensing event $OGLE-2018-BLG-0380$. This event had two peaks and a third perturbation on the decreasing side of the light curve. The third perturbation was covered well by the KMTNet-SAAO and KMTNet-CTIO telescopes in their fields BLG02 and BLG42 respectively. In the images of KMTNet-SSO and KMTNet-SAAO for the BLG42 field, the source star lies on the edge of the images. Thus, pyDIA was inaccurate in forming reference images and the resultant photometry was poor. The photometry was also not good enough for KMTNet-SSO BLG-02 field due to poor quality of images. Some OGLE outliers were also removed to model the event and constrain the parameters.

It was found that conventional methods of modelling failed to yield a light curve model with a third bump. Therefore the light curve was analysed heuristically and it was found that the third peak can be fitted with binary lens orbital motion. The orbital motion parameters were guessed in the orbital motion plane by keeping the separation between the masses constant and allowing the masses to rotate. The final model is explained by two masses nearly perpendicular to the line of site.

The location of the source and the blend on CMD suggests that the source is in the bulge while the blend is very faint and blue. Bayesian analysis of the galactic model, which is constrained by θ_E and t_E, suggests that the lens is comprised of a brown dwarf mass secondary orbiting a low mass stellar host at a distance of $7.52^{+0.51}_{-0.51}$ kpc. However, the ratio of the projected Kinetic energy to Potential energy is more than unity which suggests that the system is not bound. If this is indeed the case then this is the first microlensing event where two low mass unbound objects have formed a binary lens system.

Chapter 8

Summary

With the improvements in the technologies to detect gravitational microlensing events, we are able to detect several lens masses towards the galactic bulge. The involvement of the wide field survey groups like OGLE, MOA and KMTNet have increased the number of detections drastically in this decade. Out of these groups, KMTNet is monitoring the bulge round the clock (weather permitting) through its three different telescopes KMT-SAAO, KMT-CTIO and KMT-SSO. Due to continuous monitoring of the galactic bulge, KMTNet is proving useful in observing small scale perturbations in the light curve eg. as discussed in Chapter 5, Chapter 6 and Chapter 7.

This thesis shows the analysis of five microlensing events observed during 2017 and 2018 microlensing season. These events were detected by OGLE-EWS and also observed by KMTNet via its three telescopes. Chapter 1, discusses the background of gravitational microlensing and the analysis of the microlensing events. It also shows the modelling of the light curve if higher order effects like parallax and binary lens orbital motion are present in the light curve. Out of the different methods to characterise lens mass and distance using astrometry, follow-up observations with HST or Adaptive optics, this thesis discusses the computationally feasible idea to estimate the lens mass and distance using the knowledge of the galaxy in Chapter 2. The prior knowledge of the galaxy is used to infer the lens mass and distance for all the events analysed in this thesis. OGLE-2017-BLG-0192 and OGLE-2017-BLG-0103 are two events which occur close to the vernal equinox of 2017. However, due to large t_E, parallax degeneracies are broken in OGLE-2017-BLG-0192 but jerk-parallax degeneracy is detected in OGLE-2017-BLG-0103. Analysis of the jerk-parallax degeneracy is shown in Chapter 4. Use of Spitzer spacecraft to measure the space parallax for a relatively short t_E event is a challenging task as there is a delay between the decision of target and uploading the instructions

to Spitzer. However, if Spitzer telescope observes an event completely, it helps in determining the source and blend flux with a greater precision. Chapter 5 deals with OGLE-2017-BLG-1170, a Chang-Refsdal type of event which was observed with high cadence not only from the ground based observatories but also by Spitzer telescope. The dense monitoring of this event by all the telescopes was fitted by a light curve model which gives a pair of super-Jupiter mass objects having mass $3.06^{+1.34}_{-1.16}$ M_J and $1.85^{+0.79}_{0.70}$ M_J located at a distance of $7.57^{+0.49}_{-0.47}$ kpc in the galactic bulge. In Chapter 6, the analysis of the event OGLE-2018-BLG-1647 indicates a low mass primary and a super-Jupiter mass companion. The orbital parallax in this event was weakly detected and also showed the presence of the jerk-parallax degeneracy. It is shown that due to line caustics present in a binary lens, the jerk-parallax degeneracy for the binary lens microlensing events observed towards the galactic bulge can be realised by the substitution $(u_0, \alpha, \pi_{EN}) \rightarrow (u_0, \alpha, -\pi_{EN})$, $(u_0, \alpha, \pi_{EN}) \rightarrow (-u_0, -\alpha, \pi_{EN})$ and $(u_0, \alpha, \pi_{EN}) \rightarrow (-u_0, -\alpha, -\pi_{EN})$. The galactic model when constrained by the t_E and weakly measured π_E for each degenerate parallax solution gave a low mass binary system and a bimodal distribution for the lens distance. The system comprises of an $0.06^{+0.06}_{-0.03}$ $M_\odot$ 70% - 90% chance of it lying in the disc at a distance $\sim 1.63^{+1.01}_{-0.78}$ kpc. Chapter 7 discusses the modelling of the light curve of the event OGLE-2018-BLG-0380 where the short perturbation on the decreasing side of the light curve is explained by the orbital motion of the binary lens. The small perturbation was densely observed by KMTNet and so the KMTNet data helped in characterising the binary lens orbital motion in this event. There was no parallax information present in the light curve owing to the short timescale of the event. However, the presence of finite source effects was used to constrain the lens mass and distance using the galactic model. Bayesian analysis of the galactic model gave a binary lens in close separation having mass $0.17^{+0.09}_{-0.05}$ $M_\odot$ and $48.51^{+26.67}_{-14.66}$ M_J and at a distance of $7.49^{+0.51}_{-0.51}$ kpc. The mass of the lens and distance to the lens could be estimated with a greater precision if the parallax information was present in the light curve or if the event had been observed by Spitzer telescope.

The analysis of the binary lens events in this thesis have yielded low mass objects both in disc and bulge. These events show that there are pair of low mass objects in the galaxy which can be detected by gravitational microlensing. Unfortunately the binary lens events discussed in this thesis cannot be studied further by follow-up methods because of their faintness and large distance. Nevertheless, growing samples of such low mass binaries suggest that there is a big population of such objects or even isolated low mass objects present in the galaxy. There is a great potential of WFIRST satellite to characterise such objects and study their formation mechanisms.

Appendix A

Velocity of Earth around Sun

To find the velocity of the Earth around the sun in the ecliptic plane, we use the formalism of Soszyński et al. (2001). In this formalism, x-axis is defined as the line connecting Earth and Sun on vernal equinox, z-axis is the axis pointing towards the north ecliptic pole and therefor y-axis is the direction perpendicular to both. The co-ordinate system is shown in Figure (A.1).

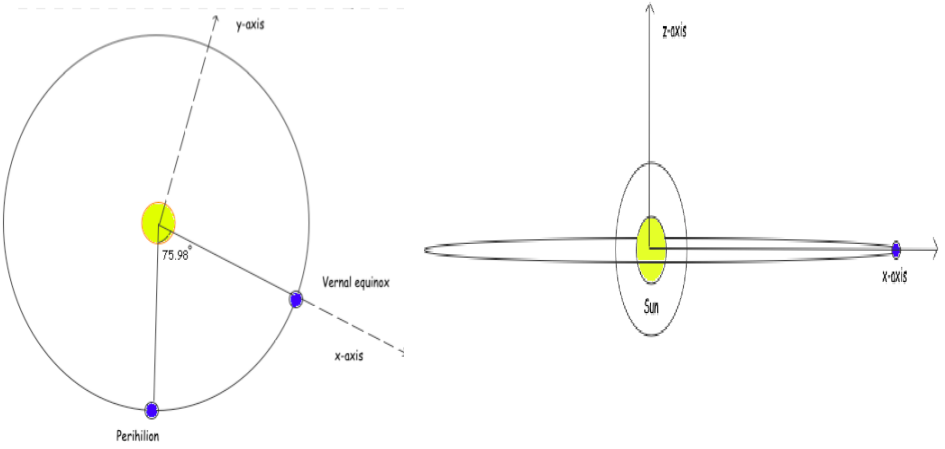

Figure A.1: The figures show the motion of the earth on the ecliptic plane around the sun . The left figure shows the face on view of the position of the earth revolving around sun and the edge-on view of the position of the earth revolving around sun. z-axis is perpendicular to the plane of the paper.

With this co-ordinate system, the x and y position of the earth in the ecliptic plane is

$$x_{\oplus}(t) = A(t)cos[\xi(t) - \phi_{\gamma}] \quad and \quad y_{\oplus}(t) = A(t)sin[\xi(t) - \phi_{\gamma}] \tag{A.1}$$

Here, $A(t) = AU(1 - \epsilon cos\Phi)$ is the mean earth-sun distance , $\xi(t) = \Phi + 2\epsilon sin(\Phi) =$ true anomaly of the earth, $\Phi = \frac{2\pi(t-t_p)}{365.25}$ is the phase of the earth's orbit, t_p is the time of

perihelion and $\phi_\gamma = 75.98^0$ is the difference in the ecliptic longitude difference between the perihelion and vernal equinox. To find the celestial velocity of the earth, we then take the derivative of this equations w.r.t. time:

$$v_{x,\oplus}(t) = -A(t)\frac{d\xi}{dt}sin[\xi(t) - \phi_\gamma] + \frac{dA(t)}{dt}cos[\xi(t) - \phi\gamma] \tag{A.2}$$

and

$$v_{y,\oplus}(t) = A(t)\frac{d\xi}{dt}cos[\xi(t) - \phi_\gamma] + \frac{dA(t)}{dt}sin[\xi(t) - \phi\gamma] \tag{A.3}$$

This gives us velocity of the earth as seen by Sun at time t $(v_x, v_y) = (v_{EN}, V_{EE})$. Here, all the arguments of the trigonometric functions are in radians. To find the projected position of the sun in the plane of the sky in ecliptic coordinates (τ_w, τ_n), we use the formula of An et al. (2002)

$$\tau_w = -A(t)sin(\xi(t) - \phi_\gamma - \lambda_0); \quad \tau_n = -A(t)cos(\xi(t) - \phi_\gamma - \lambda_0)sin(\beta_0) \tag{A.4}$$

where (λ_0, β_0) are the ecliptic co-ordinates of the event, $(\xi(t) - \phi_\gamma - \lambda_0)$ is the longitude difference between sun and the event.

Appendix B

Appendix B - Criteria for filtering the raw data

Here I show the criteria on which the data is filtered for each data set of each event discussed in the thesis. Since the location, time of observations, number of cadence fields and time of the event varies for each event, the condition of selecting good data points is different. This condition is only for KMTNet data, the images of which are reduced to photometry using pyDIA[1].

As discussed in Chapter 1, images reduced with pyDIA give us a vast information about the photometry of the event. This information consists the time of the observation[2], difference flux (δ_f), uncertainties in the difference flux ($d_{f,err}$), apparent magnitude (m), uncertainties in apparent magnitude (σ_m), quality factor denoting quality of the observation (Q), full width at half maximum of the PSF on the image (FWHM), roundness of the PSF on the image (Roundness), the sky level in the image (Sky) and the signal to noise in the image (Signal). These additional fields help us to identify and remove poor photometric measurements.

I have named KMT-A is for KMTNet -SSO, KMT-S for KMTNet-SAAO, KMT-C for KMTNet-CTIO. The numbers following the names of the telescopes are the KMTNet fields in which the event has been observed. KMT-CV or KMT-SV are the names for the observations done in V-band by KMTNet-CTIO or KMTNet-SAAO respectively.

[1]For OGLE, we have used the preliminary photometry which is available on their webpage for each event

[2]Time of observations are in Geocentric frame which are later converted to Heliocentric frame

Dataset	time (HJD-2450000)	δf	$\sigma(\delta f)$	*mag.*	σ(mag.)	Q	$FWHM$	*Roundness*	*Sky*	*Signal*
KMT-A02	-	-	-	-	≤ 0.1	≤ 2.0	≤ 10.0	≤ 1.15	≤ 1000.0	-
KMT-S02	-	-	-	-	-	≤ 2.0	≤ 10.0	≤ 1.15	≤ 950.0	-
KMT-C02	-	-	-	-	-	≤ 2.0	≤ 10.0	≤ 1.15	≤ 1050.0	-
KMT-CV	-	-	-	-	-	≤ 2.0	≤ 10.0	≤ 1.15	-	-

Table B.1: Data filtering criteria for the event OGLE-2017-BLG-0192.

B.1 OGLE-2017-BLG-0192

In the table below I show the criteria that I have used to select good data points for the event OGLE-2017-BLG-0192.

B.2 OGLE-2017-BLG-0103

In the table below I show the criteria that I have used to select good data points for the event OGLE-2017-BLG-0103.

Dataset	time (HJD-2450000)	δf	$\sigma(\delta f)$	*mag.*	σ(mag.)	Q	$FWHM$	*Roundness*	*Sky*	*Signal*
KMT-A02	-	-	-	-	≤ 0.1	-	≤ 2.5	-	≤ 2500.0	-
KMT-S02	-	-	-	-	≤ 0.1	≤ 1.2	≤ 2.0	≤ 1.3	≤ 3000.0	-
KMT-C02	-	-	-	-	≤ 0.1	-	≤ 2.5	-	≤ 2500.0	-
KMT-CV	-	-	-	-	≤ 0.1	≤ 1.0	≤ 1.8	≤ 1.2	-	-

Table B.2: Data filtering criteria for the event OGLE-2017-BLG-0103.

B.3 OGLE-2017-BLG-1170

In the table below I show the criteria that I have used to select good data points for the event OGLE-2017-BLG-1170.

Dataset	time (HJD-2450000)	δf	$\sigma(\delta f)$	*mag.*	σ(mag.)	Q	$FWHM$	*Roundness*	*Sky*	*Signal*
KMT-A11	-	-	-	-	-	≤ 2.0	≤ 10.0	≤ 2.0	-	-
KMT-S11	-	-	-	-	-	≤ 2.0	≤ 10.0	≤ 2.0	-	-
KMT-C11	-	-	-	-	-	≤ 2.0	≤ 10.0	≤ 2.0	-	-
KMT-CV	-	-	-	-	-	≤ 2.0	≤ 4.0	≤ 2.0	≤ 2000	-

Table B.3: Data filtering criteria for the event OGLE-2017-BLG-1170.

B.4 OGLE-2018-BLG-1647

In the table below I show the criteria that I have used to select good data points for the event OGLE-2018-BLG-1647.

Dataset	time (HJD-2450000)	δf	$\sigma(\delta f)$	*mag.*	σ(mag.)	Q	$FWHM$	*Roundness*	*Sky*	*Signal*
KMT-A01	-	-	-	$\leq$ 19.7	$\leq$ 0.1	$\leq$ 1.2	$\leq$ 2.5	$\leq$ 2.0	$\leq$ 2500	$\geq$ 400
KMT-S01	-	-	-	$\leq$ 19.50	$\leq$ 0.1	$\leq$ 1.5	$\leq$ 2.3	-	$\leq$ 2000	-
KMT-C01	-	-	-	$\leq$ 19.45	$\leq$ 0.1	$\leq$ 1.5	$\leq$ 2.2	-	$\leq$ 1800	-
KMT-A41	-	-	-	$\leq$ 19.70	$\leq$ 0.1	$\leq$ 1.1	$\leq$ 2.3	$\leq$ 1.3	$\leq$ 2800	$\geq$ 400
KMT-S41	-	-	-	-	$\leq$ 0.1	$\leq$ 1.5	$\leq$ 2.3	-	$\leq$ 2000	-
KMT-C41	-	-	-	$\leq$ 19.50	$\leq$ 0.1	$\leq$ 1.2	$\leq$ 2.2	-	$\leq$ 1800	-
KMT-CV	-	-	-	-	$\leq$ 0.1	-	-	-	-	-

Table B.4: Data filtering criteria for the event OGLE-2018-BLG-1647.

B.5 OGLE-2018-BLG-0380

In the table below I show the criteria that I have used to select good data points for the event OGLE-2018-BLG-0380.

Dataset	time (HJD-2450000)	δf	$\sigma(\delta f)$	*mag.*	σ(mag.)	Q	$FWHM$	*Roundness*	*Sky*	*Signal*
KMT-A02	-	-	-	$\leq$ 17.25	$\leq$ 0.1	$\leq$ 1.25	$\leq$ 2.5	-	$\leq$ 2500	$\geq$ 400
KMT-S02	-	-	-	$\leq$ 19.50	$\leq$ 0.1	$\leq$ 1.5	$\leq$ 2.3	-	$\leq$ 4500	$\geq$ 400
KMT-C02	-	-	-	$\leq$ 19.45	$\leq$ 0.1	$\leq$ 2.5	$\leq$ 3.0	-	-	$\geq$ 380
KMT-C42	-	-	-	$\leq$ 19.50	$\leq$ 0.1	$\leq$ 2.5	$\leq$ 2.2	-	$\leq$ 2500	$\geq$ 380
KMT-CV	-	-	-	-	-	-	$\leq$2.8	$\leq$2.0	-	-

Table B.5: Data filtering criteria for the event OGLE-2018-BLG-0380.

Bibliography

Agol, E., Kamionkowski, M., Koopmans, L. V. E., & Blandford, R. D. 2002, apj, 576, L131, doi: 10.1086/343758

Alard, C., & Lupton, R. H. 1998, apj, 503, 325, doi: 10.1086/305984

Albrow. 2017, doi: 10.5281/zenodo.268049

Albrow, M., Beaulieu, J.-P., Birch, P., et al. 1998, apj, 509, 687, doi: 10.1086/306513

Albrow, M. D., Beaulieu, J. P., Caldwell, J. A. R., et al. 1999, apj, 512, 672, doi: 10.1086/306820

Albrow, M. D., Beaulieu, J.-P., Caldwell, J. A. R., et al. 2000, apj, 534, 894, doi: 10.1086/308798

Albrow, M. D., An, J., Beaulieu, J.-P., et al. 2002, apj, 572, 1031, doi: 10.1086/340310

Albrow, M. D., Yee, J. C., Udalski, A., et al. 2018, apj, 858, 107, doi: 10.3847/1538-4357/aabf3f

Alcock, C., Allsman, R. A., Alves, D., et al. 1995, apjl, 454, L125, doi: 10.1086/309783

—. 1997a, apj, 479, 119, doi: 10.1086/303851

Alcock, C., Allen, W. H., Allsman, R. A., et al. 1997b, apj, 491, 436, doi: 10.1086/304974

Alcock, C., Allsman, R. A., Alves, D. R., et al. 2001, apj, 552, 582, doi: 10.1086/320554

An, J. H., Albrow, M. D., Beaulieu, J.-P., et al. 2002, apj, 572, 521, doi: 10.1086/340191

Aubourg, E., Bareyre, P., Bréhin, S., et al. 1993, nat, 365, 623, doi: 10.1038/365623a0

Aubourg, E., Bareyre, P., Bréhin, S., et al. 1994, in The Dark Side of the Universe - Experimental Efforts and Theoretical Framework, 69

Bachelet, E., Beaulieu, J.-P., Boisse, I., Santerne, A., & Street, R. A. 2018, apj, 865, 162, doi: 10.3847/1538-4357/aad63b

Bachelet, E., Shin, I.-G., Han, C., et al. 2012, apj, 754, 73, doi: 10.1088/0004-637X/754/1/73

Bahcall, J. N. 1999, ascl:9904.001, doi: 10.20356/C4RP4F

Barry, R. K., Bennett, D. P., Bhattacharya, A., et al. 2016, in American Astronomical Society Meeting Abstracts, Vol. 227, American Astronomical Society Meeting Abstracts #227, 106.03

Batista, V., Gould, A., Dieters, S., et al. 2011, aap, 529, A102, doi: 10.1051/0004-6361/201016111

Batista, V., Beaulieu, J.-P., Gould, A., et al. 2014, apj, 780, 54, doi: 10.1088/0004-637X/780/1/54

Beaulieu, J. P., Bennett, D. P., Batista, V., et al. 2016, apj, 824, 83, doi: 10.3847/0004-637X/824/2/83

Bennett, D., Akeson, R., Barclay, T., et al. 2019, in baas, Vol. 51, 149

Bennett, D. P. 2010, apj, 716, 1408, doi: 10.1088/0004-637X/716/2/1408

Bennett, D. P., Becker, A. C., Calitz, J. J., et al. 2002a, ArXiv Astrophysics e-prints

Bennett, D. P., Akerlof, C., Alcock, C., et al. 1993, in Texas/PASCOS '92: Relativistic Astrophysics and Particle Cosmology, ed. C. W. Akerlof & M. A. Srednicki, Vol. 688, 612

Bennett, D. P., Becker, A. C., Quinn, J. L., et al. 2002b, apj, 579, 639, doi: 10.1086/342225

Bennett, D. P., Bond, I. A., Udalski, A., et al. 2008, apj, 684, 663, doi: 10.1086/589940

Bennett, D. P., Batista, V., Bond, I. A., et al. 2014, apj, 785, 155, doi: 10.1088/0004-637X/785/2/155

Bennett, D. P., Akeson, R., Anderson, J., et al. 2018, arXiv e-prints, arXiv:1803.08564. https://arxiv.org/abs/1803.08564

Bensby, T., Feltzing, S., Gould, A., et al. 2017, aap, 605, A89, doi: 10.1051/0004-6361/201730560

Bessell, M. S., & Brett, J. M. 1988, pasp, 100, 1134, doi: 10.1086/132281

Bhattacharya, A., Bennett, D. P., Anderson, J., et al. 2017, apj, 154, 59, doi: 10.3847/1538-3881/aa7b80

Bodenheimer, P., & Pollack, J. B. 1986, icarus, 67, 391, doi: 10.1016/0019-1035(86)90122-3

Bond, I., Abe, F., Dodd, R., et al. 2001, Monthly Notices of the Royal Astronomical Society, 327, 868, doi: 10.1046/j.1365-8711.2001.04776.x

Bond, I. A., Abe, F., Dodd, R. J., et al. 2001, mnras, 327, 868, doi: 10.1046/j.1365-8711.2001.04776.x

—. 2002, mnras, 331, L19, doi: 10.1046/j.1365-8711.2002.05374.x

Bond, I. A., Udalski, A., Jaroszyński, M., et al. 2004, apj, 606, L155, doi: 10.1086/420928

Boss, A. P. 1997, Science, 276, 1836, doi: 10.1126/science.276.5320.1836

—. 2001, apj, 563, 367, doi: 10.1086/323694

Bowler, B. P., Liu, M. C., Shkolnik, E. L., & Tamura, M. 2014, IOP Publishing, 216, 7, doi: 10.1088/0067-0049/216/1/7

Bozza, V. 2000, aap, 355, 423

—. 2010, mnras, 408, 2188, doi: 10.1111/j.1365-2966.2010.17265.x

Bozza, V., Dominik, M., Rattenbury, N. J., et al. 2012, mnras, 424, 902, doi: 10.1111/j.1365-2966.2012.21233.x

Bozza, V., Shvartzvald, Y., Udalski, A., et al. 2016, apj, 820, 79, doi: 10.3847/0004-637X/820/1/79

Bramich, D. M., Horne, K., Albrow, M. D., et al. 2013, mnras, 428, 2275, doi: 10.1093/mnras/sts184

Calchi Novati, S., Gould, A., Udalski, A., et al. 2015a, apj, 804, 20, doi: 10.1088/0004-637X/804/1/20

Calchi Novati, S., Gould, A., Yee, J. C., et al. 2015b, apj, 814, 92, doi: 10.1088/0004-637X/814/2/92

Calchi Novati, S., Skowron, J., Jung, Y. K., et al. 2018, apj, 155, 261, doi: 10.3847/1538-3881/aac21c

Cassan, A., Kubas, D., Beaulieu, J. P., et al. 2012, nat, 481, 167, doi: 10.1038/nature10684

Chabrier, G. 2003, pasp, 115, 763, doi: 10.1086/376392

Chauvin, G., Vigan, A., Bonnefoy, M., et al. 2015, aap, 573, A127, doi: 10.1051/0004-6361/201423564

Choi, J., Dotter, A., Conroy, C., et al. 2016, apj, 823, 102, doi: 10.3847/0004-637X/823/2/102

Choi, J.-Y., Shin, I.-G., Han, C., et al. 2012, apj, 756, 48, doi: 10.1088/0004-637X/756/1/48

Chung, S.-J., Lee, C.-U., & Koo, J.-R. 2014, apj, 785, 128, doi: 10.1088/0004-637X/785/2/128

Chung, S.-J., Han, C., Park, B.-G., et al. 2005, apj, 630, 535, doi: 10.1086/432048

Chwolson, O. 1924, Astronomische Nachrichten, 221, 329

Clanton, C., & Gaudi, B. S. 2014, apj, 791, 91, doi: 10.1088/0004-637X/791/2/91

Claret, A. 2000, aap, 363, 1081

Cloutier, R., & Lin, M.-K. 2013, mnras, 434, 621, doi: 10.1093/mnras/stt1047

Dominik, M. 1998, aap, 330, 963. https://arxiv.org/abs/astro-ph/9701035

—. 1999, aap, 349, 108

—. 2006, mnras, 367, 669, doi: 10.1111/j.1365-2966.2006.10004.x

—. 2007, mnras, 377, 1679, doi: 10.1111/j.1365-2966.2007.11728.x

—. 2009, mnras, 393, 816, doi: 10.1111/j.1365-2966.2008.14276.x

Dominik, M., & Hirshfeld, A. C. 1996, aap, 313, 841

Dominik, M., & Sahu, K. C. 2000, apj, 534, 213, doi: 10.1086/308716

Dong, S., Udalski, A., Gould, A., et al. 2007, apj, 664, 862, doi: 10.1086/518536

Dong, S., Gould, A., Udalski, A., et al. 2009, apj, 695, 970, doi: 10.1088/0004-637X/695/2/970

Dotter, A. 2016, apjs, 222, 8, doi: 10.3847/0067-0049/222/1/8

Durisen, R. H., Boss, A. P., Mayer, L., et al. 2007, in Protostars and Planets V, ed. B. Reipurth, D. Jewitt, & K. Keil, 607

Dwek, E., Arendt, R. G., Hauser, M. G., et al. 1995, apj, 445, 716, doi: 10.1086/175734

Dyson, F. W., Eddington, A. S., & Davidson, C. 1923, memras, 62, A1

Einstein, A. 1936, Science, 84, 506, doi: 10.1126/science.84.2188.506

EROS Collaboration, Afonso, C., Alard, C., et al. 1998, aap, 337, L17. https://arxiv.org/abs/astro-ph/9806380

Fazio, G. G., Hora, J. L., Allen, L. E., et al. 2004, apjs, 154, 10, doi: 10.1086/422843

Foreman-Mackey, D., Hogg, D. W., Lang, D., & Goodman, J. 2013, Publications of the Astronomical Society of the Pacific, 125, 306, doi: 10.1086/670067

Fressin, F., Torres, G., Charbonneau, D., et al. 2013, , 766, 81, doi: 10.1088/0004-637X/766/2/81

Fukui, A., Gould, A., Sumi, T., et al. 2015, apj, 809, 74, doi: 10.1088/0004-637X/809/1/74

Gaudi, B. S. 1998, apj, 506, 533, doi: 10.1086/306256

—. 2010, arXiv e-prints, arXiv:1002.0332. https://arxiv.org/abs/1002.0332

Gaudi, B. S., & Gould, A. 1997a, apj, 477, 152, doi: 10.1086/303670

—. 1997b, apj, 486, 85, doi: 10.1086/304491

Goodman, J., & Weare, J. 2010, Communications in Applied Mathematics and Computational Science, Vol. 5, No. 1, p. 65-80, 2010, 5, 65, doi: 10.2140/camcos.2010.5.65

Gould, A. 1992, apj, 392, 442, doi: 10.1086/171443

—. 1995, apj, 447, 491, doi: 10.1086/175893

—. 2000, apj, 542, 785, doi: 10.1086/317037

—. 2004, apj, 606, 319, doi: 10.1086/382782

Gould, A. 2007, in American Institute of Physics Conference Series, Vol. 943, The Science Opportunities of the Warm Spitzer Mission Workshop, ed. L. J. Storrie-Lombardi & N. A. Silbermann, 215–220

—. 2008, apj, 681, 1593, doi: 10.1086/588601

Gould, A., & Horne, K. 2013, apjl, 779, L28, doi: 10.1088/2041-8205/779/2/L28

Gould, A., & Loeb, A. 1992, apj, 396, 104, doi: 10.1086/171700

Gould, A., Miralda-Escude, J., & Bahcall, J. N. 1994, apjl, 423, L105, doi: 10.1086/187247

Gould, A., & Yee, J. C. 2012, apjl, 755, L17, doi: 10.1088/2041-8205/755/1/L17

Gould, A., Udalski, A., Monard, B., et al. 2009, apjl, 698, L147, doi: 10.1088/0004-637X/698/2/L147

Gould, A., Dong, S., Gaudi, B. S., et al. 2010, apj, 720, 1073, doi: 10.1088/0004-637X/720/2/1073

Griest, K. 1991, apj, 366, 412, doi: 10.1086/169575

Griest, K., & Hu, W. 1992, apj, 397, 362, doi: 10.1086/171793

Griest, K., & Safizadeh, N. 1998, apj, 500, 37, doi: 10.1086/305729

Han, C. 2003, in Astronomical Society of the Pacific Conference Series, Vol. 289, The Proceedings of the IAU 8th Asian-Pacific Regional Meeting, Volume 1, ed. S. Ikeuchi, J. Hearnshaw, & T. Hanawa, 431–439

Han, C. 2006, apj, 638, 1080, doi: 10.1086/498937

—. 2009, apj, 700, 945, doi: 10.1088/0004-637X/700/2/945

Han, C., & Gould, A. 1995, apj, 447, 53, doi: 10.1086/175856

Han, C., Udalski, A., Gould, A., et al. 2016, apj, 828, 53, doi: 10.3847/0004-637X/828/1/53

Han, C., Udalski, A., Bozza, V., et al. 2017a, apj, 843, 87, doi: 10.3847/1538-4357/aa762f

Han, C., Udalski, A., Gould, A., et al. 2017b, apj, 834, 82, doi: 10.3847/1538-4357/834/1/82

Han, C., Jung, Y. K., Udalski, A., et al. 2018, apj, 867, 136, doi: 10.3847/1538-4357/aae536

Hearnshaw, J. B., Abe, F., Bond, I. A., et al. 2005, The MOA 1.8-metre alt-az wide-field survey telescope and the MOA project. https://arxiv.org/abs/astro-ph/0509420

Howard, A. W., Marcy, G. W., Johnson, J. A., et al. 2010, Science, 330, 653, doi: 10.1126/science.1194854

Hwang, K.-H., Han, C., Udalski, A., et al. 2011, mnras, 413, 1244, doi: 10.1111/j.1365-2966.2011.18206.x

Hwang, K.-H., Choi, J.-Y., Bond, I. A., et al. 2013, apj, 778, 55, doi: 10.1088/0004-637X/778/1/55

Hwang, K.-H., Kim, H.-W., Kim, D.-J., et al. 2018, Journal of Korean Astronomical Society, 51, 197, doi: 10.5303/JKAS.2018.51.6.197

Hwang, K.-H., Ryu, Y.-H., Kim, H.-W., et al. 2019, apj, 157, 23, doi: 10.3847/1538-3881/aaf16e

Ida, S. 2019, Formation of Planetary Systems, ed. A. Yamagishi, T. Kakegawa, & T. Usui, 179

Jaki, S. L. 1978, Foundations of Physics, 8, 927, doi: 10.1007/BF00715064

Jiang, G., DePoy, D. L., Gal-Yam, A., et al. 2004, apj, 617, 1307, doi: 10.1086/425678

Jung, Y. K., Udalski, A., Yee, J. C., et al. 2017, apj, 153, 129, doi: 10.3847/1538-3881/aa5d07

Jung, Y. K., Hwang, K.-H., Ryu, Y.-H., et al. 2018a, apj, 156, 208, doi: 10.3847/1538-3881/aae319

Jung, Y. K., Udalski, A., Gould, A., et al. 2018b, apj, 155, 219, doi: 10.3847/1538-3881/aabb51

Jurić, M., Ivezić, Ž., Brooks, A., et al. 2008, apj, 673, 864, doi: 10.1086/523619

Kains, N., Street, R. A., Choi, J.-Y., et al. 2013, aap, 552, A70, doi: 10.1051/0004-6361/201220626

Kains, N., Calamida, A., Sahu, K. C., et al. 2017, apj, 843, 145, doi: 10.3847/1538-4357/aa78eb

Kervella, P., Thévenin, F., Di Folco, E., & Ségransan, D. 2004, aap, 426, 297, doi: 10.1051/0004-6361:20035930

Kim, H.-W., Hwang, K.-H., Shvartzvald, Y., et al. 2018, arXiv e-prints, arXiv:1806.07545. https://arxiv.org/abs/1806.07545

Kim, S.-L., Lee, C.-U., Park, B.-G., et al. 2016, Journal of Korean Astronomical Society, 49, 37, doi: 10.5303/JKAS.2016.49.1.037

Kiraga, M., & Paczynski, B. 1994, apjl, 430, L101, doi: 10.1086/187448

Koshimoto, N., Udalski, A., Beaulieu, J. P., et al. 2017, apj, 153, 1, doi: 10.3847/1538-3881/153/1/1

Kuiper, G. P. 1951, Proceedings of the National Academy of Science, 37, 1, doi: 10.1073/pnas.37.1.1

Liu, L. 2008, Bioinformatics, 24, 2542, doi: 10.1093/bioinformatics/btn484

Ma, S., Mao, S., Ida, S., Zhu, W., & Lin, D. N. C. 2016, mnras, 461, L107, doi: 10.1093/mnrasl/slw110

Mao, S., & Paczynski, B. 1991, apj, 374, L37, doi: 10.1086/186066

Mao, S., Smith, M. C., Woźniak, P., et al. 2002, mnras, 329, 349, doi: 10.1046/j.1365-8711.2002.04986.x

Matsuo, T., Shibai, H., Ootsubo, T., & Tamura, M. 2007, apj, 662, 1282, doi: 10.1086/517964

McDougall, A., & Albrow, M. D. 2016, mnras, 456, 565, doi: 10.1093/mnras/stv2609

Metropolis, N., Rosenbluth, A. W., Rosenbluth, M. N., Teller, A. H., & Teller, E. 1953, jcp, 21, 1087, doi: 10.1063/1.1699114

Miyake, N., Udalski, A., Sumi, T., et al. 2012, apj, 752, 82, doi: 10.1088/0004-637X/752/2/82

Miyazaki, S., Sumi, T., Bennett, D. P., et al. 2018, apj, 156, 136, doi: 10.3847/1538-3881/aad5ee

Mizuno, H. 1980, Progress of Theoretical Physics, 64, 544, doi: 10.1143/PTP.64.544

Mizuno, H., Nakazawa, K., & Hayashi, C. 1978, Progress of Theoretical Physics, 60, 699, doi: 10.1143/PTP.60.699

Mordasini, C., Alibert, Y., Benz, W., & Naef, D. 2008, Astronomical Society of the Pacific Conference Series, Vol. 398, Giant Planet Formation by Core Accretion, ed. D. Fischer, F. A. Rasio, S. E. Thorsett, & A. Wolszczan, 235

Mróz, Przemek, Udalski, A., et al. 2019, aap, 622, A201, doi: 10.1051/0004-6361/201834557

Mróz, P., Udalski, A., Skowron, J., et al. 2017, nat, 548, 183, doi: 10.1038/nature23276

Muraki, Y., Han, C., Bennett, D. P., et al. 2011, apj, 741, 22, doi: 10.1088/0004-637X/741/1/22

Nataf, D. M., Gould, A., Fouqué, P., et al. 2013, apj, 769, 88, doi: 10.1088/0004-637X/769/2/88

Nielsen, E. L., & Close, L. M. 2010, The Astrophysical Journal, 717, 878, doi: 10.1088/0004-637x/717/2/878

Paczynski, B. 1986, apj, 304, 1, doi: 10.1086/164140

—. 1991, apj, 371, L63, doi: 10.1086/186003

Park, B.-G., DePoy, D. L., Gaudi, B. S., et al. 2004, apj, 609, 166, doi: 10.1086/420926

Park, H., Han, C., Gould, A., et al. 2014, apj, 787, 71, doi: 10.1088/0004-637X/787/1/71

Paxton, B., Bildsten, L., Dotter, A., et al. 2011, apjs, 192, 3, doi: 10.1088/0067-0049/192/1/3

Paxton, B., Cantiello, M., Arras, P., et al. 2013, apjs, 208, 4, doi: 10.1088/0067-0049/208/1/4

Paxton, B., Marchant, P., Schwab, J., et al. 2015, apjs, 220, 15, doi: 10.1088/0067-0049/220/1/15

Paxton, B., Schwab, J., Bauer, E. B., et al. 2018, apjs, 234, 34, doi: 10.3847/1538-4365/aaa5a8

Pejcha, O., & Heyrovský, D. 2009, apj, 690, 1772, doi: 10.1088/0004-637X/690/2/1772

Penny, M. T., Gaudi, B. S., Kerins, E., et al. 2019, The Astrophysical Journal Supplement Series, 241, 3, doi: 10.3847/1538-4365/aafb69

Penny, M. T., Henderson, C. B., & Clanton, C. 2016, apj, 830, 150, doi: 10.3847/0004-637X/830/2/150

Perryman, M. 2011, The Exoplanet Handbook

Poindexter, S., Afonso, C., Bennett, D. P., et al. 2005, apj, 633, 914, doi: 10.1086/468182

Poleski, R., Zhu, W., Christie, G. W., et al. 2016, apj, 823, 63, doi: 10.3847/0004-637X/823/1/63

Poleski, R., Gaudi, B. S., Udalski, A., et al. 2018, apj, 156, 104, doi: 10.3847/1538-3881/aad45e

Pollack, J. B., Hubickyj, O., Bodenheimer, P., et al. 1996, icarus, 124, 62, doi: 10.1006/icar.1996.0190

Refsdal, S. 1966, mnras, 134, 315, doi: 10.1093/mnras/134.3.315

Renn, J., Sauer, T., & Stachel, J. 1997, Science, 275, 184, doi: 10.1126/science.275.5297.184

Rhie, S. H., & Bennett, D. P. 1996, Nuclear Physics B Proceedings Supplements, Vol. 51, 51, 86, doi: 10.1016/S0920-5632(96)00487-2

Robin, A. C., Reylé, C., Derrière, S., & Picaud, S. 2003, aap, 409, 523, doi: 10.1051/0004-6361:20031117

Ryu, Y.-H., Han, C., Hwang, K.-H., et al. 2010, apj, 723, 81, doi: 10.1088/0004-637X/723/1/81

Ryu, Y.-H., Yee, J. C., Udalski, A., et al. 2018, apj, 155, 40, doi: 10.3847/1538-3881/aa9be4

Sako, T., Sekiguchi, T., Sasaki, M., et al. 2008, Experimental Astronomy, 22, 51, doi: 10.1007/s10686-007-9082-5

Santerne, A., Beaulieu, J. P., Rojas Ayala, B., et al. 2016, aap, 595, L11, doi: 10.1051/0004-6361/201527710

Schneider, P., & Weiss, A. 1986, aap, 164, 237

Schramm, T., & Kayser, R. 1987, aap, 174, 361

Shan, Y., Yee, J. C., Udalski, A., et al. 2019, apj, 873, 30, doi: 10.3847/1538-4357/ab0021

Shin, I.-G., Han, C., Gould, A., et al. 2012, apj, 760, 116, doi: 10.1088/0004-637X/760/2/116

Shin, I.-G., Sumi, T., Udalski, A., et al. 2013, apj, 764, 64, doi: 10.1088/0004-637X/764/1/64

Shin, I.-G., Udalski, A., Yee, J. C., et al. 2018, apj, 863, 23, doi: 10.3847/1538-4357/aacdf4

Shvartzvald, Y., Udalski, A., Gould, A., et al. 2015, apj, 814, 111, doi: 10.1088/0004-637X/814/2/111

Shvartzvald, Y., Maoz, D., Udalski, A., et al. 2016a, mnras, 457, 4089, doi: 10.1093/mnras/stw191

Shvartzvald, Y., Li, Z., Udalski, A., et al. 2016b, apj, 831, 183, doi: 10.3847/0004-637X/831/2/183

Shvartzvald, Y., Yee, J. C., Calchi Novati, S., et al. 2017, apjl, 840, L3, doi: 10.3847/2041-8213/aa6d09

Shvartzvald, Y., Yee, J. C., Skowron, J., et al. 2018, arXiv e-prints. https://arxiv.org/abs/1805.08778

Skowron, J., Udalski, A., Gould, A., et al. 2011, apj, 738, 87, doi: 10.1088/0004-637X/738/1/87

Skowron, J., Ryu, Y. H., Hwang, K. H., et al. 2018, actaa, 68, 43, doi: 10.32023/0001-5237/68.1.2

Smith, M. C. 2003, mnras, 343, 1172, doi: 10.1046/j.1365-8711.2003.06753.x

Smith, M. C., Belokurov, V., Evans, N. W., Mao, S., & An, J. H. 2005, mnras, 361, 128, doi: 10.1111/j.1365-2966.2005.09147.x

Smith, M. C., Mao, S., & Paczyński, B. 2003, mnras, 339, 925, doi: 10.1046/j.1365-8711.2003.06183.x

Soszyński, I., Żebruń, K., Woźniak, P. R., et al. 2001, apj, 552, 731, doi: 10.1086/320582

Spergel, D., Gehrels, N., Baltay, C., et al. 2015, arXiv e-prints, arXiv:1503.03757. https://arxiv.org/abs/1503.03757

Street, R. A., Udalski, A., Calchi Novati, S., et al. 2016, apj, 819, 93, doi: 10.3847/0004-637X/819/2/93

Street, R. A., Lund, M. B., Donachie, M., et al. 2018, arXiv e-prints. https://arxiv.org/abs/1812.04445

Sumi, T., Abe, F., Bond, I. A., et al. 2003, apj, 591, 204, doi: 10.1086/375212

Suzuki, D., Bennett, D. P., Sumi, T., et al. 2016, apj, 833, 145, doi: 10.3847/1538-4357/833/2/145

Suzuki, D., Bennett, D. P., Ida, S., et al. 2018, apj, 869, L34, doi: 10.3847/2041-8213/aaf577

Tsapras, Y., Street, R., Horne, K., et al. 2009, Astronomische Nachrichten, 330, 4, doi: 10.1002/asna.200811130

Tuomi, M., Jones, H. R. A., Barnes, J. R., Anglada-Escudé, G., & Jenkins, J. S. 2014, mnras, 441, 1545, doi: 10.1093/mnras/stu358

Udalski, A. 2003, actaa, 53, 291

Udalski, A., & Szymanski, M. 1995, iaucirc, 6164, 1

Udalski, A., Szymanski, M., Kaluzny, J., et al. 1994, actaa, 44, 227

Udalski, A., Szymański, M. K., & Szymański, G. 2015a, actaa, 65, 1. https://arxiv.org/abs/1504.05966

Udalski, A., Jung, Y. K., Han, C., et al. 2015b, apj, 812, 47, doi: 10.1088/0004-637X/812/1/47

Wang, T., Calchi Novati, S., Udalski, A., et al. 2018, apj, 860, 25, doi: 10.3847/1538-4357/aabcd2

Will, C. M. 1988, American Journal of Physics, 56, 413, doi: 10.1119/1.15622

Witt, H. J. 1990, aap, 236, 311

Witt, H. J., & Mao, S. 1995, apjl, 447, L105, doi: 10.1086/309566

Woźniak, P., & Paczyński, B. 1997, apj, 487, 55, doi: 10.1086/304607

Yee, J. C. 2015, apjl, 814, L11, doi: 10.1088/2041-8205/814/1/L11

Yee, J. C., Udalski, A., Sumi, T., et al. 2009, apj, 703, 2082, doi: 10.1088/0004-637X/703/2/2082

Yee, J. C., Shvartzvald, Y., Gal-Yam, A., et al. 2012, apj, 755, 102, doi: 10.1088/0004-637X/755/2/102

Yee, J. C., Albrow, M., Barry, R. K., et al. 2014, arXiv e-prints, arXiv:1409.2759. https://arxiv.org/abs/1409.2759

Yee, J. C., Udalski, A., Calchi Novati, S., et al. 2015a, apj, 802, 76, doi: 10.1088/0004-637X/802/2/76

Yee, J. C., Gould, A., Beichman, C., et al. 2015b, apj, 810, 155, doi: 10.1088/0004-637X/810/2/155

Yoo, J., DePoy, D. L., Gal-Yam, A., et al. 2004, apj, 603, 139, doi: 10.1086/381241

Zhu, W., Gould, A., Beichman, C., et al. 2015, apj, 814, 129, doi: 10.1088/0004-637X/814/2/129

Zhu, W., Calchi Novati, S., Gould, A., et al. 2016, apj, 825, 60, doi: 10.3847/0004-637X/825/1/60

Zhu, W., Udalski, A., Calchi Novati, S., et al. 2017, apj, 154, 210, doi: 10.3847/1538-3881/aa8ef1